RAPID AND DYNAMIC LOAD TESTING OF INSTRUMENTED PZ27 STEEL SHEET PILES

by

Corey Danton Rice

A dissertation submitted to the faculty of
The University of North Carolina at Charlotte
in partial fulfillment of the requirements
for the degree of Doctor of Philosophy in
Civil Engineering

Charlotte

2020

Approved by:

_____
Dr. Matthew Whelan

_____
Dr. David Weggel

_____
Dr. Miguel Pando

_____
Dr. Howie Fang

_____
Dr. Vincent Ogunro

_____
Dr. Tara Cavalline

©2020
Corey Danton Rice
ALL RIGHTS RESERVED

ABSTRACT

COREY DANTON RICE. Rapid and Dynamic Load Testing of Instrumented PZ27 Steel Sheet Piles. (Under the direction of DR. MATTHEW WHELAN)

Pile foundations are typically used for structures underlain by weaker soils in order to increase the soil resistance and, subsequently, the axial capacity. In bridge abutments, sheet piles are typically used as facing elements for soil retention and scour control, however using these facing elements in the axial bearing foundation design is growing in interest. Currently, no guidance on the design of the sheet pile facing elements as axial load bearing members nor guidance on the use of rapid or dynamic testing of sheet piles for axial load capacity estimation is available. This dissertation produces full-scale rapid and dynamic load tests on instrumented steel sheet piles and performs in-depth analysis of the measurement data, in parallel with static load test measurements obtained from the same piles, to assess the application of a variety of different established methodologies for obtaining estimates of the axial load bearing capacity and load transfer mechanisms.

Rapid load tests are classified to include loads with a duration greater than 5 but less than 5000 relative wavelengths, which produce significant dynamic soil resistance but are long enough in duration such that some complex dynamic phenomena, including stress wave propagation, are insignificant. This type of testing has been shown to predict the static axial bearing capacity more consistently than dynamic load testing, but requires larger equipment and setup than dynamic load testing. Several methodologies exist to analyze the results from rapid load tests, including the Unloading Point method, Modified Unloading Point method, Segmental Unloading Point method, and Embedded Data Collector method.

In addition, there are also analysis methodologies that aid in estimating soil damping and rate effects that develop during a rapid load test. This dissertation presents a full-scale rapid load testing experimental program, in which four instrumented PZ27 sheet piles installed in a laboratory geotechnical pit are subjected to a large number of rapid loads varying in duration and amplitude. The Unloading Point method, Modified Unloading Point method, Segmental Unloading Point method, and Embedded Data Collector method are applied to the measurement data and the performance of each method in estimating the static soil resistance and load transfer are evaluated by comparison to direct measurements obtained from a static load test. Damping constants and rate effect parameters are also estimated using various methodologies described in the literature. The results are compared to empirical recommendations developed for bearing piles and the variation in these damping and rate effect parameters with load duration and amplitude is investigated.

Dynamic load tests are classified to include loads with a duration less than 5 relative wavelengths, which is short enough in duration that complex dynamic phenomena, including stress wave propagation, are significant. This type of testing is particularly advantageous because it can be applied during driven pile installation and restrike testing, but it requires more complicated analysis methods to develop an estimate of the axial bearing capacity from the measurement data. The most common methods of analyzing the results of a dynamic load test are a relatively simple wave analysis approach called the Case method and a signal matching technique that involves inverse identification of parameters in nonlinear soil-structure interaction models within an analytical model of the pile. This dissertation presents a full-scale dynamic load testing experimental program, where a pair of instrumented PZ27 sheet piles and an instrumented H-pile are driven at a field site in

Matthews, North Carolina. Dynamic testing of both piles is conducted during restrike testing performed one week after installation and subsequent static load testing is performed to obtain a direct measurement of the axial capacity and load transfer mechanisms. Total static axial bearing capacities are estimated from the pile driving measurements using the Case method and an automated signal matching program. The application of these methods to sheet piles is evaluated through comparison of the results to the static load test and to the results obtained for the reference H-pile. The variation of soil-structure interaction behavior with successive blows during driving, as estimated by the dynamic methods, is further investigated.

ACKNOWLEDGMENTS

I would like to, first, express my deepest gratitude and appreciation for Dr. Matthew Whelan whose guidance, support, encouragement, and patience was a cornerstone in completing this work. I would also like to express many thanks to Dr. David Weggel and Dr. Miguel Pando in their support and belief in my abilities to initiate and complete my PhD. I am also extremely grateful for the guidance and support of Dr. Howie Fang, Dr. Tara Cavalline, and Dr. Vincent Ogunro.

Second, I cannot begin to express my thanks to Dr. Youngjin Park and Mike Moss. Without your invaluable expertise and extensive practical insight, the extensive testing involved in this work would have not been possible.

Next, I also wish to thank Dr. Matthew Sylvain for being a great colleague and friend in this journey of studying sheet piles. Thank you for your willingness to discuss many different topics through many late nights, your dedication to understanding everything we learned through the projects involved in this work, and your continued support.

I would like to gratefully acknowledge the assistance and support of the Graduate Assistantship Program, the Department of Civil and Environmental Engineering, the Graduate School, the University of North Carolina at Charlotte, and the North Carolina Department of Transportation.

Finally, my most sincere thanks goes to my family and friends for their unwavering support, advice, and patience in this journey of mine to complete this doctoral work. I hope this work serves as encouragement for anyone in my family to show that you can be anything you want to be if you work hard and never give up.

TABLE OF CONTENTS

LIST OF FIGURES x

LIST OF TABLES xxiv

CHAPTER 1: BACKGROUND 1

1.1. Background 1

1.2. Motivation, Objectives, and Scope of Research 4

1.3. Organization of Dissertation 7

CHAPTER 2: RAPID LOAD TESTING 10

2.1. Background of Rapid Load Testing 10

2.1.1. Unloading Point Method 12

2.1.2. Modified Unloading Point Method 15

2.1.3. Segmental Unloading Point Method 17

2.1.4. Embedded Data Collector Method 20

2.2. Other Considerations for Rapid Load Testing 26

2.2.1. Damping Force Determination 27

2.2.2. Pore Water Pressure Effects 33

2.2.3. Rate Effects 35

2.2.4. Plugging Effects 37

CHAPTER 3: DYNAMIC TESTING 40

3.1. Basic Wave Mechanics 40

3.2. Solution of the Wave Equation 43

3.2.1. Finite Difference Method 43

3.2.2. Method of Characteristics 44

3.3. Dynamic Testing Equipment, Procedure, and Interpretation 59

3.4. Case Method 60

3.5. Signal Matching 62

CHAPTER 4: EXPERIMENTAL TESTING OF SHEET PILES IN LABORATORY AND FIELD INSTALLATIONS 68

4.1. Laboratory Rapid Load Testing 68

4.1.1. Instrumentation for Rapid Load Test 72

4.1.2. Laboratory Setup for Rapid Load Testing 82

4.1.3. Rapid Test Program and Procedures 86

4.1.4. Static Load Testing and Capacity Estimate of Laboratory Piles 90

4.2. Field Dynamic Testing 93

4.2.1. Instrumentation for Dynamic Testing 97

4.2.2. Dynamic Test Program and Procedures 106

4.2.3. Static Load Testing and Capacity Estimate of Field Piles 113

CHAPTER 5: ANALYSIS AND DISCUSSION OF RAPID LOAD TESTS 122

5.1. Unloading Point Method 124

5.2. Modified Unloading Point Method 126

5.3. Segmental Unloading Point Method 127

5.4. Embedded Data Collector Method 135

5.5. Damping Force Determination 140

5.5.1. Time Invariant Damping Estimates 140

5.5.2. Back Calculated Time Variant Damping Constant 144

5.5.3. Rate Dependent Damping Constants 156

CHAPTER 6: ANALYSIS AND RESULTS OF DYNAMIC TESTS 168

6.1. Case Method 169

6.2. Pile Dynamic Analysis Signal Matching 173

6.2.1. Soil-Structure Interaction Model 173

6.2.2. Proposed Parameter Identification Routine 175

6.2.3. Verification of Method of Characteristics Routine 178

6.3. Application to Field Measurements 183

6.3.1. Definition of Match Quality 183

6.3.2. Application of Automated Signal Matching to Field Measurements 186

6.3.3. Comparison of Capacity and Load Transfer Estimates to Static Load Test 190

6.4. Variation in Parameter Estimates Across Blows and Optimization Runs 199

CHAPTER 7: CONCLUSION 209

7.1. Summary 209

7.2. Conclusions 211

7.3. Future Work 216

REFERENCES 219

APPENDIX A: Additional Test Information 224

APPENDIX B: Additional Information for Rapid Load Test 227

APPENDIX C: Additional Information for Dynamic Load Test 250

LIST OF FIGURES

FIGURE 1.1: Classification of loading type and significance of phenomena affecting the pile response (from Poulos (1998)) 2

FIGURE 1.2: Qualitative trends of LRFD resistance factors 4

FIGURE 2.1: Free body diagram of forces during rapid load testing 12

FIGURE 2.2: Examples of static response estimate based on hyperbolic fits of a) one rapid load test and b) multiple rapid load tests 14

FIGURE 2.3: Representation of Modified Unloading Point method model 16

FIGURE 2.4: Representation of Segmental Unloading Point model 18

FIGURE 2.5: EDC toe bearing model 22

FIGURE 2.6: EDC Side friction model 26

FIGURE 2.7: Determination of damping constant using time history analysis of rapid load test data (modified from Mullins et al. (2001)) 28

FIGURE 2.8: Schematic of volumetric change during pile loading 29

FIGURE 2.9: Comparing response from the RLT to the SLT to determine the variable damping constant, c 29

FIGURE 2.10: Relation between variable damping constant and volumetric change (adapted from Stokes et al. (2008)) 30

FIGURE 2.11: Rapid force to static force ratio in relation to the drainage factor (from Holscher et al. (2012)) 35

FIGURE 2.12: Effective depth of cross section for sheet pile plug 38

FIGURE 3.1: Stress equilibrium in a differential axial element within a homogeneous rod subjected to a force 41

FIGURE 3.2: Wave equation models of pile foundation 43

FIGURE 3.3: Method of characteristics simulation of wave propagation in a pile with a free toe boundary condition (black lines used for head and toe positions while the red line used for measured location) 50

FIGURE 3.4: Example force time histories at a fictitious measurement site for a pile with a free toe boundary condition 51

FIGURE 3.5: Method of characteristics simulation of wave propagation in a pile with a fixed toe boundary condition (black lines used for head and toe positions while the red line used for measurement location) 53

FIGURE 3.6: Example force time histories at a fictitious measurement site for a pile with a fixed toe boundary condition 54

FIGURE 3.7: Typical nonlinear elasto-plastic static soil resistance model used for dynamic pile analysis and signal matching 55

FIGURE 3.8: Dynamic soil resistance models 56

FIGURE 3.9: Method of characteristics simulation of wave propagation in a pile with side friction resistance at a discrete location and a free toe boundary condition (black lines used for head and toe positions while the red line used for measurement location) 58

FIGURE 3.10: Example force time histories at a fictitious measurement site for a pile with side friction at a discrete location and a free toe boundary condition 59

FIGURE 3.11: Example force time histories from measurement instrumentation of a dynamic load test to be used for the Case method axial capacity estimation 61

FIGURE 3.12: Zones used in the signal matching process (from Hannigan et al. (2016)) 65

FIGURE 4.1: Photograph of geotechnical pit used for laboratory tests 69

FIGURE 4.2: Stratigraphy and in-situ test results for laboratory pit (from Sylvain (2019)) 70

FIGURE 4.3: Grain size distribution for soil used in the geotechnical pit in Structural Highbay Laboratory of the EPIC building at UNC Charlotte (from Sylvain (2019)) 70

FIGURE 4.4: Location and numbering scheme of sheet piles (red indicates piles with below grade instrumentation) 71

FIGURE 4.5: Photographs of the pile driving process 72

FIGURE 4.6: Photograph of reusable strain transducer and high shock accelerometer installed on the laboratory pile 74

FIGURE 4.7: Sensor schematic for laboratory testing 76

FIGURE 4.8: Sensor locations across cross section of laboratory test pile 77

FIGURE 4.9: Alignment of bondable resistive strain gages along the centerline of the flange during installation 78

FIGURE 4.10: Photograph of installed and wired bondable resistive strain gage with protective coating 79

FIGURE 4.11: Cover plates over subgrade instrumentation 80

FIGURE 4.12: Placement of an LVDT on each pile web to measure displacement 81

FIGURE 4.13: Design and configuration of pile head system 84

FIGURE 4.14: Pore water pressure time history for rapid load tests 88

FIGURE 4.15: Typical time histories for applied load and pile displacement during a rapid load test 89

FIGURE 4.16: Example of applied load versus head displacement response of a pile during a rapid load test 90

FIGURE 4.17: Head load versus displacement response of the laboratory pile wall from static load test 91

FIGURE 4.18: Load transfer along the length of the pile measured form the SLT 92

FIGURE 4.19: Experimental t-z load transfer curves for laboratory static axial load test of sheet pile wall based on strain gage layout 93

FIGURE 4.20: Experimental Q-z load transfer curve for laboratory static axial load test of sheet pile wall 93

FIGURE 4.21: Field site prior to installation (Note: leftmost bucket indicates future sheet pile location, rightmost bucket indicates future H-pile location) 95

FIGURE 4.22: Stratigraphy and in-situ test results for the field site 95

FIGURE 4.23: Grain size distribution for soil near the sheet pile at the Matthews, NC site used for dynamic load testing (from Sylvain (2019)) 96

FIGURE 4.24: Sensor configuration at pile head for field tests 99

FIGURE 4.25: Overview of instrumentation for dynamic testing 101

FIGURE 4.26: Photographs of string potentiometers installed on test piles 103

FIGURE 4.27: Photograph of welded and bonded cover plate on field piles 104

FIGURE 4.28: Tapered end of cover plate at pile toe 105

FIGURE 4.29: Setup of impact hammer for restrike 107

FIGURE 4.30: Typical dynamic force and velocity for sheet pile driving restrike test 109

FIGURE 4.31: Typical dynamic force and velocity for H-pile driving restrike test 109

FIGURE 4.32: Typical up-wave and down-wave forces in sheet pile during restrike test 110

FIGURE 4.33: Typical up-wave and down-wave forces in H-pile during restrike test 110

FIGURE 4.34: Displacement records from string potentiometer during restrike testing 112

FIGURE 4.35: Maximum energy transfer per blow displacement for sheet pile and H-pile 113

FIGURE 4.36: Schematics of static load test setup for field site 114

FIGURE 4.37: Photographs of static load test setup for field site 115

FIGURE 4.38: Static head load-displacement response of the field PZ27 pair (from Sylvain (2019)) 117

FIGURE 4.39: Static head load-displacement response of the field HP12x53 (from Sylvain (2019)) 118

FIGURE 4.40: Experimental force distribution along the depth of the pile during the field static axial load test of the sheet pile pair (from Sylvain (2019)) 119

FIGURE 4.41: Experimental t-z load transfer curves for field static axial load test of sheet pile pair based on strain gage layout (from Sylvain (2019)) 120

FIGURE 4.42: Experimental t-z load transfer curves for field static axial load test of sheet pile pair based on geotechnical stratigraphy (from Sylvain (2019)) 120

FIGURE 4.43: Experimental Q-z load transfer curve for field static axial load test of sheet pile pair (from Sylvain (2019)) 121

FIGURE 5.1: Summary of all rapid load test responses at the head of the pile group 123

FIGURE 5.2: Comparison of all rapid load test responses to the static load test response 123

FIGURE 5.3: Separation of forces for the pulse corresponding to 6Hz and 0.40in peak input displacement 125

FIGURE 5.4: Derived unloading points and envelope used to estimate the static load versus displacement response 125

FIGURE 5.5: Determination of rate effect correction parameter 126

FIGURE 5.6: Calculated accelerations used in UP method and MUP method 127

FIGURE 5.7: Experimental t-z curves developed from SUP method and SLT for the layer from 0in to 34in in depth 129

FIGURE 5.8: Experimental t-z curves developed from SUP method and SLT for the layer from 34in to 49in in depth 130

FIGURE 5.9: Experimental t-z curves developed from SUP method and SLT for the layer from 49in to 64in depth 130

FIGURE 5.10: Experimental t-z curves developed from SUP method and SLT for the layer from 64in to 79in in depth 131

FIGURE 5.11: Experimental t-z curves develop from SUP method and SLT for total side friction resistance 132

FIGURE 5.12: Load transfer along length of pile a) derived by the SUP method with $\eta = 0.80$ and b) measured from the SLT 133

FIGURE 5.13: Comparison of the toe resistance estimated by SUP method to the toe resistance measured in the SLT 134

FIGURE 5.14: Comparison of experimentally derived static load versus displacement response of obtained by the SUP method to the SLT and UP method 135

FIGURE 5.15: Measured axial acceleration and numerically integrated velocities and displacements at the toe for rapid load tests 137

FIGURE 5.16: Energy and force balance obtained by minimizing the objective function and force components estimated using the optimal parameter set 139

FIGURE 5.17: Comparison between toe resistance obtained from static load test and static toe resistance estimated by EDC method (unloading shown as dashed line) 140

FIGURE 5.18: Estimating the damping constant for 6Hz 0.40in pulse using the UP method 142

FIGURE 5.19: Comparison of forces in time domain using constant damping estimated by Mullins et al. (2002) for 6Hz 0.40in pulse 142

FIGURE 5.20: Comparison of force displacement response using a time invariant damping constant for 6Hz 0.40in pulse 143

FIGURE 5.21: Average damping constant for all applied pulses in RLT plotted as a function of the measured peak displacement 143

FIGURE 5.22: Comparing response from the RLT to the SLT to determine the variable damping constant, c which now includes the contribution of forces produced from pore water pressure effects 145

FIGURE 5.23: Determination of rate effect correction factor for 6Hz pulse with 0.40 in input displacement 146

FIGURE 5.24: Rate effect correction factors obtained for each individual RLT plotted as a function of the peak measured displacement 147

FIGURE 5.25: Comparison of force components in the from rapid load test using computed time variant damping constant for the 6Hz pulse with input peak displacement of 0.40in 148

FIGURE 5.26: Time variant damping constants back calculated for the 6Hz pulses plotted as a function of measured displacement 150

FIGURE 5.27: Time variant damping constants back calculated for the 4Hz pulses plotted as a function of measured displacement 151

FIGURE 5.28: Time variant damping constants back calculated for the 2Hz pulses plotted as a function of measured displacement 151

FIGURE 5.29: Time variant damping constants back calculated for the 1Hz pulses plotted as a function of measured displacement 152

FIGURE 5.30: Comparison of time variant damping constants calculated for the largest amplitude load pulses 153

FIGURE 5.31: Time variant damping constants back calculated for the 6Hz pulses plotted as a function of measured velocity 154

FIGURE 5.32: Time variant damping constants back calculated for the 4Hz pulses plotted as a function of measured velocity 154

FIGURE 5.33: Time variant damping constants back calculated for the 2Hz pulses plotted as a function of measured velocity 155

FIGURE 5.34: Time variant damping constants back calculated for the 1Hz pulses plotted as a function of measured velocity 155

FIGURE 5.35: Estimated static load versus displacement response for the 6Hz 0.40in pulse using empirical damping constants for sand and clay from Randolph and Deeks (1992) 157

FIGURE 5.36: Estimated static load versus displacement response for the 4Hz 0.40in pulse using empirical damping constants for sand and clay from Randolph and Deeks (1992) 158

FIGURE 5.37: Estimated static load versus displacement response for the 2Hz 0.50in pulse using empirical damping constants for sand and clay from Randolph and Deeks (1992) 158

FIGURE 5.38: Estimated static load versus displacement response for the 1Hz 0.50in pulse using empirical damping constants for sand and clay from Randolph and Deeks (1992) 159

FIGURE 5.39: Estimated static load versus displacement response for the 6Hz 0.40in pulse using empirical damping constants based on plasticity index 160

FIGURE 5.40: Estimated static load versus displacement response for the 4Hz 0.40in pulse using empirical damping constants based on plasticity index 161

FIGURE 5.41: Estimated static load versus displacement response for the 2Hz 0.50in pulse using empirical damping constants based on plasticity index 161

FIGURE 5.42: Estimated static load versus displacement response for the 1Hz 0.50in pulse using empirical damping constants based on plasticity index 162

FIGURE 5.43: Calculated rate dependent damping constant, α, obtained using the SLT data in parallel with the RLT measurements 163

FIGURE 5.44: Estimated rate dependent damping constant, α, as a function of peak measured displacement for the RLT pulses 164

FIGURE 5.45: Estimated rate dependent damping constant, α, as a function of peak measured velocity for the RLT pulses 164

FIGURE 5.46: Estimated static load versus displacement response for the 6Hz 0.40in pulse using damping constants computed using the SLT 166

FIGURE 5.47: Estimated static load versus displacement response for the 4Hz 0.40in pulse using damping constants computed using the SLT 166

FIGURE 5.48: Estimated static load versus displacement response for the 2Hz 0.50in pulse using damping constants computed using the SLT 167

FIGURE 5.49: Estimated static load versus displacement response for the 1Hz 0.50in pulse using damping constants computed using the SLT 167

FIGURE 6.1: Case method total dynamic resistance at the instance of maximum internal force for sheet pile and H-pile 170

FIGURE 6.2: Case damping coefficient back calculated at the instance of maximum internal force for sheet pile and H-pile 170

FIGURE 6.3: Case method analysis results for sheet pile 172

FIGURE 6.4: Representation of pile elevation and corresponding analytical model 175

FIGURE 6.5: Schematic of FEA models used to verify the developed method of characteristics software routine 179

FIGURE 6.6: Load applied to the head of the pile in the models used for verification of the developed software routine 180

FIGURE 6.7: Forces in downward and upward traveling waves for Case #1 verification 181

FIGURE 6.8: Forces in downward and upward traveling waves for Case #2 verification 182

FIGURE 6.9: Forces in downward and upward traveling waves for Case #3 verification 182

FIGURE 6.10: Modified definitions of match quality zones superimposed on typical force measurement signal 184

FIGURE 6.11: Modified definitions of match quality zones superimposed on typical pile head displacement 185

FIGURE 6.12: Representative signal match for the upward traveling wave from one blow 191

FIGURE 6.13: Predicted load transfer in the sheet pile and H-pile from the average parameter estimates obtained from signal matching 193

FIGURE 6.14: Side friction resistance shown as t-z curves from parameters identified through the traditional MQ definition signal match of the sheet pile 195

FIGURE 6.15: Side friction resistance shown as t-z curves from parameters identified through the RSS definition signal match of the sheet pile 195

FIGURE 6.16: Side friction resistance shown as t-z curves from parameters identified through the traditional MQ definition signal match of the H-pile 196

FIGURE 6.17: Side friction resistance shown as t-z curves from parameters identified through the RSS definition signal match of the H-pile 196

FIGURE 6.18: Toe bearing resistance shown as q-z curve from parameters identified through the traditional MQ definition signal match of the sheet pile 198

FIGURE 6.19: Toe bearing resistance shown as Q-z curve from parameters identified through the RSS definition signal match of the sheet pile 198

FIGURE 6.20: Distributions of shaft, toe, and total resistance obtained when applying the RSS match quality definition for signal matching of the sheet pile blows (red line equates to total static capacity from corresponding SLT) 200

FIGURE 6.21: Distributions of shaft, toe, and total resistance found through the RSS definition signal match of the H-pile (red line equates to total static capacity from corresponding SLT) 201

FIGURE 6.22: Distributions of shaft, toe, and total resistance found through the traditional MQ definition signal match of the sheet pile (red line equates to total static capacity from corresponding SLT) 201

FIGURE 6.23: Distributions of shaft, toe, and total resistance found through the traditional MQ definition signal match of the H-pile (red line equates to total static capacity from corresponding SLT) 202

FIGURE 6.24: Change of shaft, toe, and total resistance estimated through the traditional MQ definition signal matching routine of sheet pile 204

FIGURE 6.25: Change of shaft, toe, and total resistance estimated through the traditional MQ definition signal matching routine of H-pile 204

FIGURE 6.26: Variation of shaft, toe, and total resistance estimated from signal matching routine using the RSS match quality definition of the sheet pile 205

FIGURE 6.27: Variation of shaft, toe, and total resistance estimated from signal matching routine using the RSS match quality definition of H-pile 205

FIGURE 6.28: Distributions of parameters found through the traditional match quality definition signal match of the sheet pile 207

FIGURE 6.29: Distributions of parameters found through the traditional match quality definition signal match of the H-pile 208

FIGURE B.1: Separation of forces for the pulse corresponding to 6Hz and 0.35in peak input displacement 227

FIGURE B.2: Separation of forces for the pulse corresponding to 6Hz and 0.25in peak input displacement 228

FIGURE B.3: Separation of forces for the pulse corresponding to 6Hz and 0.20in peak input displacement 228

FIGURE B.4: Separation of forces for the pulse corresponding to 6Hz and 0.15in peak input displacement 229

FIGURE B.5: Separation of forces for the pulse corresponding to 6Hz and 0.10in peak input displacement 229

FIGURE B.6: Separation of forces for the pulse corresponding to 4Hz and 0.40in peak input displacement 230

FIGURE B.7: Separation of forces for the pulse corresponding to 4Hz and 0.35in peak input displacement 230

FIGURE B.8: Separation of forces for the pulse corresponding to 4Hz and 0.30in peak input displacement 231

FIGURE B.9: Separation of forces for the pulse corresponding to 4Hz and 0.25in peak input displacement 231

FIGURE B.10: Separation of forces for the pulse corresponding to 4Hz and 0.20in peak input displacement 232

FIGURE B.11: Separation of forces for the pulse corresponding to 4Hz and 0.15in peak input displacement 232

FIGURE B.12: Separation of forces for the pulse corresponding to 4Hz and 0.10in peak input displacement 233

FIGURE B.13: Separation of forces for the pulse corresponding to 2Hz and 0.50in peak input displacement 233

FIGURE B.14: Separation of forces for the pulse corresponding to 2Hz and 0.40in peak input displacement 234

FIGURE B.15: Separation of forces for the pulse corresponding to 2Hz and 0.30in peak input displacement 234

FIGURE B.16: Separation of forces for the pulse corresponding to 2Hz and 0.20in peak input displacement 235

FIGURE B.17: Separation of forces for the pulse corresponding to 2Hz and 0.10in peak input displacement 235

FIGURE B.18: Separation of forces for the pulse corresponding to 1Hz and 0.50in peak input displacement 236

FIGURE B.19: Separation of forces for the pulse corresponding to 1Hz and 0.40in peak input displacement 236

FIGURE B.20: Separation of forces for the pulse corresponding to 1Hz and 0.30in peak input displacement 237

FIGURE B.21: Separation of forces for the pulse corresponding to 1Hz and 0.20in peak input displacement 237

FIGURE B.22: Separation of forces for the pulse corresponding to 1Hz and 0.10in peak input displacement 238

FIGURE B.23: Estimating the damping constant for 6Hz and 0.30in pulse using the UP method 238

FIGURE B.24: Estimating the damping constant for 6Hz and 0.25in pulse using the UP method 239

FIGURE B.25: Estimating the damping constant for 6Hz and 0.20in pulse using the UP method 239

FIGURE B.26: Estimating the damping constant for 6Hz and 0.15in pulse using the UP method 240

FIGURE B.27: Estimating the damping constant for 6Hz and 0.10in pulse using the UP method 240

FIGURE B.28: Estimating the damping constant for 4Hz and 0.40in pulse using the UP method 241

FIGURE B.29: Estimating the damping constant for 4Hz and 0.35in pulse using the UP method 241

FIGURE B.30: Estimating the damping constant for 4Hz and 0.30in pulse using the UP method 242

FIGURE B.31: Estimating the damping constant for 4Hz and 0.25in pulse using the UP method 242

FIGURE B.32: Estimating the damping constant for 4Hz and 0.20in pulse using the UP method 243

FIGURE B.33: Estimating the damping constant for 4Hz and 0.15in pulse using the UP method 243

FIGURE B.34: Estimating the damping constant for 4Hz and 0.10in pulse using the UP method 244

FIGURE B.35: Estimating the damping constant for 2Hz and 0.50in pulse using the UP method 244

FIGURE B.36: Estimating the damping constant for 2Hz and 0.40in pulse using the UP method 245

FIGURE B.37: Estimating the damping constant for 2Hz and 0.30in pulse using the UP method 245

FIGURE B.38: Estimating the damping constant for 2Hz and 0.20in pulse using the UP method 246

FIGURE B.39: Estimating the damping constant for 2Hz and 0.10in pulse using the UP method 246

FIGURE B.40: Estimating the damping constant for 1Hz and 0.50in pulse using the UP method 247

FIGURE B.41: Estimating the damping constant for 1Hz and 0.40in pulse using the UP method 247

FIGURE B.42: Estimating the damping constant for 1Hz and 0.30in pulse using the UP method 248

FIGURE B.43: Estimating the damping constant for 1Hz and 0.20in pulse using the UP method 248

FIGURE B.44: Estimating the damping constant for 1Hz and 0.10in pulse using the UP method 249

FIGURE C.1: Distributions of parameters found through the RSS definition signal match of the sheet pile 258

FIGURE C.2: Distributions of parameters found through the RSS definition signal match of the H-pile 259

LIST OF TABLES

TABLE 2.1: Damping constants (modified from Holscher et al. (2012)) 33

TABLE 2.2: Summary of empirical rate effect correction factor from tests (adapted from Holscher et al. (2012)) 37

TABLE 3.1: Case damping factors 62

TABLE 3.2: Recommended bounds for parameters in soil-structure interaction models for dynamic testing of axially loaded piles from Rausche et al. (2010) 63

TABLE 4.1: Perimeter (P) and area (A) of laboratory sheet piles without and with cover plates 80

TABLE 4.2: Summary of actual peak displacements applied to pile head from each of the rapid load tests 87

TABLE 4.3: Summary of final pile set developed from each of the rapid load tests 87

TABLE 4.4: Perimeter (P) and area (A) of field piles without and with cover plates 105

TABLE 5.1: Toe resistance model parameters identified by EDC method 139

TABLE 6.1: Identified optimal Case damping coefficients for the Case method at the instance of maximum static resistance 172

TABLE 6.2: Parameter bounds used in the signal matching routine for analysis of the field tests 188

TABLE 6.3: Average of identified soil-structure interaction parameters across all blows (note: values in italics are summations and not independent parameter estimates) 190

TABLE A.1: Instrumentation information for rapid load tests 225

TABLE A.2: Instrumentation information for dynamic load tests 226

TABLE C.1: Identified resistance parameters for sheet pile Using the RSS definition 251

TABLE C.2: Identified resistance parameters for H-Pile using the RSS definition 252

TABLE C.3: Identified other parameters for sheet piles using RSS match quality definition 253

TABLE C.4: Identified other parameters for H-pile using RSS match quality definition 254

TABLE C.5: Identified resistance parameters for sheet pile Using the traditional MQ definition 255

TABLE C.6: Identified resistance parameters for H-Pile using the traditional MQ definition 256

TABLE C.7: Identified resistance parameters for H-pile using traditional MQ definition 256

TABLE C.8: Identified other parameters for H-pile using traditional MQ definition 257

CHAPTER 1: BACKGROUND

1.1 Background

In-situ tests of pile foundations can be classified based on the significance of various phenomena affecting the pile response. The development of several aspects of the dynamic soil resistance and the significance of these phenomena depend on the duration of the loading relative to the pile characteristics. Figure 1.1 presents established criteria for classifying different loading types, as well as the significance of certain phenomena that contribute to the soil resistance, and likewise the pile response, within each respective loading regime (Poulos (1998)). By the criteria presented in this figure, dynamic loads are classified as those with a loading duration of less than 5 relative wavelengths, rapid loads are classified as those with a loading duration greater than 5 but less than 500 relative wavelengths, and static loads are those with a loading duration greater than 500 relative wavelengths. The relative wavelength is defined as:

$$\lambda = \frac{c_L t_l}{2L} \tag{1.1}$$

where c_L is the characteristic longitudinal wave speed for the pile material, t_l is the relative loading duration, and L is the length of the pile.

It can be seen that certain phenomena qualitatively have more influence on the pile response as the relative duration of the loading is shortened. For example, all of the phenomena listed are potentially present with significant influence within dynamic pile testing,

which leads to greater complexity in analyzing the soil-pile interaction. Rapid load testing yields a moderately less complex scenario, since the longer loading duration does not generate significant stress wave propagation and radiation damping and viscous damping are less apparent when testing is performed in sandy soils. Static load tests provide a direct means of measuring the static soil-structure interaction resistance because the long duration of loading essentially eliminates any dynamic forces in most scenarios. As indicated by Figure 1.1, the loading rate for static tests performed in clay soils needs to be slower than for static tests performed in sandy soils to reduce the presence of viscous damping and effects of excess pore water pressures developed as a result of changes in the soil-structure interaction during the test.

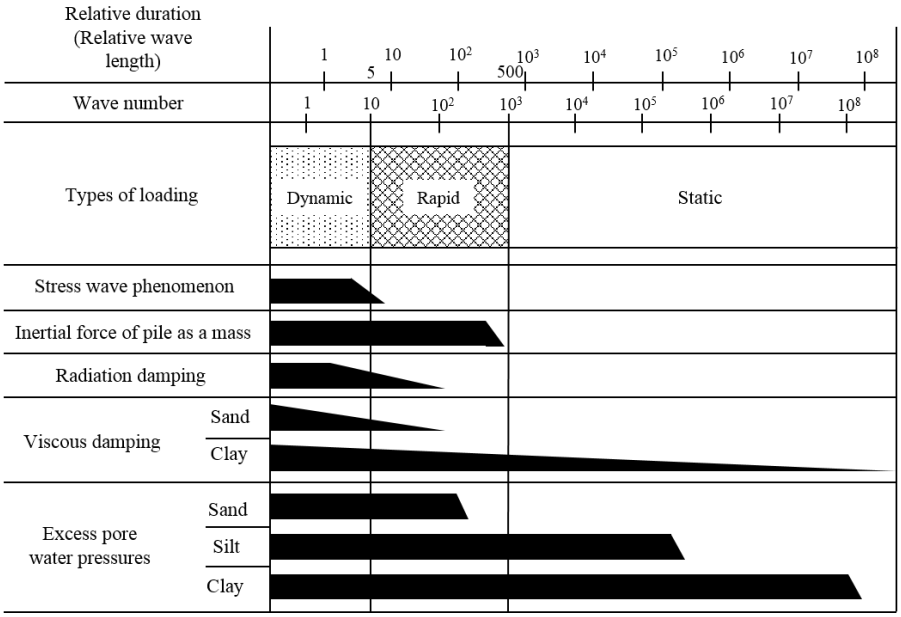

Figure 1.1: Classification of loading type and significance of phenomena affecting the pile response (from Poulos (1998))

The design of axially loaded pile foundations, including piles in bridge abutments, relies on the use of static methods to estimate the capacity of the pile, which is then confirmed

through either field testing or refined capacity estimates developed from wave equation analysis. For piles in bridge foundations, AASHTO (2016) specifies resistance factors for the design axial strength of pile elements that depend on the method used to confirm the static axial capacity. Figure 1.2 presents the AASHTO resistance factors associated with acceptable methods for developing the axial static capacity estimate. As reflected in the figure, the resistance factor, and consequently the design strength, depends significantly on the methodology used. At the extremes, a foundation where the static axial capacity is determined using only the Engineering News dynamic formula would require eight times as many nominally identical piles as the same foundation where the pile capacity was determined using a static test combined with dynamic testing of 2% of the piles in the foundation. However, the reduced material cost provided by the increased reliability offered by static testing requires the trade off of extensive time and effort required to setup and perform a static load test at a construction site. Dynamic and rapid testing have been pursued as a compromise between reliance on dynamic formula or wave equation analysis that are penalized by very low resistance factors and static load testing, as dynamic and rapid load tests can be performed without assembling large reaction structures at the field site and can be completed much quicker than static load tests. However, as previously noted, dynamic and rapid load tests invoke significant time dependent phenomena in the soil-structure interaction that make the interpretation of such tests more challenging. In some cases, empirical corrections and specialized soil-structure interaction models are required for the accurate interpretation of dynamic and rapid field tests.

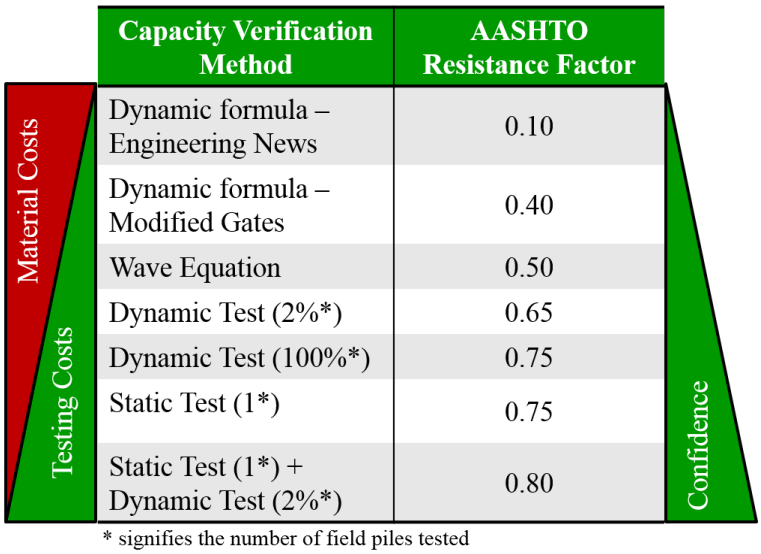

Capacity Verification Method	AASHTO Resistance Factor
Dynamic formula – Engineering News	0.10
Dynamic formula – Modified Gates	0.40
Wave Equation	0.50
Dynamic Test (2%*)	0.65
Dynamic Test (100%*)	0.75
Static Test (1*)	0.75
Static Test (1*) + Dynamic Test (2%*)	0.80

* signifies the number of field piles tested

Figure 1.2: Qualitative trends of LRFD resistance factors

1.2 Motivation, Objectives, and Scope of Research

AASHTO does not provide specific guidance on the design of sheet pile facing elements as axial load bearing members nor is guidance on the use of dynamic testing of sheet pile facing for load capacity estimation available. The Eurocode (2007) does give some special considerations for sheet piles, such as compactness criteria for elements of the cross section, but in general there is no specific guidance related to obtaining axial load capacity estimates of sheet piles from dynamic testing. The majority of the literature on the dynamic axial response of sheet piles involves studies investigating the driveability of this particular type of driven pile (Deckner et al. (2015); Holeyman (1993); Holeyman and Whenham (2017); Viking (2002); Whenham et al. (2009)).

Review of published literature revealed one case study where dynamic testing was performed on sheet piles to estimate their axial load bearing capacity. Underwood and Greenlee (2010) presents the use of AZ type sheet pile as axial bearing elements within parking

structures, in which two examples consisted of sheet pile foundations designed as an end bearing piles on shallow bedrock, and two other examples consisted of sheet pile foundations design as friction piles. In this study, Pile Driving Analysis (PDA) was applied to measurements obtained during dynamic testing with an impact hammer, after being vibratory driven to the final embedment depth, to estimate the axial bearing capacity of the sheet piles used for the parking structure and estimate the skin friction resistance above and below the groundwater table. The unit skin friction resistances were estimated based on conventional analysis of piles, design experience, and relationships developed from full-scale static axial load testing of instrumented sheet pile walls. The axial capacities were determined through PDA to be in the range of 150-250kip per single AZ sheet pile, which were driven to approximately 24ft below grade into soils that were noted to be generally granular outwash, alluvial soil, and granular glacial till. The authors noted that the PDA interpretation of results differed from that applied with conventional H-piles, however they did not explicitly explain the differences in interpretation or speculate on reasons for the differences (Underwood et al. (2019)). The study concluded that additional test data is needed to draw better conclusions on difference in skin friction capacities for sheet piles installed in granular soils both above and below the groundwater table.

Although the existing literature on dynamic testing of steel sheet piles is very limited, the available studies suggest that unique empirical corrections or specialized soil-structure interaction models may be required for the accurate interpretation of either dynamic or rapid load test measurements. This dissertation seeks to add to the limited experimental literature on dynamic and rapid testing of steel sheet piles and assess the performance of established methods for interpreting these field measurements that are conventionally

applied to H-piles to arrive at estimates of the static axial bearing capacity and load transfer down the length of the pile.

While valuable guidance on rapid load testing of piles, in general, is given by Hannigan et al. (2016), Holscher et al. (2012) provides in-depth interpretation guidelines for rapid load testing on piles. The guidelines provide considerations for estimating the magnitude of, and compensating for, damping and inertia forces as well as rate effects from the rapid load test in order to accurately estimate the static axial capacity of a pile. Most damping parameters are based on empirical data, thus this dissertation looks to contribute additional data to the literature by producing empirical data for sheet pile sections as well as more generally evaluate the use of the provided guidance for determining damping forces and rate effects during a rapid load test. Additionally, a newer method, called the Embedded Data Collector method, has been introduced by Tran et al. (2016) to provide an efficient way to determine side friction and toe bearing capacity contributions during a rapid load test using additional instrumentation installed at the toe of the pile. This dissertation applies several methodologies for analysis of rapid load test data based on unloading point measurements, as well as the Embedded Data Collector method, to a suite of rapid load tests performed at different load durations and amplitudes on a sheet pile wall installed in a laboratory geotechnical pit. The performance of each methodology is assessed by comparing the static axial load capacity, side friction resistance distribution, and toe bearing resistance estimates to direct measurements of the static soil resistance and load transfer obtained from a static load test.

Similarly to the rapid load tests guidance, Hannigan et al. (2016) also provides guidance for performing and analyzing dynamic measurements obtained during driving of piles

to obtain estimates of static load capacity and soil-structure interaction models. Conventionally used signal matching programs prove to be a valuable way to estimate static axial capacity of piles during installation and restrike. However, it has been noted that the estimation of static axial capacity of piles can be influenced by the engineer performing the test and results for the identified parameters in the soil-structure interaction models may not be unique, or may not be representative of the actual underlying physical behavior, due to the challenges associated with inverse analysis with a large set of uncertain parameters, with nonlinear system behavior, and in the presence of measurement uncertainties (Rausche et al. (2010)). Likins et al. (2012) discusses the development of a quick and automatic signal matching program for determining important static and dynamic soil properties that would provide a time savings in determining the static axial bearing capacity of piles. This dissertation aims to contribute to the knowledge base on automated signal matching by applying a global optimization algorithm to perform the inverse identification of parameters in soil-structure interaction models for a pair of sheet piles and a single H-pile installed at a field site. Different match quality functions for model correlation are evaluated and the variability in the identified parameters across different blows are explored. Estimates of the static load capacity and load transfer obtained from applying the signal matching routines to the pile driving measurements are compared to direct measurements of these quantities obtained through static load testing.

1.3 Organization of Dissertation

The outline of this dissertation is as follows:

- Chapter 2 provides an overview of traditional and newly developed methodologies

used in analyzing rapid load test data to arrive at estimates for the static axial load capacity of, and load transfer in, driven piles. This overview includes details on the Unloading Point method, Modified Unloading Point method, Segmental Unloading Point method, and Embedded Data Collector method. Methods for estimating damping coefficients, as well as considerations and empirical corrections, for rate effects, pore water pressure, and plugging are discussed.

- Chapter 3 provides an overview of methodologies used in analyzing dynamic load test data to arrive at estimates for the static axial load capacity of, and load transfer in, driven piles. This chapter reviews basic one-dimensional wave mechanics and methodologies for solving the wave equation to analyze the response of piles under impact loading. This overview includes the Case method and signal matching analysis used to predict the static axial load capacity of driven piles from instrumentation placed at the head of the pile during driving.

- Chapter 4 presents the experimental testing programs conducted on instrumented steel sheet piles for this dissertation research. The instrumentation and test setup is described in detail for rapid load tests conducted on an instrumented group of sheet piles installed in a laboratory geotechnical pit as well as for dynamic load tests conducted on an instrumented pair of sheet piles and an H-pile installed at a field site. For both locations, measured axial static load capacity and load transfer obtained through static load tests are presented.

- Chapter 5 provides results, analysis, and discussion from the rapid load tests on the sheet piles at the laboratory site. This chapter includes analysis produced using the

Unloading Point method, Modified Unloading Point method, Segmental Unloading Point method, and Embedded Data Collector method. Furthermore, rate effect correction factors are developed for the experimental analysis and damping coefficients are calculated for different loading rates and amplitudes. The rate effect correction factors and damping coefficients developed through experimental estimates are compared to empirical values and models from the literature.

- Chapter 6 provides the results, analysis, and discussion from the dynamic load tests on the sheet piles and H-pile at a field site. This chapter includes Case method analysis as well as signal matching applied after numerical verification of routines developed to implement the method of characteristics for the solution of the wave equation. Automated signal matching is performed using a global optimization technique and the performance of the parameter identification is assessed by comparing the estimated static axial load capacity and load transfer down the length of the pile to measurements obtained from the static test program.

- Chapter 7 presents a summary of the dissertation and conclusions related to the application and interpretation of rapid load testing and dynamic load testing of sheet piles. This chapter also provides recommendations for future research on rapid and dynamic load testing, with specific focus on the use of these method to assess the axial load capacity of steel sheet piles.

CHAPTER 2: RAPID LOAD TESTING

2.1 Background of Rapid Load Testing

Rapid load testing has been developed over the past several decades as an economical alternative to static load testing of deep foundations. This type of loading has been defined by the relative loading duration on the piling system, as shown in Figure 1.1. Rapid loads are characterized by a loading duration that is short enough that dynamic phenomena are significant factors during the test, but long enough such that the effects of longitudinal stress waves are insignificant. There have been multiple loading devices that have been developed to generate this type of loading in the field, which include the Dynatest (Gonin (1984)), Statnamic (Janes and Bermingham (1986))), Pseudo-Static Pile Load Tester (Schellingerhout and Revoort (1996)), and the Spring Hammer Device (Matsuzawa et al. (2008)). The most common method for applying the rapid load is the Statnamic loading method, where an ignition device propels a large mass vertically away from the pile head, thus applying, through the reaction force, a large load to the pile system. The mass is then retained by a catching apparatus to avoid subsequent impact loading of the pile. Typically, a load cell is attached to the head of the pile and a pair of accelerometers are installed on the pile to measure the force and acceleration at the pile head, respectively. However, numerous instrumentation schemes and data analysis approaches have been developed for use with rapid load testing of piles and these approaches will be reviewed in subsequent subsections

of this chapter. Specifically, the Unloading Point Method (UP), the Modified Unloading Point Method (MUP), the Segmental Unloading Point Method (SUP), and the Embedded Data Collector Method (EDC) will be summarized. Furthermore, different techniques to account for damping and rate effects will be reviewed.

Regardless of the method or device used to generate the rapid loading, the general consensus is that the equation of motion for a single degree of freedom (SDOF) model is an appropriate simplified model for interpreting forces within the pile system during rapid loading due to the absence of significant stress wave phenomenon. A free body diagram of a SDOF pile model is shown in Figure 2.1 and the accompanying equation of motion is provided in Eq. 2.1. The forces in this model consist of the applied rapid load, F_{RLT}, the inertial force of the pile, $F_{inertia}$, the damping resistance of the soil, $F_{damping}$, the pore water resistance, F_{pore}, and the nonlinear static resistance of the soil-pile system, F_{static}. Through measurements acquired at the head of the pile with appropriate instrumentation, the rapidly applied load, $F_{RLT}(t)$, head accelerations, $a(t)$, integrated head velocity, $v(t)$, and head displacement, $x(t)$, are obtained as experimentally observed responses.

$$F_{RLT}(t) = F_{static}(t) + F_{damping}(t) + F_{pore}(t) + F_{inertia}(t) \tag{2.1}$$

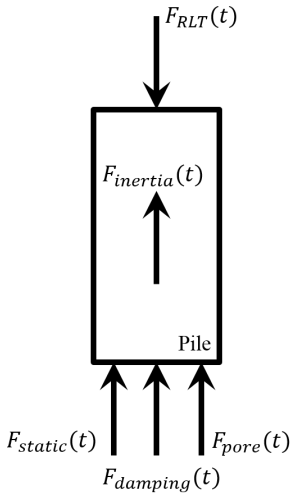

Figure 2.1: Free body diagram of forces during rapid load testing

2.1.1 Unloading Point Method

The UP method (Middendorp et al. (1992)) analyses the response at the head of the pile under a series of simplifying assumptions to estimate the axial bearing capacity of the pile and elastic stiffness under a characteristic load. In this method, only instrumentation at the head of the pile capable of measuring both strain and acceleration is required. The pile is assumed to be rigid and modeled as a SDOF system using the equation of motion in Eq. 2.1.

Since the static soil resistance, radiation and viscous damping, and pore water pressure effects are all attributed to the soil, the equation of motion can also be written as

$$F_{soil}(t) = F_{static}(t) + F_{dynamic}(t) + F_{pore}(t) = F_{RLT}(t) - F_{inertia}(t) \tag{2.2}$$

after collecting terms attributed to the soil resistance. However, it should be noted that pore water pressure effects are not explicitly accounted for within the unloading point method.

With the exception of the static soil resistance, force components within Equation 2.2 are

determined from measurement data obtained during the rapid load test. The total applied load is determined from either the load cell or from a measurement of the strain at the head of the pile, ϵ, and the axial rigidity, from the elastic modulus, E, and cross sectional area, A, as shown in Equation 2.3. The dynamic soil resistance is computed using a viscous damping constant, c, and the pile velocity, $v(t)$, which can be determined by integrating the measured accelerations (Equation 2.4). Lastly, and the pile inertia force is calculated from the mass of the pile, m, and the measured acceleration, $a(t)$ (Equation 2.5). In some cases, additional mass of the surrounding soil is included in this mass.

$$F_{RLT}(t) = EA\epsilon(t) \tag{2.3}$$

$$F_{damping}(t) = cv(t) \tag{2.4}$$

$$F_{inertia}(t) = ma(t) \tag{2.5}$$

The analysis technique used in the UP method revolves around analyzing the response at the unloading point, which is the moment in time when the maximum displacement has been achieved (t_{umax}). At this instance in time, the velocity is zero, thus eliminating the influence of damping forces to simplify the force equilibrium to the applied load, inertial force, and static soil resistance. Therefore, the static soil resistance at the time and displacement corresponding to the unloading point can be computed as the applied rapid load minus the computed inertia force at this same instant in time (Eq. 2.6).

$$F_{static}(t_{umax}) = F_{RLT}(t_{umax}) - F_{inertia}(t_{umax}) = F_{RLT}(t_{umax}) - ma(t_{umax}) \tag{2.6}$$

Following the determination of the static soil resistance at the unloading point, the static

load versus displacement response can be approximated using a hyperbolic best fit curve, as presented in Holscher et al. (2012). If the static response is to be approximated from a single load pulse, the initial stiffness and unloading point static soil resistance are used to establish the coefficients in the hyperbolic curve. The initial stiffness is estimated from a characteristic load that is 1/4 the peak observed load and the corresponding characteristic displacement. An example of a hyperbolic fit of a single rapid load test pulse is shown in Figure 2.2a. With multiple tests, more unloading points can be used to obtain a better hyperbolic fit, however the initial stiffness is taken from the first load pulse and the hyperbolic fit uses the envelope of the remaining unloading points, as shown in Figure 2.2b. Multiple tests can also provide information on potential rate dependence of the damping constant due to the nature of different rates of loading. If a static load test is performed in conjunction with the rapid load tests, the accuracy of the estimated static load curve can be evaluated and rate dependent variables can be introduced.

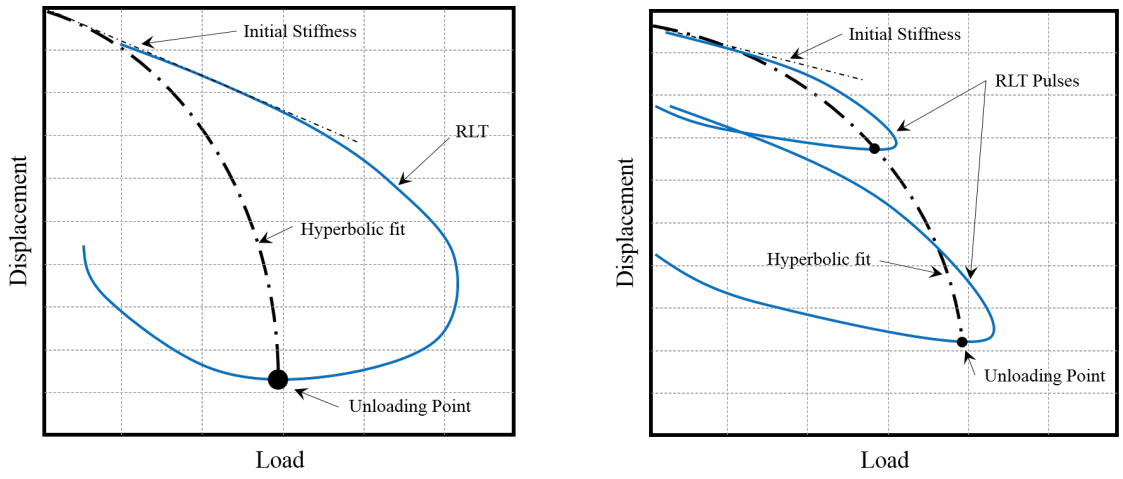

Figure 2.2: Examples of static response estimate based on hyperbolic fits of a) one rapid load test and b) multiple rapid load tests

As an alternative to the hyperbolic fit, the damping force can be estimated and subsequently subtracted from the applied rapid load to estimate the static load versus displacement response. The estimated damping constant is determined at the instance of maximum applied load, t_{fmax}, under the assumption that the maximum static soil resistance has already been fully mobilized at this point. Under this assumption, the damping constant can be approximated as:

$$c = \frac{F_{RLT}(t_{fmax}) - F_{static}(t_{umax}) - ma(t_{fmax})}{v(t_{fmax})} \tag{2.7}$$

Using this damping constant across all time increments with the assumption of time invariant properties, the derived static load versus displacement response can be calculated using the measured applied rapid load, accelerations, and integrated velocities, by rewriting Eq. 2.2 as:

$$F_{static}(t) = F_{RLT}(t) - cv(t) - ma(t) \tag{2.8}$$

However, the assumption of time invariant damping is generally thought to be invalid, especially when the soil-structure interaction exceeds elastic response (Stokes et al. (2008)). Alternative methods that introduce nonlinear damping are reviewed in subsequent sections of this chapter.

2.1.2 Modified Unloading Point Method

For longer piles, the motion at the head of the pile could be significantly different than the motion at the toe of the pile, thus making the rigid pile assumption invalid. To address such cases, a modified approach to the UP method has been developed. Justason (1997) developed the Modified Unloading Point (MUP) method by introducing an additional pair of

accelerometers to measure the response at the toe of the pile (Figure 2.3). This method assumes the pile to be represented by a SDOF system, but the motion of the system are taken as the average of the measured responses at the head and toe of the pile. This advancement in the technique has been shown to address issues arising from the simplifying assumptions in the UP method (Mullins et al. (2002)) and is recommended when the additional toe information is available. The implementation of the MUP method is otherwise identical to the UP method for obtaining the velocities and accelerations for use in the equation of motion for the SDOF model as well as determining the static capacity, static load versus displacement response, stiffness at a characteristic load, and damping constant.

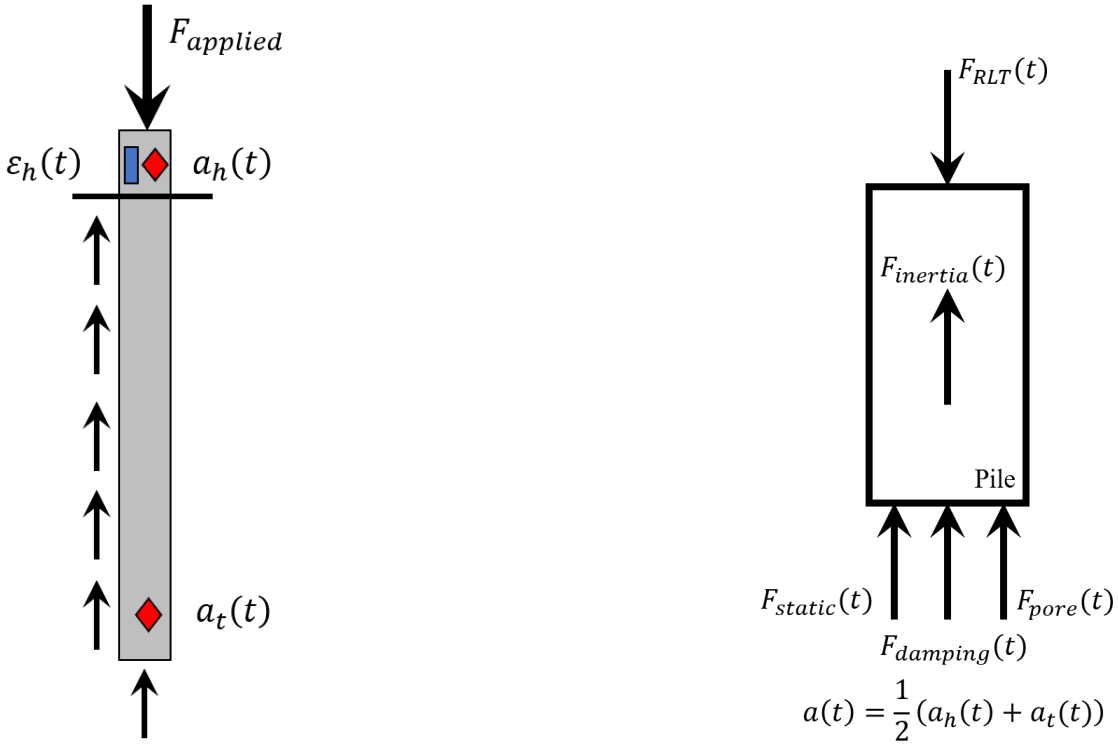

(a) Instrumentation Schematic

(b) Free Body Diagram

Figure 2.3: Representation of Modified Unloading Point method model

2.1.3 Segmental Unloading Point Method

The Segmental Unloading Point (SUP) method was developed by Mullins et al. (2002) for use on relative long piles with a wave number, N_w, less than 10. This method separates the pile into discrete segments of shorter lengths, each with segmental wave numbers greater than 12, thus classifying the loading within each segment as rapid. The boundaries of each segment are defined by the locations of additional strain gages placed down the depth of the pile. These additional strain gages are used to estimate both the relative motion and internal force in each pile segment. The MUP method is used for each individual segment and the total of these segmental forces results in the pile ultimate static resistance versus displacement response. The nomenclature for the theory hereafter follows the schematic shown in Figure 2.4, where *n* defines a segment and *i* defines the node.

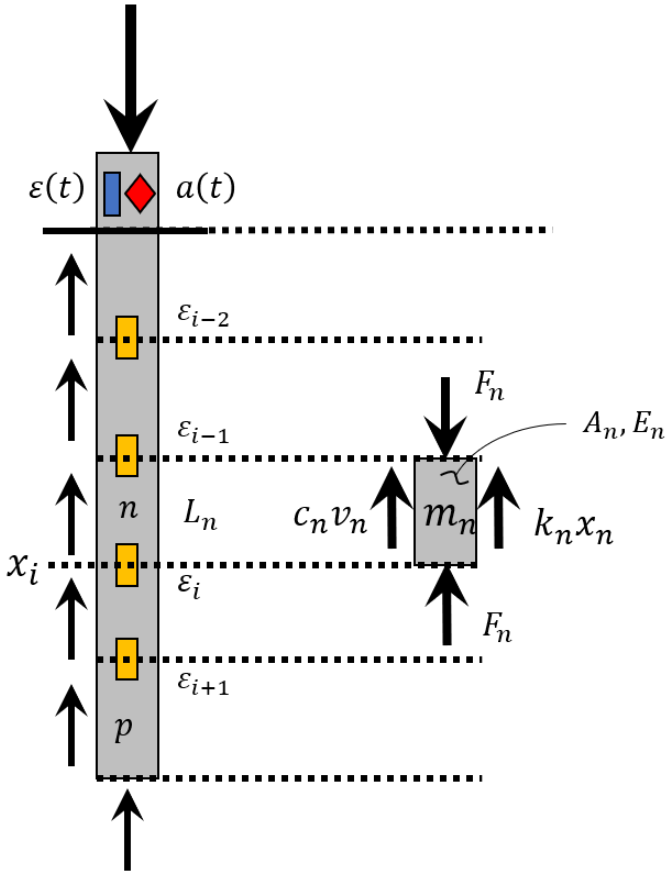

Figure 2.4: Representation of Segmental Unloading Point model

In the SUP method, the relative motion of each node is estimated by numerical integration of the measured axial strain. If the strain is assumed to vary linearly between strain gage locations, the displacement of each gage location can be determined as:

$$x_i(t) = x_{i-1}(t) - \left(\frac{\epsilon_i(t) + \epsilon_{i-1}(t)}{2}\right)L_n \tag{2.9}$$

where x_i is the displacement at node i, x_{i-1} is the displacement of the previous node $i-1$, ϵ_i is the strain measurement at node i, ϵ_{i-1} is the strain measurement at node $i-1$, and L_n is the length of segment n. All of the nodal displacements are computed relative to the displacement of the node one gage elevation higher and ultimately are referenced to the displacement at the head of the pile, which is measured directly or determined through

double integration of the accelerometer measurement. The average segmental displacement is computed as:

$$x_n(t) = \frac{x_{i-1}(t) + x_i(t)}{2} \tag{2.10}$$

Through numerical differentiation over a time step, Δt, using a simple two-point estimation by Newton's difference quotient, the velocities, v, and accelerations, a, of each segment n are determined by:

$$v_n(t) = \frac{x_n(t) - x_n(t+1)}{\Delta t} \tag{2.11}$$

$$a_n(t) = \frac{v_n(t) - v_n(t)}{\Delta t} \tag{2.12}$$

To determine the total force, F, in each segment, n, strains at the ends of each segment are used with the axial rigidity in a force equilibrium:

$$F_n = A_{i-1}E_{i-1}\epsilon_{i-1} - A_iE_i\epsilon_i \tag{2.13}$$

where A and E are the area and the modulus of elasticity respectively, at the nodes $i-1$ and i of segment n. Using the segmental motion and force derived above in the SDOF equation of motion, the UP method can be performed on each segment. The SDOF equation of motion for each segment is:

$$F_n(t) = m_n a_n(t) + c_n v_n(t) + F_{n\,static}(t) \tag{2.14}$$

where m_n is the segment mass, c_n is the segment viscous damping constant, and $F_{n\,static}(t)$ is the static soil resistance of segment n. To solve for the static soil resistance of each segment, Eq. 2.14 is reorganized as:

$$F_{n\,static}(t) = F_n(t) - m_n a_n(t) - c_n v_n(t) \tag{2.15}$$

Using the methodology of the UP method approach, the above equation can be used at the unloading point of each segment where the damping force is zero to solve for the static resistance mobilized at the unloading point::

$$F_{n\,static}(t_{umax}) = F_n(t_{umax}) - m_n a_n(t_{umax}) \tag{2.16}$$

By performing and analyzing multiple tests with different amplitudes of loading, the SUP method can develop static load versus displacement responses for the individual segments by fitting the unloading point static resistance estimates from each test, analogously to the approach used in the UP method to obtain the static load versus displacement response of the full pile. The static load versus displacement responses for individual segments developed by the SUP method are estimates of the t-z and Q-z curves representing the soil-structure interaction down the length of the pile. In contrast to the UP and MUP methods, this capability uniquely provides the SUP method with the ability to produce estimates of the side friction and toe bearing resistance contributions to the axial load capacity of the pile.

The summation of the static soil resistances calculated for the individual segments also allows for the determination of the overall static soil resistance of the pile:

$$F_{static}(t) = \sum_{n=1}^{p} F_{n\,static}(t) \tag{2.17}$$

where p is the total number of number of segments.

2.1.4 Embedded Data Collector Method

The Embedded Data Collector (EDC) method, originally developed in Tran et al. (2012b,a) but extended to rapid load testing in Tran et al. (2016, 2017), uses separate numerical analy-

ses for the determination of tip resistance and skin friction contributions in piles from rapid load test data. The separate analyses are facilitated by the inclusion of additional strain and acceleration instrumentation near the toe of the pile. Since the estimations of tip resistance and skin friction are decoupled by independent analyses, the processes used to estimate each are summarized and separate subsections.

2.1.4.1 EDC Toe Resistance Determination

The EDC method uses the strain and acceleration transducers placed at the toe of the pile to measure the motion and internal force at the toe. The toe resistance, $Q(x)$, is modeled as a piecewise linear function defined by three loading stiffnesses (k_1, k_2, k_3), an unloading stiffness (k_4), and displacements (l_1 and l_3) (Figure 2.5).

In order to determine these six unknown parameters in the toe resistance model, the toe is assumed to behave as a SDOF system such that:

$$m\ddot{x}(t) + c\dot{x}(t) + Q(x) = P(t) \tag{2.18}$$

where m is the mass of toe segment, c is the damping constant of the toe segment, $\ddot{x}(t)$ is the acceleration of the pile toe, $\dot{x}(t)$ is the velocity of the pile toe, $Q(x)$ is the static soil resistance according to the piecewise linear function, and $P(t)$ is the applied force at the toe of the pile. The acceleration at the pile toe is directly measured, the velocity and displacement at the pile toe are determined through numerical integration of the measured acceleration, and the applied force at the toe is calculated as the product of the measured strain and axial rigidity of the pile. The mass of the toe segment and damping constant of the toe segment are treated as additional unknowns, so with the unknown parameters in

the toe resistance model there are a total of eight unknown scalar parameters in the SDOF equation of motion. Tran et al. (2016) proposed to use a genetic algorithm to identify all

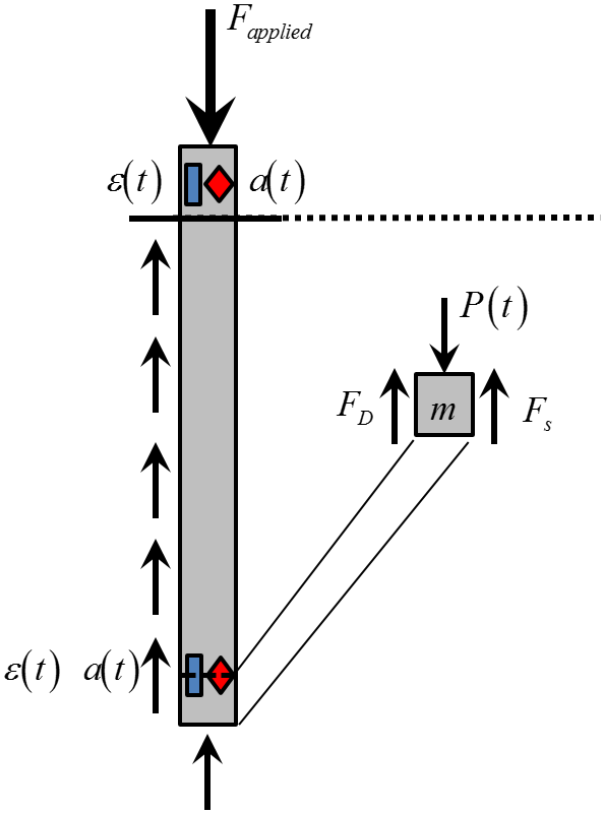

(a) EDC toe schematic

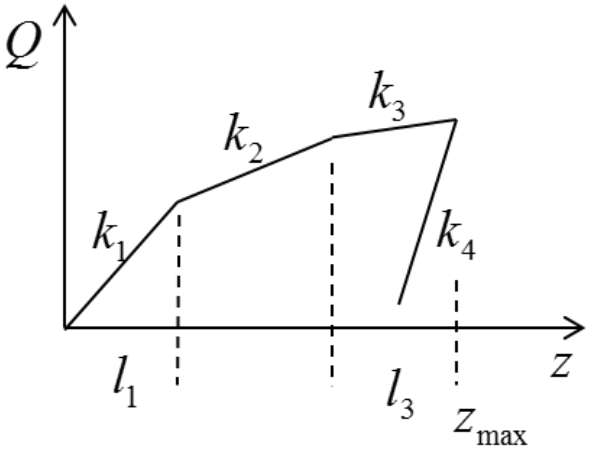

(b) EDC toe resistance model

Figure 2.5: EDC toe bearing model

eight unknown scalars by minimizing the force imbalance in the SDOF equation of motion as well as simultaneously minimizing the energy imbalance.

Energy balance requires that the input energy, which can be computed by multiplying the applied force, $P(t)$, by the velocity at the toe, $v(t)$, is equal to the energy of the soil resistance, defined by the inertia, damping, and static resistances multiplied by the toe velocity, over a time period, T, such that:

$$\int_{t}^{t+T} \Big(ma(t) + cv(t) + Q(t) \Big) v(t) dt = \int_{t}^{t+T} P(t) v(t) dt \tag{2.19}$$

The genetic algorithm for the parameter identification is set up to minimize the least-squares error, $J(n)$, between the applied force and calculated soil resistance force as well as the input energy and calculated soil resistance energy for a given set of assignments for the mass, damping, and toe bearing resistance model parameters, n. This weighted least-squares error objective function is shown in Equation 2.20. Here, N is the number of data points, E_{input} is the applied energy calculated using the right side of Equation 2.19, E_{soil} is the energy of the soil resistance calculated using the accelerations, velocities, and displacements measured during the RLT and selected soil parameters for mass, damping, and static stiffness for parameter set n, P_{input} is the measured force at the toe, and P_{soil} is the total soil resistance at time t calculated using the measured acceleration, velocity, and displacement at the toe during the RLT and the soil parameters for mass, damping and static stiffness for parameter set n.

$$J(n) = \frac{1}{N} \sum_{i=1}^{N} \Big[E_{input}(t) - E_{soil}(n,t) \Big]^2 + \alpha_{EDC} \frac{1}{N} \sum_{i=1}^{N} \Big[P_{input}(t) - P_{soil}(n,t) \Big]^2 \tag{2.20}$$

The variable α_{EDC} is a scalar weight that is set to scale the magnitude of the forces

to be comparable to the magnitude of the energies in order to approximately balance the importance of force balance and energy balance in the parameter inversion process. In Tran et al. (2016), the total toe resistance calculated using the EDC method on a drilled shaft with statnamic data was found to compare well to measurements obtained from a static load test and to an estimate obtained from the application of the SUP method. However, the piecewise linear Q-z curve was not compared directly to either estimates from the static test or the SUP method analysis and no other application or the EDC method to statnamic tests have been identified in the literature.

2.1.4.2 EDC Shaft Resistance Determination

To estimate the soil-structure interaction along the shaft of the pile in statnamic tests, the EDC method discretizes the pile into a series of segments, as shown in Figure 2.6a. The side friction resistance in each segment is assumed to obey an elastic-perfectly plastic behavior that can be defined by a loading stiffness, K, unloading stiffness, K', and quake, q (Figure 2.6b). The 1-D partial differential equation for the segments shown in Figure 2.6a is:

$$\left(\frac{E}{\rho}\right)\frac{\partial^2 u}{\partial x^2} = \frac{\partial^2 u}{\partial t^2} + \left(\frac{cP}{\rho A}\right)\frac{\partial u}{\partial t} + \left(\frac{P}{A\rho}\right)\tau(u) \tag{2.21}$$

where P is the perimeter of the pile, A is the cross sectional area of the pile, and ρ is the density of the pile. A finite-difference approach is taken to solve for the displacements of each segment for any given set of assignments for the unknown parameters in the side friction resistance model as well as the unknown damping constant. The measured strains at the top and bottom of the pile are used to provide boundary conditions in the finite difference solution. The computed displacements are then used to estimate the velocities at

the top and bottom of the pile, which are compared to the velocities computed by numerically integrating the measured accelerations at the top and bottom of the pile. To arrive at estimates of the unknown parameters in the side friction soil-structure interaction model, a genetic algorithm is used to minimize the least squares error between the computed and measured velocities at the top and bottom of the pile.

As with the EDC toe resistance method, the available literature on the EDC side friction estimation for statnamic testing is limited to a single case study (Tran et al. (2016)). The side friction resistance was computed over two segments in this case study and was found to compare favorably to estimates obtained from a static load test and SUP method analysis. However, the authors note that applying the method to segments less than 3-5m in length can lead to inconsistent estimates.

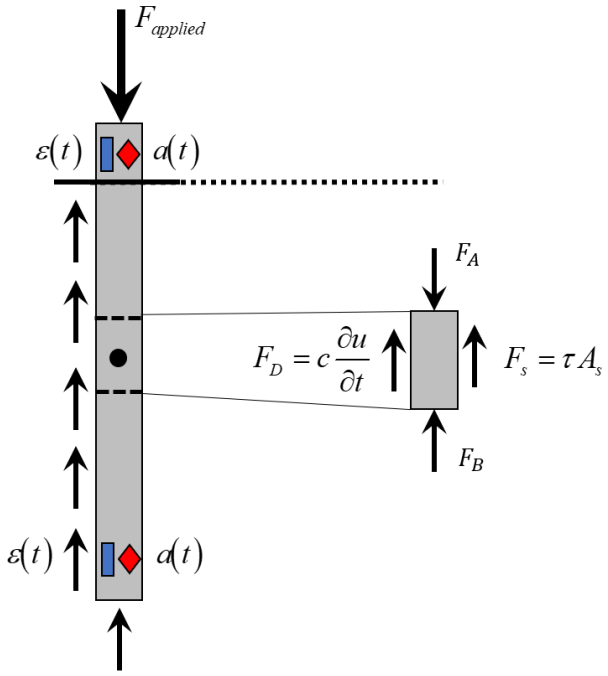

(a) EDC side friction schematic

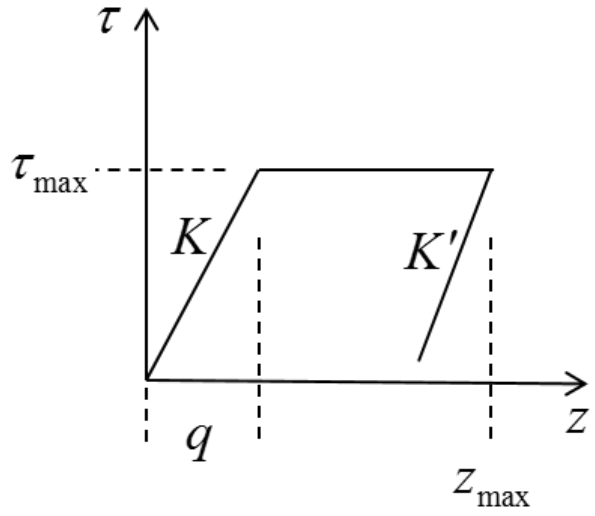

(b) EDC side friction resistance model

Figure 2.6: EDC Side friction model

2.2 Other Considerations for Rapid Load Testing

This section will discuss various improvements suggested for rapid load testing analysis and techniques for considering additional phenomena potentially affecting rapid load test responses. These topics include improved determination of damping contributions,

techniques to account for rate effects and pore water effects, and recommendations for considering inertial contributions from added soil mass due to plugging.

2.2.1 Damping Force Determination

2.2.1.1 Time Invariant Damping

Mullins et al. (2002) proposed determining the damping constant, c, with the assumption that the damping coefficient is considered constant throughout the test and the static capacity is considered constant while the pile is plunging. The damping coefficient is considered as the average calculated damping constant from the time of maximum load, t_{fmax}, to the time of maximum displacement, t_{umax}. Within this approach, it is assumed that the static soil resistance is already fully mobilized at t_{fmax} and remains constant through the time duration up to t_{umax}. By this assumption, the static soil resistance mobilized over this time duration can be taken as the calculated static soil resistance at the unloading point, $F_{static}(t_{umax})$. By manipulating the SDOF equation of motion with a constant static soil resistance, a time variant damping constant over this time period from t_{fmax} to t_{umax} can be calculated as:

$$c(t) = \frac{F_{RLT}(t) - F_{static}(t_{umax}) - ma(t)}{v(t)} \quad \text{for } [t_{fmax} < t < t_{umax}] \tag{2.22}$$

Since the assumption of a constant static soil resistance over this time period is not necessarily valid and since there is often uncertainty in the contribution of added soil mass to the mass used in this equation, the derived damping constant is not time invariant (Figure 2.7). To arrive at a scalar damping constant, the average damping constant calculated across this period of time is typically assumed for the duration of the load. However, if there is

a constant value over this range, it is suggested by Mullins et al. (2002) that the constant value should be considered as the damping constant instead.

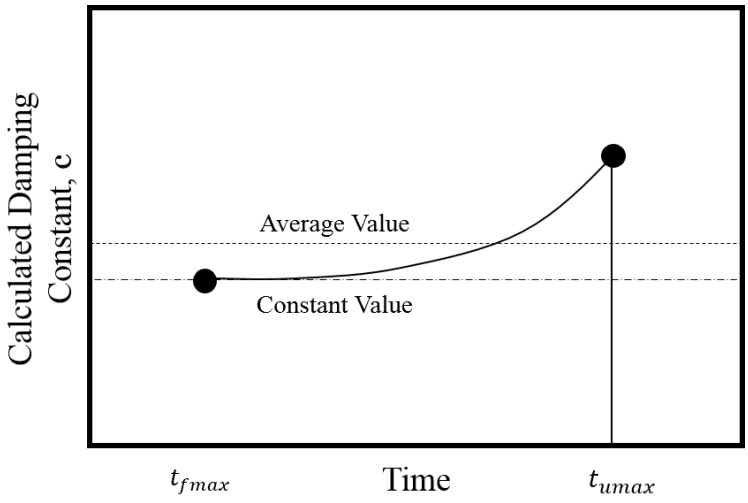

Figure 2.7: Determination of damping constant using time history analysis of rapid load test data (modified from Mullins et al. (2001))

2.2.1.2 Time Variant Damping

Through studying the time variant damping constant, Stokes et al. (2008) identified that changes in the damping parameter, c, are primarily related to the displacement-dependent volume change of the soil around the pile during loading, shown in Figure 2.8. The numerical analysis employed by Stokes et al. (2008) produces an estimate of the time variant damping constant by back calculating for the value of the damping constant at each time increment. In order to do this, the static soil resistance at each increment must be known. To facilitate this, results from a static load test can be incorporated to define the nonlinear static soil resistance as a function of head displacement. Consequently, the back calculated time variant damping constant is calculated as:

$$c(t) = \frac{F_{RLT}(t) - ma(t) - F_{SLT}(x)}{v(t)} \tag{2.23}$$

This process is illustrated graphically in Figure 2.9. In applying this technique to case study data, Stokes et al. (2008) noted a rapid transition between the damping constant prior to yielding of the soil-structure interaction and the damping constant afterward (Figure 2.10).

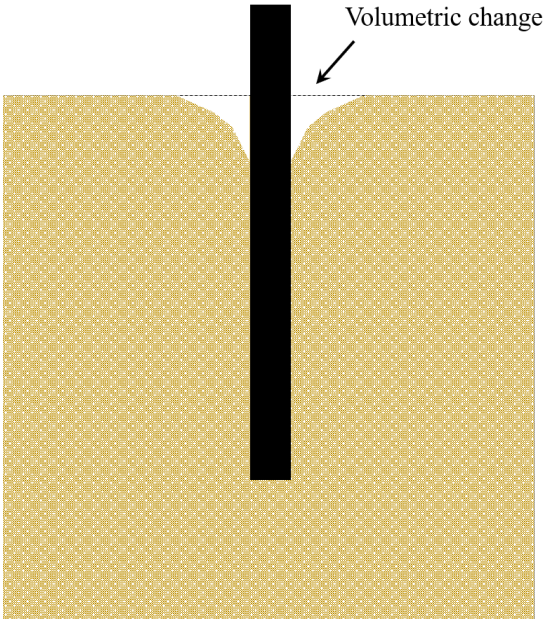

Figure 2.8: Schematic of volumetric change during pile loading

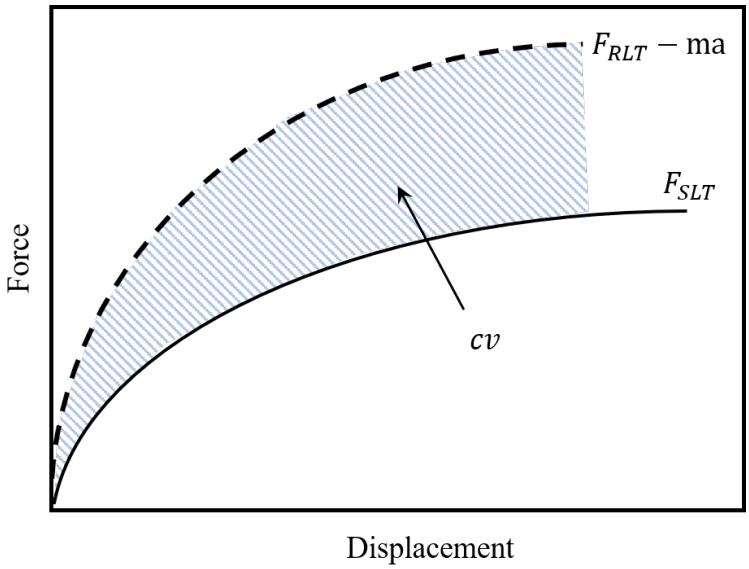

Figure 2.9: Comparing response from the RLT to the SLT to determine the variable damping constant, *c*

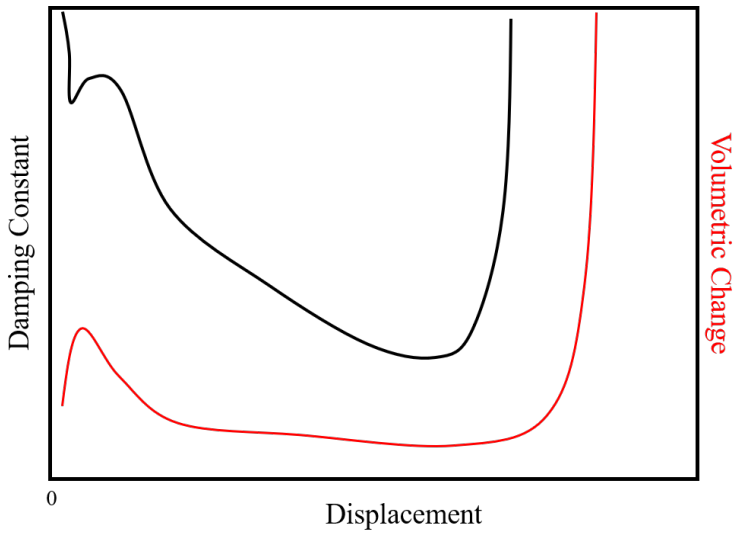

Figure 2.10: Relation between variable damping constant and volumetric change (adapted from Stokes et al. (2008))

2.2.1.3 Rate Dependent Damping Constants

A more advanced approach for accounting for both damping and rate effects in the shear soil resistance in rapid load testing of piles in clays soils introduces two soil damping constants and a power law. The relationship of rate effects on the shear resistance for clays commonly uses the power law from Randolph and Deeks (1992) shown in Equation 2.24.

$$\tau_d = \tau_s\left(1 + \alpha\left(\frac{\Delta v}{v_o}\right)^{\beta}\right) \tag{2.24}$$

where τ_d is the dynamic shear resistance, τ_s is the static shear resistance, Δv is the relative velocity of pile and soil, v_o is a reference velocity, and α and β are soil dependent damping constants. Hyde et al. (2000) modified Equation 2.24 so that the dynamic shear resistance would equal the static shear resistance while the velocity is equal to or less than the velocity of static testing as:

$$\tau_d = \tau_s\left(1 + \alpha\left(\frac{\Delta v}{v_o}\right)^{\beta} - \alpha(10^{-6})^{\beta}\right) \tag{2.25}$$

This equation was modified and validated against measured pile behavior during several rapid load tests by Brown (2004); Brown et al. (2006) and the static reference velocity was changed from 10^{-6}mm/s to 10^{-5}mm/s, such that:

$$F_{static}(t) = \frac{F_{RLT}(t) - ma(t)}{1 + \alpha\left[(\Delta v(t))^{\beta} - (10^{-5})^{\beta}\right]} \tag{2.26}$$

Balderas-Meca (2004) found that the rate parameter α is strain dependent and varies to 1.2% of pile settlement. After this strain level, the rate parameter α was found to be constant and defined by:

$$F_{static}(t) = \frac{F_{RLT}(t) - ma(t)}{1 + \frac{F_{RLT}(t)}{F_{RLT\,max}}\alpha\left[\left(\frac{\tilde{v}(t)}{v_{ref}}\right)^{\beta} - \left(\frac{v_{static}}{v_{ref}}\right)^{\beta}\right]} \tag{2.27}$$

In this equation, $F_{RLT\,max}$ is the maximum applied rapid load, $\tilde{v}(t)$ is a modified velocity function described below, v_{static} is the velocity associated with a loading rate associated with the static resistance, v_{ref} is a reference velocity to which the other velocities are normalized (v_{ref} = 1000mm/s), and α and β are soil dependent damping constants that can be established through several approaches subsequently described. The function for the modified velocity, $\tilde{v}(t)$ is:

$$\tilde{v}(t) = \begin{cases} |v(t)| & \text{if} \quad t < t_{v_{max}} \\ v_{max} & \text{if} \quad t >= t_{v_{max}} \\ v_{static} & \text{if} \quad \tilde{v}(t) < v_{static} \end{cases} \tag{2.28}$$

There are three main approaches for establishing the damping constants, α and β, used in Eq. 2.27. These methods include derivation from laboratory testing, the use of empirical

values sourced from existing literature, and analysis of the RLT in parallel with SLT data. While it is recommended by Holscher et al. (2012) to use laboratory testing, the other approaches may be used depending on the amount of prior data available on the soil.

In the first approach, laboratory testing of soil using high, or variable, speed triaxial testing, penetrometer testing, or model scale pile testing can be used to estimate α and β parameters. Brown (2004) and Balderas-Meca (2004) discuss developing these rate parameters from laboratory testing, however Balderas-Meca (2004) uses the last method involving a static load test, which will be described later. Brown (2004) used constant rate penetration (CRP) testing on a model pile in KSS clay. The applied rates varied from 0.01mm/s (0.000394in/s) to 500mm/s (19.685in/s), where v_{static} was 0.01mm/s (0.000394in/s) and v_{ref} is 1000mm/s (39.37in/s).

The second approach involves sourcing the damping constants from existing literature. A summary of estimated parameters sourced from previous studies with different soil types is provided in Table 2.1 with soil index properties. It is understood that soil is a highly variable material and can be classified in different ways, many of which include the Atterburg limits, but care must be taken to select appropriate empirical damping constants using this method. Ideally, the full grain size distribution should be used when comparing a soil at a site to the soil types listed in the table to select appropriate empirical values of α and β. Additionally, Powell and Brown (2006) developed a relationship for α based on the plasticity index, PI, of clay for a fixed value of β taken as 0.2:

$$\alpha = 0.031PI + 0.46 \tag{2.29}$$

Finally, Balderas-Meca (2004) studied the relationship between damping constant α and

Table 2.1: Damping constants (modified from Holscher et al. (2012))

Source	Soil Type	LL	PL	PI	α	β
Litkouhi and Poskitt (1980)	London Clay	70	27	43	1.77	0.18
	Forties Clay	38	20	18	0.99	0.23
	Magnus Clay	31	17	14	0.86	0.46
Poskitt and Leonard (1982)	Cowden Till	40	20	20	1.00	0.27
Randolph and Deeks (1992)	Sand	-	-	-	0.10	0.20
	Clay	-	-	-	1.00	0.20
Balderas-Meca (2004)	Grimsby Glacial Till	20-36	12-18	7-20	0.90	0.20
Brown (2004)	Model Clay	37	17	20	1.26	0.34

pile displacement and developed a bilinear model for the damping constant where the damping constant α linearly increases to a quake value of 1-1.2%, then remains constant. This model was developed by fixing β to 0.2 and determining the damping constant α at each time step in the rapid load test, using available static load test data rearranging Eq. 2.27, such that:

$$\alpha = \frac{\frac{F_{RTL}-ma}{F_{SLT}} - 1}{\left[\left(\frac{\Delta v}{v_o}\right)^{0.20} - \left(\frac{0.01}{v_o}\right)^{0.20}\right]} \tag{2.30}$$

Comparison of the RLT results to the load versus displacement response obtained from the SLT was satisfactory. The disadvantage of this method is that a SLT is required to be performed, which prohibits the direct determination of the static capacity of a pile foundation from only rapid load test data.

2.2.2 Pore Water Pressure Effects

The effect of pore water pressure on effective stresses is another important issue to considering during rapid load testing. Dense sands typically dilate during loading, producing negative excess pore water pressures and an apparent increase in the strength of the soil during a rapid load test. In contrast, sands with lower densities will develop positive pore

water pressures during loading and, therefore, an apparent decrease in the strength of the soil during a rapid load test is observed. Holscher et al. (2012) found that the pore pressures, developed in a scaled centrifuge RLT in sands with viscous fluids and water, generally have the same trend as the total rapid force and vary with velocity, suggesting that a correction factor, related to pore water pressures, should be used to predict the static capacity of the pile. Various studies have sought to evaluate whether particular soils act as partially drained, drained, or undrained soil during a rapid load test (Holscher et al. (2012)). Following work completed by Eiksund and Nordal (1996), a dynamic drainage factor, θ, was proposed to quantify the influence of pore water pressures according to the duration of the load and consolidation behavior of the soil. The dynamic drainage factor is calculated as:

$$\theta = \frac{Gt_l}{g\rho_w R^2}k \tag{2.31}$$

where, G is the shear modulus of the soil, t_l is the duration of the applied load, g is the gravitational constant, ρ_w is the density of water, R is the radius of the pile, and k is the permeability of the soil. Holscher et al. (2012) found that if this factor was less than 10, which is typically the case for medium and fine sands, then the soil can considered partially drained and the effects of excess pore water pressures should be considered in the overall response. If the dynamic drainage factor is 100 or greater, which is typically the case for coarse sands, then the soil can be considered drained and pore water pressures have negligible effect on the response of the pile in the rapid load test (Holeyman (1992)). There were no conclusions on what to consider when the drainage factor is between these two values, however the authors do provide a relationship of a normalized force, specifically

the rapid force divided by the static force at the unloading, to the drainage factor shown in Figure 2.11. This work postulates that a correction for the excess pore pressure effect is required to predict the static capacity of the pile and suggest using Figure 2.11 as guidance in calculating the required correction factor based on the drainage factor. However, this would only allow for a constant correction factor for the total static capacity estimate when in reality the correction factor would be time variant.

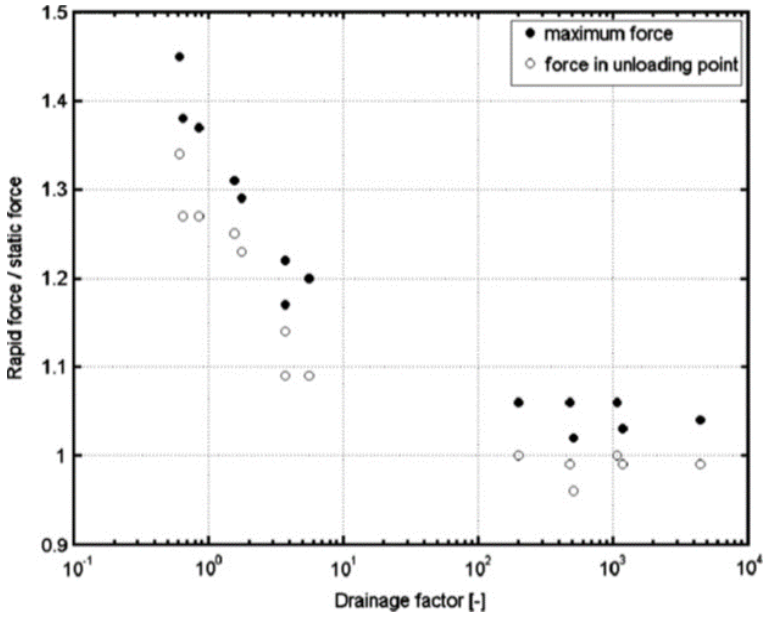

Figure 2.11: Rapid force to static force ratio in relation to the drainage factor (from Holscher et al. (2012))

2.2.3 Rate Effects

A collection and analysis of a database of rapid load tests by Paikowsky (2006) concluded that rapid load tests typically over predict of axial capacities in cohesive soils. In developing a practical approach to correct this over prediction for immediate testing needs, a correction factor was developed to account for general rate effects, including strain rate effects and pore water pressure effects, for different soil types. The database encompassed

34 rapid load tests that included driven H-piles, pipe piles, and concrete drilled shafts. The rate effect reduction factors recommended for clay, silt, sand, and rock were 0.65, 0.69, 0.91, and 0.96, respectively. These rate effect reduction factors are applied directly to the static capacity estimates obtained from rapid load testing.

Holscher et al. (2012) developed interpretation guidelines for rapid load testing in an attempt to standardize the methodology for determining static capacity. In this work, an empirical factor, η, was introduced as a correction factor that attempts to approximate the effects of both rate and pore pressure effects during a rapid load test. This factor is applied to the derived static soil response at the unloading point such that:

$$F_{static}(t_{umax}) = \eta\left(F_{RLT}(t_{umax}) - ma(t_{umax})\right) \tag{2.32}$$

A hyperbolic best fit relationship can still be used to derive the estimated static load versus displacement response after applying the rate effect correction factor. The determination of the exact rate effect correction factor requires that a static load test be performed, however an estimation of the static load versus displacement response can alternatively be obtained using empirically developed rate effect correction factors for the given soil type. In order to produce guidance on appropriate empirical rate effect correction factors to apply in the absence of a complementary static load test, statistical analysis was performed on a database of rapid load tests completed for different pile types and soil conditions (McVay et al. (2003); Holscher et al. (2008, 2012)). This database encompassed 33 rapid load tests conducted at 16 different sites. The recommended empirical rate effect correction factors are summarized in Table 2.2. It is notable that the standard deviation and coefficient of variation are quite large, especially for tests conducted on piles in clay soil.

Table 2.2: Summary of empirical rate effect correction factor from tests (adapted from Holscher et al. (2012))

Pile type/soil type	All/Clay	Displacement/Sand
Empirical factor, η	0.66	0.94
Standard deviation	0.32	0.15
Coefficient of variation	0.49	0.15
Number of cases	12	21
Number of sites	6	10

Holscher et al. (2012) also suggest that the estimate of the rate effect correction factor, η, can be related to damping constant parameters, α and β, from the rate dependent damping method presented earlier. Using the maximum velocity, $\tilde{v}_{max}$, and using the maximum force where $F_{RLT}/F_{max} = 1$, the estimate for the rate effect correction factor is calculated as:

$$\eta = \frac{1}{1 + \alpha\left[\left(\frac{\tilde{v}_{max}}{v_{ref}}\right)^{\beta} - \left(\frac{v_{static}}{v_{ref}}\right)^{\beta}\right]} \tag{2.33}$$

It was concluded that this equation will give an average rate effect correction factor of 0.5 for all soil types but varies between 0.35 and 0.65. This method has also not been used on existing empirical data and it is suggested that more work is required if this is to be an established valid method.

2.2.4 Plugging Effects

For open ended piles, such as a pipe piles or sheet piles, changes in system mass, damping, and soil resistance are possible during the installation, testing, or the designed function of the pile. The changes in soil mass can arise due to the formation of a plug in open cross sections. Iversen et al. (2010) collected several different recommendations into the amount of plugging that should be considered in the bearing design of sheet piles. A range of percentages, predominately between 40% and 80%, are given with no clear direction as when

to use the increased bearing area. One recommendation prescribes Equation 2.34, which produces an effective sheet pile height reduction factor, κ_F, that is dependent on the section angle, α_s, shown in Figure 2.12. Using this factor, an effective soil plug bearing area can be calculated and used in the determination of toe stresses in the pile.

$$\kappa_F = 0.015\alpha_s - 0.35 \tag{2.34}$$

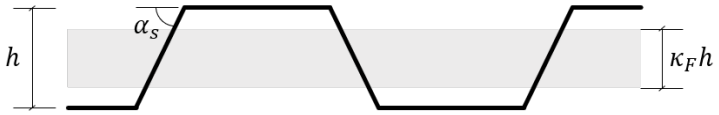

Figure 2.12: Effective depth of cross section for sheet pile plug

For an open ended steel pipe pile driven in a diluvial sand and clay layer bridge site (Ochiai et al. (1997)), it was found that a plug did not form during dynamic testing, but did form during a Statnamic test of the same pile. The tested pile had a length of 156.17ft with a diameter of 4.92ft and cross sectional area of 1.167ft^2 and was driven 106.63ft below the ground level. This pile was instrumented with six strain gages along the depth of the pile and force and velocity were measured at the pile head. One week after driving, the Statnamic test was performed on the pile and then one week after this test, the dynamic test was performed. For the Statnamic analysis, the pile was modeled as the typical one-dimensional mass-spring system coupled with another mass-spring system that attempted to model the soil plug. A signal matching routine was used with the given models for both the Statnamic (rapid) test and the dynamic test and several observations were made. Specifically, the accelerations from the Statnamic testing were significantly lower than those produced from the dynamic test and the calculated relative displacements between the pile and the soil plug were small for the Statnamic test and larger in the dynamic test, suggesting that

the Statnamic test simulates the same plugging condition as developed under static loads.

This is a benefit of rapid load testing over dynamic load testing as, in cases where soil plugging is likely to develop, the static capacity estimates obtained from rapid load testing should be more representative of the actual capacity under static loads than the static capacity estimates obtained from dynamic testing. However, no methods have been identified in the literature for modifying the UP, MUP, or SUP methods to account for changes in soil mass due to plugging. The additional mass can affect the static capacity estimates if the inertia force is significant in the rapid load test.

CHAPTER 3: DYNAMIC TESTING

This section presents an overview of the commonly used methods for analyzing high strain rate measurements obtained from dynamic testing of piles to provide capacity estimates as well as identify parameters within soil-structure interaction models. The theory behind the conventionally used programs such as TNOWAVE, CAPWAP, and others will be presented and the advantages and disadvantages of dynamic testing for pile capacity determination will be discussed.

The dynamic testing method involves measurement of strains and accelerations at the pile head when the pile is struck by a driving hammer during installation and restrike. Valuable information about the soil and pile system can be derived from these data sets, including the magnitude of the pile stresses during installation, the pile integrity, and, ultimately, an estimate of the static pile capacity. Dynamic pile testing measurements are usually evaluated with signal matching techniques employed on wave equation analysis to determine the soil-structure interaction along the shaft of the pile and at the toe.

3.1 Basic Wave Mechanics

As presented by Hannigan et al. (2016), when a homogeneous rod is subjected to an axial force with respect to time, normal stresses are developed within the rod, as shown in Figure 3.1. Newton's second law states that the acceleration is dependent on the applied

force and the mass of the rod such that:

$$F(t) = ma(t) \tag{3.1}$$

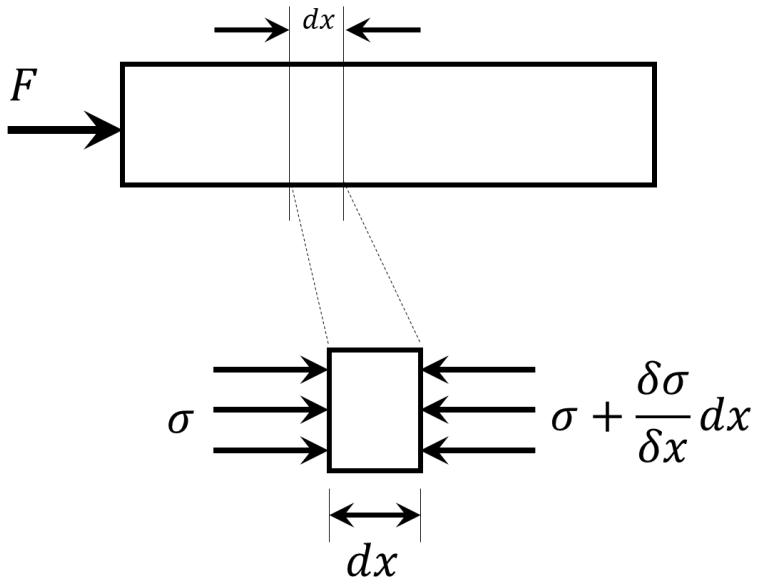

Figure 3.1: Stress equilibrium in a differential axial element within a homogeneous rod subjected to a force

When Equation 3.1 is applied to an infinitesimal element at an arbitrary location, x, along the length of the homogeneous rod, the dynamic force equilibrium is:

$$-\sigma + \sigma + \frac{\partial \sigma}{\partial x} dx = \rho dx \frac{\partial^2 u}{\partial t^2} \tag{3.2}$$

which simplifies to:

$$\frac{\partial \sigma}{\partial x} = \rho \frac{\partial^2 u}{\partial t^2} \tag{3.3}$$

where ρ is the density of the rod, σ is the axial stress developed within the rod, u is the displacement at position x within the rod, and t is time. Assuming that the material behavior remains linear elastic, the axial stress can be related to the axial strain, which is the partial

derivative of the displacement with respect to the position x:

$$\sigma = E\epsilon = E\frac{\partial u}{\partial x} \tag{3.4}$$

By then taking the partial derivative of the axial stress with respect to position x, the relationship

$$\frac{\partial \sigma}{\partial x} = E\frac{\partial^2 u}{\partial x^2} \tag{3.5}$$

is obtained, which can be substituted into Equation 3.3. By doing so, the one dimensional wave equation for a homogeneous rod is developed as:

$$\frac{\partial^2 u}{\partial t^2} = \frac{E}{\rho}\frac{\partial^2 u}{\partial x^2} \tag{3.6}$$

or

$$\frac{\partial^2 u}{\partial t^2} = c_L^2\frac{\partial^2 u}{\partial x^2} \tag{3.7}$$

where the one dimensional compression wave speed, c_L, is dependent on the elastic modulus and the material density of the pile by the relation:

$$c_L = \sqrt{\frac{E}{\rho}} \tag{3.8}$$

Since the wave speed is a constant for elastic materials, the time it takes for the compression wave to travel to the end of a rod or a pile of length, L, is L/c_L and the time it takes for the compression wave to travel back to the end of the rod or pile where the wave originated is $2L/c_L$.

3.2 Solution of the Wave Equation

The solution to the wave equation in piles is most commonly obtained using either the finite difference method or the method of characteristics. The respective models are shown in Figure 3.2. This section briefly describes both methods, but goes into more detail with the method of characteristics since it is more commonly used in modern wave computational programs for pile driving analysis and dynamic signal matching.

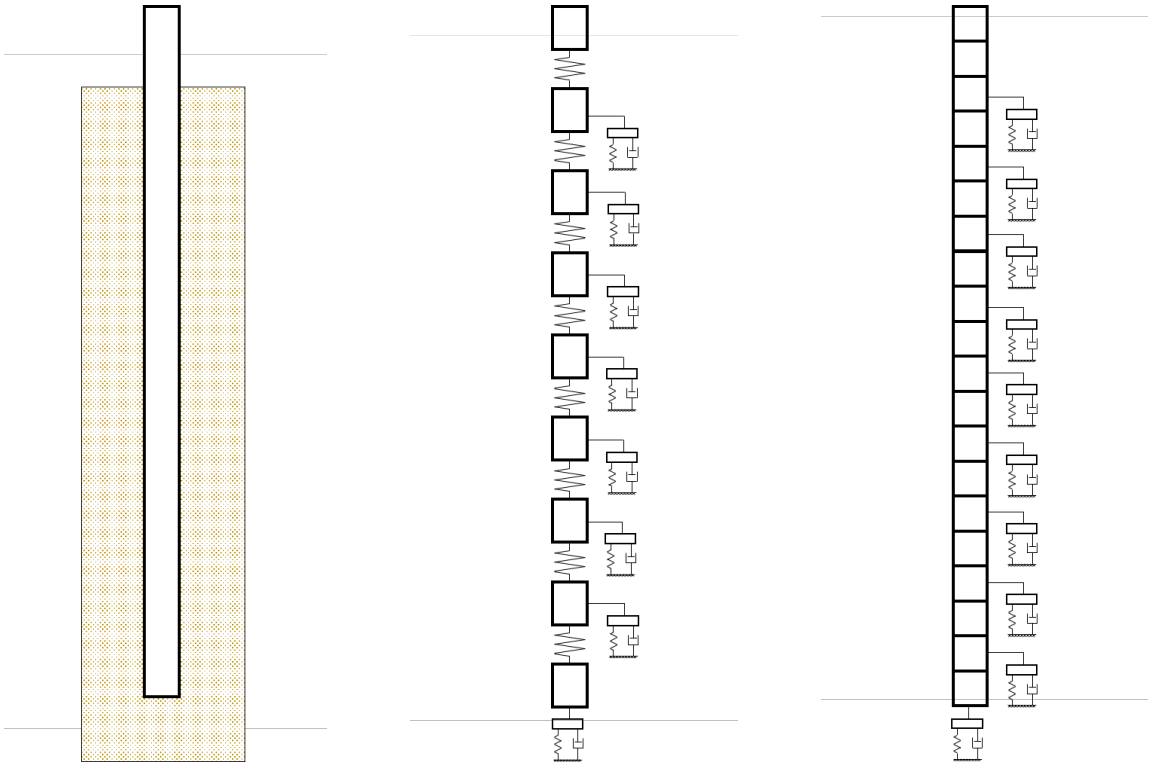

(a) 3-D continuous soil (b) Lumped mass model (c) Characteristic model

Figure 3.2: Wave equation models of pile foundation

3.2.1 Finite Difference Method

In order to give an approximate solution to the wave equation problem during pile installation, Smith (1960) proposed a lumped mass model with the finite difference method to divide the pile into a series of elastic springs and lumped pile masses along with a mechan-

ical model of the hammer system. The lumped-mass model of the pile system is shown in Figure 3.2b. The soil resistance was defined using nonlinear springs along the pile to represent side friction and a nonlinear spring at the toe of the pile to represent bearing resistance. Soil damping was modeled as a viscous damping factor, J_s, which was related to the static soil resistance, W_u, as shown in Eq. 3.9.

$$W_d(t) = W_u(t)(1 + J_s v(t)) \tag{3.9}$$

The original solution of the wave equation for dynamic signal matching, used initially in the Case Pile Wave Analysis Program (CAPWAP), was generated using a lumped-mass pile model (Rausche et al. (1972)), which was an extension of the Smith model (Smith (1960)). However, while this model was found to provide flexibility with respect to modeling the pile and nonlinear soil-structure interaction response, it was found that a mismatch between calculated and measured responses resulting from errors inherent to the finite difference method solution affected the inverse method of signal match quality. Specifically, the application of the finite difference method for pile driving analysis has been found to produce numerical inaccuracies causing elements to continue to vibrate after the wave front had passed (Van Weele and Kay (1984)). Consequently, the use of the finite difference method requires a very small time step that may be prohibitive for signal matching, especially when the pile response includes higher frequencies and cases with large toe resistance.

3.2.2 Method of Characteristics

Since the finite difference solution of the lumped-mass model was found to present problems with the accuracy of the solution, the method of characteristics (Fischer (1960)) was

introduced as an alternative in wave analysis programs such as Hydroblock (Voitus van Hamme et al. (1974)), TNOWAVE (Van Koten et al. (1980)), and more recent versions of the CAPWAP program (Rausche et al. (1985)) to more accurately model the pile and soil resistance without the issues previously described. In general, the method of characteristics assumes that stress waves in a frictionless pile travel through the pile based on a characteristic stress wave velocity, or wave speed c_L, and models the pile as a continuous member with a number of equally dimensioned 'slices', or elements, as shown in Figure 3.2c. Initially, the pile was modeled as frictionless rod with a soil toe resistance and then later the model was extended to include shaft soil resistance in the model (Voitus van Hamme et al. (1974)). Using the characteristics of the down wave force and up wave force and theoretical soil models, a signal matching routine, described in a later section, can be used to estimate the pile's axial capacity and soil resistance distribution. The relationship between time steps and the dimension of the slices is defined by the material wave speed such that:

$$dt = \frac{dx}{c_L} \tag{3.10}$$

It is important to note that the method of characteristic calculates the pile response at the slices, but the method does not discretize the system like the finite difference method. In fact, the method of characteristics yields a closed form analytical solution for the wave equation that introduces none of the errors or stability issues created by the finite difference method.

Using the method of characteristics, the wave equation has the general solution:

$$u = f^{\downarrow}(x - c_L t) + f^{\uparrow}(x + c_L t) \tag{3.11}$$

which describes the displacement as the superposition of two waves traveling throughout a position of the pile, x, a downward traveling wave via $f^{\downarrow}$ and an upward traveling wave via $f^{\uparrow}$, both associated with a constant wave speed, c_L.

Within dynamic testing of pile foundations, the strain is measured at the head of the pile and then this strain is used to calculate the internal axial force in the pile at the measurement location as

$$F(t) = \sigma(t)A = EA\epsilon(t) \tag{3.12}$$

The force within the pile, F, is comprised of two force waves, $F^{\downarrow}$ and $F^{\uparrow}$, which by superposition must sum together to obtain the total internal force at any location:

$$F(x,t) = -EA\frac{\partial u(x,t)}{\partial x} = -EA\frac{\partial f^{\downarrow}}{\partial(x - c_L t)} - EA\frac{\partial f^{\uparrow}}{\partial(x + c_L t)} = F^{\downarrow}(x,t) + F^{\uparrow}(x,t) \tag{3.13}$$

Likewise, the velocity at any position in the pile is the superposition of the velocity of the downward traveling wave, $v^{\downarrow}(x,t)$, and the velocity of the upward traveling wave, $v^{\uparrow}(x,t)$:

$$v(x,t) = \frac{\partial u(x,t)}{\partial t} = -c_L\frac{\partial f^{\downarrow}(x,t)}{\partial(x - c_L t)} + c_L\frac{\partial f^{\uparrow}(x,t)}{\partial(x + c_L t)} = v^{\downarrow}(x,t) + v^{\uparrow}(x,t) \tag{3.14}$$

Through Equations 3.13 and 3.14, the velocity and internal force in the downward traveling wave and upward traveling wave are related according to:

$$v^{\downarrow}(x,t) = \frac{c_L}{EA}F^{\downarrow}(x,t) \tag{3.15}$$

and

$$v^{\uparrow}(x,t) = -\frac{c_L}{EA}F^{\uparrow}(x,t) \tag{3.16}$$

Mechanical impedance, Z, is a property that relates applied harmonic force to velocity for a system. For a homogeneous linear elastic pile, the impedance as a function of the

wave speed is expressed as:

$$Z = \frac{EA}{c_L} \tag{3.17}$$

Using this definition of mechanical impedance, the equivalent force in an assumed friction-less pile can be computed from the measured velocity as

$$F_v(t) = Zv(t) = \frac{EA}{c_L}v(t) \tag{3.18}$$

Also, by this definition of mechanical impedance:

$$v^{\downarrow}(x,t) = \frac{F^{\downarrow}(x,t)}{Z} \tag{3.19}$$

and

$$v^{\uparrow}(x,t) = -\frac{F^{\uparrow}(x,t)}{Z} \tag{3.20}$$

By adding Equation 3.13 to 3.14 multiplied by Z, the down wave force can be computed from the total force and velocity as

$$F^{\downarrow}(x,t) = \frac{1}{2}[F(x,t) + v(x,t)Z] \tag{3.21}$$

and likewise subtracting Equations 3.14 multiplied by Z from Equation 3.13, the up wave force can be computed as

$$F^{\uparrow}(x,t) = \frac{1}{2}[F(x,t) - v(x,t)Z] \tag{3.22}$$

These relationships are employed at the top of the pile where the strain and acceleration transducers are installed to calculate the downward traveling wave force time history and upward traveling wave force time history. The measured strain time history is multiplied by the axial rigidity of the pile to obtain the total internal force at the instrumented elevation

of the pile, while the measured acceleration is numerically integrated to obtain the total velocity at this location.

If the soil side resistance is defined as a force, W, and soil toe resistance is defined as a force, F_g, then the method of characteristics can be applied to pile analysis with side friction resistance and bearing at the toe. The soil toe resistance can be defined based on an idealized boundary condition assumed at the toe or modeled by a spring with nonlinear stiffness. With the side frictional force included in the force equilibrium of each segment, the forces corresponding to the downward and upward traveling waves become:

$$F^{\downarrow}_{n,i} = F^{\downarrow}_{n-1,i-1} - \frac{1}{2}W_{n,i} \tag{3.23}$$

$$F^{\uparrow}_{n,i} = F^{\uparrow}_{n+1,i-1} + \frac{1}{2}W_{n,i} \tag{3.24}$$

and at the toe, force equilibrium with the toe bearing resistance produces:

$$F^{\uparrow}_{m,i} = F_g - F^{\downarrow}_{m,i} \tag{3.25}$$

where n is the element number, m is the element number at the toe, and thus the total number of elements, and i is the time increment.

If the boundary condition at the toe is considered to be a free condition, such that the soil resistance is zero ($F_g = 0$), then the toe force and resulting velocity is determined as

$$F^{\uparrow}_{m,i} = -F^{\downarrow}_{m,i} \tag{3.26}$$

$$v^{\uparrow}_{m,i}(t) = -\frac{F^{\uparrow}_{m,i}}{Z} = \frac{F^{\downarrow}_{m,i}}{Z} = v^{\downarrow}_{m,i}(t) \tag{3.27}$$

$$v_{m,i} = \frac{2F^{\downarrow}_{m,i}}{Z} \tag{3.28}$$

An example of the fictitious force and velocity responses for a pile with a free toe boundary condition, shown as a waterfall plot to illustrate changes in force and velocity along the depth of the pile with respect to time, is provided in Figure 3.3. This figure illustrates the generation of a compression wave that travels at a constant speed down the length of the pile and then reflects as a tension wave of equal magnitude force that travels back to the head of the pile. The particle velocity at the toe of the pile doubles in magnitude under the free toe boundary condition as well as at the head of the pile that is also modeled as unrestrained. Figure 3.4 provides the time histories for the force measurement that would be obtained at a location 12in from the head of the pile. It is important to recognize that the force computed from velocity doubles when the wave returns to the measurement location at $^{2L}/_{c_L}$, while the force measured from the strain gages is reduced to approximately half of the original magnitude due to the interaction of the upward traveling tension wave and downward traveling compression wave reflected at the unrestrained head of the pile. The general response produced by a pile with a free end at the toe is similar to the response obtained in driven piles where the toe bearing resistance is small.

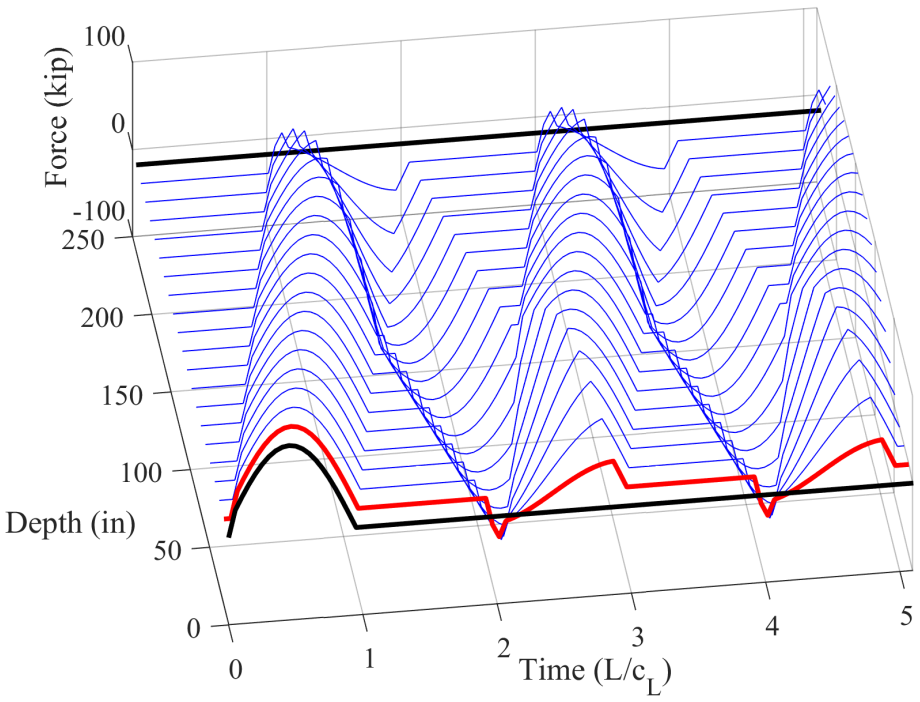

(a) Force waves

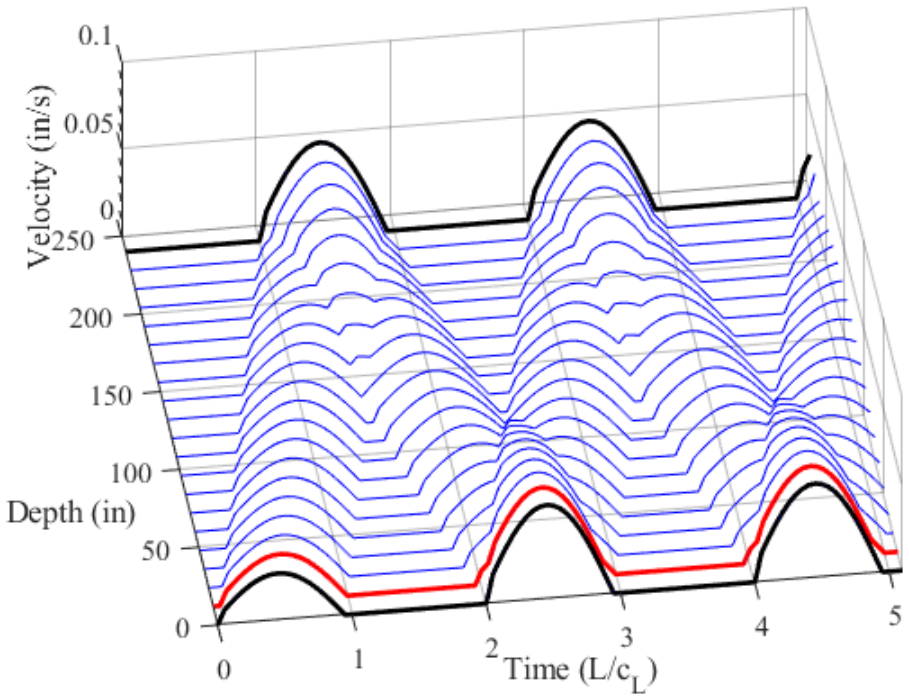

(b) Particle velocity

Figure 3.3: Method of characteristics simulation of wave propagation in a pile with a free toe boundary condition (black lines used for head and toe positions while the red line used for measured location)

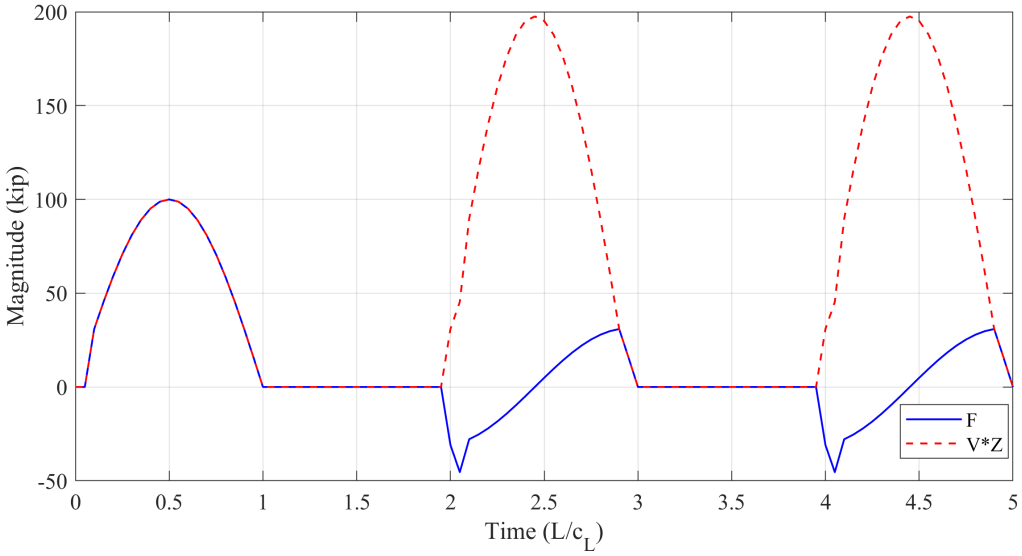

Figure 3.4: Example force time histories at a fictitious measurement site for a pile with a free toe boundary condition

Conversely, if the boundary condition at the toe is considered to be a fixed or fully restrained condition, there will be no displacement at the toe of the pile and, consequently, the velocity at the toe will be zero ($v_{m,i}(t) = 0$). The force and particle velocity at the toe is derived as:

$$v^{\downarrow}_{m,i}(t) + v^{\uparrow}_{m,i}(t) = 0 \tag{3.29}$$

$$v^{\uparrow}_{m,i}(t) = -v^{\downarrow}_{m,i}(t) \tag{3.30}$$

$$-\frac{F^{\uparrow}_{m,i}}{Z} = -\frac{F^{\downarrow}_{m,i}}{Z} \tag{3.31}$$

$$F^{\uparrow}_{m,i} = F^{\downarrow}_{m,i} \tag{3.32}$$

$$F_{m,i} = 2F^{\downarrow}_{m,i} \tag{3.33}$$

An example of fictitious force and velocity responses for a pile with a fixed toe boundary condition, shown as a waterfall plot to illustrate changes in force and velocity along the depth of the pile with respect to time, is provided in Figure 3.5. This figure illustrates

the generation of a compression wave that travels at a constant speed down the length of the pile and then reflects as a compression wave at the fixed toe. Due to the interaction of the downward traveling compression wave and the reflected upward traveling compression wave, the magnitude of the compression force at the toe effectively doubles. As expected by the prescribed boundary condition, the particle velocity at the toe is zero. The particle velocity at the head of the pile alternates between negative and positive as the wave alternates between compression and tension at the unrestrained head of the pile. Figure 3.6 provides the time histories for the measurement that would be obtained at a location 12in from the head of the pile. It is important to recognize that the force computed from velocity reverses direction and doubles in magnitude when the wave returns to the measurement location at $^{2L}/_{c_L}$, while the force measured from the strain gages is reduced to approximately half of the magnitude of the applied load due to the interaction of the upward traveling compression wave and downward traveling tension wave reflected at the unrestrained head of the pile. The general response produced by a pile with a fixed toe is similar to the response obtained in driven piles with large toe bearing resistance.

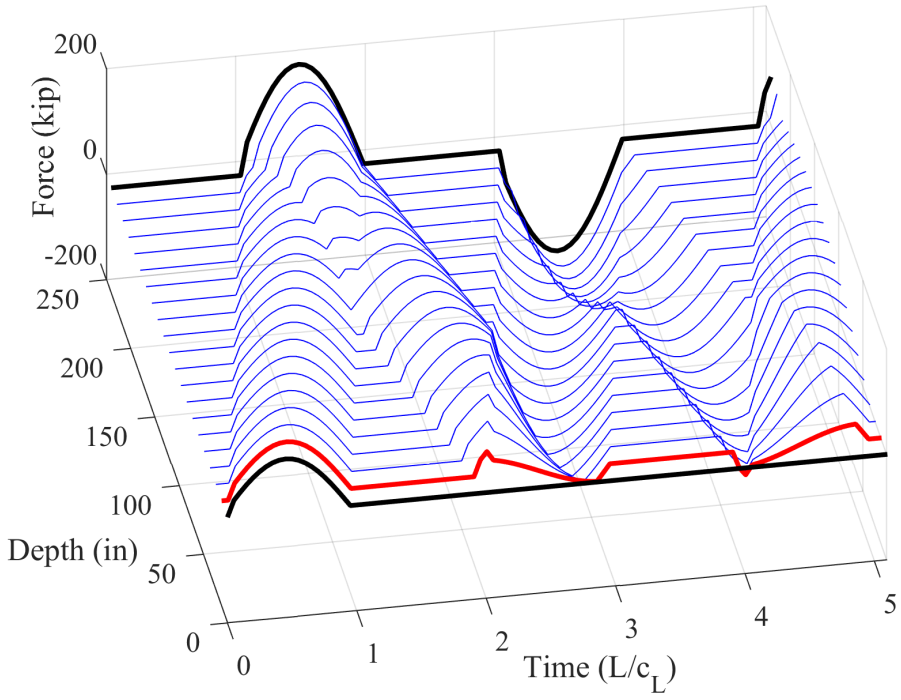

(a) Force waves

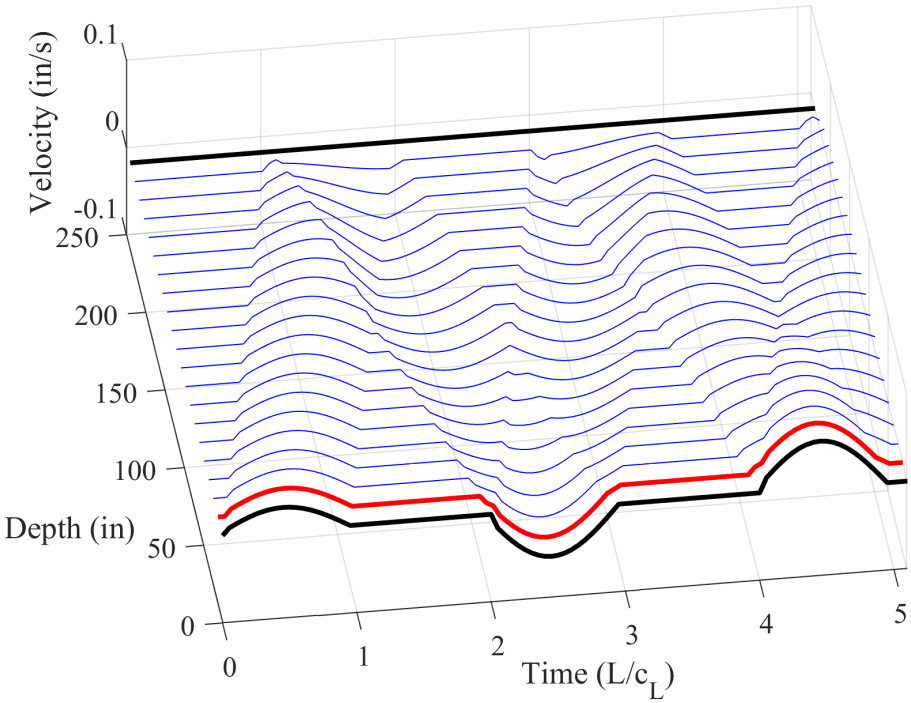

(b) Particle velocity

Figure 3.5: Method of characteristics simulation of wave propagation in a pile with a fixed toe boundary condition (black lines used for head and toe positions while the red line used for measurement location)

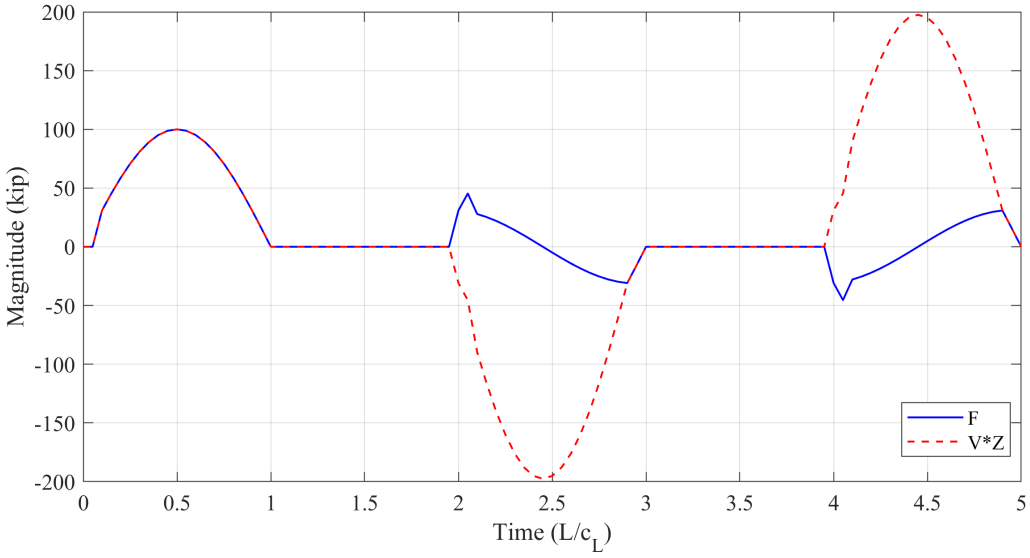

Figure 3.6: Example force time histories at a fictitious measurement site for a pile with a fixed toe boundary condition

When soil resistance is modeled for either the side friction or toe resistance, the soil resistance force includes both static and dynamic resistance such that:

$$W = W_u + W_v + W_a \tag{3.34}$$

Where W_u is the static soil resistance, W_v is dynamic soil resistance proportional to velocity, and W_a is dynamic soil resistance proportional to acceleration. The static soil resistance, W_u, is typical defined by a elasto-plastic response dependent on local displacements such that:

$$W_u(t) = R_s(u_p) \tag{3.35}$$

where the nonlinear function, $R_s(u_p)$, is dependent on the displacement, u_p, at a particular location, as shown in Figure 3.7. This function is dependent on soil characteristics that include gap, g, loading quake, q, ultimate loading soil resistance, R_u, unloading quake, q_u, ultimate unloading soil resistance, R_{nu}, and reloading soil resistance, R_L.

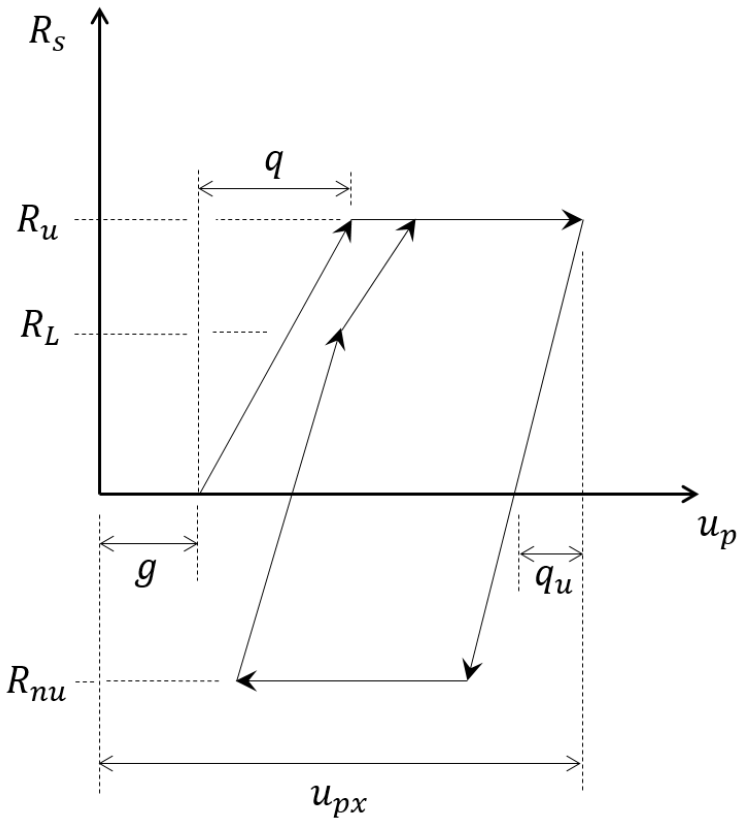

Figure 3.7: Typical nonlinear elasto-plastic static soil resistance model used for dynamic pile analysis and signal matching

The dynamic soil resistance can be defined using Smith damping, Case damping, or the Coyle and Gibson (1970) damping model, although it should be noted that the Smith and Case models can be expressed as a function of each other. The force versus velocity relationships for each of these dynamic soil resistance models are shown in Figure 3.8 and the equations for each dynamic soil resistance model are:

- Smith Damping (1960), J_s

$$W_v(t) = W_u(t)J_s v(t) = Cv(t) \tag{3.36}$$

- Case Damping (Rausche (1970)), J_c

$$W_v(t) = J_c Z v(t) = C v(t) \tag{3.37}$$

- Coyle & Gibson (1970)

$$W_v(t) = W_u(t) J_s v(t)^{\alpha} = C v(t)^{\alpha} \tag{3.38}$$

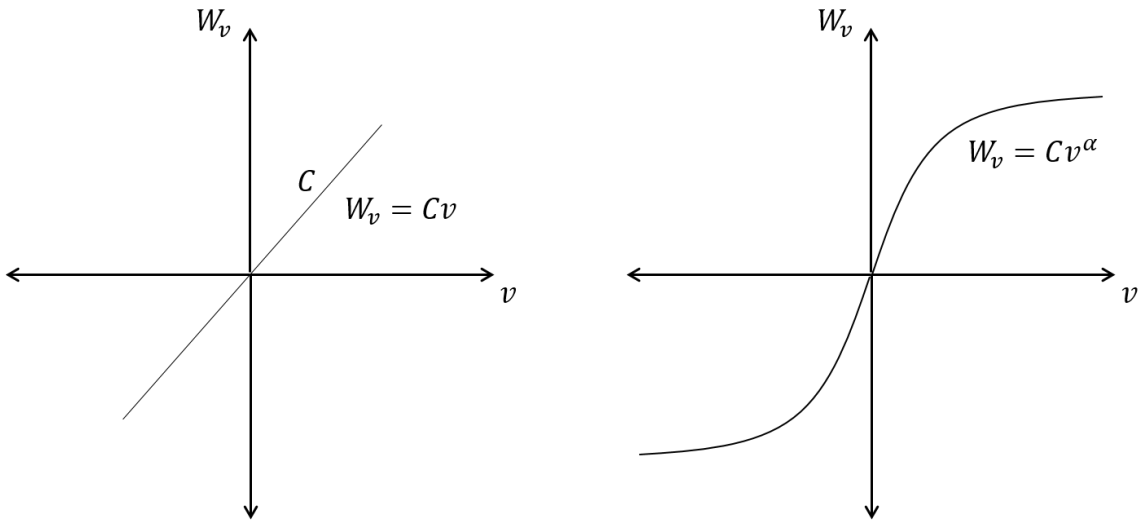

(a) Smith (1960) and Case (Rausche (1970)) definitions

(b) Coyle & Gibson (1970) definitions

Figure 3.8: Dynamic soil resistance models

Finally, although though not commonly used due to the difficulty of estimating soil mass contributions, the dynamic soil resistance developed by inertial effects from possible added mass of the soil attached to the pile, m_s, is defined as:

$$W_a(t) = m_s a(t) \tag{3.39}$$

An example of fictitious force and velocity responses for a pile with side friction modeled only at a depth of 108in from the head of the pile and with a free toe boundary condition,

shown as waterfall plot to illustrate changes in force and velocity along the depth of the pile with respect to time, is provided in Figure 3.9. This figure illustrates the generation of a compression wave at the head of the pile that travels at a constant velocity down the length of the pile and a reflected stress wave is generated at the location where the side friction is modeled. The remaining unreflected waves continue to travel to the toe of the pile and follow the theory previously described for the free toe boundary condition. Figure 3.10 provided the time histories for the measurement that would be obtained at a location 12in from the head of the pile. It is important to recognize that there is a separation between the force measurement and the velocity measurements between the time of impact and the measured toe reflection at $^{2L}/_{c_L}$, specifically in this example at approximately $^{L}/_{c_L}$, which results due to the side friction resistance along the pile. When the side friction is present along the full depth of the pile, which is more characteristic of a drive pile model, the separation in the force traces is more significant and interpretation of the pile behavior from the force traces become more difficult due to the complexities of the stress wave reflections occurring along the full length of the pile.

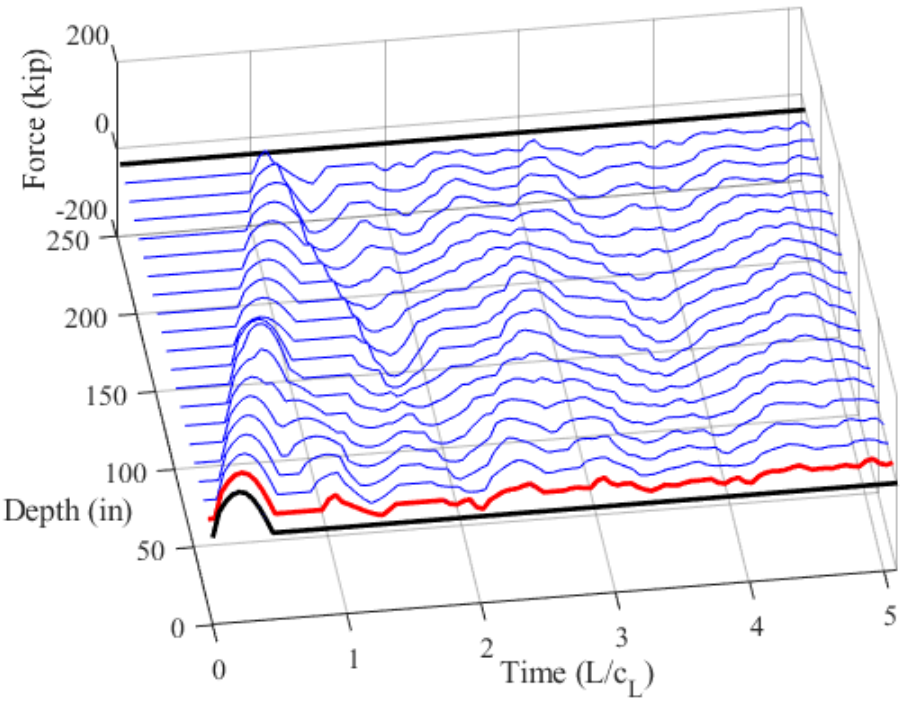

(a) Force waves

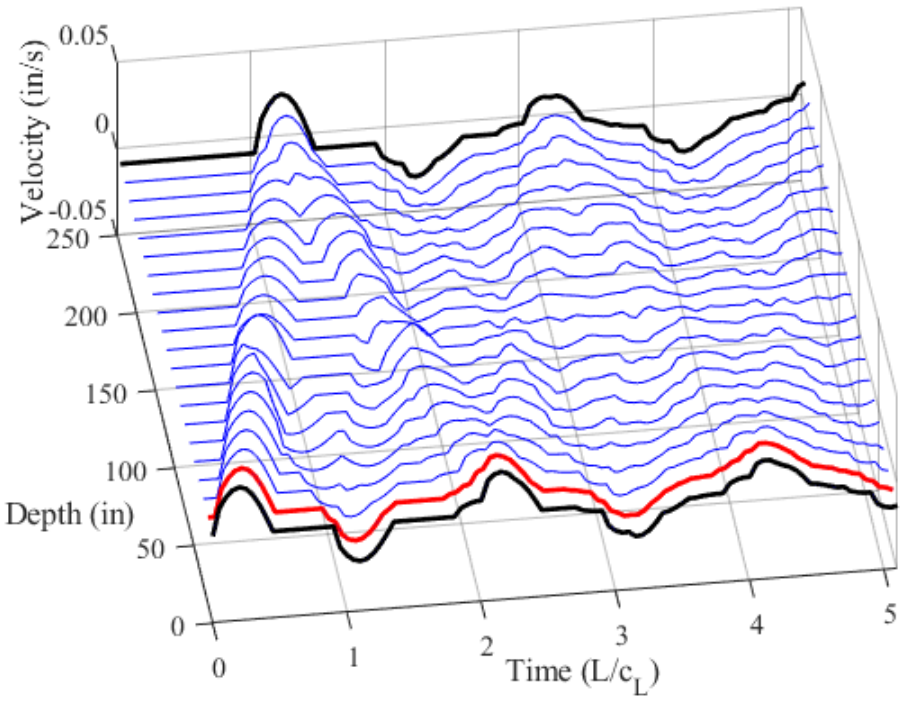

(b) Particle velocity

Figure 3.9: Method of characteristics simulation of wave propagation in a pile with side friction resistance at a discrete location and a free toe boundary condition (black lines used for head and toe positions while the red line used for measurement location)

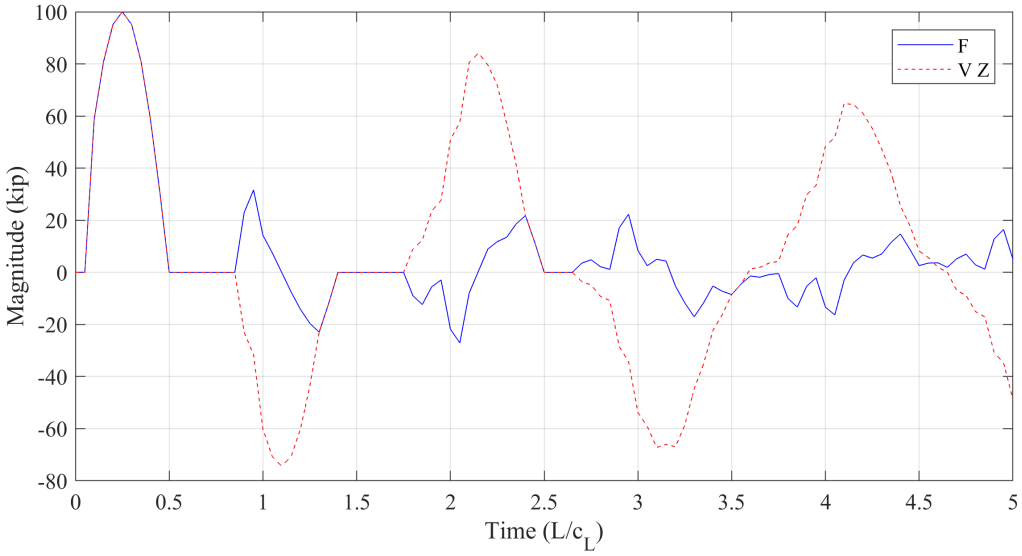

Figure 3.10: Example force time histories at a fictitious measurement site for a pile with side friction at a discrete location and a free toe boundary condition

3.3 Dynamic Testing Equipment, Procedure, and Interpretation

Dynamic testing methods typically use measured strains and accelerations at the pile head. At a minimum, the ASTM D4945 (2017) standard requires two strain transducers and two accelerometers installed at the pile head at a distance of at least 1.5 times the diameter or width of the pile from the pile head. These pairs of sensors are installed as a couple along, or equidistant from, the neutral axis of the pile section in order to produce measurements of longitudinal strain and axial acceleration by nulling any bending effects in the measurements through averaging. This data is collected with a data acquisition unit capable of recording the measurement signals at a minimum of 10kHz sampling rate. According to the standard, the pile must be installed into the ground with a impact hammer type system and will ideally produce an appropriate response which can be recorded and verified during the installation process. This response verification is done by a qualified en-

gineer by comparing the pile head force, F, to the pile head velocity, V, after a single blow. In order to determine these values, the strain, ϵ, is converted to a force according to Equation 3.12 and the measured acceleration, a, is numerically integrated with respect to time to derive the particle velocity at the head of the pile. Using the mechanical impedance of the pile, the velocity time history can be converted into an equivalent force from the frictionless pile, according to Equation 3.18. The measurements of force and velocity are compared on magnitude proportionality, energy, and consistency in the measurements obtained between similar sensors (GRL Engineers Inc and Pile Dynamics Inc (2008)). Commercially developed programs are available to complete such task during dynamic testing.

3.4 Case Method

Prior to the installation event in the field, the wave equation is typically solved via a computer program to determine pile driving stresses and expected axial capacity. This process requires an engineer to make assumptions about the soil response and dynamic properties of the impact hammer, cushion, and pile cap. Wave analysis programs provide the engineer a relationship between blow counts and ultimate static load capacity, which is the driving criteria for the driven piles. In order to produce an estimate of ultimate static capacity and for comparison to the driving criteria, the field measurements are used to quickly estimate the soil resistance and the ultimate static capacity. In order to quickly estimate these values, the Case method is used, which was developed from research conducted by Case Western Reserve University, Cleveland, Ohio (Eiber (1958)).

Hannigan et al. (2016) states that the Case method models the pile as linearly elastic with a constant cross sectional area to develop the total soil resistance, RTL, is defined as:

$$RTL = \frac{1}{2}[F(t_1) + F(t_2)] + \frac{1}{2}[v(t_1) - v(t_2)](Z) \tag{3.40}$$

where $F(t)$ is the force measurement at the gage location at time t, $V(t)$ is the velocity measurement at the gage location at time t, t_1 is the time of the first peak of the signal adjusted by a time shift based on the time, t_2 to the reflection of the first peak of the signal from the pile toe $\left(t_1 + \frac{2L}{c_L}\right)$, L is the length of the pile below the gage location, c_L is the wave speed of the pile material, Z is the mechanical impedance of the pile. This is schematically presented in Figure 3.11.

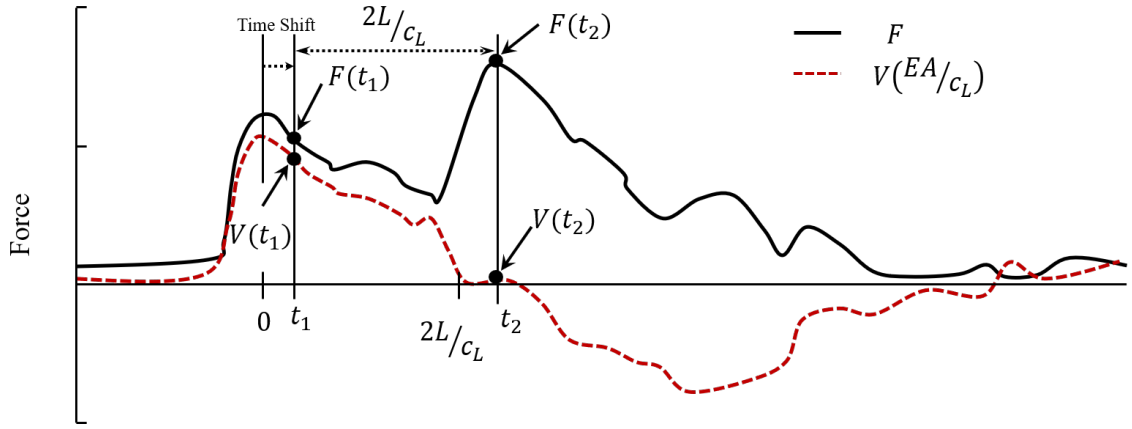

Figure 3.11: Example force time histories from measurement instrumentation of a dynamic load test to be used for the Case method axial capacity estimation

In order to determine the static resistance in the soil (RSP), the dynamic resistance is subtracted from the total soil resistance. Following Goble et al. (1975), dynamic resistance can be approximated as a linear product of a damping constant and the pile toe velocity at the first peak. By subtracting this dynamic resistance from the total soil resistance, the

Table 3.1: Case damping factors

Soil Type	Original Case Damping Range (Goble et al. (1975))	Updated Case Damping Range (Pile Dynamics, Inc. (2015) & Hannigan et al. (2016))
Clean Sand	0.05 - 0.20	0.10 - 0.15
Silty Sand, Sand Silt	0.15 - 0.30	0.15 - 0.25
Silt	0.20 - 0.45	0.25 - 0.40
Silty Clay, Clayey Silt	0.40 - 0.70	0.40 - 0.70
Clay	0.60 - 1.10	0.70+

static soil resistance can be computed as:

$$RSP = RTL - J\Big[v(t_1)(Z) + F(t_1) - RTL\Big] \tag{3.41}$$

where J is the Case damping factor. The Case damping factor is an unknown property of the soil-structure interaction, so the accuracy of the static capacity estimate developed by the Case method depends heavily on the accuracy of the assume Case damping factor. A summary of recommended Case damping factors, based on the soil type at the pile toe, is shown in Table 3.1.

3.5 Signal Matching

After pile installation, the measurements of force and velocity can be used to obtain an improved estimate of the axial capacity of the tested pile through a process called signal matching. The first step of the signal matching process includes estimating reasonable properties for the soil-structure interaction included in the method of characteristics model of the pile. These properties include the soil ultimate loading and unloading resistance distribution, the loading and unloading soil quake, and soil damping parameters. These initially assume properties are used to predict the measured pile response using the method of characteristics and then the properties are subsequently updated through an iterative process until an acceptable match quality is reached. Table 3.2 presents some suggested values

Table 3.2: Recommended bounds for parameters in soil-structure interaction models for dynamic testing of axially loaded piles from Rausche et al. (2010)

Parameter	Symbol	Unit	Min. Shaft	Max. Shaft	Min. Toe	Max. Toe
Quake	q	in	0.0394	0.2953	0.0394	Max. Displacement - g
Unloading Quake	$\frac{q_u}{q}$		0.3	1.0	0.3	1.0
Negative Ult. Resist.	$\frac{R_{nu}}{R_u}$		0.0	1.0	0.0	0.0
Gap	g	in	0.0	0.0	0.0	Max. Displacement - g
Reloading	$\frac{R_L}{R_u}$		-1.0	1.0	0.0	1.0
Damping Option			0	2	0	2
Smith-Case Damping Factor	J	s/in	0.001016	0.03556	0.001016	0.03556

and ranges for each respective parameter involved in the signal matching routine (Rausche et al. (2010)). The options specified in the table refer to different approaches to determine the dynamic resistance that are used within one of the most popular commercial signal matching software applications, CAPWAP. Option 1 defines the dynamic soil resistance as:

$$R_d(t) = J_s R_s(t) v(t) \tag{3.42}$$

while another option, Option 0, defines the dynamic soil resistance as truly viscous using the Smith damping model such that:

$$R_d(t) = J_s R_u v(t) \tag{3.43}$$

Option 2 calculates the dynamic resistance using the Option 1 definition until the quake has been reached, at which point it then uses the Option 0 definition.

To initiate the signal matching, the downward traveling wave force, calculated directly from the measured force and velocity through Equation 3.21, is used to initiate the pile head into motion. The method of characteristics is then used to compute the force of the upward traveling wave, which is then compared to the upward traveling wave force calculated from the measured force and velocity using Equation 3.22. The correlation between the pre-

dicted and measured upward traveling wave force is defined as the match quality, MQ, and is determined by accumulating the difference between measured ($F_M^{\uparrow}$) and calculated ($F_c^{\uparrow}$) upward traveling wave forces and then dividing by the maximum observed upward traveling wave force ($F_{max}^{\uparrow}$) windowed time periods, or zones, to normalize the match quality magnitude (GRL Engineers Inc and Pile Dynamics Inc (2013)). The match quality function also includes a Blow Count Penalty (BCP) that is based on the difference between the measured settlement and settlement calculated by the method of characteristics solution. The resulting equation used to determine the match quality is shown in Equation 3.44. The Blow Count Penalty has been reported as shown in Equation 3.44 by (GRL Engineers Inc and Pile Dynamics Inc (2013)). Depending on the accuracy required, adjustments to the soil properties are iteratively made and this calculation is repeated until a satisfactory fit is obtained.

$$MQ = \sum_{period} \sum_{time} \frac{F_M^{\uparrow} - F_c^{\uparrow}}{F_{max}^{\uparrow}} + BCP \tag{3.44}$$

Rausche et al. (2010) presents a definition of zones within the time history of the response and indicates that specific properties of the soil-structure interaction models influence each particular zone most significantly. These zones are presented in Figure 3.12. Zone 2 is defined to have a time duration equal to the rise time, t_r plus 3ms, while Zone 3 extends for a time duration equal to the rise time plus 5ms. Zone 4 begins immediately after Zone 2 and extends for a fixed duration time of 20ms. The shaft resistance distribution is considered the dominant influence for Zone 1, the toe model most significantly affects Zone 2, the overall nominal resistance influences the signal fit in Zone 3, and the unloading behavior dominates the Zone 4 response. An understanding of how the parameters in the

soil-structure interaction models affect different zones in the measured response helps a practitioner manually adjust individual parameters in the soil-structure interaction models to obtain improved correlation during the signal matching process.

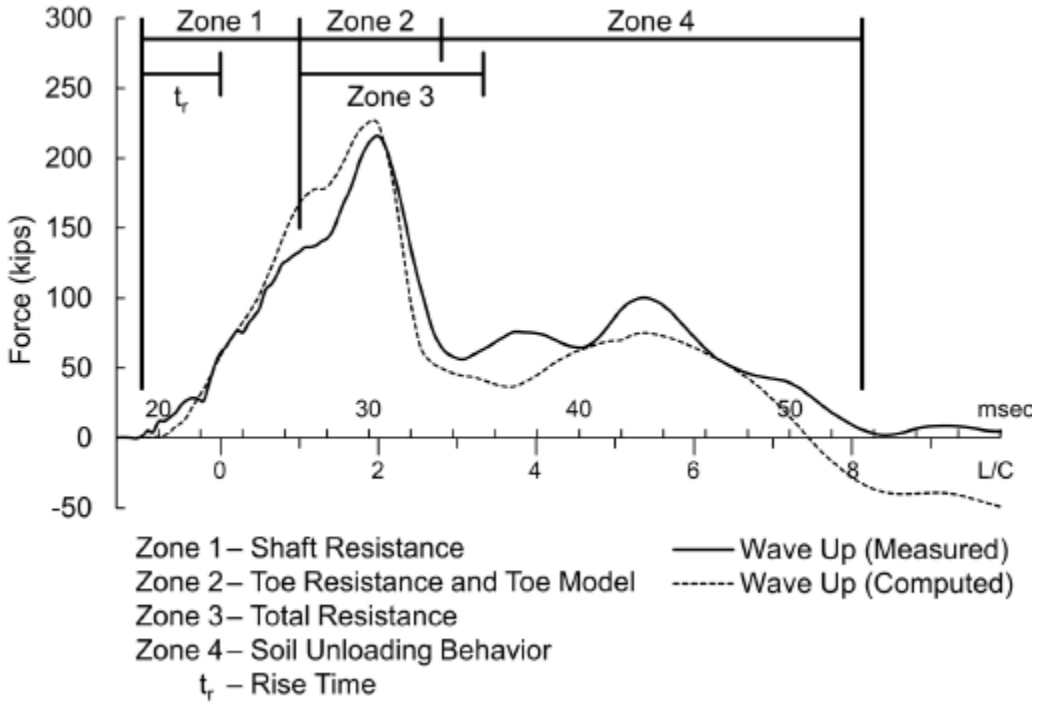

Figure 3.12: Zones used in the signal matching process (from Hannigan et al. (2016))

CAPWAP is one commercial software application that is widely utilized for signal matching of dynamic pile response measurements. The CAPWAP analysis goes through a iteration process, changing soil parameters, until an acceptable wave match through the match quality determination is achieved. This process starts with an engineer selecting an estimated total capacity, typically from the Case method, soil resistance distribution, and soil damping and quake parameters (Rausche et al. (2010)). CAPWAP proceeds to determine remaining soil model parameters, either through changing the resistance distribution manually or by performing a grid search to optimize the match quality by adjusting a subset of the parameters in the soil-structure interaction models. Several stages of manual or

automatic tuning are typically applied on subsets of the parameters in the soil-structure interaction models, selected by practitioner experience, until the practitioner determines that the best possible match quality has been achieved. In some cases, the practitioner may hold certain parameters constant based on their expectation for the distribution of soil resistance or information from in-situ tests. Consequently, the final model may not always represent the one that develops the global minimum of the match quality function and, in general, the signal matching process in CAPWAP can be driven by many subjective decisions provided by the practitioner. Once the program presents graphical results for the signal match, estimated static load-displacement response of the pile, and load transfer down the depth of the pile, as forecast by the soil-structure interaction models associated with the parameters in the final model.

Rausche et al. (2010) identified uniqueness issues when identifying soil parameters within the CAPWAP model and suggested that an experienced engineer carefully review the results from CAPWAP. However, the authors concluded that, despite the uniqueness issues, CAPWAP effectively predicts the total axial bearing capacity of piles. In order to facilitate rapid quality control during the pile driving process by increasing speed of results from a CAPWAP analysis, Likins et al. (2012) presents a new program, iCAP, to perform immediate automatic signal matching analysis that can be completed on the day of testing. The iCAP analysis is initially similar to the CAPWAP analysis in that it uses the same force and acceleration measurements as well as soil-structure interaction models within a signal matching routine facilitated by a method of characteristics solution of the wave equation. However, the iCAP analysis performs automated identification of the parameters in the soil-structure interaction models through a multi-stage optimization routine. The routine

first establishes an acceptable shaft resistance distribution, followed by selecting a set of standard soil parameters, which include Smith side and toe damping constants, side and toe loading and unloading quakes, side unloading ratio, toe resistance gap and possible soil plug weight, and total capacity. If the total capacity is over a specified limit defined by the user, the search is performed again. A quicker version of iCAP skips the iterative searching for the soil parameters and only estimates the shaft resistance distribution, soil variables, and total capacity once. However, using soil-structure interaction parameters identified from previous blows, the accuracy of total capacity can be increased. According to the authors, iCAP is limited in application to uniform, non-timber piles and does not include radiation damping. Likins et al. (2012) found that the quick iCAP axial capacity estimates were within 10% of the CAPWAP estimates in more than 80% of the cases. The initial estimates of soil parameters, such as shaft distribution and total axial capacity, and acceptance of the final identified soil-structure interaction models still requires an experienced engineer's review and approval.

In summary, while there have been attempts at automating or semi-automating the signal matching process, there is no established set procedure or technique for solving the inverse problem of signal matching for dynamic testing of driven piles. Given the nature of signal matching as an inverse analysis method, there are also potential issues with uniqueness of the solution and sensitivity of the parameters in the soil-structure interaction models to measurement noise and errors. Furthermore, the large set of uncertain parameters in the soil-structure interaction models makes global optimization of the match quality function difficult.

CHAPTER 4: EXPERIMENTAL TESTING OF SHEET PILES IN LABORATORY AND FIELD INSTALLATIONS

This chapter presents the laboratory test program where rapid testing was conducted on a sheet pile wall and the field test program where dynamic testing was conducted on a pair of sheet piles as well as a H-pile for comparison. Each section describes the instrumentation and test setup, the testing program, a summary of representing response measurements for each test program, and static capacity estimates for both the laboratory and field dynamic tests.

4.1 Laboratory Rapid Load Testing

Laboratory testing was completed in the Structural Highbay Laboratory of the Energy Production and Infrastructure Center (EPIC) building at UNC Charlotte. The test was conducted in a 12ft by 12ft wide by 10ft deep geotechnical pit and in soil of clayey sand to silty, clayey sand that was selected by the North Carolina Department of Transportation (NCDOT). A photograph of the geotechnical pit prepared with the soil is shown in Figure 4.1. The PVC tubing, shown in the photograph, was placed for cross-hole velocity testing before and after loading events, although this measurement was not specifically used within the rapid testing program. In addition to the cross-hole velocity testing, several in-situ geotechnical tests were conducted in the test pit and the results of these investigations are presented in Figure 4.2. Standard penetration test (SPT) blow counts, cone penetrometer test (CPT) tip and sleeve resistances, and dilatometer (DMT) readings were generally

uniform with respect to depth throughout the test pit. It should be noted that the in-situ testing was performed before and after pile installation but prior to inundating the test pit with water to approach a saturated soil condition. The grain size distribution for the soil used in the test pit is shown in Figure 4.3. The maximum dry unit weight was calculated as 118.8lb/ft^3 with a optimum water content of 12.25%, a liquid limit (LL) ranging between 26-34%, and a plastic limit (PL) ranging between 20-23%. More details on the characterization of the soil used in the test pit are presented by Sylvain (2019).



Figure 4.1: Photograph of geotechnical pit used for laboratory tests

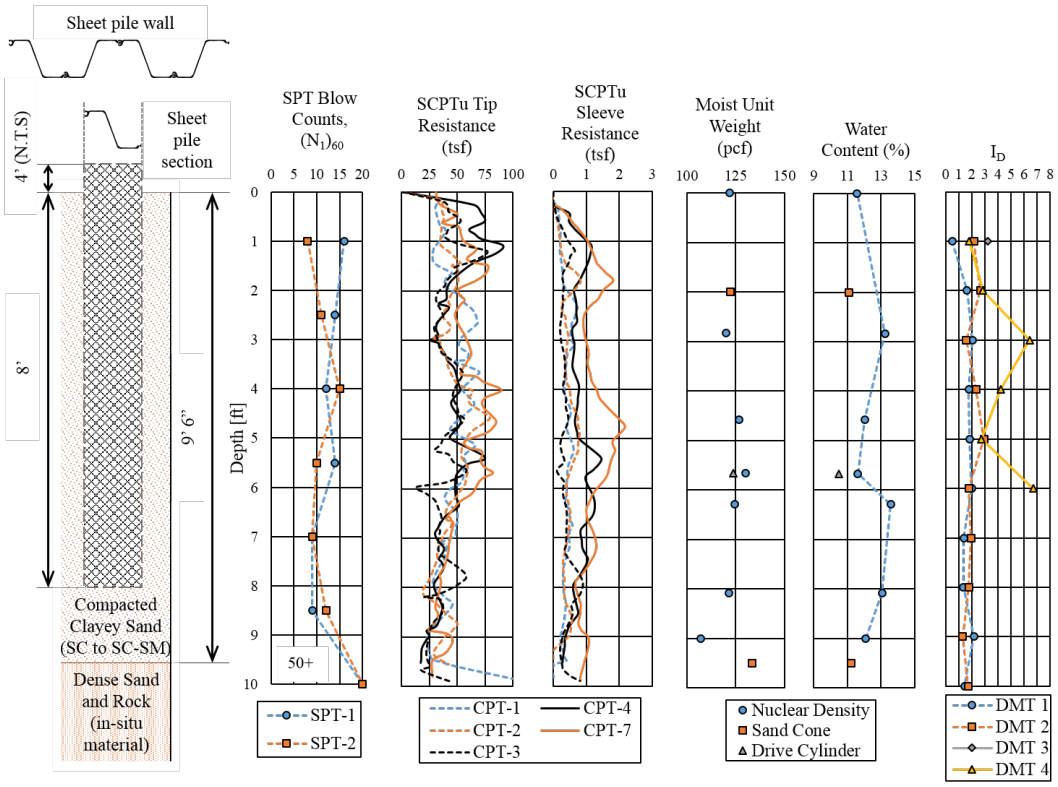

Figure 4.2: Stratigraphy and in-situ test results for laboratory pit (from Sylvain (2019))

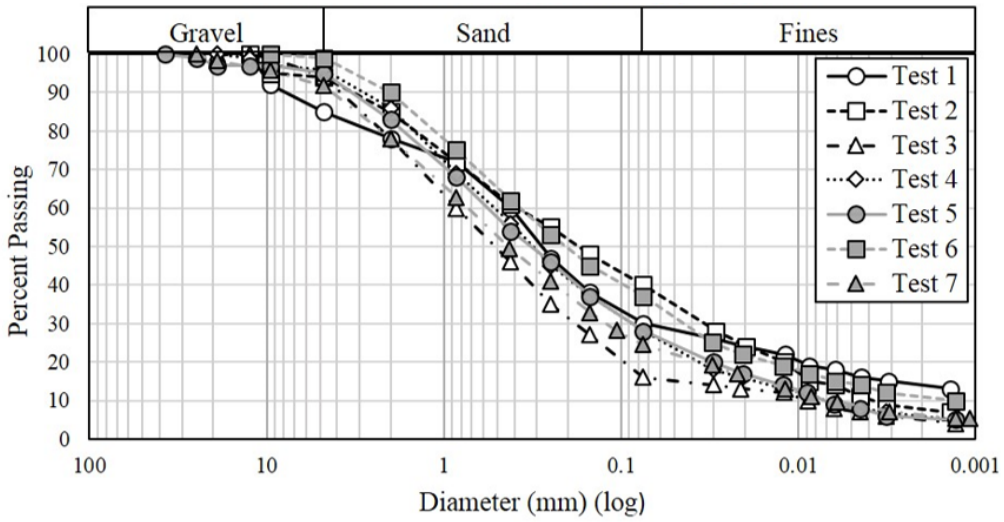

Figure 4.3: Grain size distribution for soil used in the geotechnical pit in Structural Highbay Laboratory of the EPIC building at UNC Charlotte (from Sylvain (2019))

The PZ27 sheet pile section was selected as the sheet pile profile for the test specimen and a sheet pile wall was constructed as an arrangement of four sections in order to mimic

a short length of sheet pile facing within a standard bridge abutment design. For identification, the sheet piles were numbered in order from the North to South sides of the wall. Figure 4.4 presents the numbering scheme used to identify each sheet pile and location of the tested wall in the geotechnical pit. Each pile was driven independently with an ICE Model 6E vibratory hammer to a depth of 8ft. The process of installing and aligning the individual piles, shown in Figure 4.5, began by first positioning and driving Pile #2 to a depth of approximately 4ft. Then, Pile #3 was connected to and aligned with Pile #2 and driven to the same depth. Pile #2 was then driven to the final 8ft embedment depth, followed by Pile #3. Pile #4 was driven directly to 8ft of embedment and finally, Pile #1 was driven to the final depth.

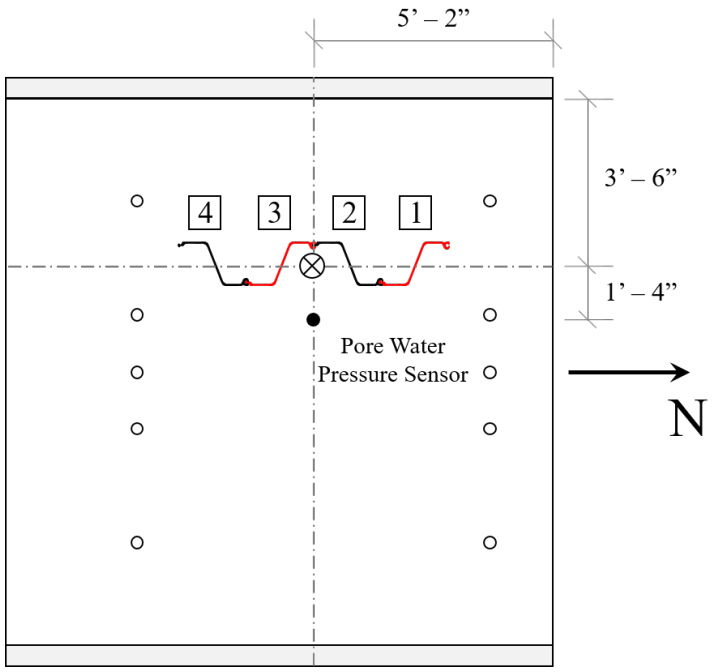

Figure 4.4: Location and numbering scheme of sheet piles (red indicates piles with below grade instrumentation)



(a) Driving Pile #1 to final depth



(b) Checking alignment of Pile #3 prior to driving to final depth

Figure 4.5: Photographs of the pile driving process

4.1.1 Instrumentation for Rapid Load Test

In order to study and estimate axial bearing capacity of the sheet pile system using the Unloading Point (UP), Modified Unloading Point (MUP), Segmental Unloading Point (SUP), and Embedded Data Collector (EDC) methods facilitated by rapid load testing, instrumentation was selected and installed at specific locations to enable each analysis method and provide supplemental data for verification. At a minimum, instrumentation must be placed at the head of the pile to measure strains and accelerations in order to satisfy the requirements of the UP method. The EDC method requires installation of another set of strain and acceleration sensors near the toe of the pile, and the SUP method requires a series of strain measurements at an array of discrete locations down the depth of the pile.

To meet these requirements, the laboratory testing included an array of reusable strain transducers, high shock accelerometers, and resistive strain gages (RSG). A pair of reusable strain transducers and high shock accelerometers were installed 1ft - 10in below the pile head on Piles #1 and #3. The strain transducers were oriented one inch away from the centerline of the outside flanges of the sheet pile and mounted using bolts. The accelerometers were mounted to aluminum blocks to orient them for measurement in the longitudinal direction of motion and were bolted adjacent to the strain transducers at a distance of two inches. A photograph of an installed reusable strain transducer and accelerometer is provided in Figure 4.6. Since these sensors are placed symmetric with respect to the centroid and principal axes of the cross section of the pile, the average of the measured strains and accelerations from these pairs results in cancellation of any bending effects in order to produce measurements of axial force and longitudinal motion. An additional pair of reusable strain transducers and high shock accelerometers were installed 2ft above the pile toe on Pile #3 in order to satisfy the requirements of the MUP and EDC methods. These transducers and accelerometers were placed above the pile toe in order to protect these sensors from damage during installation. The reusable strain transducers are model ST350 gages manufactured by Bridge Diagnostics, Inc. These gages feature a full Wheatstone bridge of 350Ω resistive gages providing temperature compensation and internal nulling of any bending strains developed in the transducer. The measurement range of the transducers is $\pm$ 4,000$\mu\epsilon$ and the nominal sensitivity is 500$\mu\epsilon$/mV/V. The two types of high shock accelerometers used include PCB Piezotronics 353B03, 353B04, and 353B31 accelerometers. Piles #2, #3, and #4 had pairs of model 353B31 accelerometers installed at the head of each pile. The 353B31 accelerometer has a nominal sensitivity of 50mV/g, a measure-

ment range of ± 100g, and a 3dB frequency range of 0.35-15,000Hz. On Pile #1, a pair of 353B03 accelerometers were installed at the head. For Pile #3, a pair of 353B04 accelerometers were used at the toe location. The only difference between the 353B03 and 353B04 accelerometers is the connector location. Both accelerometers have a nominal sensitivity of 10mV/g, a measurement range of ± 500g, and a 3dB frequency range of 0.35-20,000Hz.



Figure 4.6: Photograph of reusable strain transducer and high shock accelerometer installed on the laboratory pile

Two individual piles within the wall were selected for additional instrumentation consisting of bondable resistive strain gages to facilitate use of the SUP method. Pile #3, an interior pile, was selected for dense instrumentation down the length of the pile, while Pile #1, an exterior pile, featured a sparser instrumentation layout. The instrumentation of mul-

tiple pile sections was performed in order to provide insight into any differences in load transfer between interior and exterior piles. Pile #3 included resistive strain gages starting at 3ft - 1in below the pile head (11in above the ground line), in order to directly measure the applied force on that particular pile, and continued along the length of the pile every 15in for a total of eight elevations of resistive strain gage pairs. Pile #1 included resistive strain gages starting at 3ft - 1in below the pile head and continued along the length of the pile every 2ft - 11in for a total of four elevations of resistive strain gage pairs. The instrumentation layout described here is shown in Figure 4.7. Bondable CEA-06-250UN-350 general purpose resistive strain gages were used, which have a 0.25in gage length and a grid resistance of 350 $\Omega \pm 0.3\%$. All resistive strain gages were installed as single gages in a quarter Wheatstone bridge configuration with completion and shunt calibration resistors provided at the signal conditioner.

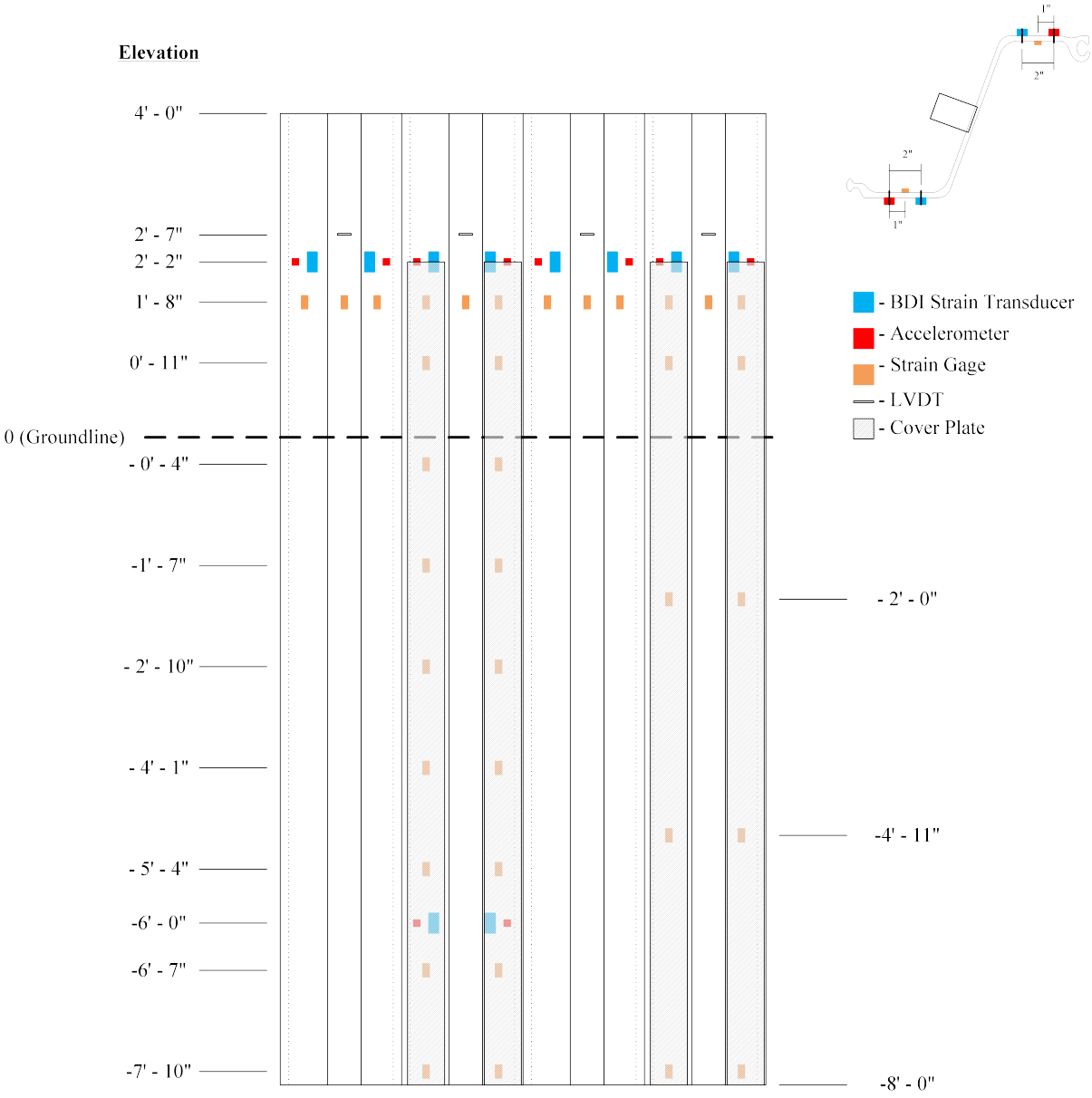

Figure 4.7: Sensor schematic for laboratory testing

The resistive strain gages were installed in the longitudinal direction of the pile along the center line of each flange. Resistive strain gages were installed on both flanges so that the individual strain measurements could be used to determine flexural moments as well as axial forces along the length of the pile. The reusable strain transducers and high shock accelerometers were installed one inch from this center line at the given elevations. The

location of each sensor on the cross section of each pile is dimensioned in Figure 4.8.

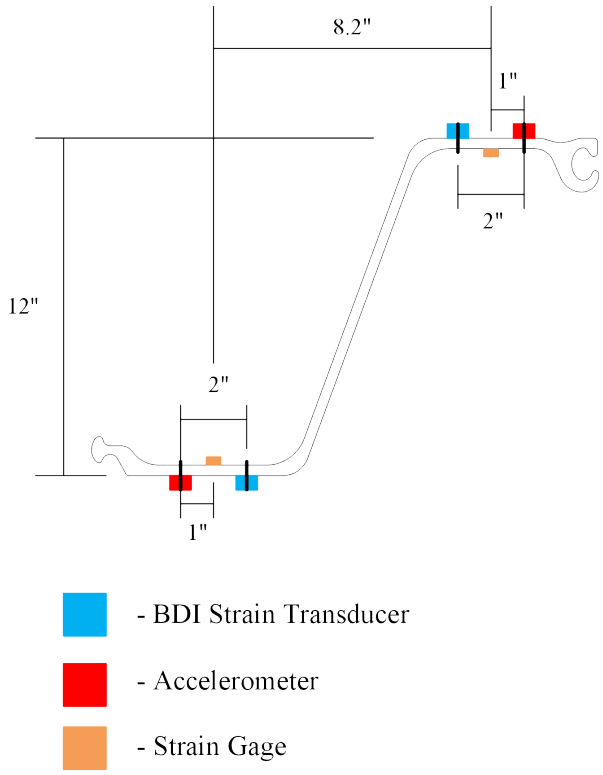

Figure 4.8: Sensor locations across cross section of laboratory test pile

For installation of resistive strain gages, the preparation of the surface included degreasing with isopropyl alcohol, then progressively dry abrading the surface with 60-, 120-, 220-, and 320-grit silicon-carbide sand paper. Final wet abrading of the surface was then completed using a combination of Micro-Measurements M-Prep Conditioner A with 320-grit silicon-carbide sandpaper followed by 400-grit silicon-carbide sandpaper. Finally, M-Prep Neutralizer 5A was used on the surface and allowed to air dry. During gage installation, a laser level was used to assist in grid alignment, as shown in Figure 4.9. The resistive strain gage and solder terminal were positioned using a clean glass plate and mylar installation tape. Once positioned, M-Bond 200 catalyst was applied to the bonding surface of the gage and terminal pair followed by M-Bond 200 adhesive and firm thumb pressure was placed

on the gage while the adhesive cured. Following gage installation, the resistive strain gages were connected to the solder terminal with 36 gage hookup wire. Three conductors from a four conductor shielded pair cable were then used to connect the solder terminal to the data acquisition unit. The resistive strain gage, solder terminal, and hookup wire were covered with a silicone sealant for protection and to enhance the longevity of the bond to the surface by sealing the gage and connections from contaminants (Figure 4.10).

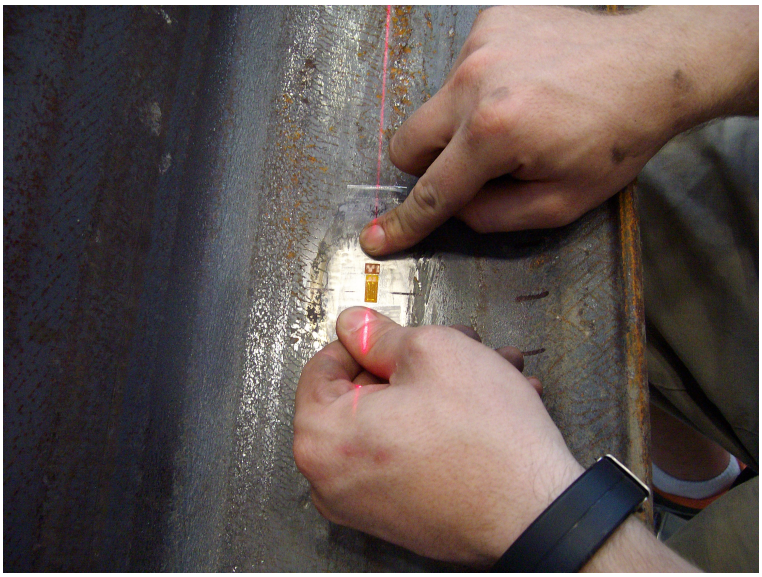

Figure 4.9: Alignment of bondable resistive strain gages along the centerline of the flange during installation

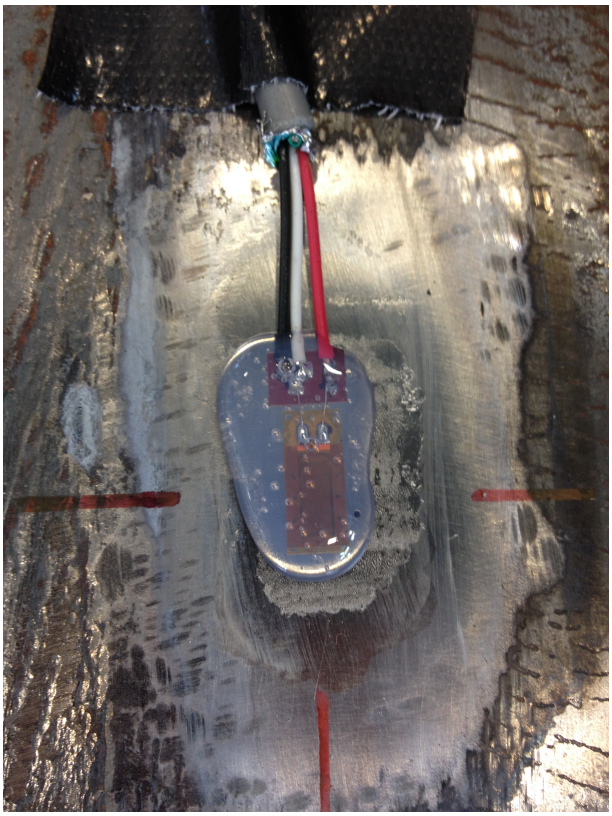

Figure 4.10: Photograph of installed and wired bondable resistive strain gage with protective coating

To protect subgrade instrumentation during installation and testing, a 1/4in thick steel plate was placed over the installed below grade instrumentation and cabling and continuously welded to the pile (Figure 4.11). The cover plate was formed with a taper over the final two inches above the toe of the pile. This was done to minimize the addition of toe bearing area from the cover plates. The cover plate was 5.5in wide for the 'finger' side of the pile and 6in wide with an approximately 1/2in bend for the 'thumb' side of the pile. These cover plates provided a minimum 1in gap for placement of the reusable strain transducers and high shock accelerometers near the toe. The differences between the perimeters and cross sectional areas of the individual sheet piles and the sheet pile wall with and without cover plates included are shown in Table 4.1.

Table 4.1: Perimeter (P) and area (A) of laboratory sheet piles without and with cover plates

	Single Pile		Wall	
	No Cover	w/ Cover	No Cover	w/ Cover
P (in)	53.76	49.76	215.04	207.04
A (in^2)	11.91	14.91	47.64	53.64

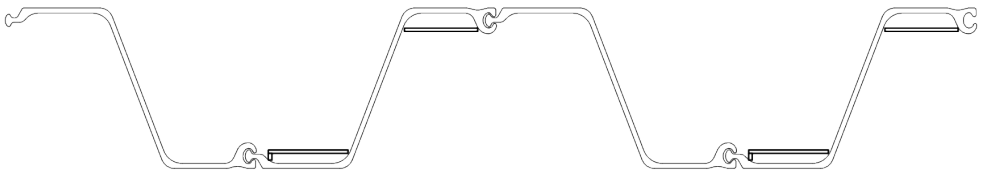

(a) Cross section of sheet pile wall



(b) Photograph of coverplate on finger side of wall

Figure 4.11: Cover plates over subgrade instrumentation

To directly measure head displacement as a supplement to the response measurement ob-

tained from the accelerometers, a series of four 2in stroke linear variable differential transformers (LVDTs) were installed 1ft - 5in below the pile head. This direct measurement of pile displacement was necessary due to the relatively low magnitudes of acceleration generated during the rapid load tests and the errors associated with numerically double integrating accelerations to obtain displacements, in particular permanent set displacements. Aluminum plates were secured to the center of the web on the same side of the pile wall to provide a surface for each LVDT to measure displacement of the head of the pile (Figure 4.12). The LVDTs were supported by an aluminum framework that allowed for plumbing of the transducers prior to the testing. This framework was supported by timber beams spanning the full length of the geotechnical pit and anchored to the strong floor foundation so that ground motions did not affect the response of the transducers.



Figure 4.12: Placement of an LVDT on each pile web to measure displacement

The pile instrumentation was connected to signal conditioning and data acquisition modules housed in a National Instruments PXIe-1075 chassis with a PXIe-8133 controller. Specifically, the LVDTs were connected to a PXIe-4300 general purpose analog input module offering 16-bit analog-to-digital converter resolution. These LVDTs were driven by a 10 V DC excitation source from a bench-top laboratory supply. Calibration of each transducer was performed using a set of reference blocks. The reusable strain transducers and resistive strain gages were connected via PXIe-4330 Wheatstone bridge input modules that offer 24-bit analog-to-digital converter resolution and were supplied with a 10 V excitation. The accelerometers were connected via a PXIe-4497 dynamic signal analyzer module that offers integrated electronic piezoelectric (IEPE) conditioning and 24-bit analog-to-digital converter resolution. All sensors were sampled at a rate of 20kS/s per channel. The channel configuration for the dynamic testing program is provided in Appendix A.

4.1.2 Laboratory Setup for Rapid Load Testing

A head beam system was developed and welded to the sheet pile wall to encourage the piles to behave as a group during axial loading, since the PZ27 sheets would otherwise act independently absent of interlock friction. The pile head was designed to distribute the force from an actuator uniformly across the four piles in the group. First, sheet pile splicers were fillet welded to the top of each sheet pile to achieve a level plane on which a 2in thick, 6in wide, and 6ft long steel plate was placed and welded. This produced a sufficiently level bearing surface for placement of an 8 ft long W14x90 beam, which was fillet welded to the steel plate at the locations shown in Figure 4.13. An additional 4ft long W14x90 beam was then secured on top of the longer beam using eight 1in diameter bolts.

To apply controlled rapid loading to the system, a MTS 244.51S Dynamic Double Acting actuator was used. This actuator has a stroke of 10in and a load cell capacity of 220kip. The piston was attached vertically to a steel portal reaction frame constructed above the PZ27 wall system. The head of the piston was left unconnected from the piling system to allow for free response of the pile group after the loading event. The actuator also allowed for the measurement of the applied loading force and displacement at the actuator head, which provided preliminary force-displacement measurements for each test.

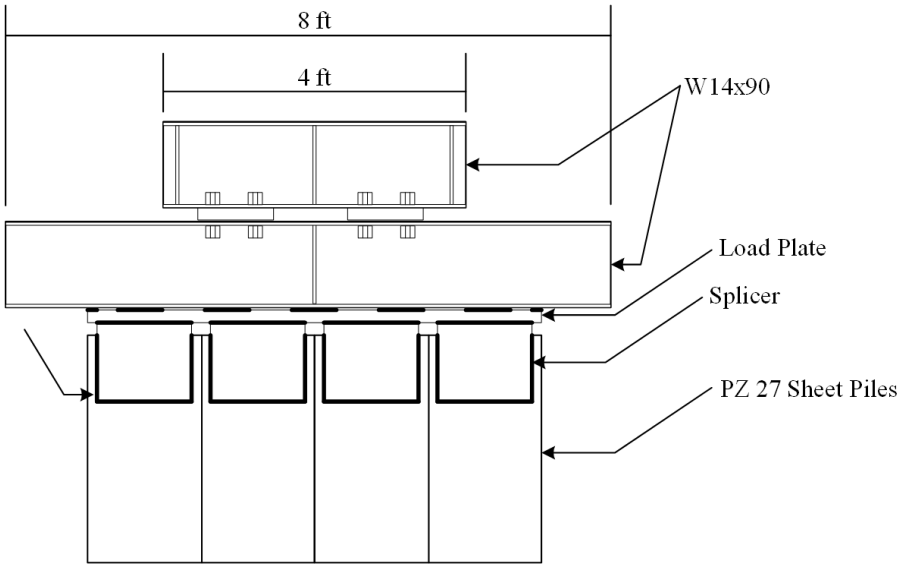

(a) Dimensional schematic



(b) Photograph showing assembly of pile head and actuator

Figure 4.13: Design and configuration of pile head system

4.1.2.1 Other Instrumentation

Additional instrumentation was installed for static load testing of the pile group that was not used in the rapid load testing program, but will be used to provide comparisons of estimates derived from the analysis of the rapid load testing measurements with the results of the static load testing program. They include additional bondable resistive strain gages, digital dial gages, and a push-in type pore water pressure cell. Additional resistive strain gages were installed on each of the four piles in the wall. These gages were installed above the ground line on each flange and in the center of the web of each pile. They were predominately used in the static load testing program to determine the actual load distribution across each of the piles in the wall system. In addition, four 2 in stroke digital dial gages replaced the LVDTs for the static load testing. This was done to increase the long-term stability of the head displacement measurement over the duration of the static testing. The LVDTs were instead used for measuring lateral displacements during the static load tests. In order to measure excess pore water pressure over time during static load testing and dissipation rates after rapid load pulses, a single GEOKON Model 4830 push-in type vibrating wire pressure cell was driven approximately 1ft - 4in away from the center of the sheet pile wall with the active sensing element placed approximately 3ft - 9.5in below the ground surface (4.4). During rapid load testing, the development and dissipation of the excess pore water pressure was monitored with a sampling rate of about 3 seconds. A period of approximately 7-8 minutes was provided between each rapid load pulse to allow for dissipation of the excess pore water pressure. This observation of the pore water pressure and delay between rapid load pulses ensured that there were was minimal influence

from cumulatively developed excess pore water pressures on the capacity of the sheet pile wall.

4.1.3 Rapid Test Program and Procedures

As previous described, the laboratory testing conditions are designed to replicate those used in the field for a rapid load testing of a pile, where applied axial loading and pile response via measured strains and accelerations are analyzed to estimate the axial bearing capacity of the pile. Since rapid load testing involves a loading rate that produces dynamic effects, including inertia and damping forces, without inducing significant stress waves in the piles, the testing program in the laboratory condition consisted of applying a series of short duration load pulses to the head of the piling system with the dynamic actuator. The applied load pulses were designed to replicate a typical rapid loading profile, such as that produced by Statnamic loading mechanisms. Thus, a half sine wave was used as the model of the loading pulse. The duration of the pulse was determined by the pile wave number, N_w, which was estimated to range from 266 to 1600 for the sheet piles used. Following recommendations from previous reports (Middendorp et al. (1992), Middendorp (1995), and Brown (1994)) and the ASTM standard (ASTM D7383-10 2010), the relative duration of the pulse was subsequently controlled to ensure that it was greater than $12L/c$.

The prescribed duration and peak displacement applied across the matrix of experimental tests are presented along with the actual observed maximum head displacement and resulting permanent settlement in Tables 4.2 and 4.3, respectively. The amplitude and duration of the applied load pulses are restricted by limitations in the hydraulic actuator system to drive actuator motion at higher loading rates. It can first be observed that the load pulses with the

1Hz frequency has a wave number of 1600 and by referring to Figure 1.1 these would result in a pseudo-static test rather than a RLT. It can also be observed that the actual applied peak displacement at the head of the pile, as measured by the LVDTs, was approximately 40-50% lower than the input target. This is a result of several phenomena, including elastic compression of the pile head assembly, deformation in the load frame under the applied loading, and, in some cases, undershoot in the actuator control.

Table 4.2: Summary of actual peak displacements applied to pile head from each of the rapid load tests

	Wave Number	1600	800	400	266
	Frequency (Hz)	1	2	4	6
	Duration (s)	1	0.5	0.25	0.167
Peak Input Displacement (in)	0.1	0.0538	0.0554	0.0550	0.0469
	0.15			0.0855	0.0774
	0.2	0.1093	0.1095	0.1126	0.1069
	0.25			0.1396	0.1315
	0.3	0.1628	0.1616	0.1652	0.1710
	0.35			0.1892	0.1851
	0.4	0.2172	0.2165	0.2116	0.2072
	0.5	0.2824	0.2600		

Table 4.3: Summary of final pile set developed from each of the rapid load tests

	Wave Number	1600	800	400	266
	Frequency (Hz)	1	2	4	6
	Duration (s)	1	0.5	0.25	0.167
Peak Input Displacement (in)	0.1	0.0033	0.0036	0.0051	0.0015
	0.15			0.0055	0.0030
	0.2	0.0077	0.0064	0.0055	0.0057
	0.25			0.0073	0.0093
	0.3	0.0164	0.0133	0.0118	0.0079
	0.35			0.0189	0.0148
	0.4	0.0372	0.0346	0.0269	0.0152
	0.5	0.0796	0.0578		

The process of applying the load pulse started with seating the piston head on the load beam assembly at the pile head. Typically, this resulted in a nominal static preload due

to contact force of around 500 lbs on the piling system. With synchronous data acquisition of the instrumentation running, the loading program, which applies the displacement-controlled loading pulse with given amplitude and duration, was initiated at the controller for the hydraulic system. The controller was programmed to then immediately retract the actuator away from the piling system a distance of approximately one inch. This allowed the piling system to exhibit an unrestrained free response after the loading. The data acquisition routine was continued for approximately two seconds after the load had been applied to capture the complete response of pile group and the final pile set. This process was then repeated for the remaining loading pulses after allowing the excess pore water pressures to dissipate. This period of rest lasted about 7-8 minutes between pulses during active testing and about 100 minutes between morning and afternoon testing sessions. These pore pressures increased immediately following application of each load pulse with a maximum observed change of 0.25psi, which corresponds to a water elevation change of approximately 0.57ft (Figure 4.14).

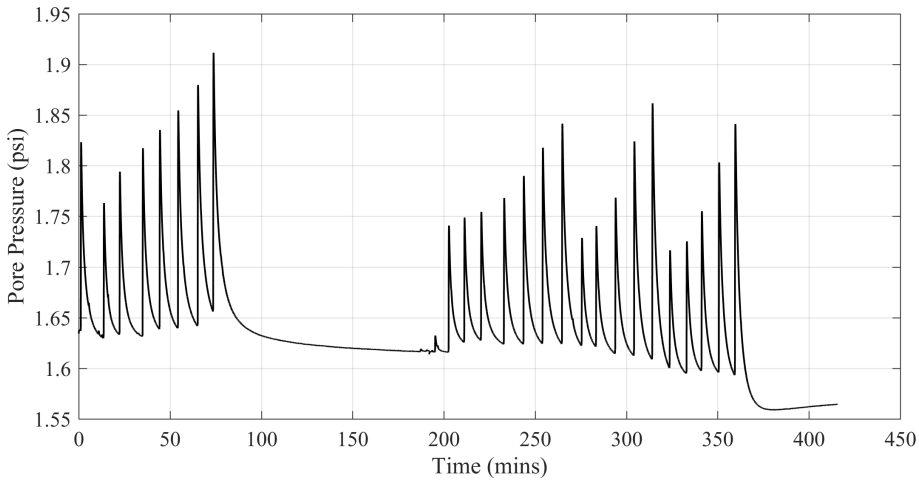

Figure 4.14: Pore water pressure time history for rapid load tests

An example of a typical measurement of the applied load and pile displacement as a function of time are provided in Figure 4.15. The data shown is for the case of a target displacement amplitude of 0.4in and loading duration of 0.167 seconds. The corresponding applied load versus head displacement response for the pile during the rapid load test is shown in Figure 4.16. Analysis and discussion of the rapid load testing measurements is presented in a subsequent chapter.

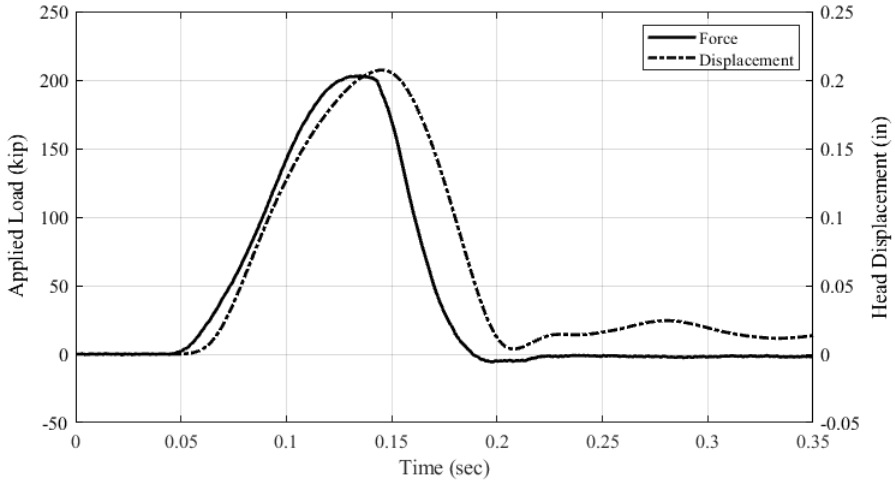

Figure 4.15: Typical time histories for applied load and pile displacement during a rapid load test

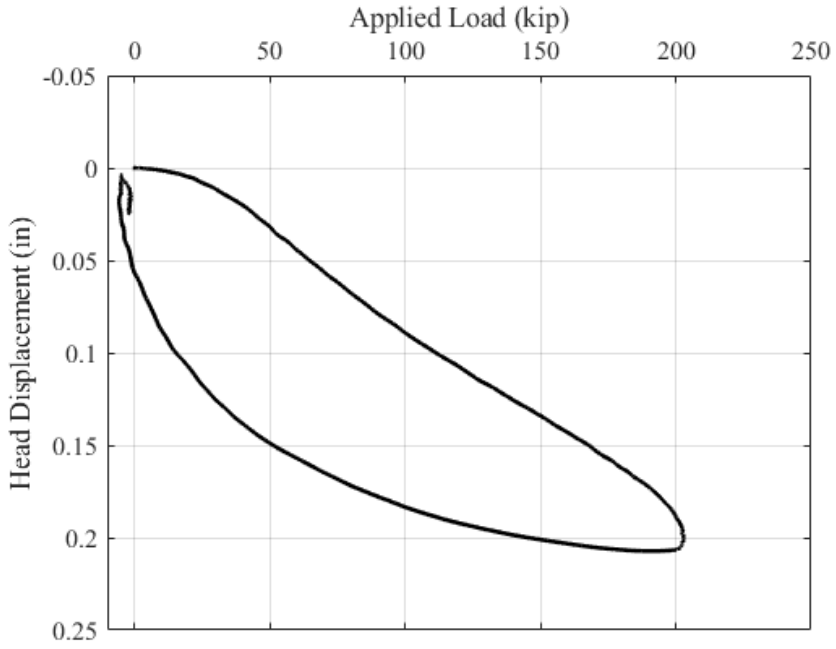

Figure 4.16: Example of applied load versus head displacement response of a pile during a rapid load test

4.1.4 Static Load Testing and Capacity Estimate of Laboratory Piles

Static load testing was conducted at a constant rate of penetration of 0.02in/min using a hydraulic actuator. From measurements of the applied load and displacement at the head of the laboratory pile wall from the static load test, the secant stiffness and the static capacity can be estimated (Figure 4.17). From this response, it was estimated that the secant stiffness was 1206kip/in for a characteristic load of 20kip and the measured static axial capacity of the sheet pile wall in the laboratory setting was 151kip by Davisson's Criteria. Figure 4.18 presents the load transfer along the length of the pile from the scope of the SLT. Note that measurements from sensors placed at the toe were not reliable, therefore the experimental measurement of the side friction resistance is determined to the depth of 79in and the load below this location is considered the toe bearing resistance, which may contain some

side friction resistance. From measurements of the resistive strain gages from the static load test, the experimentally derived side friction resistance and toe bearing resistance are shown in Figure 4.19 and Figure 4.20, respectively. The measured ultimate side friction resistances, ranging from approximately 2 to 18psi, correlate relatively well with the CPTu sleeve resistances, ranging from approximately 3 to 20psi, presented in Figure 4.22. It was found by Sylvain (2019) that empirically derived side friction resistance curves did not accurately predict the side friction resistance response obtained from the SLT. One possible explanation for this discrepancy could be due to boundary effects due to the confinement of the soil within the laboratory pit.

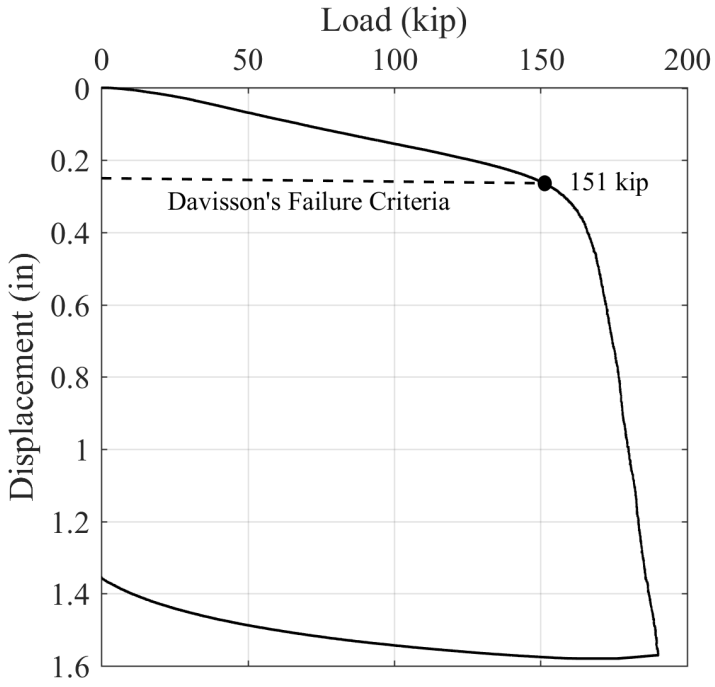

Figure 4.17: Head load versus displacement response of the laboratory pile wall from static load test

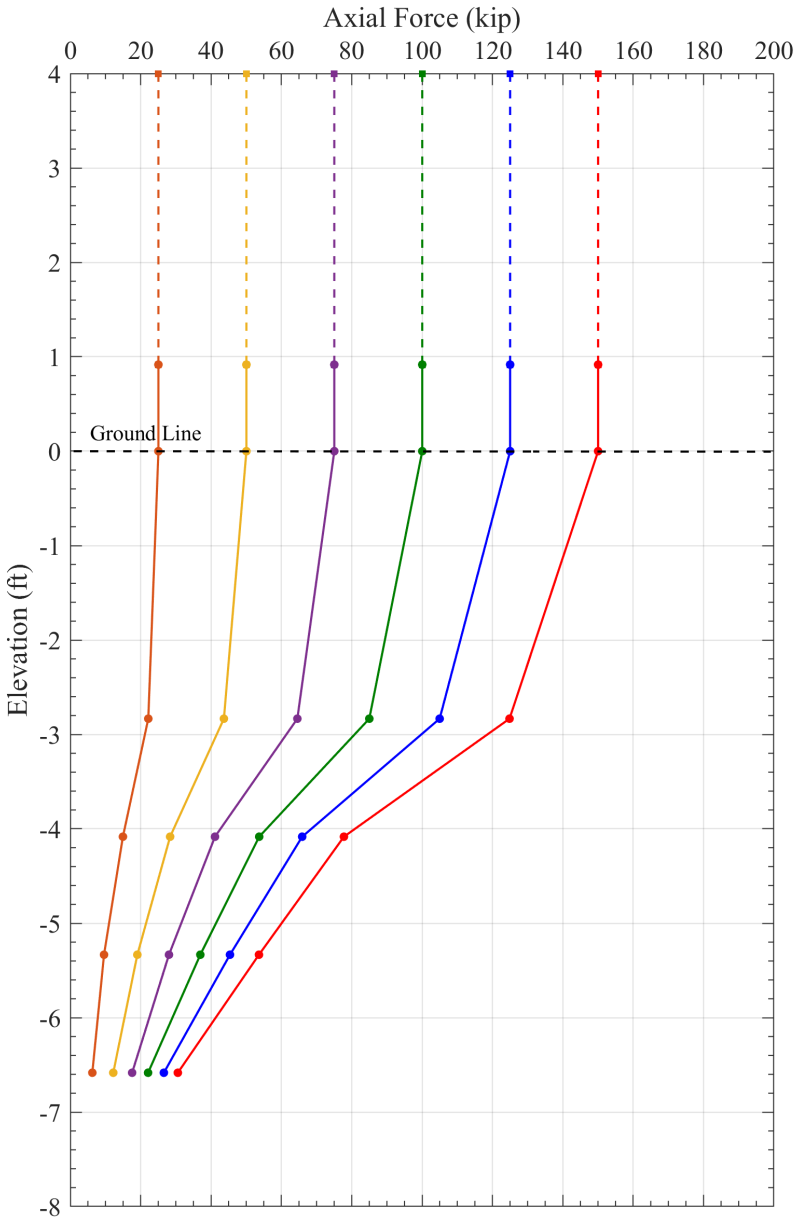

Figure 4.18: Load transfer along the length of the pile measured form the SLT

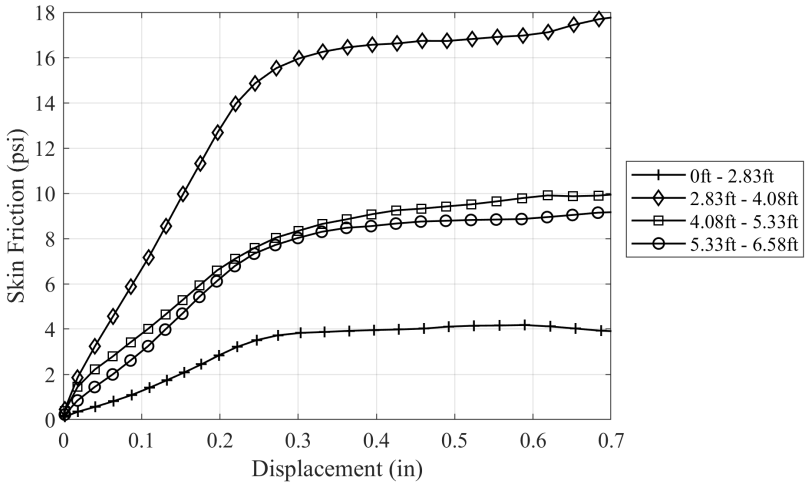

Figure 4.19: Experimental t-z load transfer curves for laboratory static axial load test of sheet pile wall based on strain gage layout

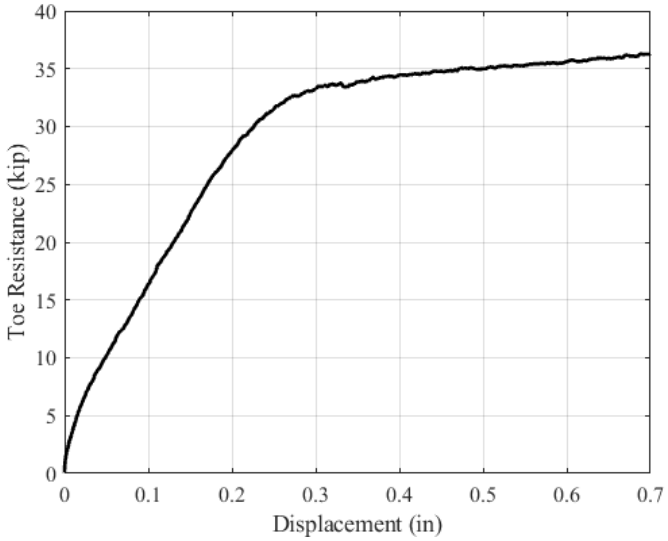

Figure 4.20: Experimental Q-z load transfer curve for laboratory static axial load test of sheet pile wall

4.2 Field Dynamic Testing

A field test of a pair of sheet piles and a single H-pile was conducted in the field yard of the International Construction Equipment (ICE) facility in the town of Matthews, North Carolina (Figure 4.21). The site stratigraphy included a gravel fill with sand from the

ground line to a depth of 6in, medium stiff sandy lean clay from the 6in depth to 4ft depth, soft to medium stiff sandy lean clay to sandy silt from the 4ft depth to 10ft depth, soft to medium stiff sandy silt from the 10ft depth to 19ft depth, and medium dense to dense silty sand from the 19ft depth to practical auger refusal at the 30ft depth. The ground water elevation was observed around 7 to 8ft below the ground line. The soil stratigraphy is depicted graphically in Figure 4.22 along with in-situ geotechnical testing results. The SPT blow count near the surface elevation started around 20 blows and diminishes with depth to around 8 blows around 15ft, after which, the blow count begins to increase again with depth. A similar trend is reflected in the CPT sleeve and tip resistance profiles. From the in-situ test results, it is expected that the side friction of the pile would be largest near the surface and decrease with depth, while the bearing resistance is expected to be low relative to side friction based on measurements obtained near the elevation of the toe of the pile. The grain size distribution for the soil at the test site is shown in Figure 4.23. More details on the characterization of the soil at the test site are presented by Sylvain (2019).



Figure 4.21: Field site prior to installation (Note: leftmost bucket indicates future sheet pile location, rightmost bucket indicates future H-pile location)

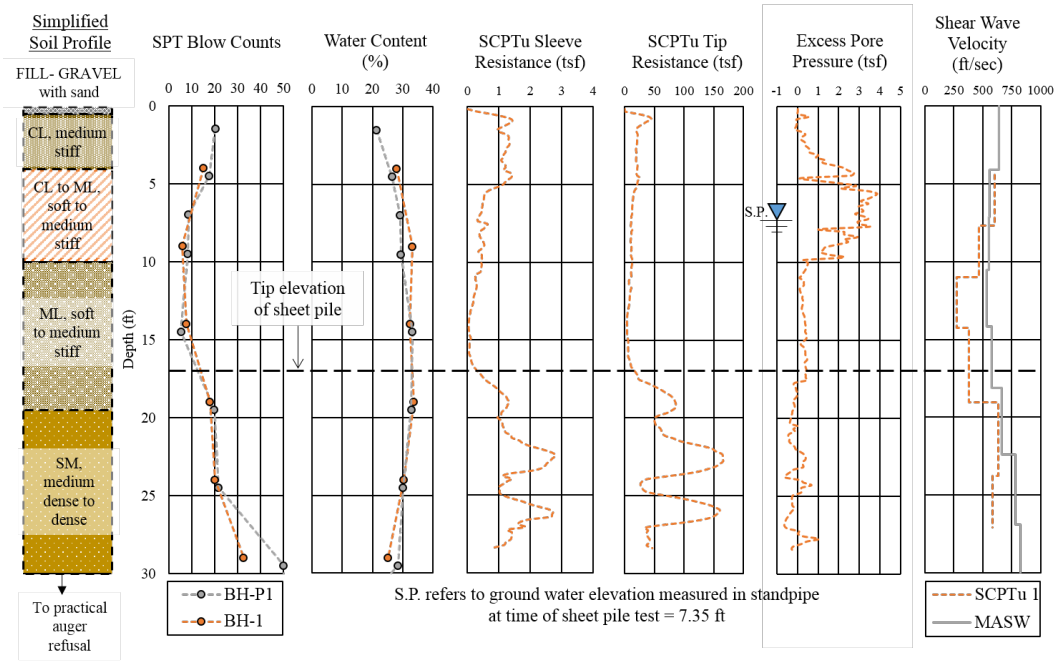

Figure 4.22: Stratigraphy and in-situ test results for the field site

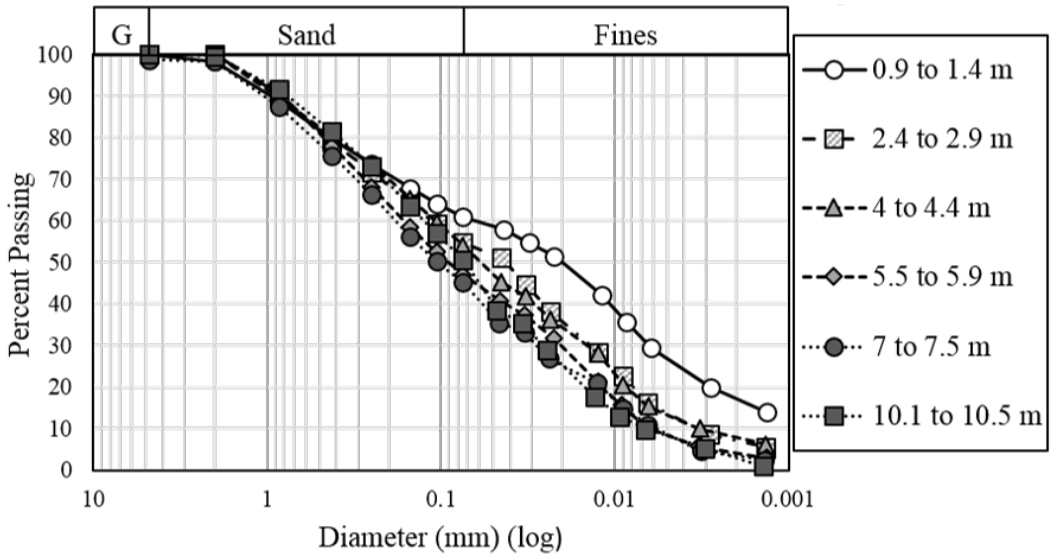

Figure 4.23: Grain size distribution for soil near the sheet pile at the Matthews, NC site used for dynamic load testing (from Sylvain (2019))

In contrast to the laboratory testing, the instrumented sheet piling consisted of a single pair of PZ27 sheet piles of 20ft length. In addition, a single HP12x53 pile of 20ft length was installed at the same site for comparison testing. Both test piles were initially installed using an ICE 28C vibratory hammer to a depth of 8ft below the ground level. Using an ICE I12 impact hammer, both test piles were then driven to approximately 16ft embedment. Due to the low blow counts observed from both the H-pile and sheet pile groups during this part of the installation, 3 blows/ft and 8 blow/ft respectively, it was decided to terminate initial driving at this depth, reserving the final 1ft for restrike testing. Restrike testing occurred 11 days after initial driving. The restrike testing was performed until the test piles were driven to the final embedment of 17ft. Dynamic monitoring during both initial pile installation and restrike testing was performed using strain transducers and accelerometers, as described in the following subsection.

4.2.1 Instrumentation for Dynamic Testing

In order to study the dynamic responses and estimate axial bearing capacity of both test piles using the Case method as well as signal matching, temporary instrumentation was installed at the head of the pile to collect measurements on the dynamic response of each test pile during the impact installation and restrike testing. Additional instrumentation was installed at specific locations along the depth of both test piles to provide supplemental data for validation of the capacity estimates and soil-structure interaction models estimated by the signal matching techniques. In addition, this instrumentation was used in a static load test to further support experimental validation of the results obtained through signal matching. Instrumentation placed at the head of the pile measured strains and accelerations in order to satisfy the minimum requirements for all of the dynamic testing methods. In order to measure the dynamic axial load transfer in the pile along the depth, additional strain gages were installed at a number of locations along the pile length.

The field testing instrumentation included an array of reusable strain transducers, high shock accelerometers, and spot welded resistive strain gages (RSG). A pair of reusable strain transducers and high shock accelerometers were installed 1ft - 6in below the pile head on both sheet pile sections. A pair of reusable strain transducers and two pairs of high shock accelerometers were installed 1ft - 6in below the pile head on the H-pile section. The strain transducers were oriented on the centerline of the webs and mounted using bolts passed through holes drilled into the pile. The accelerometers were mounted on aluminum blocks to orient them for measurement in the longitudinal direction of motion and these mounting blocks were bolted on the web of the pile sections adjacent to the strain transduc-

ers at a distance of two inches. A diagram and photograph of the installed reusable strain transducer and accelerometers for both test piles is provided in Figure 4.24. This photograph shows an additional pair of strain transducers and accelerometers mounted six inches away from those used in this dissertation. The second set of transducers were installed and monitored by GRL Engineers, Inc. These sensors are placed symmetric with respect to the centroid and principal axes of the cross section of the pile so that the average measured strains and accelerations from these arranged pairs nulls any bending effects in order to attempt to measure only axial strain and longitudinal acceleration. The reusable strain transducers are model ST350 gages manufactured by Bridge Diagnostics, Inc. These transducers feature a temperature compensated full Wheatstone bridge of 350Ω resistive gages with a measurement range of ± 4,000$\mu\epsilon$ and nominal sensitivity of 500$\mu\epsilon$/mV/V. The high shock accelerometers are PCB Piezotronics model 350B04 accelerometers. The 350B04 accelerometer has a nominal sensitivity of 1mV/g, a measurement range of ±5000g, and a 3dB frequency bandwidth of 0.2 to 25,000Hz.

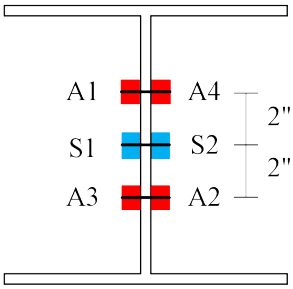

(a) Strain transducer and accelerometer placement on H-pile

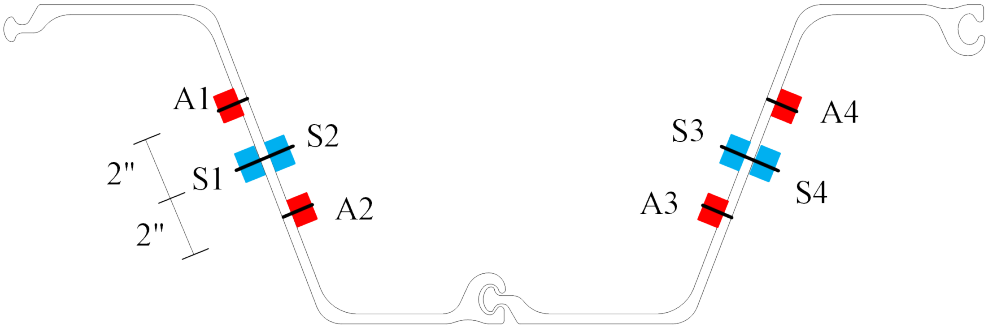

(b) Strain transducer and accelerometer placement on sheet pile

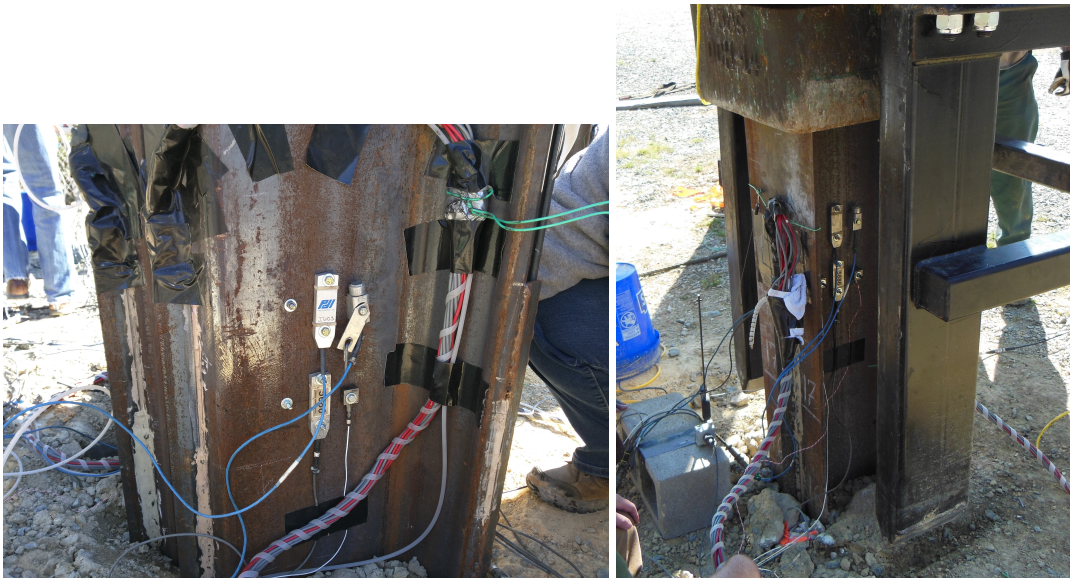

(c) Photographs of pile head instrumentation on sheet pile (left) and H-pile (right)

Figure 4.24: Sensor configuration at pile head for field tests

Both piles were instrumented with spot weldable resistive strain gages in order to facilitate comparisons between measured and computed dynamic load transfer along the length

of the pile as well as validate soil-structure interaction models developed through signal matching. Each pile had eight pairs of spot weldable resistive strain gages installed along the centerline of each web. The first set of these gages were installed six inches below the reusable strain transducers and accelerometers (2ft from the head of the pile). The next set of resistive strain gages were installed 2ft - 4in below the first set and the remainder of the sets continued along the length of the pile every 2ft - 6in for a total of eight elevations of resistive strain gage sets. The instrumentation layout described here is shown in Figure 4.25. The spot weldable LWK-06-W250B-350 resistive strain gages used have a 0.25in. active gage length and a grid resistance of 350Ω ±0.4%. All resistive strain gages were installed as single gages in a quarter Wheatstone bridge configuration with completion and shunt calibration resistors provided at the signal conditioner.

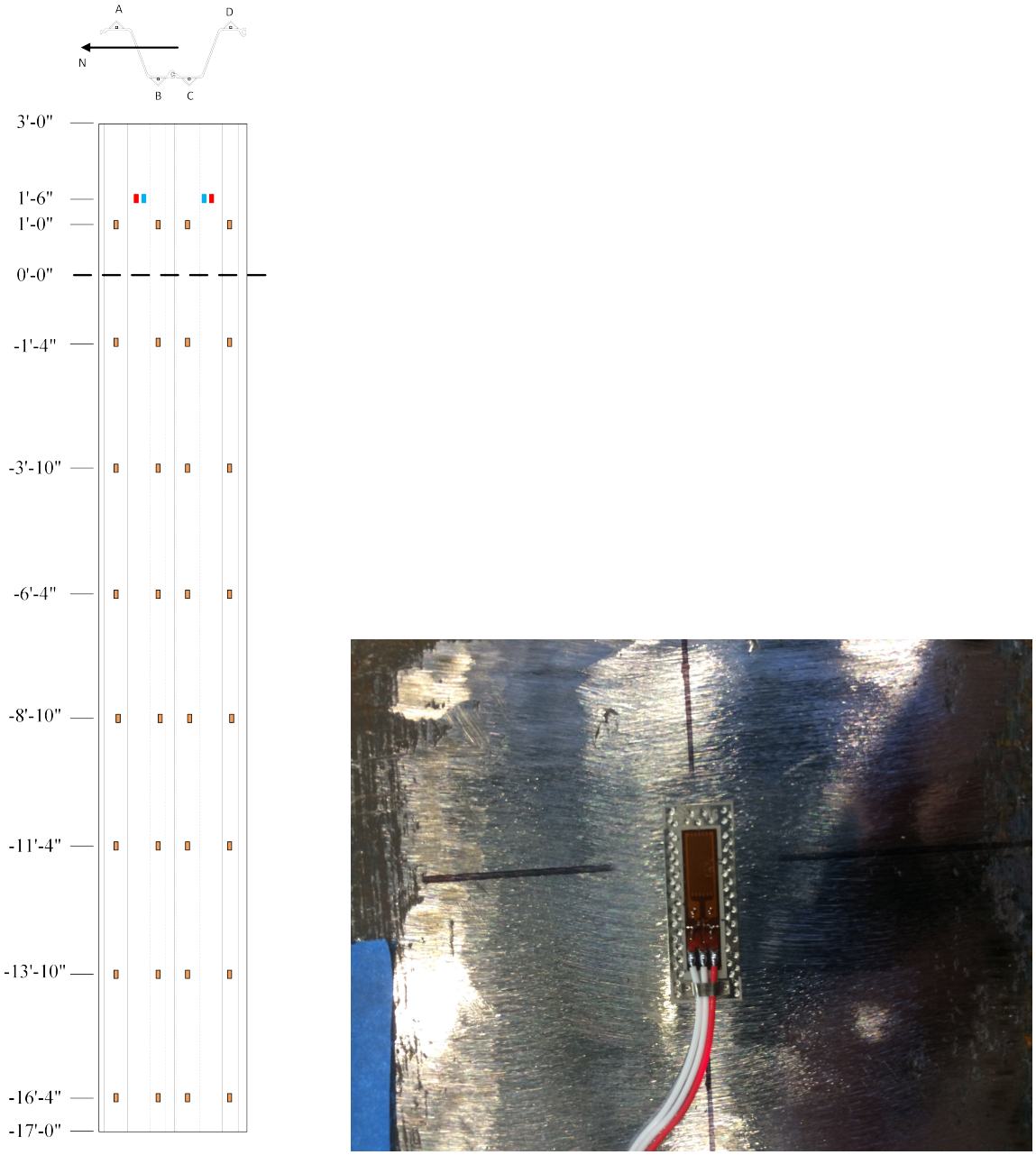

(a) Sensor schematic

(b) Photograph of spot weldable resistive strain gage

Figure 4.25: Overview of instrumentation for dynamic testing

For the installation of the resistive strain gages, the preparation of the surface included dry grinding of the steel at the gage locations using a grinding wheel. Then, a rotary steel wire brush was used to continue the dry abrading of the surface after which silicon-

carbide paper of 60- and 120-grit was used to complete the abrasive surface preparation. The surface was then degreased using isopropyl alcohol. During installation, a laser level was used to assist in grid alignment and positioning, after carefully marking exact gage locations with a marker. A Micro-measurements Model 700 portable strain gage welding unit was used to spot weld the strain gages to the steel surface. To protect the gages from moisture, two coats of polyurethane sealant was applied to metal sections of the gages and the entire gage was covered with a silicone sealant. To measure head displacement directly, a Measurement Specialties SP2-25 string potentiometer sensor with a 25in full-scale range was connected near the north side of the pair of PZ27 piles, and the H-pile section during the dynamic testing (Figure 4.26).

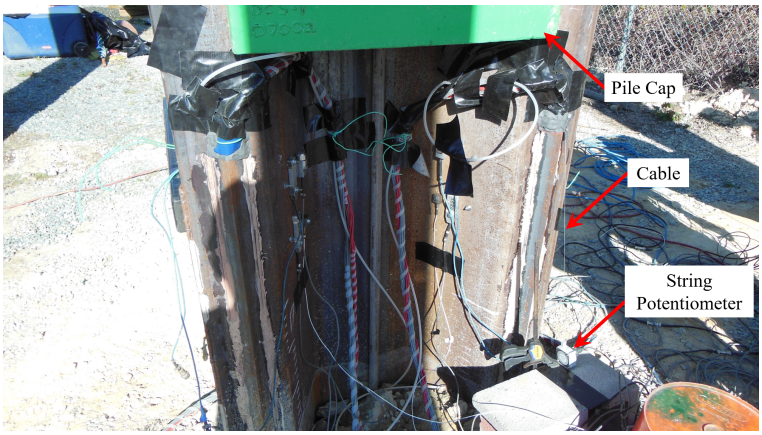

(a) String potentiometer on sheet pile pair

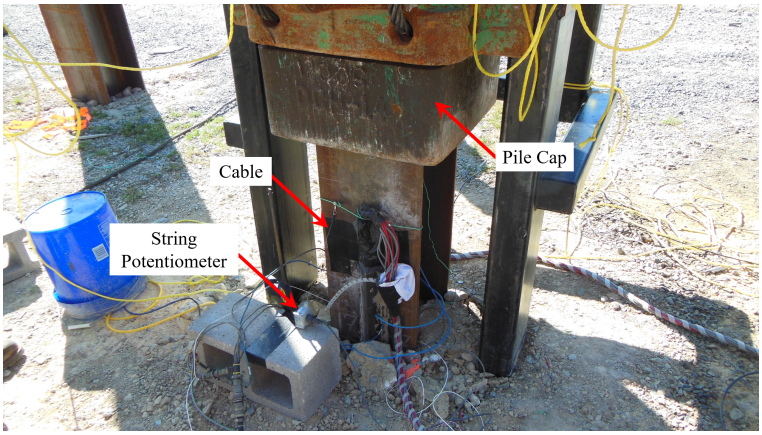

(b) String potentiometer on H-pile

Figure 4.26: Photographs of string potentiometers installed on test piles

To protect subgrade instrumentation during installation and testing, a L2x2x1/4 steel angle was placed over each line of the installed spot weldable strain gages and cabling. This steel angle cover was fillet welded to the pile using intermittent welds placed between each gage location in order to reduce possible thermal damage to the gages as well as to avoid the development of any stress concentrations that might affect the strain field at each gage. Gaps between the intermittent welds were filled in with a two part bonding filler material (3M Bondo) that hardened to produce a water resistant seal along the edges of the protective cover. This cover plate is shown in Figure 4.27. At the toe of the pile, the cover

plate was formed with a taper starting at eight inches above the toe (Figure 4.28). This taper was introduced to minimize the mobilization of additional toe bearing resistance due to the additional cross sectional area of the covered instruments. The presence of the cover plates does increase the perimeter of the pile, which will slightly increase the shaft resistance. The differences between the perimeters and cross sectional areas with and without cover plates included, for the sheet pile pair and H-pile, are shown in Table 4.4.

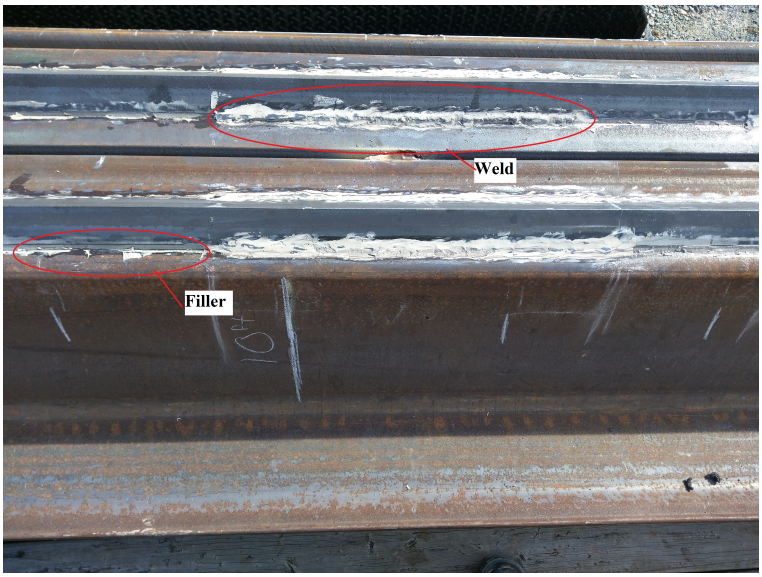

Figure 4.27: Photograph of welded and bonded cover plate on field piles



Figure 4.28: Tapered end of cover plate at pile toe

Table 4.4: Perimeter (P) and area (A) of field piles without and with cover plates

	PZ27 Pair		HP12x53	
	No Cover	w/ Cover	No Cover	w/ Cover
P (in)	107.52	112.2	69.72	72.12
A (in^2)	23.82	27.57	15.50	17.37

All instrumentation was connected to a NI PXIe-1075 data acquisition chassis with PXIe-8133 controller through signal conditioning modules. Specifically, the reusable strain transducers and resistive strain gages were interfaced to PXIe-4330 Wheatstone bridge input modules with 24-bit synchronous sampling analog-to-digital conversion. These sensors were provided with 10V excitation sourced from these modules. The accelerometers were

interfaced to a PXIe-4497 dynamic signal analyzer. This module provided 4mA IEPE excitation to the accelerometers and 24-bit synchronous sampling analog-to-digital conversion. The accelerometers were AC coupled to the dynamic signal analyzer to remove the bias voltage from the excitation. The string potentiometer was also interfaced with the PXIe-4497, but was provided a 10V DC excitation from an external power supply and was DC coupled to the dynamic signal analyzer. All signals were synchronously sampled at a 25kHz sampling rate. The channel configuration for the dynamic testing program is shown in Appendix A.

4.2.2 Dynamic Test Program and Procedures

While both test piles were installed by a vibratory hammer to a depth of 8ft, the dynamic testing program used impact driving provided by an ICE I-12 impact hammer. This hammer was equipped with an appropriate pile head, respectively for the H-pile and sheet pile pair, to seat the hammer on the pile group. The two sheet piles were tack welded together at several locations along the length of the pile to restrict relative slip between the piles. After connecting all instrumentation to the data acquisition unit, the signals of each transducer were checked for responsiveness. A crane was used to position the impact hammer over the respective pile (Figure 4.29) to drive the piles to 16ft, which was considered as the end of driving (EOD) condition for the initial installation. The piles were then marked in 6in increments to allow for estimating the number of blows per foot as well as ensuring that the driving was halted at the final driven elevation. The same impact hammer was used for restrike testing conducted 11 days after EOD. The restrike tests consisted of nine blows for the sheet pile and three blows for the H-pile to achieve a final driven depth of 17ft.



(a) Positioning impact hammer over sheet pile pair



(b) Checking impact hammer seating on sheet pile pair prior to restrike event

Figure 4.29: Setup of impact hammer for restrike

Typical measurements obtained during the restrike impact event on the sheet pile pair and H-pile in the field are presented in Figures 4.30 and 4.31, respectively. In these plots, the x-axis has been normalized by the characteristic length of the pile. This normalization was performed by aligning the peak amplitudes in the velocity trace with multiples of $2L/c_L$. This normalization corresponds to a wave speed of 206,897in/s for the sheet pile pair and 191,379in/s for the H-pile. As described in Chapter 3, the force response from the strain transducer and accelerometer located at the head of the pile can reveal general aspects of the soil-structure interaction in the pile. The recorded dynamic measurements for the sheet pile and the H-pile are characterized by high amplitude velocity reflections with corresponding tensile internal axial forces. Consequently, this sheet pile pair and H-pile should be considered as a non-bearing, or friction, pile. This means that most of the axial bearing capacity on this particular system is carried along the shaft of the pile and there is relatively minimal resistance at the toe of the pile. Additionally, the corresponding up-wave and down-wave responses for the sheet pile pair and H-pile are shown in Figures 4.32 and 4.33, respectively. While the down-wave corresponds to the average between applied load and the corresponding force determined from the velocity, the up-wave is the difference in the quantities that results due to soil resistances along the length of the pile. From this figure, it can be preliminarily determined that each pile is still in motion throughout the observed time as well as that the pile exhibits low toe bearing resistance.

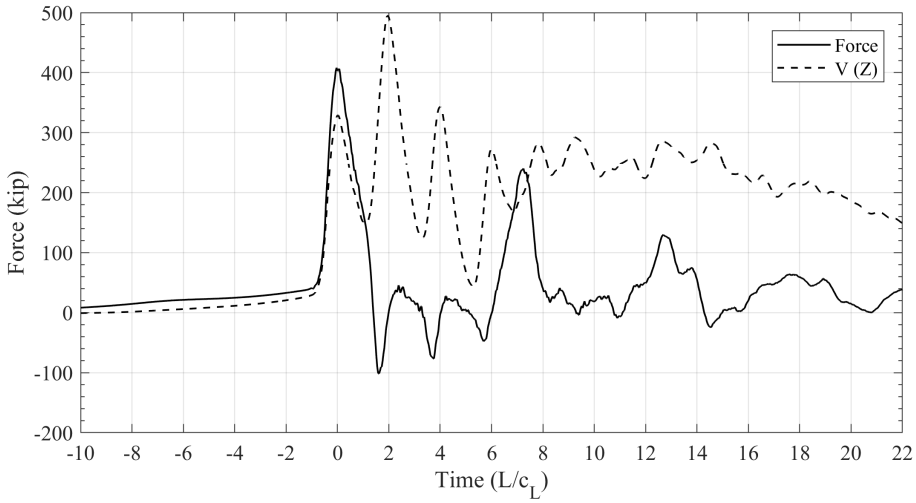

Figure 4.30: Typical dynamic force and velocity for sheet pile driving restrike test

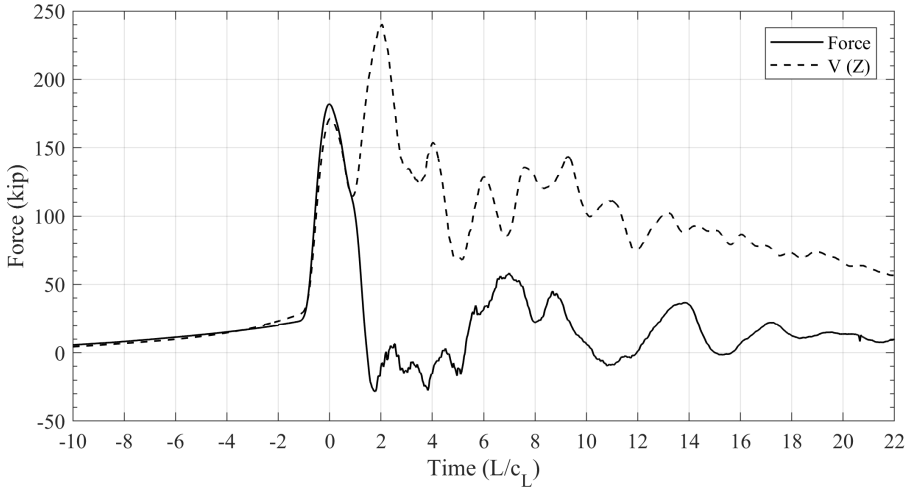

Figure 4.31: Typical dynamic force and velocity for H-pile driving restrike test

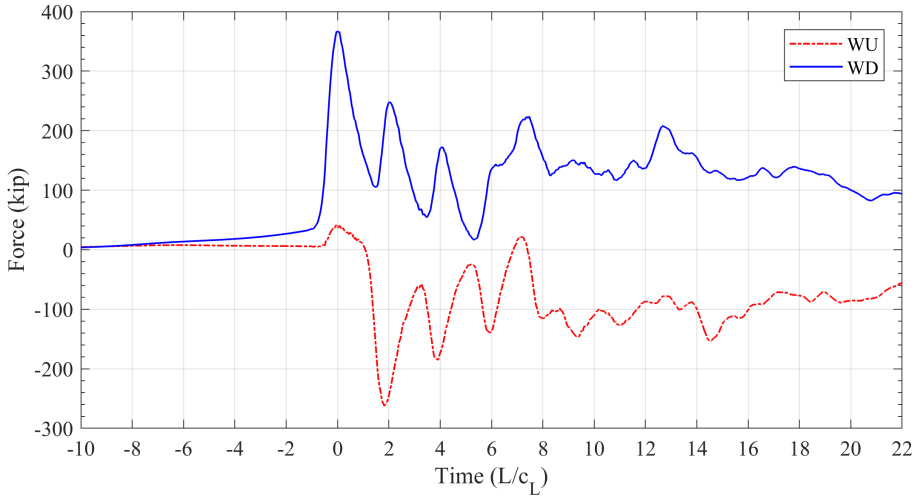

Figure 4.32: Typical up-wave and down-wave forces in sheet pile during restrike test

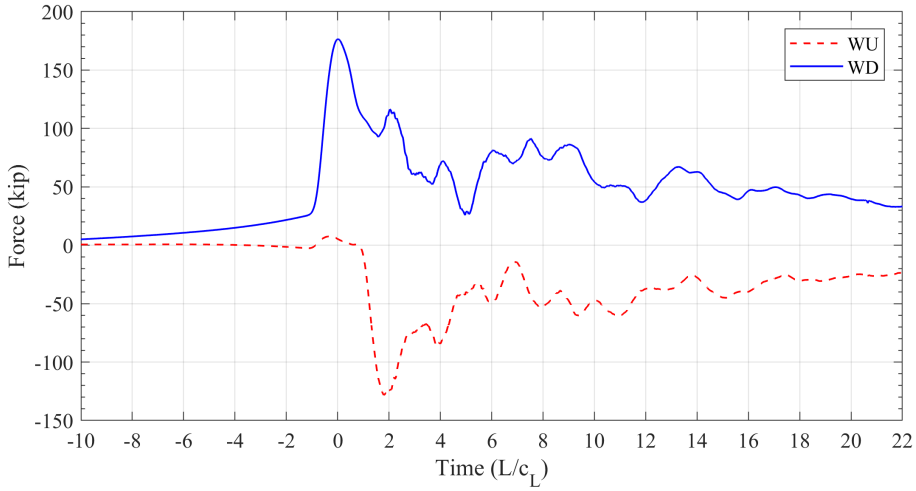

Figure 4.33: Typical up-wave and down-wave forces in H-pile during restrike test

The measured displacements from the string potentiometer sensor during restrike testing is presented in Figure 4.34. This information will be useful for validating acceleration measurements by comparing head displacements computed by double integration. It also allows for estimation of blows per foot and confirmation of final elevations of the pile head. For the restrike tests, the sheet pile pair had an estimated 8 blows/ft while the H-pile had considerably lower 3 blow/ft, suggesting that the sheet pile pair would have a

higher capacity than the H-pile. The maximum energy delivered to the pile is also used to determine acceptable blows to be used in dynamic analysis, shown in Figure 4.35. While the energy delivered varied throughout each blow, the first (HP #1 and PZ #1 and #2) and last (HP #4 and PZ #8 and #9) blows are low in energy and suggest poor quality for further axial capacity processing. This figure also explains why the H-pile required less blows than the sheet pile as blows #2 and #3 to the H-pile provided more energy to the pile, while also displacing the pile farther than blows of similar energy applied to the sheet pile.

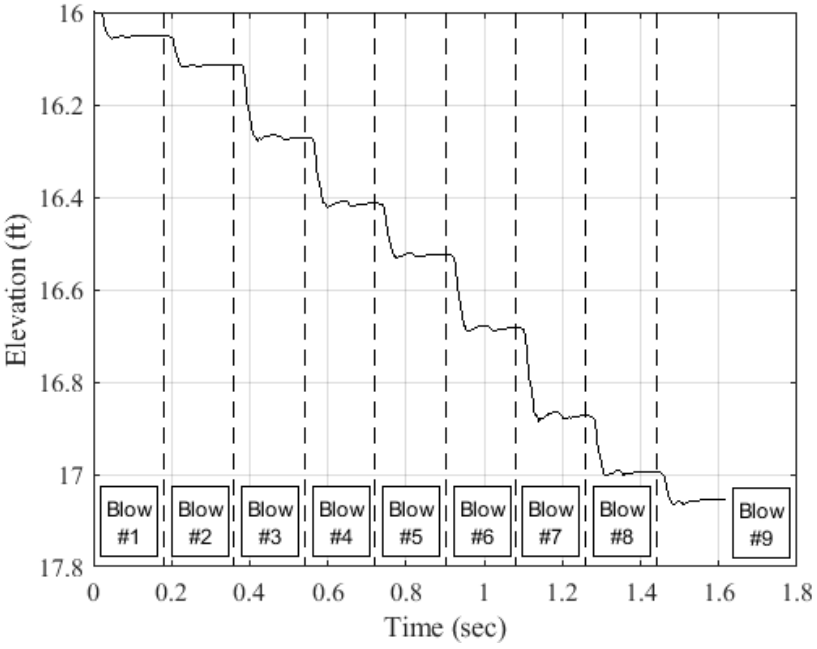

(a) Displacement data per blow for sheet pile pair

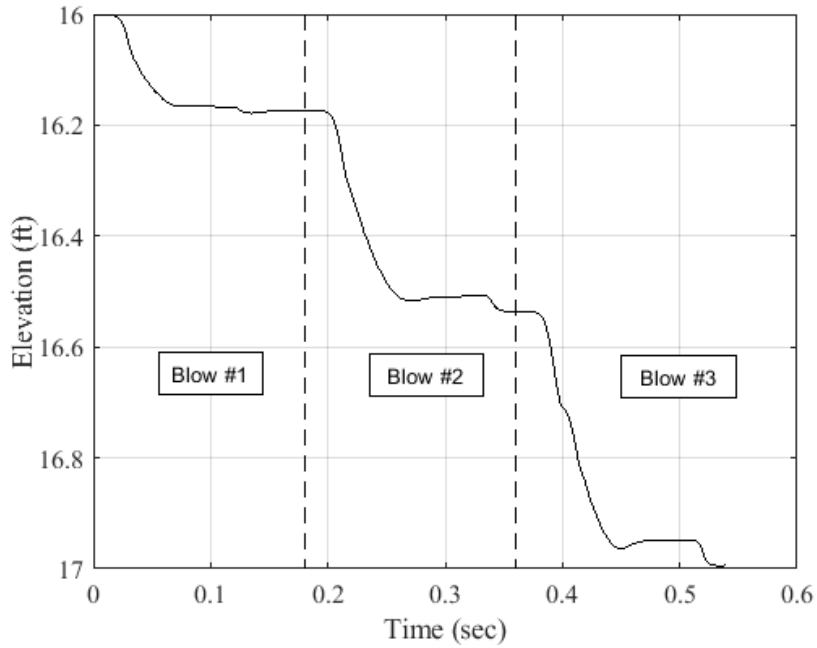

(b) Displacement data per blow for H-pile

Figure 4.34: Displacement records from string potentiometer during restrike testing

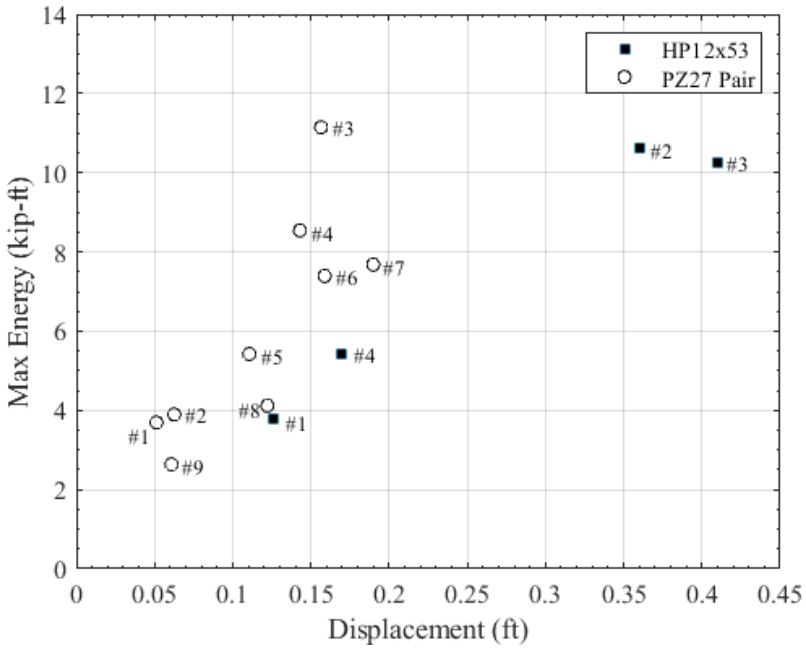

Figure 4.35: Maximum energy transfer per blow displacement for sheet pile and H-pile

4.2.3 Static Load Testing and Capacity Estimate of Field Piles

Additional instrumentation was installed on the pile that were not used in the dynamic testing program, but were used during a static load testing program. The static load testing program provided a ground truth measurement of the stiffness and capacity of the pile group as well as the load transfer due to the soil-structure interaction. These static measurements are ultimately used for comparison to the results obtained from the application of the dynamic methods. The additional instruments used in the static test include a load cell, a series of vibrating wire strain gages, and dial gages. A model TD175 Industrial Commercial Scales canister load cell with a 100kip full-scale range was used to measure the applied axial load at the pile head. This was secured on top of a W14x90 head load beam that was tack welded to each test pile. A schematic of the static load test setup, including the reaction frame, is shown in Figure 4.36. Photographs of the test setup are provided in

Figure 4.37.

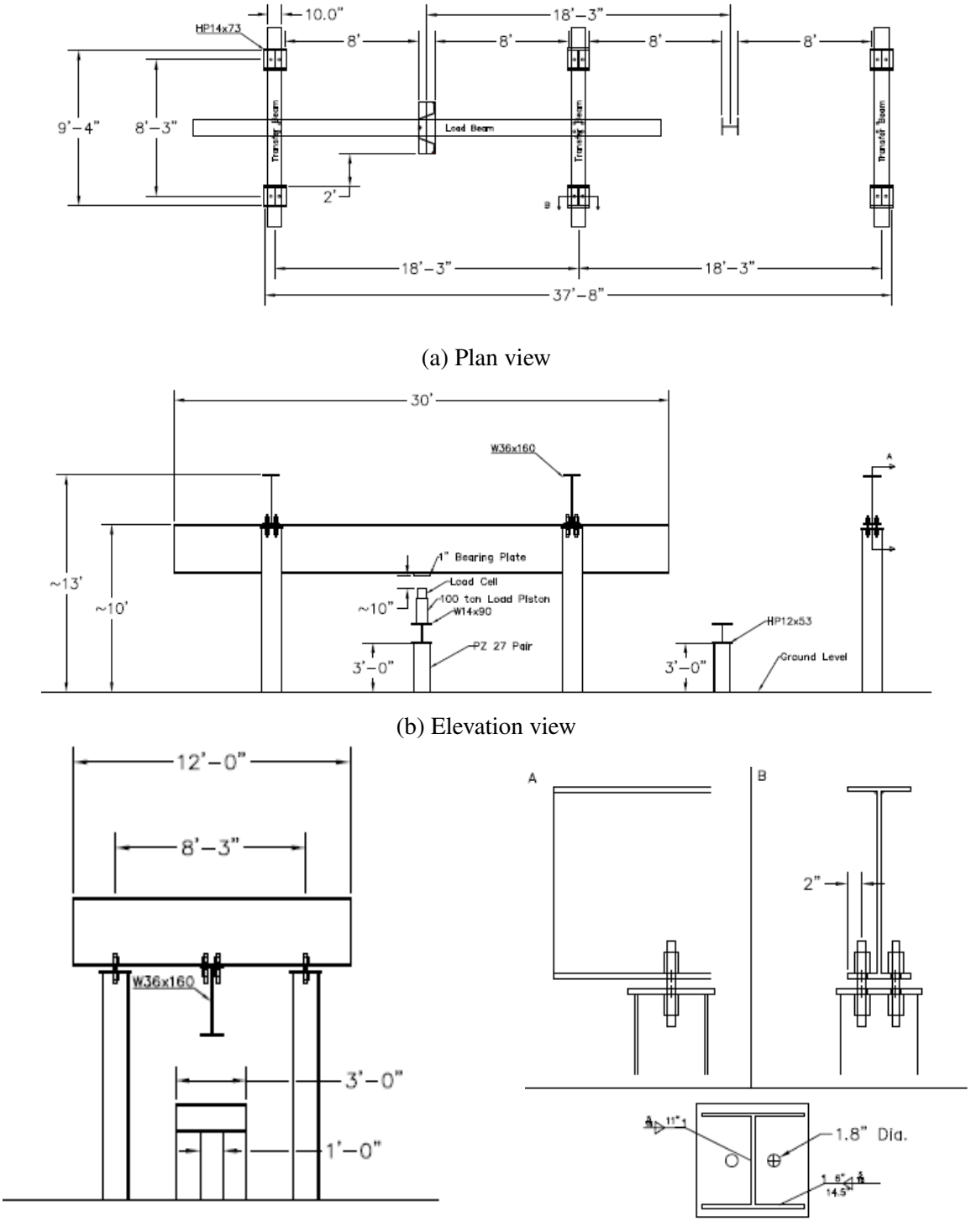

Figure 4.36: Schematics of static load test setup for field site



(a) Elevation view



(b) Side view

Figure 4.37: Photographs of static load test setup for field site

Additional vibrating wire strain gages were installed starting at 3ft - 10in from the pile head and continued at a 5ft spacing interval to the toe of the pile. These strain gages, while not appropriate for dynamic strain measurements, provided long-term stable measurements of static strains immune from drift due to electrical heat dissipation. These 16 additional strain measurements were used in analyzing the load transfer along the length of the pile during the static testing program. Dial gages were also installed on each flange of each PZ27 section during the static load test and pairs of dial gages were installed on each flange of the HP12x53 section, resulting in a total of four displacement measurements equidistant from the centroid of each pile group. Readings from these four dial gages were averaged to obtain the displacement at the pile head. Static load tests were conducted at an approximately constant rate of 0.005in/min using a hand operated hydraulic jack.

From measurements of the applied load and displacement at the head of the sheet pile pair and the H-pile during these static tests, the secant stiffness and the static capacity can be estimated (Figures 4.38 and 4.39, respectively). It was estimated that the secant stiffness of the sheet pile wall in the field setting was 2474kip/in for a characteristic load of 5kip and the static axial capacity by Davisson's Criteria was 34.3kip. The secant stiffness of the H-pile was 1044 kip/in for a characteristic load of 5kip and the static axial capacity by Davisson's Criteria was 22.5kip. Figure 4.40 presents the load distribution along the length of the pile from measurements in the SLT. Furthermore, based on the strain measurements, the shaft resistance and tip resistance, presented as t-z (developed by gage locations and then subsequently by geotechnical stratigraphy) and Q-z load transfer curves, are shown in Figures 4.41, 4.42, and 4.43, respectively. These load transfer curves will be particularly important for validation of derived load transfer curves generated from the signal matching

process. As expected based on the stratigraphy and in-situ geotechnical testing results, the sheet pile wall exhibited relatively little bearing resistance and the side friction decreased with depth. The measured ultimate side friction resistances, ranging from approximately 0.8 to 2.5psi, correlate relatively well with the CPTu sleeve resistances, averaging approximately 3.5psi, presented in Figure 4.22. It was found by Sylvain (2019) that empirically derived side friction resistance curves generally predict well the side friction resistance response obtained from the SLT.

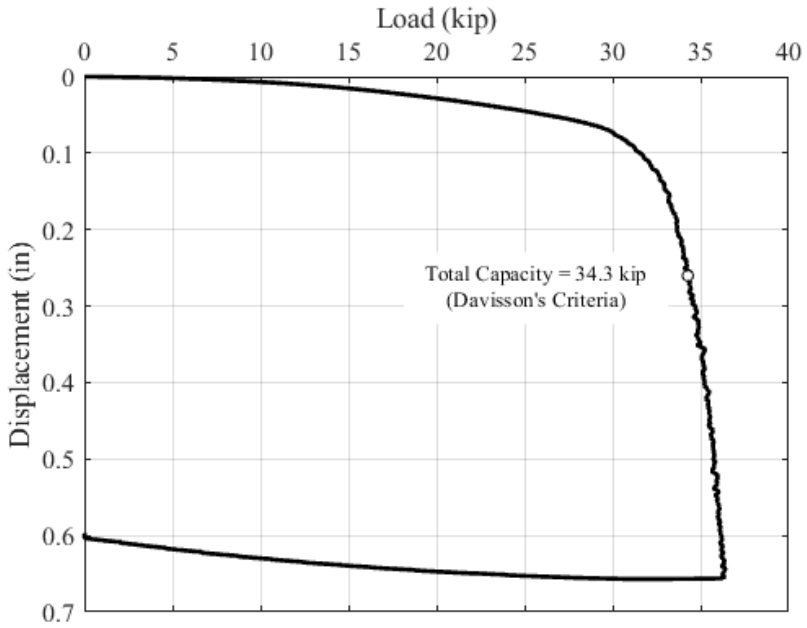

Figure 4.38: Static head load-displacement response of the field PZ27 pair (from Sylvain (2019))

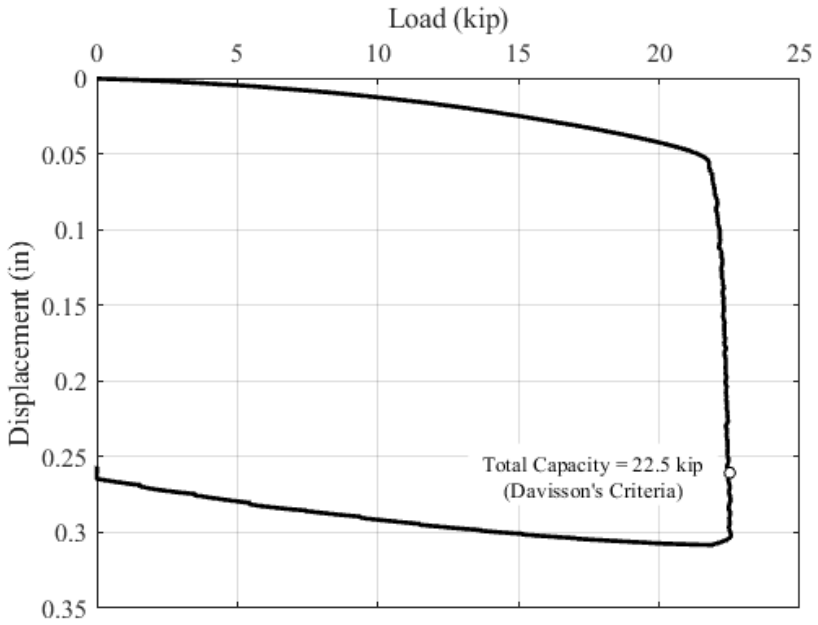

Figure 4.39: Static head load-displacement response of the field HP12x53 (from Sylvain (2019))

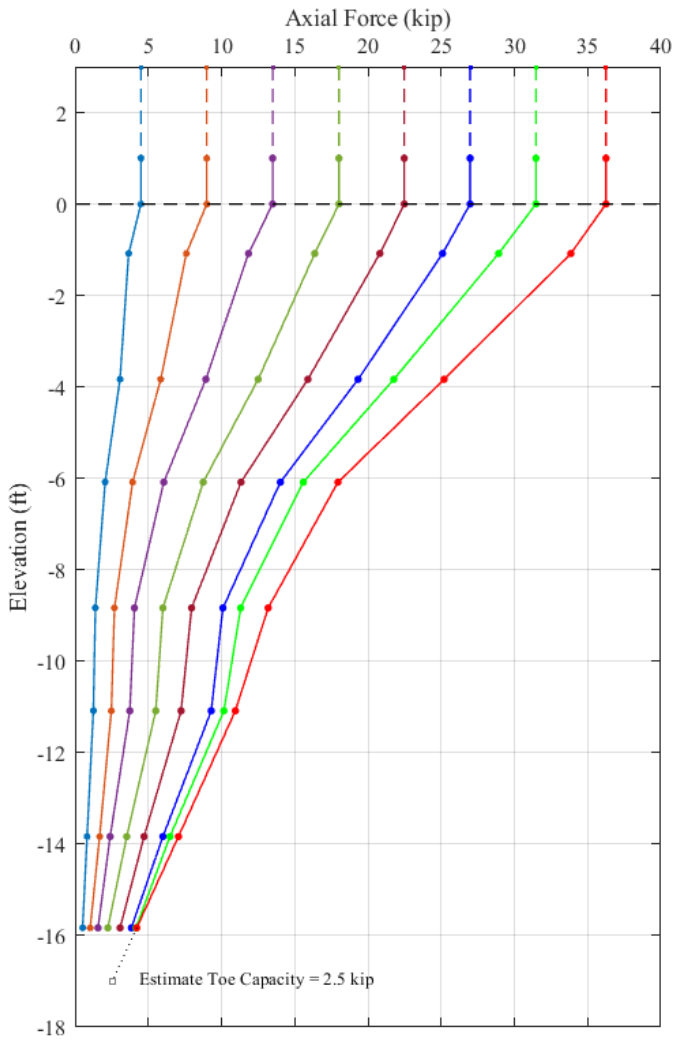

Figure 4.40: Experimental force distribution along the depth of the pile during the field static axial load test of the sheet pile pair (from Sylvain (2019))

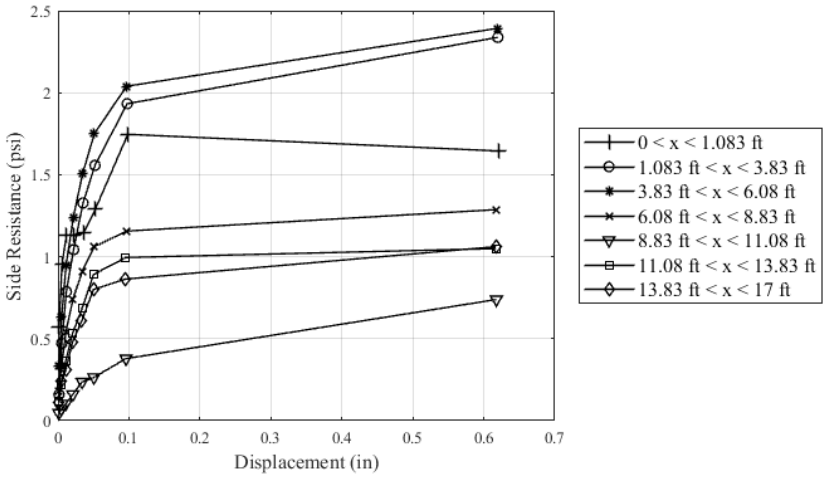

Figure 4.41: Experimental t-z load transfer curves for field static axial load test of sheet pile pair based on strain gage layout (from Sylvain (2019))

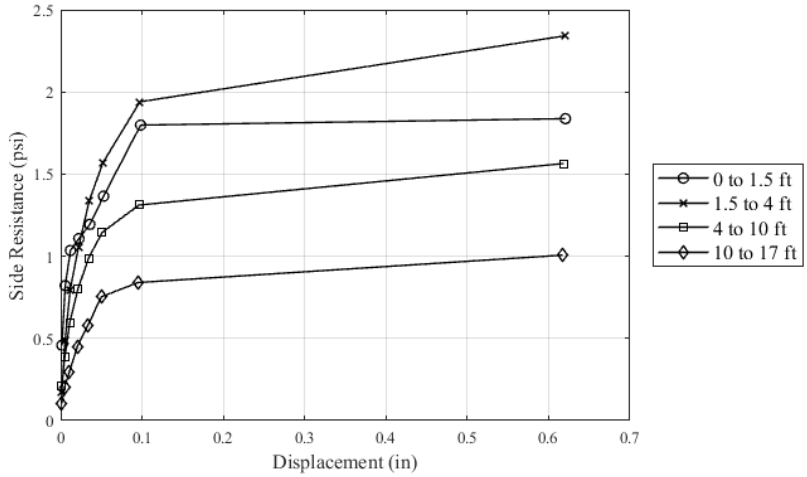

Figure 4.42: Experimental t-z load transfer curves for field static axial load test of sheet pile pair based on geotechnical stratigraphy (from Sylvain (2019))

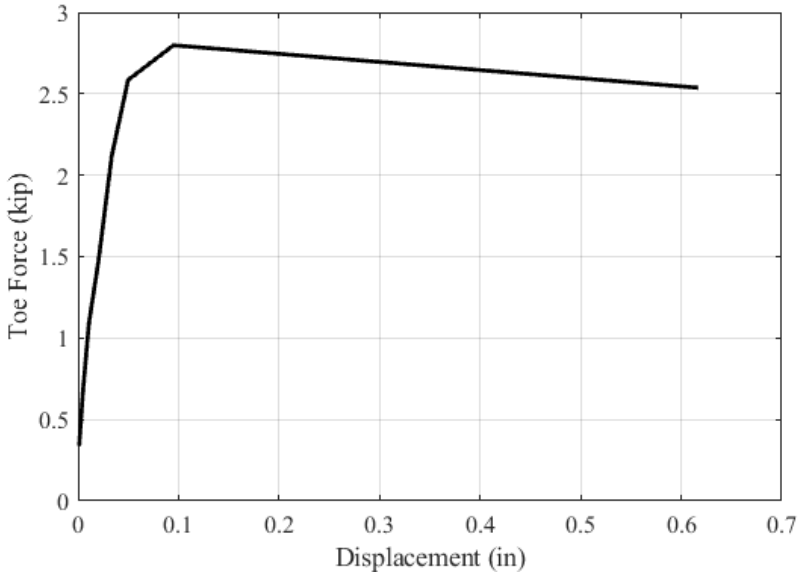

Figure 4.43: Experimental Q-z load transfer curve for field static axial load test of sheet pile pair (from Sylvain (2019))

CHAPTER 5: ANALYSIS AND DISCUSSION OF RAPID LOAD TESTS

The experimental program for the Rapid Load Test (RLT) procedure concluded with 24 applied pulses with target input parameters for load duration and displacement amplitude described in Chapter 4.1. The measured head displacement with respect to the applied force for each pulse is presented in Figure 5.1. These response curves are also presented with comparison to the load-displacement response obtained from the static load test (SLT) that proceeded the rapid load tests (RLT) in Figure 5.2. These measured responses are used to assess the static capacity of the pile group and soil-structure interaction using the Unloading Point (UP) method, Modified Unload Point (MUP) method, Segmental Unloading Point (SUP) method and Embedded Data Collector (EDC) method. To examine damping and rate effects during testing, the SLT data was used in parallel with the RLT data to estimate rate effect correction factors and back calculate time variant damping constants across each test. Changes in rate effects and in damping with the duration and amplitude of the applied rapid load are investigated. Lastly, damping constants for the power law model recommended in (Brown (2004)) are developed by fitting the RLT data to the model using the SLT to provide the static soil resistance in the equation of motion.

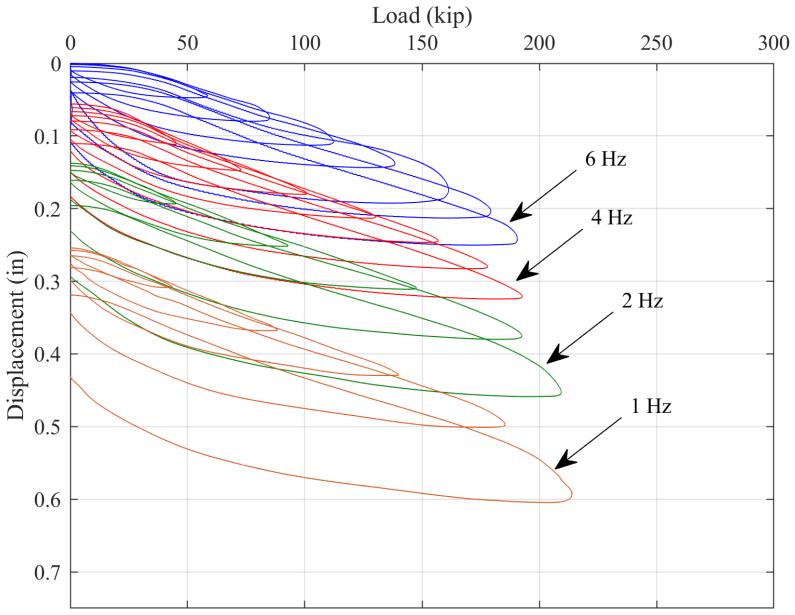

Figure 5.1: Summary of all rapid load test responses at the head of the pile group

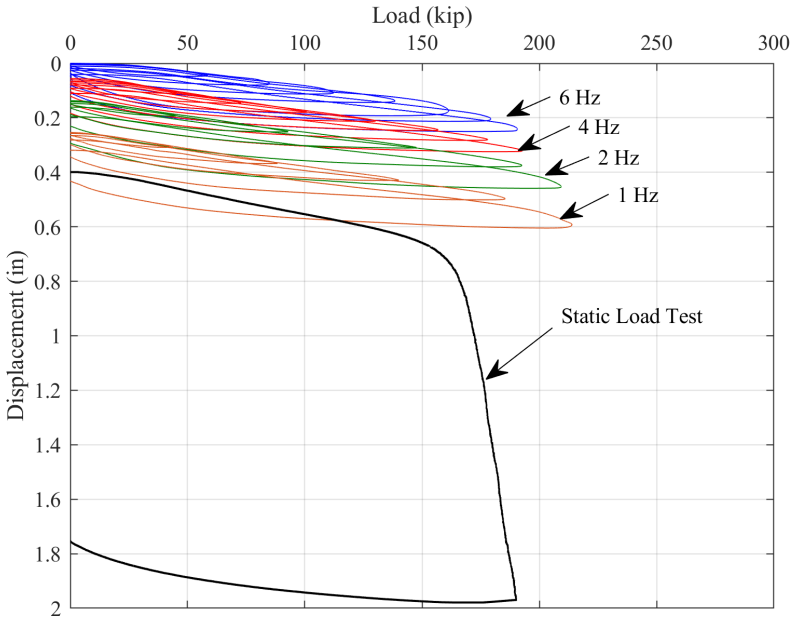

Figure 5.2: Comparison of all rapid load test responses to the static load test response

5.1 Unloading Point Method

Using the procedure described in Chapter 2 for the UP method, the derived static unloading point of each pulse is used to predict the static response of the sheet pile wall. During the process of determining the unloading point, it was found that the inertia force estimated using the measured acceleration and mass of the sheet pile wall did not contribute significantly to the dynamic resistance (Figure 5.3). The largest acceleration measured at the unloading point was 198 in/s^2, producing a calculated inertia force of 2.4 kip, which is approximately 1.3% of the derived static force at the unloading point (t_{umax}). Thus, the inertia effects were ignored in determining the unloading points of each pulse. Figure 5.4 presents a plot of the unloading points as well as the envelope of the unloading points, which is assumed to approximate the static load versus displacement response of the pile. The 24 individual pulses processed to determine the unloading points are presented in Appendix B.

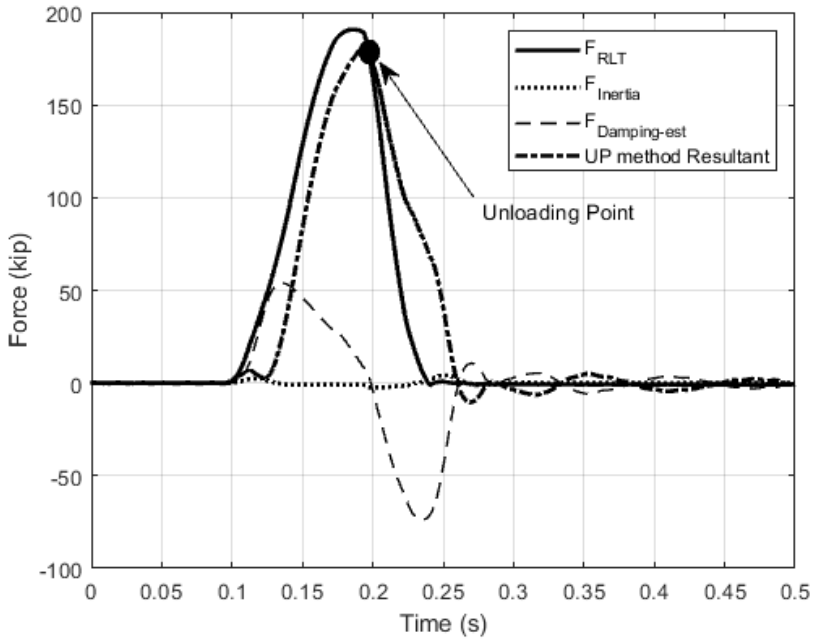

Figure 5.3: Separation of forces for the pulse corresponding to 6Hz and 0.40in peak input displacement

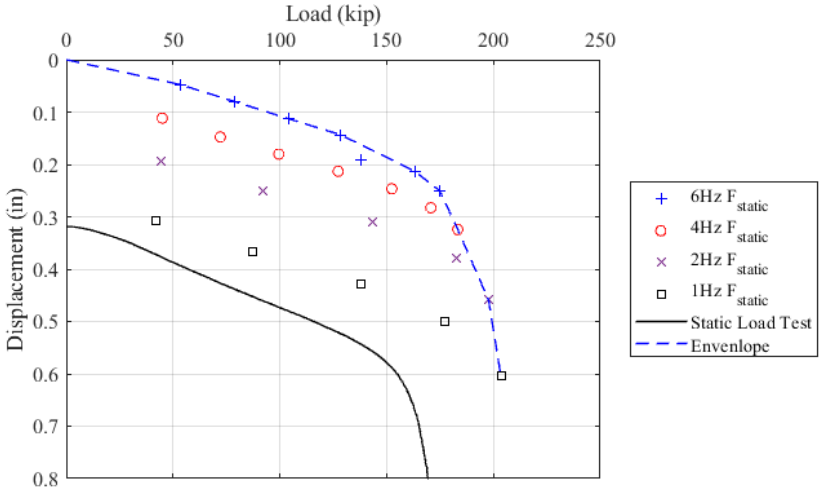

Figure 5.4: Derived unloading points and envelope used to estimate the static load versus displacement response

Rate effect correction parameters, η, were applied considering both sand and clay conditions as described previously in the literature review in Chapter 2.2.3. The suggested

rate effect correction value for sand (η = 0.94) and clay (η = 0.66) is expected to bound the scope of the rate effects for the clayey sand to silty, clayey sand used in the laboratory testing, as shown in Figure 5.5. By iteratively adjusting the rate effect correction parameter to fit to the SLT response, a rate effect correction parameter of η = 0.80 was found to optimally predict the static load versus displacement response. Coincidentally, this optimal rate effect correction parameter is the average of the values for sand and clay recommended in the literature.

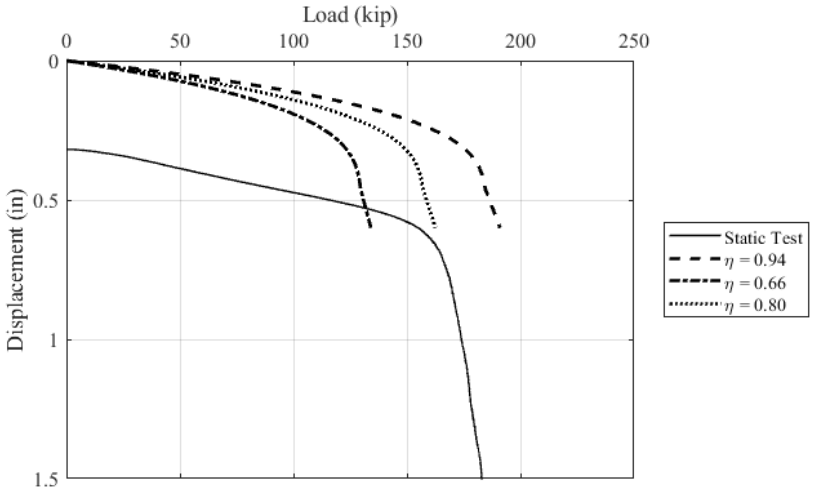

Figure 5.5: Determination of rate effect correction parameter

5.2 Modified Unloading Point Method

The measured accelerations at the head and toe were averaged per the Modified Unloading Point (MUP) method and presented in Figure 5.6. There was a 22% reduction in acceleration at the unloading point, t_{umax}, using this method. However, due to the low system mass, the derived estimate of static force between the UP method, $(F_{RLT} - ma)_{UP}$, and the MUP method, $(F_{RLT} - ma)_{MUP}$, differed less than 1% in all RLT pulses. Therefore, it was concluded that the MUP method would not offer significant changes in the information

provided for inertia effects on the system and would not significantly change the estimated static bearing capacity. This was expected since the MUP method was developed to address shortcomings of the rigid body assumption when applied to longer piles where the toe accelerations are significantly different than the head accelerations.

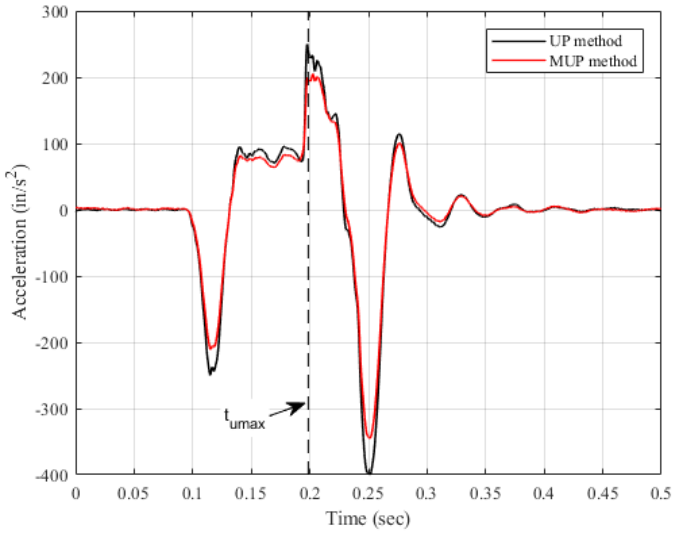

Figure 5.6: Calculated accelerations used in UP method and MUP method

5.3 Segmental Unloading Point Method

Following the procedure presented in Chapter 2.1.3, the Segmental Unloading Point (SUP) method analysis was completed for the RLT data using the strain measurements obtained from the strain gauges installed along the length of Pile #3. The strains at these instrumented locations were assumed to be consistent across the three remaining piles at each corresponding elevation. The forces developed and used in this method were computed using the wall cross sectional area and the shear stresses were determined using the wall perimeter previously presented in Table 4.1. Both the cross sectional area and perimeter used account for the contribution of cover plates but assume an unplugged soil condi-

tion. Figures 5.7 through 5.10 present the envelope of the unloading points for computed side friction resistances for each segment along the depth of the pile using the full series of RLTs. These envelopes of the unloading points in each segment are experimental estimates of the t-z curves for the soil-structure interaction across each segment and are compared to t-z curves experimentally derived from the same strain gages in the static load test. Note that the segments extend only to 79in below the ground line since the strain gages below the 79in elevation were not reliably functional during either the RLT or the SLT. Consequently, the side frictional resistance estimates presented in this section only account for the side friction from the ground line to 79in, while the toe resistance estimates also include any side friction resistance below 79in. In these figures, the t-z curves derived from the SUP method are present without rate effect correction, with the rate effect correction factor obtained from calibrating the UP method estimate to the SLT, and with the empirical rate effect correction factors recommended in the literature (Holscher et al. (2012)) for sand and clay. In each of these figures, the t-z curve from the SLT is offset by the cumulative permanent set that occurred after the series of RLTs. This was done because subsequent tests can result in residual stresses that may cause an apparent increase in the axial resistance of the pile. In other words, since the SLT was performed after that RLTs, the SLT soil-structure interaction should behave as an extension of the RLT response, which is easier to observe if the curves are offset.

Examination of the force mobilization across the individual segments along the depth of the pile reveals that the side friction resistances obtained from the SUP method nearly exactly predicted the side friction resistance in the first segment of the pile, when the rate effect correction factor obtained from the UP method was applied. However, the SUP

method under-predicts the side friction resistance in the second segment and over-predicts the side friction resistance in the third segment. The SUP method nearly exactly predicts the side friction resistance in the fourth segment, when the rate effect correction factor obtained from the UP method was applied. Despite moderate differences in estimated side friction resistances for some segments, the initial slope and general shapes of the t-z curves developed by the SUP method agree well with those of the t-z curves developed from the SLT.

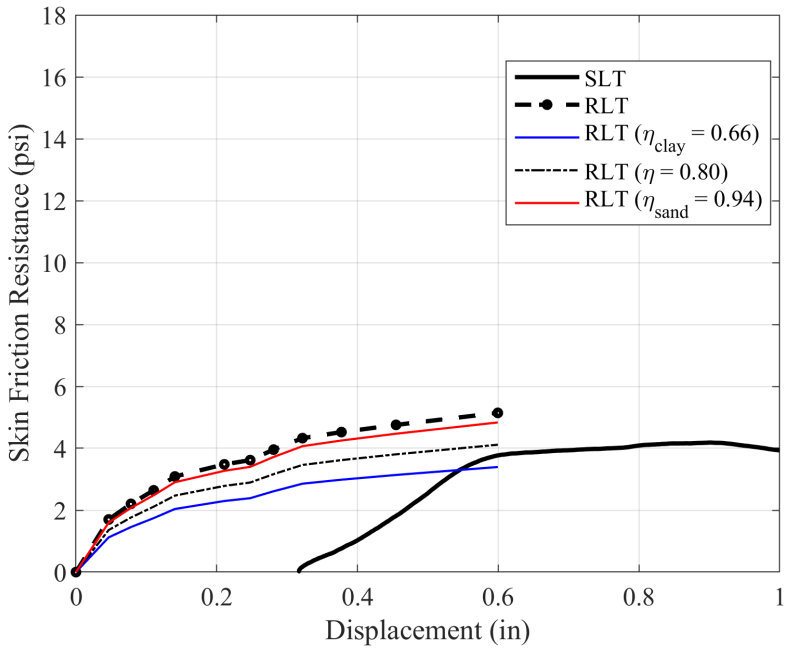

Figure 5.7: Experimental t-z curves developed from SUP method and SLT for the layer from 0in to 34in in depth

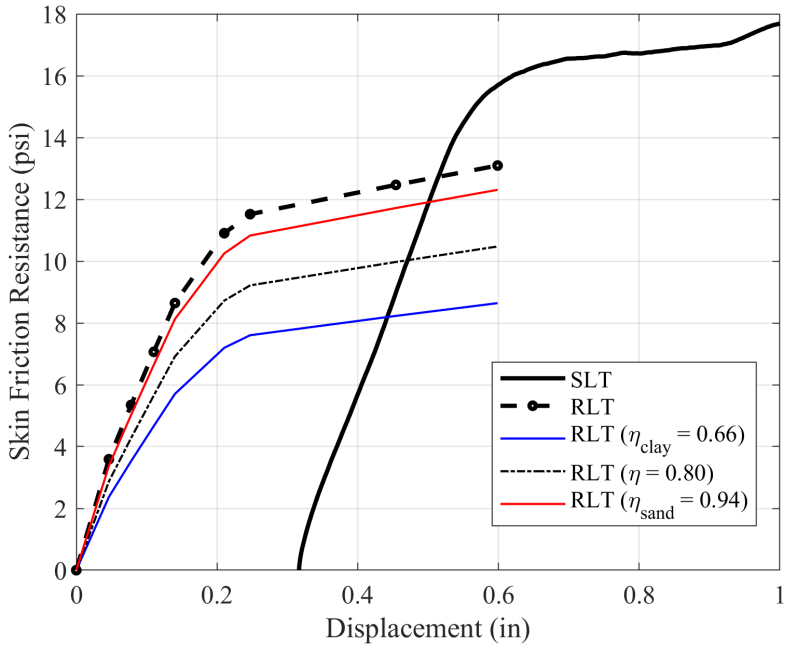

Figure 5.8: Experimental t-z curves developed from SUP method and SLT for the layer from 34in to 49in in depth

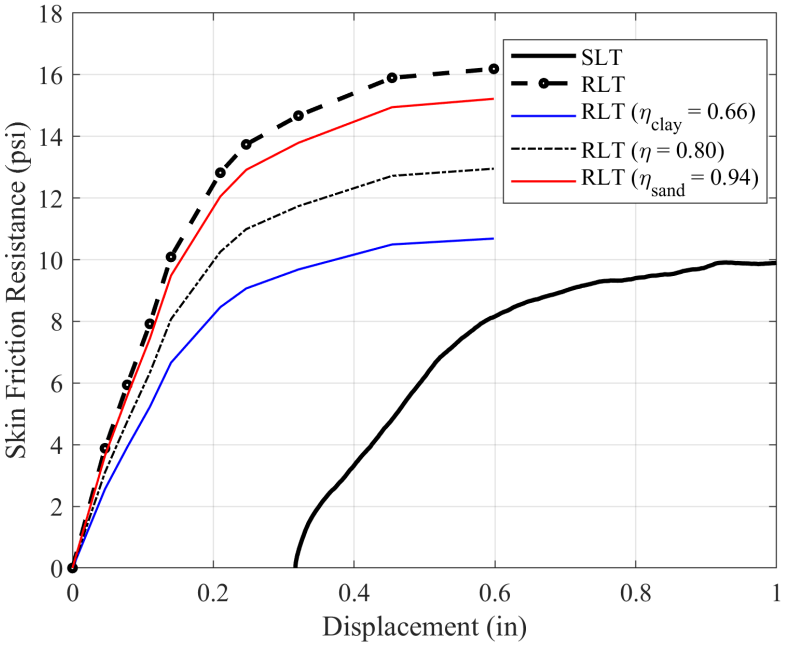

Figure 5.9: Experimental t-z curves developed from SUP method and SLT for the layer from 49in to 64in depth

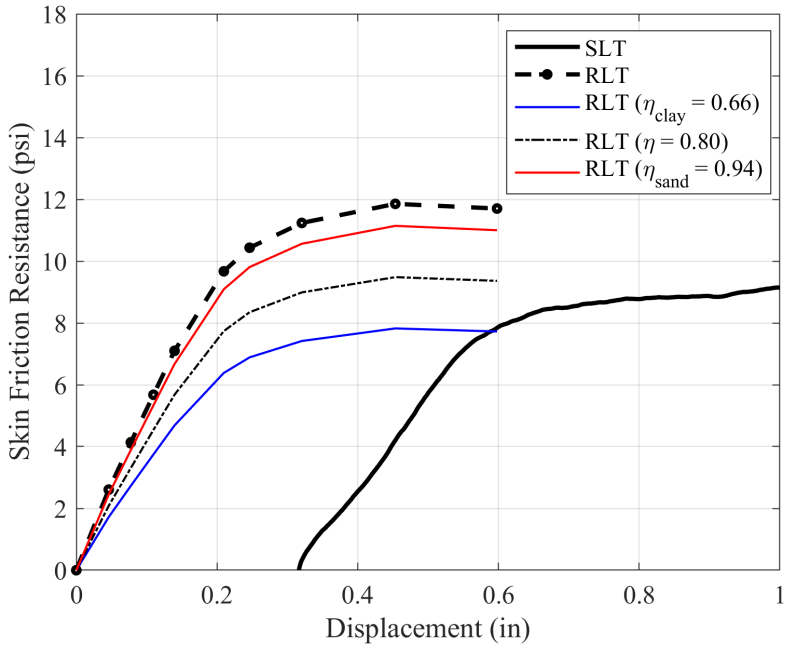

Figure 5.10: Experimental t-z curves developed from SUP method and SLT for the layer from 64in to 79in in depth

The individual t-z curves developed for each segment are combined into a total side frictional resistance response along the full length of the pile in Figure 5.11. This analysis revealed that the total side frictional resistance estimated by the SUP method strongly agreed with the measured SLT response when the rate effect correction factor of η = 0.80 derived from the UP method analysis was applied. The initial slope of the composite t-z curve and general shape correlate well with the side frictional resistance measured in the SLT and the maximum mobilized side friction appears to extend from RLT estimate to the measured SLT response. Also, the ultimate side friction resistance of approximately 10psi correlates well with the average sleeve resistance, ranging approximately 3-13psi, found by the CPTu tests, presented earlier in Figure 4.2. Figure 5.12 presents the load transfer down the length of the pile derived by the SUP method analysis compared to the load transfer

measured in the SLT. As expected, the strong similarity in estimated t-z curves produces consistent estimates in the load transfer. Interestingly, the load transfer produced by the SUP method analysis is slightly smoother and more consistent with expectations for the uniform soil profile used in the laboratory testing. It is possible that the t-z curves developed from the SLT data were affected by drift in the resistive strain gage measurements, which the RLT data would be immune to such effects due to the very short duration of the rapid load pulses.

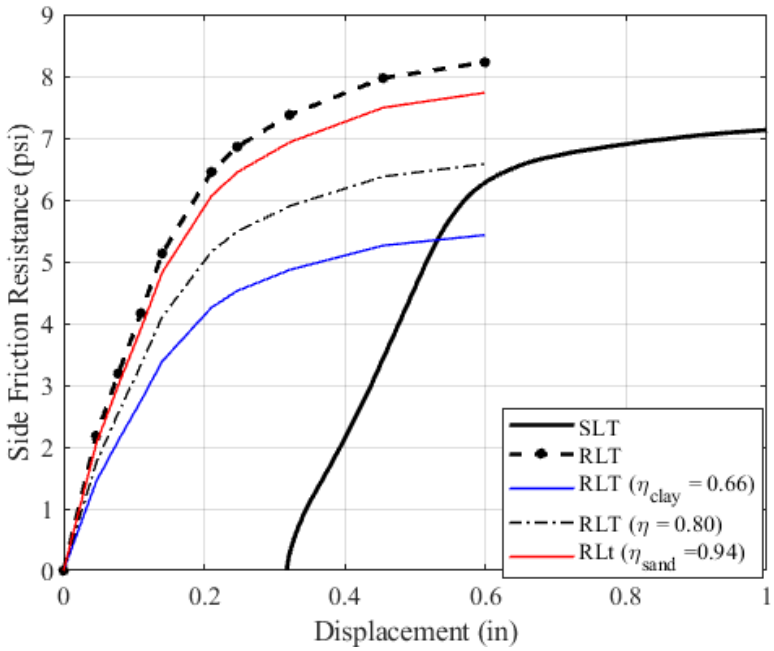

Figure 5.11: Experimental t-z curves develop from SUP method and SLT for total side friction resistance

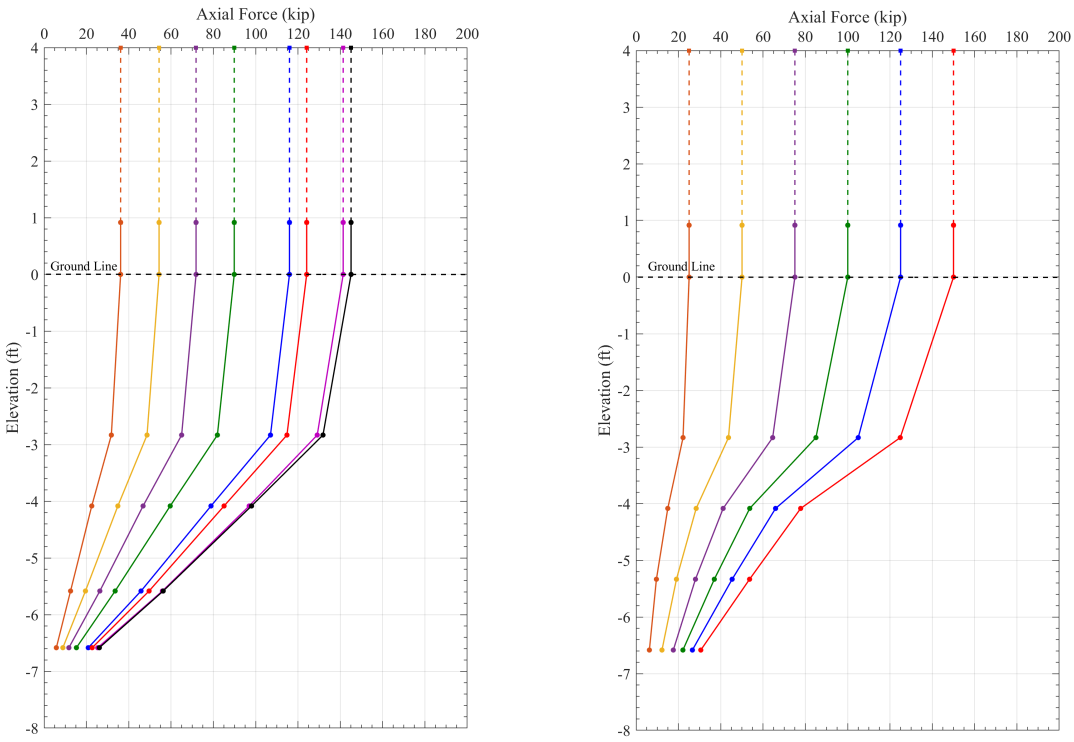

(a) (b)

Figure 5.12: Load transfer along length of pile a) derived by the SUP method with η = 0.80 and b) measured from the SLT

The toe resistance estimated from the SUP method, which also includes any side frictional resistance below the deepest functional strain gage at 79in, is presented in Figure 5.13. The SUP method mildly under-predicts the total toe resistance when the rate effect correction factor is used. However, it should be noted that the contribution of the toe bearing resistance to the total axial capacity is only approximately 15-20% and the error in the toe bearing estimated by the SUP method is less than 5% of the total measured capacity of the pile. Interestingly, the toe bearing resistance estimated by the SUP method without a rate effect correction factor compares well to the toe bearing resistance measured in the SLT. This may support the use of different rate effect correction factors for the side friction

and toe bearing contributions, but the limited data available in this study is not sufficient to conclude the suitability of such an approach.

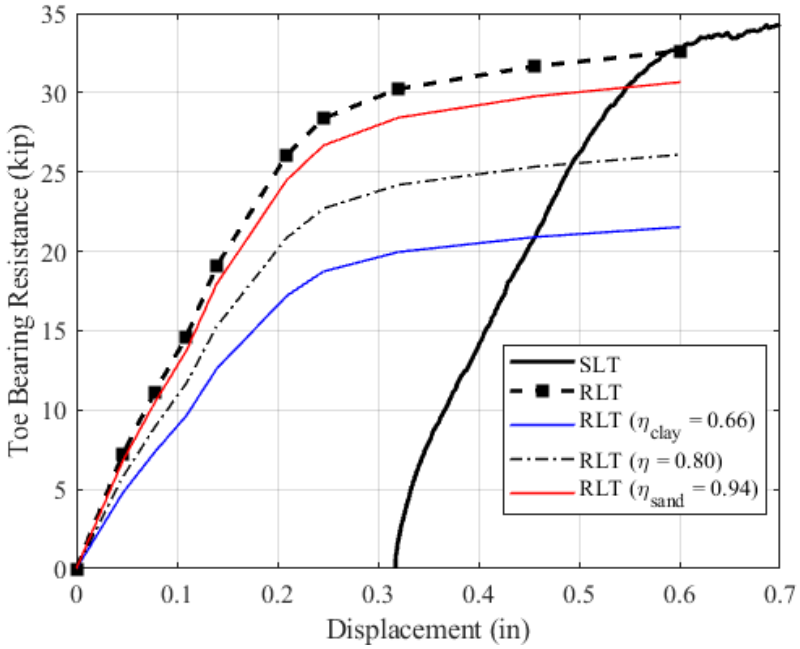

Figure 5.13: Comparison of the toe resistance estimated by SUP method to the toe resistance measured in the SLT

Finally, Figure 5.14 provides the total static load versus displacement response obtained by summing the side friction contributions across each segment as well as the toe bearing contribution. This response compares favorably to the SLT measurement and is nearly identical to the estimate obtained with the UP method using the same rate effect correction factor.

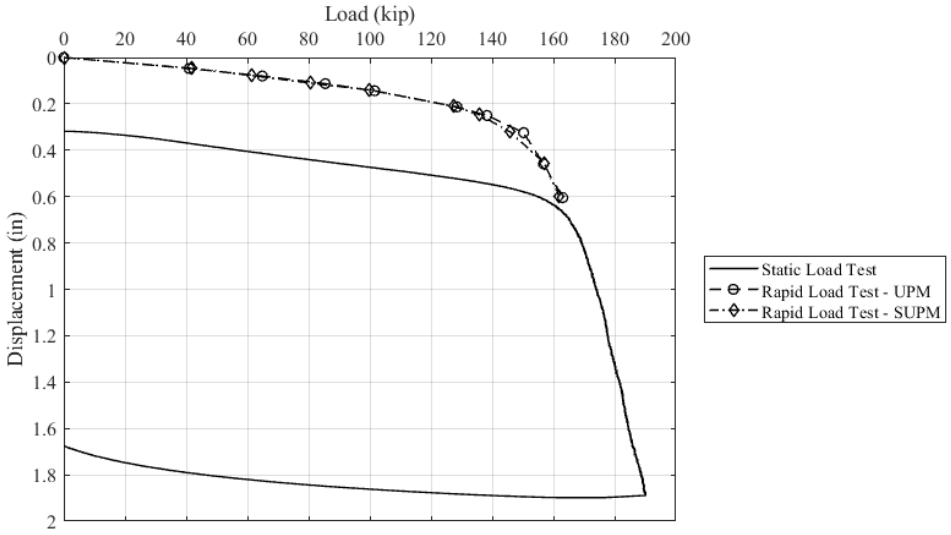

Figure 5.14: Comparison of experimentally derived static load versus displacement response of obtained by the SUP method to the SLT and UP method

5.4 Embedded Data Collector Method

In addition to applying the well-established UP, MUP, and SUP methods for analysis of the rapid load tests, the newly developed EDC method was also applied to the measurement data. As noted in the literature review, this method uses measured accelerations and strains at both the head of the pile and the toe to identify parameters in a toe resistance and shaft resistance models through separate analyses relying on genetic algorithms for inverse modeling. The method was originally developed for dynamic testing of pile foundations, but was extended to rapid load testing in Tran et al. (2016). However, aside from a single case study presented in the original manuscript, no other applications of the EDC method for rapid load testing have been reported in the literature.

To facilitate application of the EDC method to determine the toe resistance model, accelerations measured by the pair of accelerometers installed at the toe were averaged over

the measurement time history and numerically integrated to develop the velocity and displacement time histories. During this development of the motion time histories, it was discovered that the signal-to-noise ratios in the acceleration measurements at the toe of the pile were very low for most of the tests. This was a consequence of using shock accelerometers with a full-scale range of $\pm 193{,}200 in/s^2$ at the toe, which were originally selected to provide for measurement of toe accelerations during the driving process. The low frequency and relatively low amplitude displacements generated at the toe during the rapid load tests only generated peak accelerations that were less than 0.2% of the full-scale range of the accelerometer. Figure 5.15 presents the motion time histories for the only two tests that are included in the EDC method analysis reported in this dissertation. These tests are for the 6Hz and 4Hz load pulses at the maximum amplitudes of displacement. The motion time histories, while likely limited in accuracy due to signal-to-noise issues, were the deemed plausible for these two tests, while the accelerations developed in the 2Hz and 1Hz tests were found to be too low to produce plausible estimates for the displacement at the toe of the pile. Interpolation of strain measurements was performed to arrive at the strain at the location of these accelerometers and the strain was converted to internal axial force using the axial rigidity of the pile.

Following the guidance in Tran et al. (2016), a genetic algorithm was used to determine the eight unknown parameters in the toe resistance model (m, c, k_1, k_2, k_3, k_4, l_1, and l_3) by minimizing the objective function previously presented in Equation 2.20. When applying the genetic algorithm, bounds were established to restrict the mass to the range of $7.7x10^{-4}$ to $31x10^{-4} \frac{k\, s^2}{in}$, the damping coefficient to the range of 0.05 to $60 \frac{k\, s}{in}$, and the stiffness parameters to the range of 5 to $5000 \frac{k}{in}$. The lower bound of the mass estimate

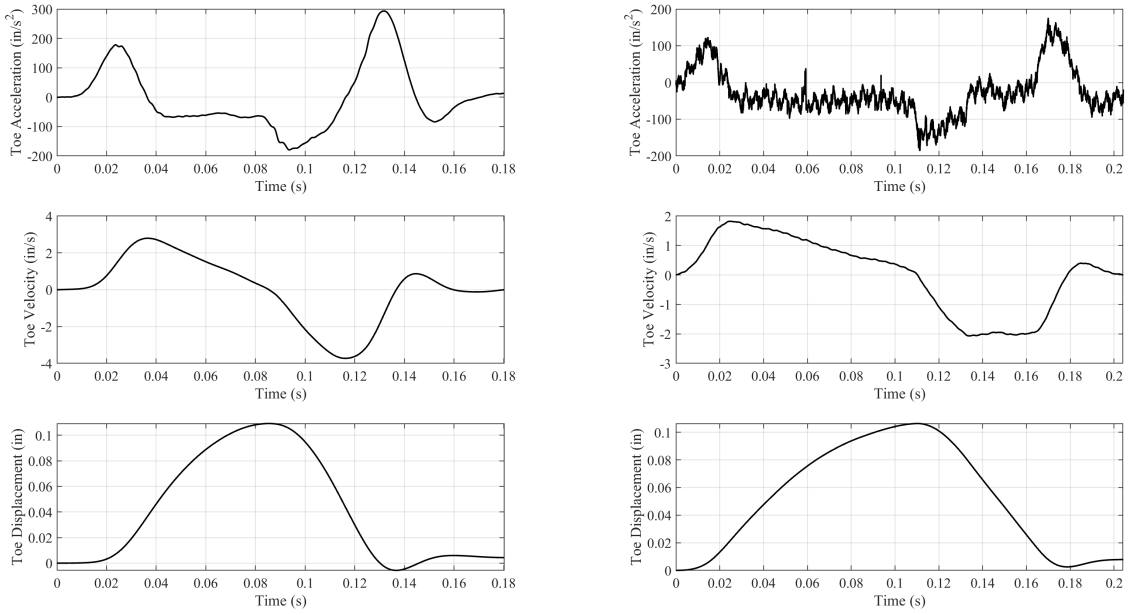

(a) 6Hz 0.4in

(b) 4Hz 0.4in

Figure 5.15: Measured axial acceleration and numerically integrated velocities and displacements at the toe for rapid load tests

represents the mass of steel sheet pile below the toe measurement location, while the upper bound was set to be four times that mass. However, as previously noted, the inertial force developed during these tests has been should to be relatively insignificant, so the little confidence should be placed in the estimate obtained from the genetic algorithm for the mass parameter. A population size of 10,000 individuals was used over 20 generations with 5% of the population retained as elites, 80% generated by crossover, and the remaining 15% introduced by mutation between generations.

Figure 5.16 presents the results obtained from applying the genetic algorithm to arrive at the optimal set of parameter assignments for the toe resistance model. For both tests, very strong correlation was achieved in the energy balance, while strong correlation was also achieved in the force balance. The relative significance of inertia, damping, and static

resistance to the overall soil resistance at the toe of the pile was found to be generally consistent across both tests and similar to that previously estimated at the head of the pile in the UP method (Figure 5.3). Table 5.1 provides the identified parameter assignments for the toe resistance model for each test. The identified parameters are generally consistent across the two tests, with exceptions being a higher damping coefficient and lower initial static resistance for the 4Hz test. Figure 5.17 presents the static resistance at the toe during loading and unloading as estimated by the EDC method compared to the toe resistance derived using strain measurements obtained from the static load test. While both of the EDC analyses predict consistent static toe resistance that are indicated to be essentially linear elastic, the EDC method over-predicts the static soil resistance relative to the toe model obtained from the static load test by a factor of approximately two. This may be a result of possible shortcomings in the EDC method, especially the lack of compensation for rate effects, which were found in the previous unloading point methods to be significant in these tests. Additionally, the EDC method assumes a time invariant damping coefficient, which has been suggested in the literature on rapid load testing to be an invalid assumption (Stokes et al. (2008)). However, it is not possible to conclude that the poor correlation between the toe model obtained from the EDC method and the one derived from the static load test is a result of shortcomings in the EDC method due to the previously mentioned signal-to-noise ratio issues in the measurement of accelerations at the toe of the pile in these tests. The EDC method relies on force and energy balances that directly use the measured acceleration and numerically integrated velocity and displacement, so inaccuracy in these motion time histories, particularly the double integrated displacement, will lead to errors in the parameters identified for the soil resistance models. Due to the uncertainty in the measured

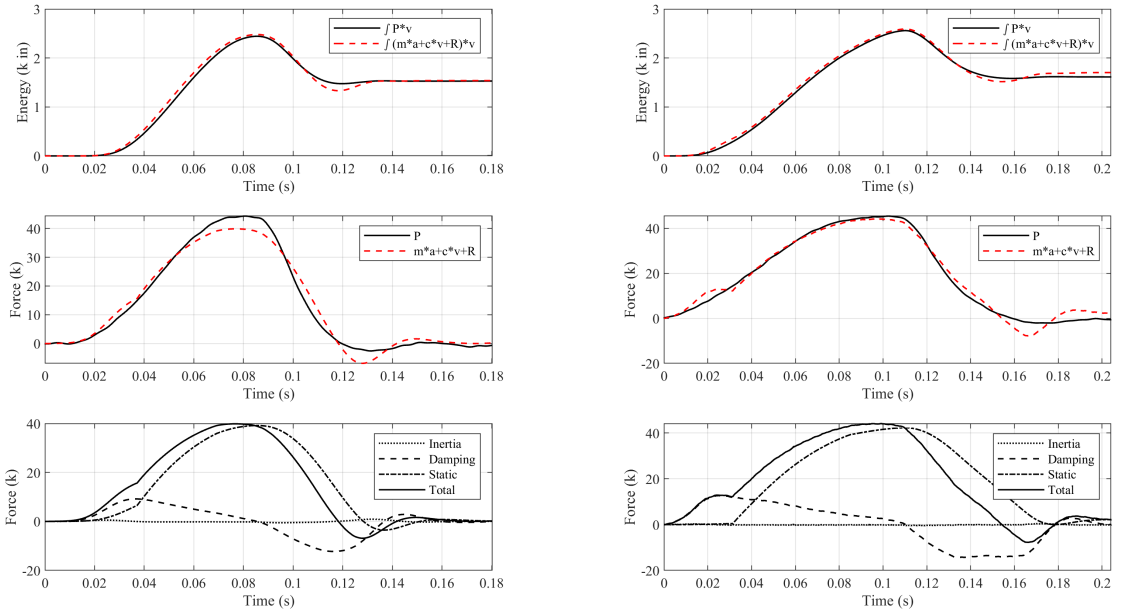

(a) 6Hz 0.4in

(b) 4Hz 0.4in

Figure 5.16: Energy and force balance obtained by minimizing the objective function and force components estimated using the optimal parameter set

Table 5.1: Toe resistance model parameters identified by EDC method

Test	$m\left(\frac{kip\ s^2}{in}\right)$	$c\left(\frac{kip\ s}{in}\right)$	$k_1\left(\frac{kip}{in}\right)$	$k_2\left(\frac{kip}{in}\right)$	$k_3\left(\frac{kip}{in}\right)$	$k_4\left(\frac{kip}{in}\right)$	$l_1\ (in)$	$l_3\ (in)$
6Hz 0.4in	$3.1x10^{-3}$	3.29	170.7	472.6	377.6	372.1	0.35	0.08
4Hz 0.4in	$2.7x10^{-3}$	6.95	13.2	612.4	319.2	407.5	0.31	0.09

accelerations at the toe of the pile and the reliance of the EDC shaft resistance determination on accurate measurement of motion at both the head and toe of the pile, plausible EDC shaft resistance estimates were not successfully obtained and are not presented in this dissertation.

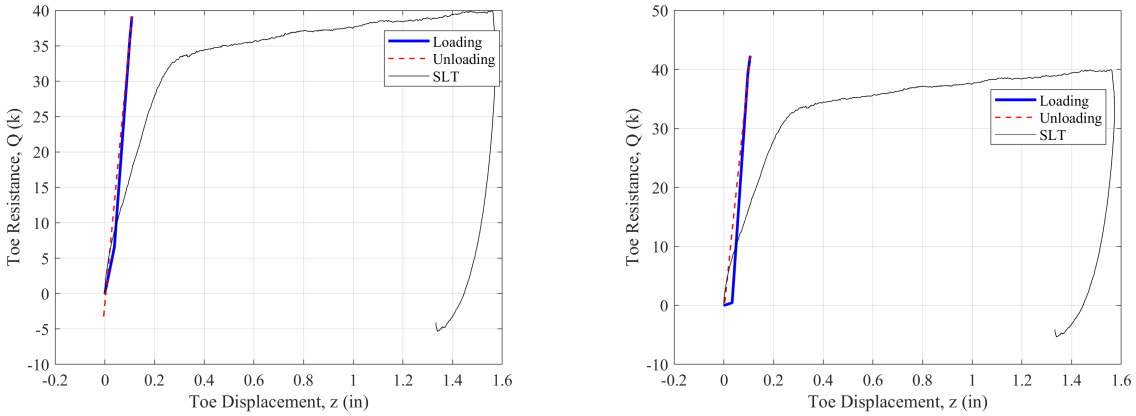

(a) 6Hz 0.4in (b) 4Hz 0.4in

Figure 5.17: Comparison between toe resistance obtained from static load test and static toe resistance estimated by EDC method (unloading shown as dashed line)

5.5 Damping Force Determination

5.5.1 Time Invariant Damping Estimates

Following the theory presented in Chapter 2.2.1 by Mullins et al. (2002), the damping constant between maximum force, t_{fmax}, and maximum displacement or unloading point, t_{umax}, was calculated using Equation 2.22 for all 24 applied RLT pulses. Figure 5.18 presents the calculated damping constant across this range for the 6Hz 0.40in pulse as well as the average. Using the average damping constant calculated in this range as a time invariant parameter in the SDOF equation of motion, the force components were determined over the full range of the pulse (Figure 5.19) and the computed static force response to the head displacement was estimated, as shown in Figure 5.20. The back calculated static force response shows an unfavorable result as it produces a negative static response at the beginning of the response, which suggests that the time invariant damping constant produced excessively high damping force estimates early in the pile response. This is consistent with the conclusions from Mullins et al. (2002) and suggests that damping is not

constant throughout the rapid load test. The estimation of time invariant damping constants and separation of component forces over time from the all 24 pulses with time invariant damping constant are provided in Appendix B. The average damping constant for each pulse is compared across all applied pulses in Figure 5.21, where the estimated damping constant is plotted as a function of the measured maximum displacement. The average damping constant is observed to be relatively consistent during the 6Hz pulses and linearly increases with respect to displacement with the 4Hz pulses. It is noted that the 2Hz pulses exhibited significantly more variation in the average damping constants, while the 1Hz pulse produced unexpectedly large average damping constants that were deemed implausible. However, it should be noted that the 1Hz and 2Hz pulses produced wave numbers that classify these tests very close to the transition between the static and rapid load test classifications according to Figure 1.1. Consequently, the dynamic effects that developed during these low frequency, long duration tests may be so small that signal-to-noise ratio issues affect the damping constant estimates or that the significance of certain phenomena, such as viscous damping or pore water pressure effects, was different for these test.

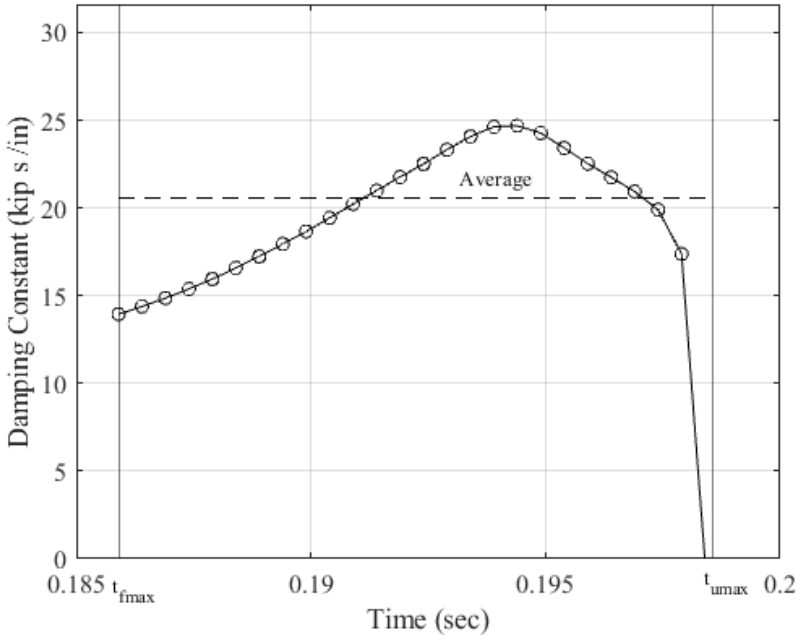

Figure 5.18: Estimating the damping constant for 6Hz 0.40in pulse using the UP method

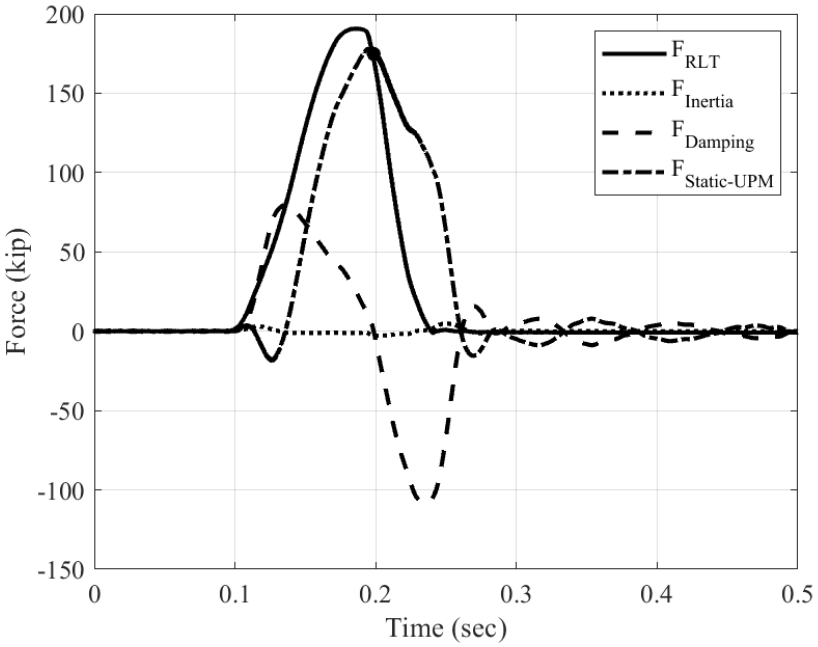

Figure 5.19: Comparison of forces in time domain using constant damping estimated by Mullins et al. (2002) for 6Hz 0.40in pulse

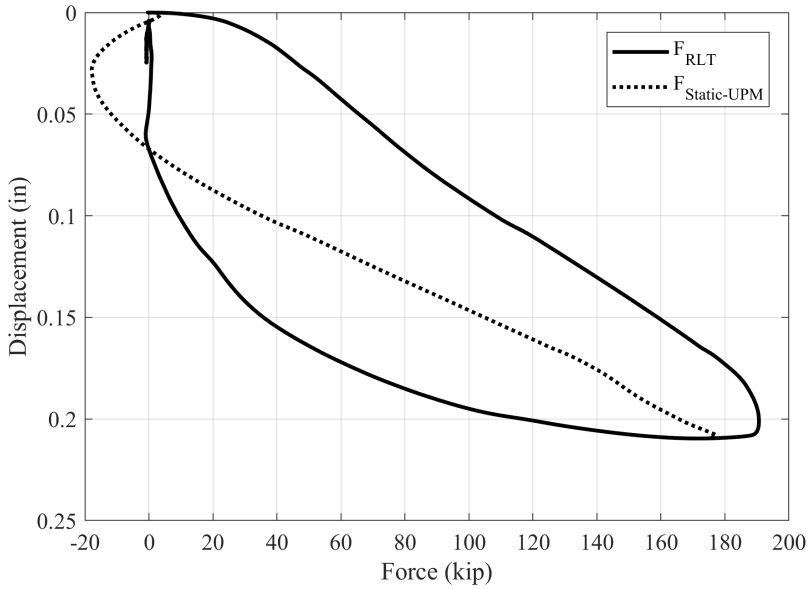

Figure 5.20: Comparison of force displacement response using a time invariant damping constant for 6Hz 0.40in pulse

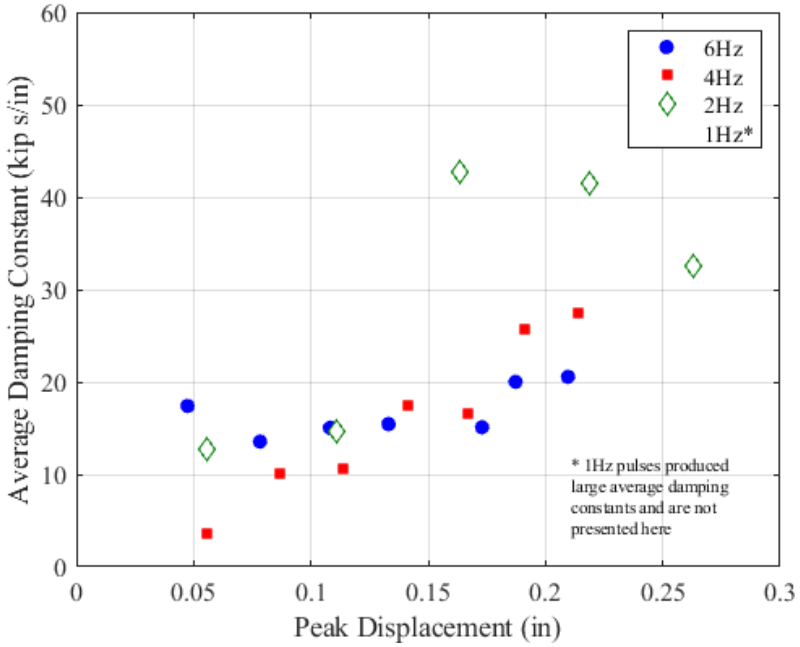

Figure 5.21: Average damping constant for all applied pulses in RLT plotted as a function of the measured peak displacement

5.5.2 Back Calculated Time Variant Damping Constant

From Stokes et al. (2008), it is known that the damping constant, c, cannot be assumed constant throughout the duration of the rapid load tests. With the information provided by an existing SLT, a time variant damping constant can be determined because the static resistance can be taken as known providing a direct means of calculating the dynamic soil resistance, which included damping, pore water pressure effects, and rate effects. However, it was noted by Stokes et al. (2008) that the time variant damping constant obtained through the back calculated approach is related to the volumetric change in the soil that results during loading. This, therefore, assumes that the rate effects and pore water pressure effects are not captured by this time variant damping constant parameter. It is also important to note that the unloading point exists at the instance of maximum displacement, and thus, zero velocity, so therefore no damping forces exist. This means that the unloading point will still need to be adjusted by the rate correction factor, η, in order to account for rate effects and pore water pressure effects to accurately estimate the corresponding static resistance.

The process of determining the time variant damping constant starts with estimating the rate correction factor for each applied pulse. This was completed similarly to estimating the rate correction factor with the UP method. However, in this approach, the applied force during the RLT minus the inertia effects, $F_{RLT} - ma$, was compared to the static load versus displacement response obtained from the corresponding SLT measurements for each individual test and a test dependent rate effect correction factor was determined. Test dependent rate effect correction factors are needed to ensure that the static resistance is correctly recovered at the unloading point of every individual data set. It is also important

to note that, even though it is shown that pore water pressure effects are likely to vary with time throughout the pulse, the estimated rate effect correction factor, which accounts for both rate effects and pore pressure effects, is assumed to be constant throughout the load duration and the estimated pore water pressure force is calculated by substituting a general form of Equation 2.32 into Equation 2.2, as presented in Equation 5.1. This inclusion of pore water pressure forces modifies the theory presented by Stokes et al. (2008) in such a way that the back calculated damping forces includes not only the theorized volumetric changes, but pore water pressures as well, which is illustrated graphically in Figure 5.22.

$$F_{pore}(t) = (1 - \eta)(F_{RLT}(t) - ma(t)) \tag{5.1}$$

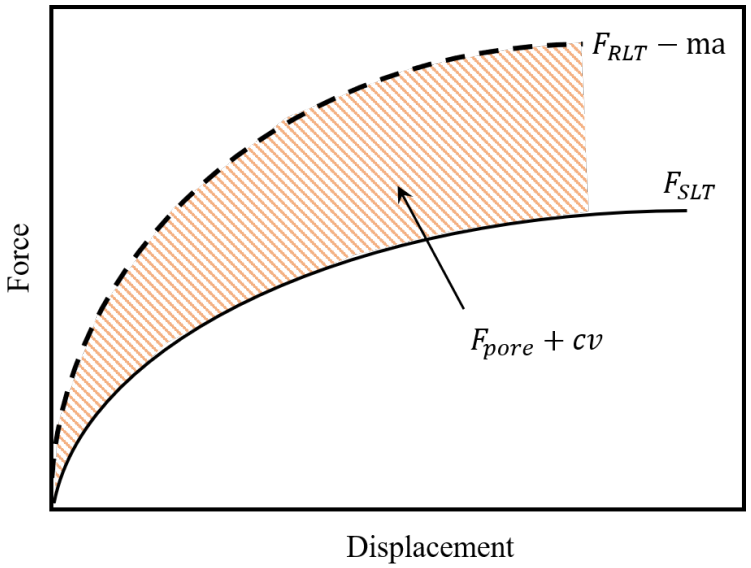

Figure 5.22: Comparing response from the RLT to the SLT to determine the variable damping constant, c which now includes the contribution of forces produced from pore water pressure effects

An example of this determination for one of the RLT data sets is presented in Figure 5.23. The reason why test dependent rate effect correction factors were produced for the

damping constant determination is to ensure that the unloading point for each individual RLT is consistent with the static resistance obtained from the SLT. Figure 5.24 presents the experimentally derived rate effect correction factors from each individual RLT as a function of the measured peak displacement. The results clearly show an increased significance of strain rate and pore water pressure with decreased duration of loading and increased peak displacement. This is expected since shorter durations and larger peak displacements produce higher velocities during the rapid load test and would produce greater changes in pore water pressures. The only outlier to this observation is the result for the 6Hz pulses, where the rate effects become slightly less significant as the peak displacement increased. In general, the results suggest that the rate effect correction factor converges on a value of approximately 0.75 when peak displacements exceeding 0.25in are achieved.

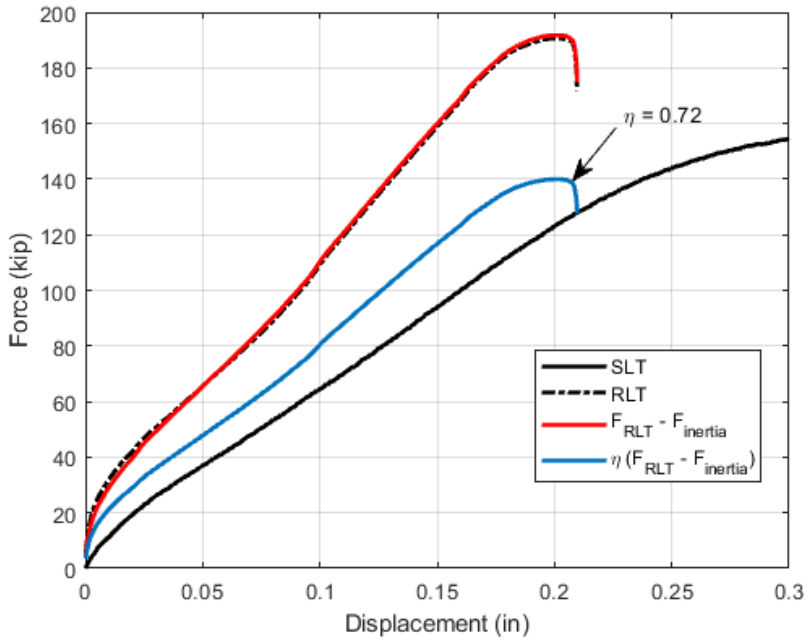

Figure 5.23: Determination of rate effect correction factor for 6Hz pulse with 0.40 in input displacement

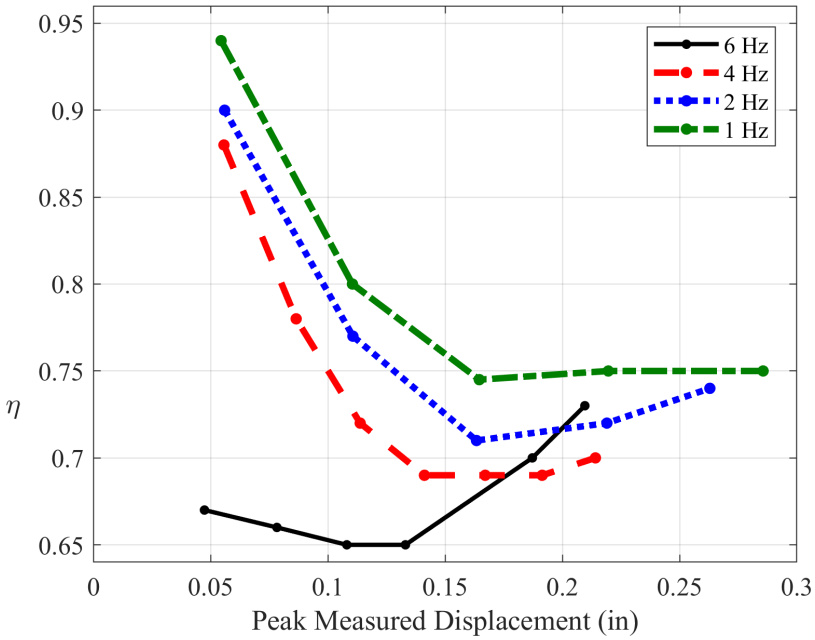

Figure 5.24: Rate effect correction factors obtained for each individual RLT plotted as a function of the peak measured displacement

After the rate effect correction factor has been determined for each individual pulse, the method presented in Stokes et al. (2008) was used to back calculate the time variant damping constant throughout the test using the equation:

$$c(t) = \frac{\eta(F_{RLT}(t) - ma(t)) - F_{SLT}(x)}{v(t)} \tag{5.2}$$

where each force component corresponds to a consistent displacement at the head of the pile, x. To facilitate this, the static load versus displacement response measured from the static test is used to obtain $F_{SLT}(x)$ corresponding to the head displacement measured at each time increment in the RLT.

Figure 5.25 presents the force components calculated for one of the RLT tests after back calculating the time variant damping constant. The derived static resistance force component, $F_{static,der}$, equals the static resistance measured in the SLT, which confirms that the

time variant damping constant is derived to exactly replicate the measured static resistance.

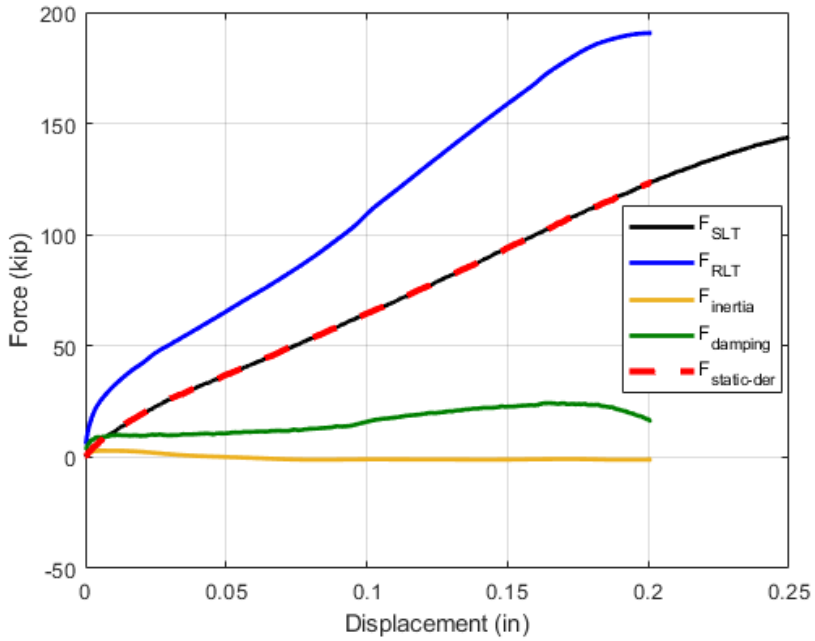

Figure 5.25: Comparison of force components in the from rapid load test using computed time variant damping constant for the 6Hz pulse with input peak displacement of 0.40in

Figures 5.26, 5.27, 5.28, 5.29 present the back calculated time variant damping constant as a function of measured displacement for the 6Hz, 4Hz, 2Hz, and 1Hz pulses, respectively. In these figures, the back calculated damping constant is presented from $t = 0$ up to the instance in time of the maximum force, t_{fmax}. This windowing of the estimate is performed because, after this instance the apparent damping constant increases rapidly due to the velocity approaching zero at the unloading point. In general, the back calculated time variant damping constants are consistent with displacement for each of the tests conducted with the same load duration, especially for cases when the peak displacement exceeded 0.1 inches. By comparing these time variant damping constants to the time invariant damping constants previously obtained by the UP method and presented in Figure 5.20, it is apparent that the time variant damping constants approach the time invariant estimates as

the displacement of each pulse approaches the unloading point. However, the time variant damping constant is significantly reduced at time instances early in the RLT response.

Instances of zero, or slightly negative, damping constants were computed for some of the 1Hz and 2Hz pulses. This was not expected and is unlikely to reflect the actual behavior of the system. There are two possibilities that may explain the observations, which include the effects of added soil mass and the assumptions incorporated in the rate effect correction, η, applied to account for the change in resistance due to pore water pressures. If a full plug existed within the profile of the sheet pile wall, it was found that the mass of the system would increase by a factor of approximately 1.8. However, since the accelerations were small, the effect of added soil mass for a fully plugged condition was found to not significantly affect the estimated damping constants. Consequently, the negative damping constants are most likely the result of the assumption that the resistance produced by changes in pore water pressure during the test was proportional to the total dynamic resistance less the inertia force, as enforced by Equation 5.1. Since the soil was saturated during testing, it is expected that pore water pressure effects were significant during the rapid load tests. While the assumption that the rate effect correction factor, η, is constant throughout the load duration, following Equation 5.1, is considered reasonable for this application, it is likely not accurate since the pore pressure effects will change as the soil dilates or contracts. With no way to uniquely differentiate the nonlinear pore water pressure forces and nonlinear damping within the equation of motion, the assumption that the rate effect correction factor is constant throughout the duration of loading is required. In conclusion, the unexpected damping, either low or negative, shown in these results are likely a result of not effectively accounting for the pore water pressure effects as a result of using a constant

rate effect correction factor throughout the duration of loading.

It should also be noted that the wave number for the 1Hz and 2Hz RLT pulses classifies these tests close to the transition between static and rapid load tests according to the loading classification presented in Figure 1.1. Consequently, damping is expected to be less significant of a phenomenon in these tests.

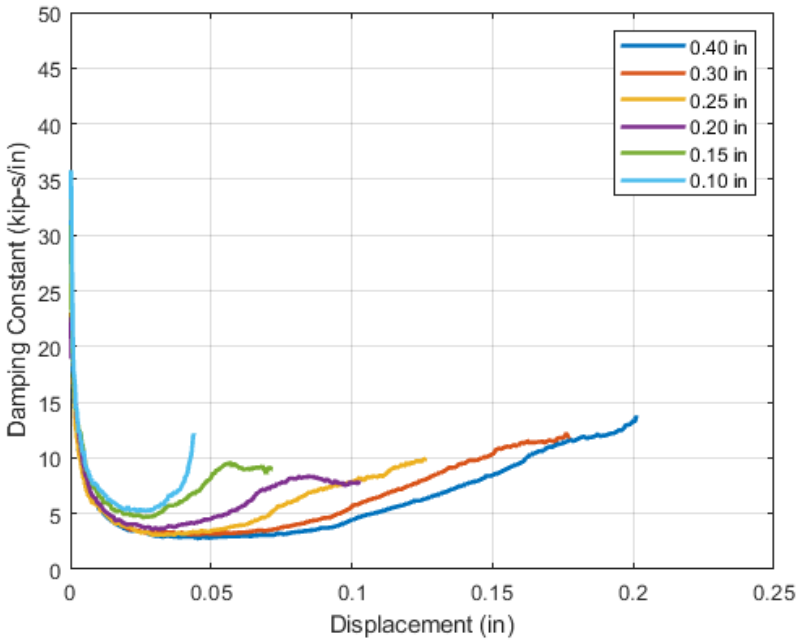

Figure 5.26: Time variant damping constants back calculated for the 6Hz pulses plotted as a function of measured displacement

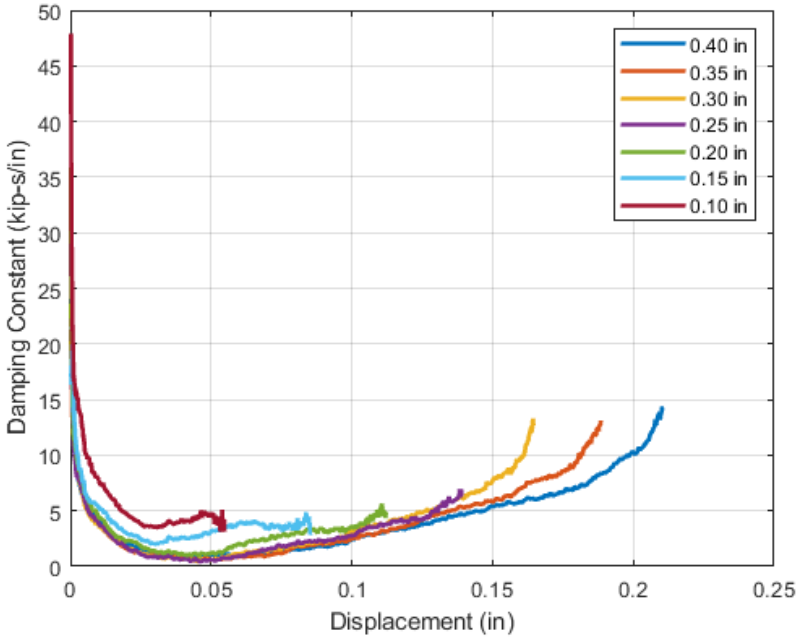

Figure 5.27: Time variant damping constants back calculated for the 4Hz pulses plotted as a function of measured displacement

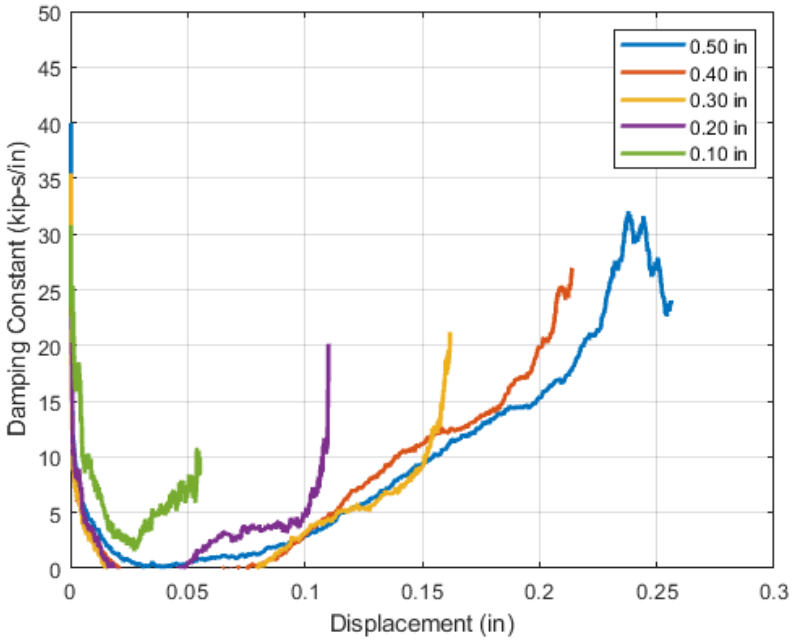

Figure 5.28: Time variant damping constants back calculated for the 2Hz pulses plotted as a function of measured displacement

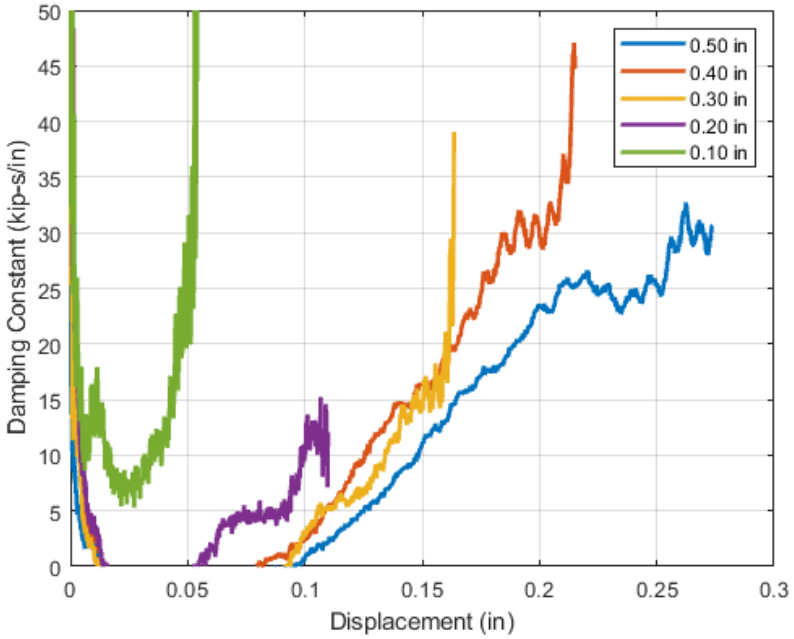

Figure 5.29: Time variant damping constants back calculated for the 1Hz pulses plotted as a function of measured displacement

Figure 5.30 compares the back calculated damping constant obtained for the largest amplitude loading for each load duration. The result suggests that the damping constant is dependent on the rate at which the load is applied. As load duration is decreased, damping is greater at displacement less than 0.11in, but lower at displacements exceeding 0.11in. The results obtained from the testing resemble those presented in by Stokes et al. (2008) and therefore suggest that the volumetric change of the soil adjacent to the pile may be influencing the damping. While volumetric changes were not directly measured during the static load test to attempt to validate this, it was observed that the soil within the area inside the sheet piles settled deeper than the soil outside the profile of the sheet pile system.

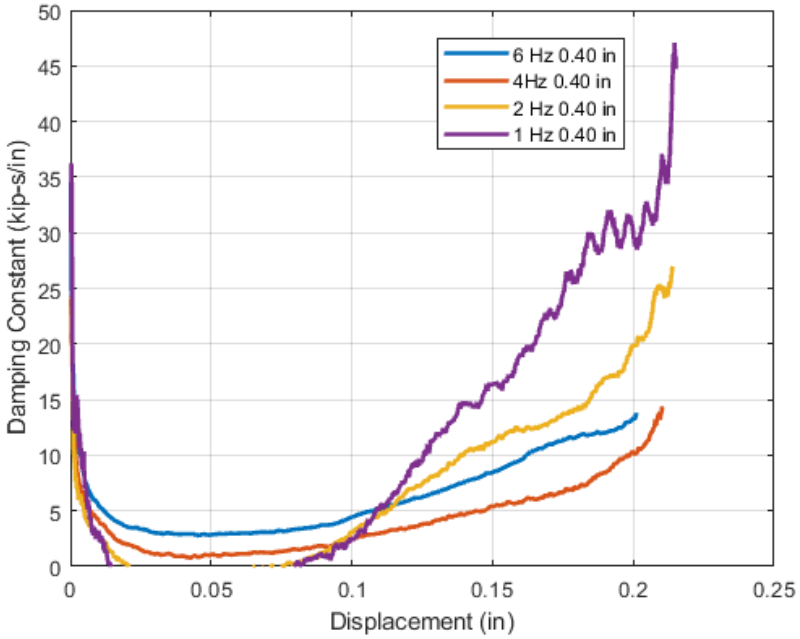

Figure 5.30: Comparison of time variant damping constants calculated for the largest amplitude load pulses

The back calculated damping constant is also plotted as a function of the measured velocity in Figures 5.31, 5.32, 5.33, 5.34 for the 6Hz, 4Hz, 2Hz, and 1Hz pulses, respectively. These figures clearly indicate that the damping constant is consistent with velocity across the different load amplitudes while the acceleration is positive (i.e. while the velocity is increasing). The damping constant also follows a similar trend when the acceleration is negative. The correlation of the damping constant with velocity and acceleration may be a result of the underlying phenomenon of the damping mechanism during the RLT. However, these trends may also suggest that the back calculated damping constant is being influenced by additional soil mass that is not accounted for when determining the inertia force during the rapid load test.

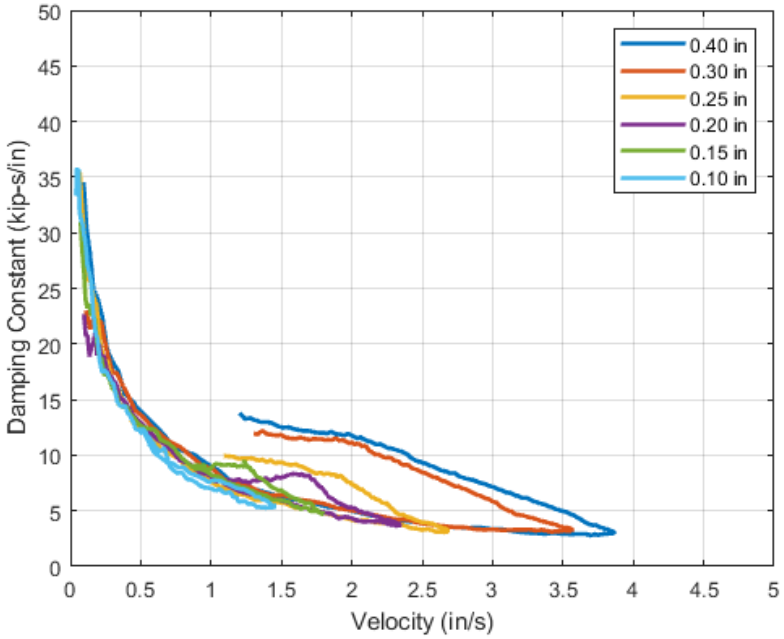

Figure 5.31: Time variant damping constants back calculated for the 6Hz pulses plotted as a function of measured velocity

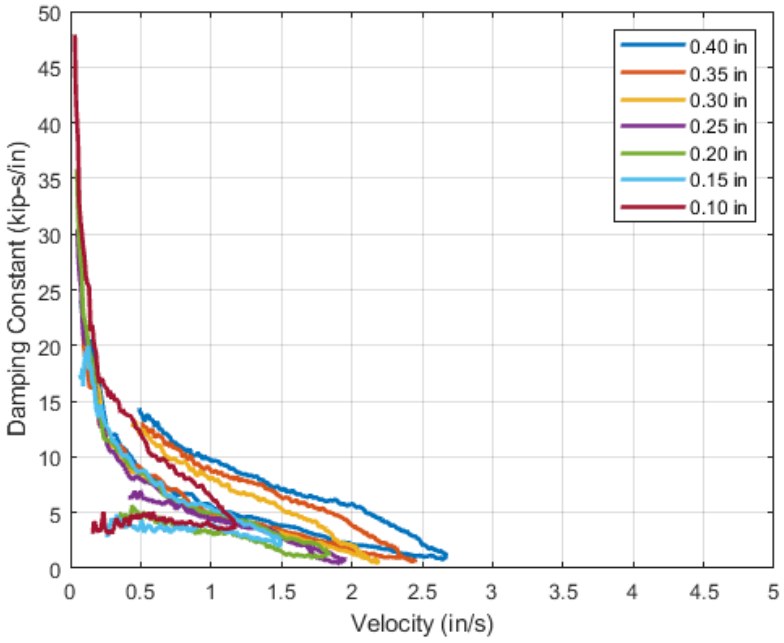

Figure 5.32: Time variant damping constants back calculated for the 4Hz pulses plotted as a function of measured velocity

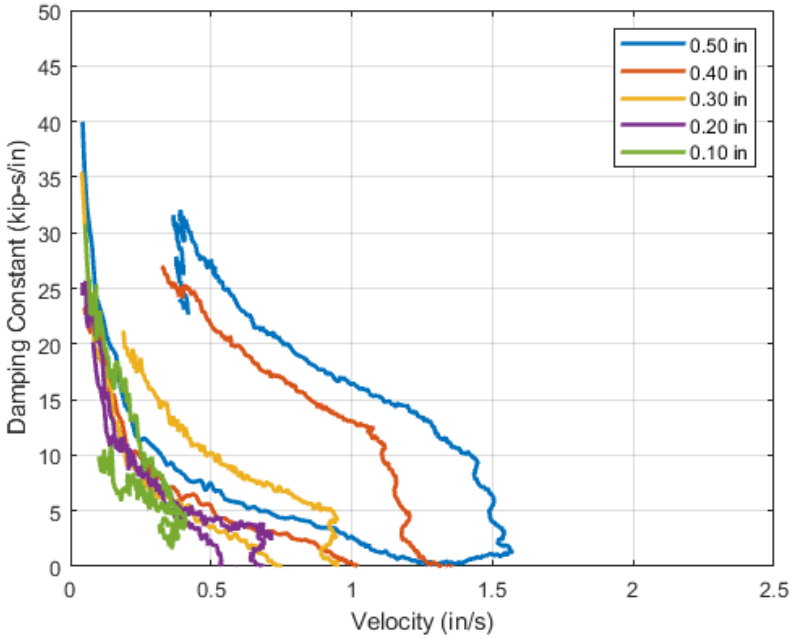

Figure 5.33: Time variant damping constants back calculated for the 2Hz pulses plotted as a function of measured velocity

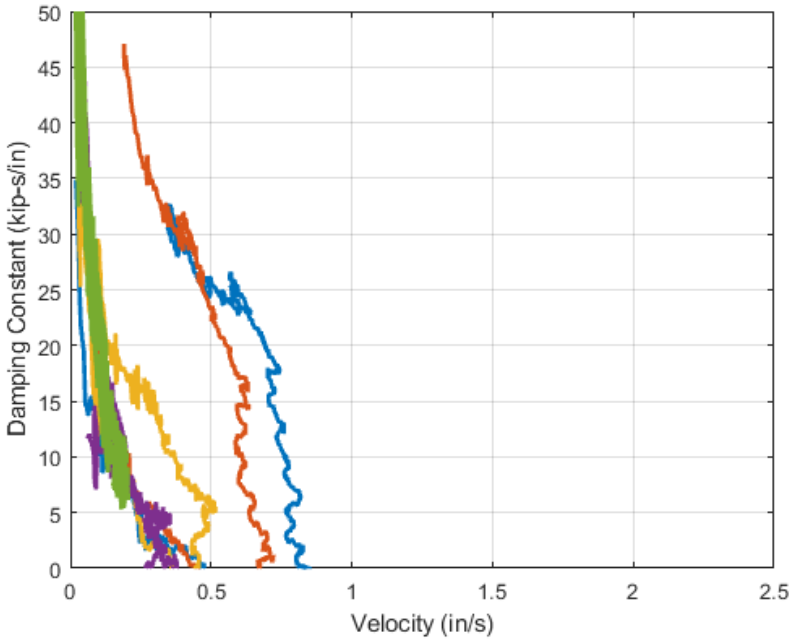

Figure 5.34: Time variant damping constants back calculated for the 1Hz pulses plotted as a function of measured velocity

5.5.3 Rate Dependent Damping Constants

As discussed in Section 2.2.1.3, there are three approaches for establishing the rate dependent damping constants, α and β. Each approach is attempted in this dissertation to compare the consistency of the methods when applied to the available measurement data. The first approach presented is the use of empirical rate dependent damping constants sourced from the published literature. From experimental soil testing, it was determined that the soil used in the laboratory testing had a liquid limit between 26-34% and a plastic limit between 20-23% (Sylvain (2019)). While selecting empirical rate dependent damping constants from a closely matched soil from Table 2.1 would be ideal, the only soil index properties in this table are the Atterburg limits, which are measured on only the fines fraction of the soil. Energy dissipation through soil damping will be affected by not only the index properties of the fines in the soil, but also the relative fraction of the soil that is fines as well as the characteristics of the granular portion of the soil. Consequently, empirical damping constants should ideally be obtained by comparing the full gradation curve. Since the classification of the soil used in this test was defined as clayey sand to silty, clayey sand and a direct comparison of grain size distribution to the soils in Table 2.1 could not be performed due to lack of published grain size distributions for these soils, a bounded approach was used. Specifically, the recommended rate dependent damping constants for sand ($\alpha = 0.1$, $\beta = 0.2$) and clays ($\alpha = 1.0$, $\beta = 0.2$) in Randolph and Deeks (1992) were used to establish empirical bounds. These damping constants are used in Eq. 2.27 for the largest displacement pulses of each duration to estimate the static load versus displacement response. Figures 5.35, 5.36, 5.37, and 5.38 present the static displacement response

for the 6Hz 0.40in, 4Hz 0.40in, 2Hz 0.50in, and 1Hz 0.50in pulses, respectively. In all pulses, use of the damping constants found in the literature over predicts the static force displacement response by approximately 10-15% when comparing the static response estimate using the rate effect damping constants of clay to the SLT. These results suggest that the empirical values for clays work reasonably well for these RLT pulses. However, from the discrepancy between the estimated static response and the measured load-displacement response obtained from the SLT, it is suspected that the effects of pore water pressures are not captured using this method. This is supported by the literature since these rate dependent damping constant relationships are directly related to the strain rate of the soil material and do not consider forces produced by pore water pressure effects.

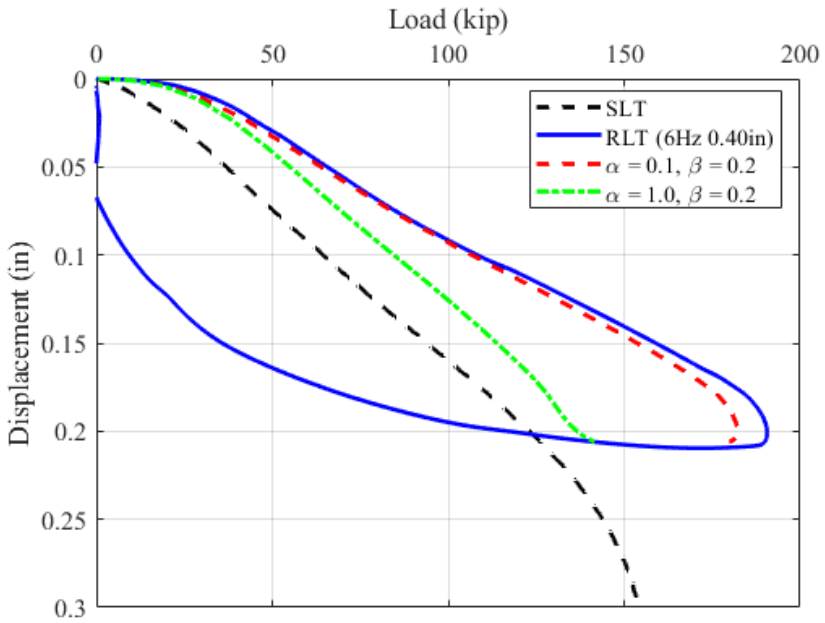

Figure 5.35: Estimated static load versus displacement response for the 6Hz 0.40in pulse using empirical damping constants for sand and clay from Randolph and Deeks (1992)

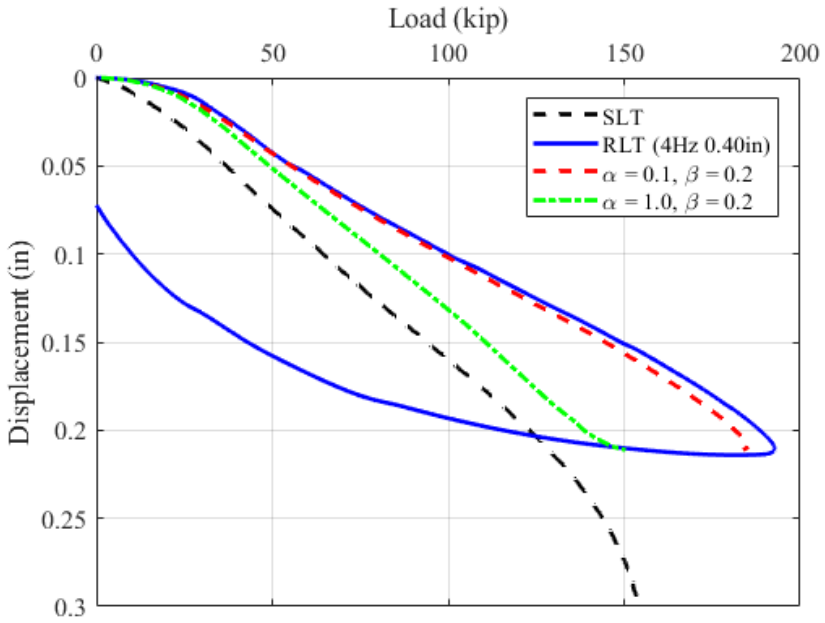

Figure 5.36: Estimated static load versus displacement response for the 4Hz 0.40in pulse using empirical damping constants for sand and clay from Randolph and Deeks (1992)

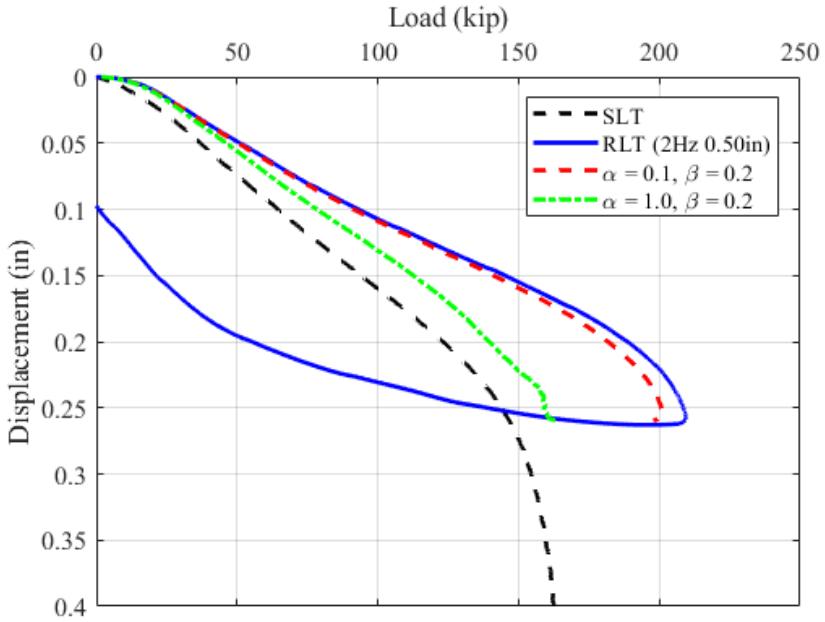

Figure 5.37: Estimated static load versus displacement response for the 2Hz 0.50in pulse using empirical damping constants for sand and clay from Randolph and Deeks (1992)

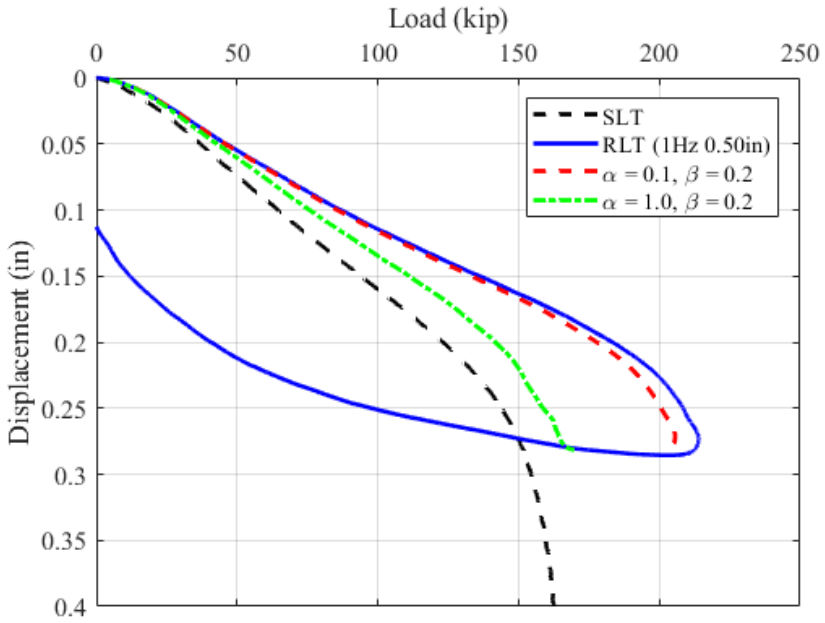

Figure 5.38: Estimated static load versus displacement response for the 1Hz 0.50in pulse using empirical damping constants for sand and clay from Randolph and Deeks (1992)

A second empirical approach from the literature bases the damping constant on the plasticity index for the soil, as indicated by Equation 2.29. The plasticity index calculated from the liquid and plastic limits reported by Sylvain (2019) for the test soil used in this dissertation produce an estimated damping parameter, α, within the range of 0.553 to 0.894. Figures 5.39, 5.40, 5.41, and 5.42 present the static displacement response for the 6Hz 0.40in, 4Hz 0.40in, 2Hz 0.50in, and 1Hz 0.50in pulses, respectively, using the upper and lower bounds of the damping parameter estimate for α with β fixed as 0.2. Similar to the other empirical approach, the results obtained from this method of estimating the damping constant, α, over predicted the static load versus displacement response measured in the SLT. This suggest that the approach of estimating the damping constants either from the literature on similar soil or from the empirical equation based on the plasticity index

may not be the best approach to estimating the rate dependent damping constants, as the static capacity may be over estimated. However, it should be noted that the predicted static response is only moderately over estimated and these rate dependent damping constants produced more accurate estimates of the static capacity than the empirical rate effect correction factors, η, sourced from the literature.

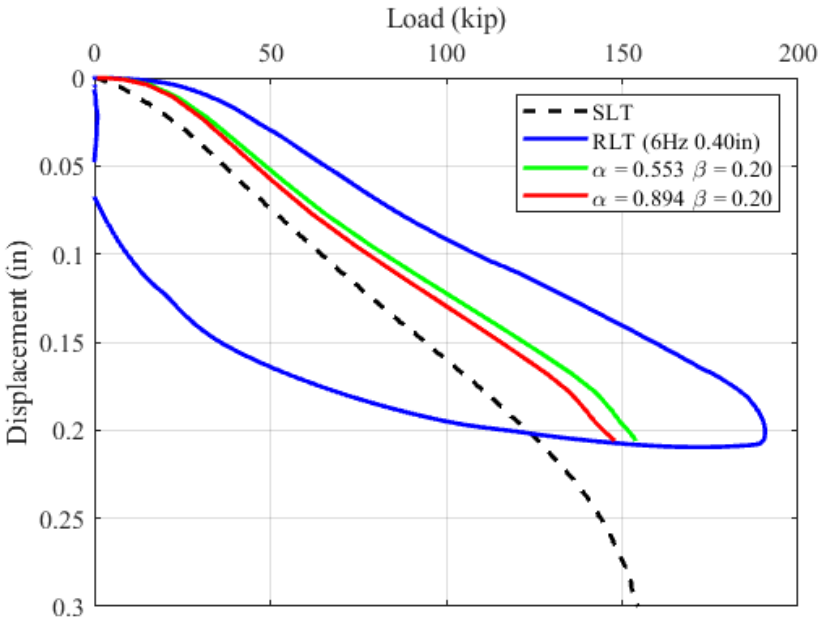

Figure 5.39: Estimated static load versus displacement response for the 6Hz 0.40in pulse using empirical damping constants based on plasticity index

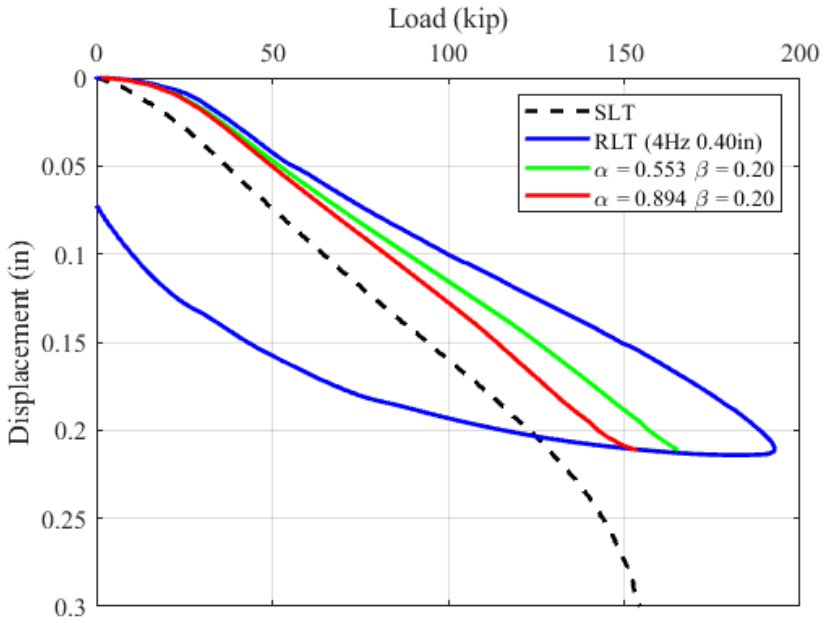

Figure 5.40: Estimated static load versus displacement response for the 4Hz 0.40in pulse using empirical damping constants based on plasticity index

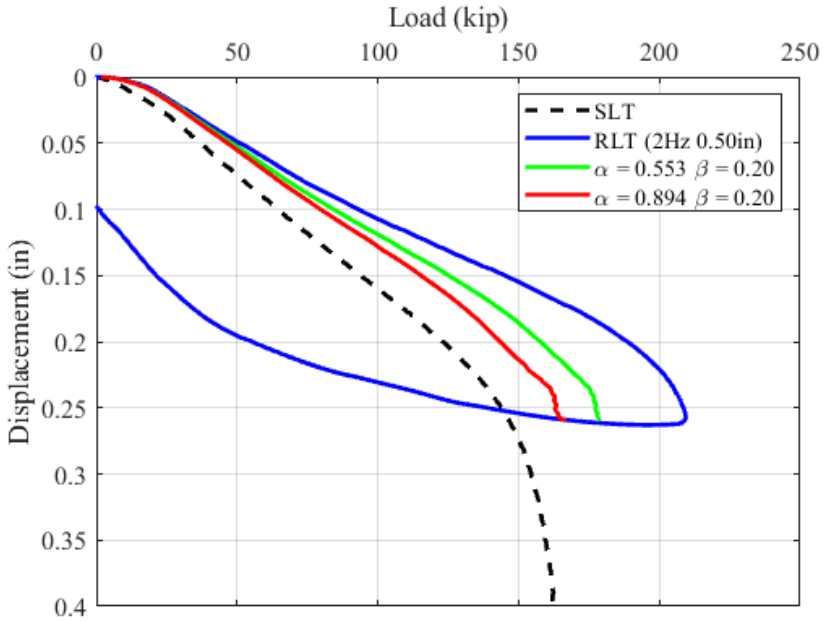

Figure 5.41: Estimated static load versus displacement response for the 2Hz 0.50in pulse using empirical damping constants based on plasticity index

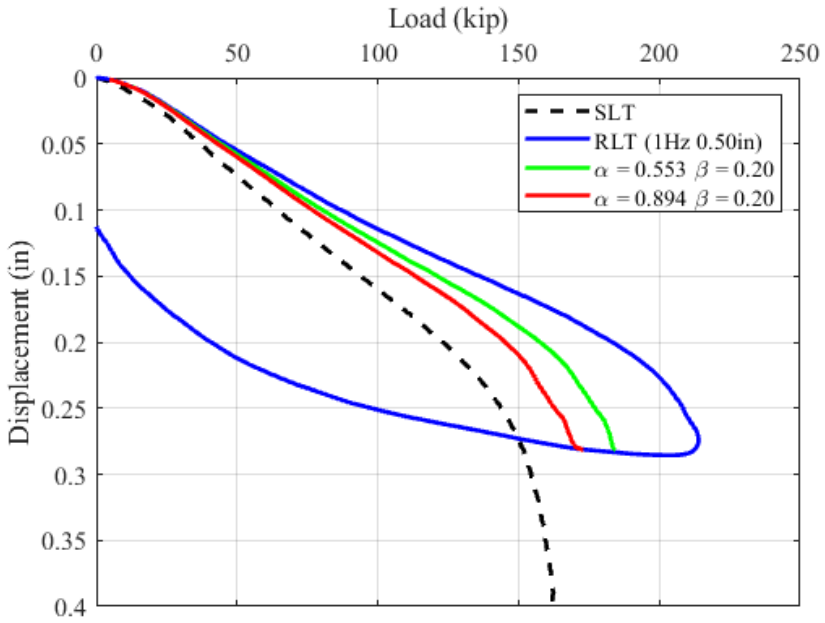

Figure 5.42: Estimated static load versus displacement response for the 1Hz 0.50in pulse using empirical damping constants based on plasticity index

In addition to using empirical rate dependent damping constants, the damping constants were determined using the available static load test data. Using Eq. 2.27 and the procedure described in Section 2.2.1.3 that includes the use of the SLT data to back calculate α at each measured time increment while holding the damping constant parameter, β, to 0.2, the damping constant parameter, α, was determined for each load pulse performed the RLT. Figure 5.43 presents damping constant parameter, α, values calculated for all of the pulses performed at 1Hz, 2Hz, 4Hz, and 6Hz pulse duration as a function of the displacement at the head of the pile. These plots indicate that the damping constant α is consistent with displacement across the different amplitude pulses for each pulse duration. Furthermore, the damping constant as a function of displacement is generally consistent across the different pulse duration. However, the average converged value damping constant value for

each load duration, represented by the dashed line, varies.

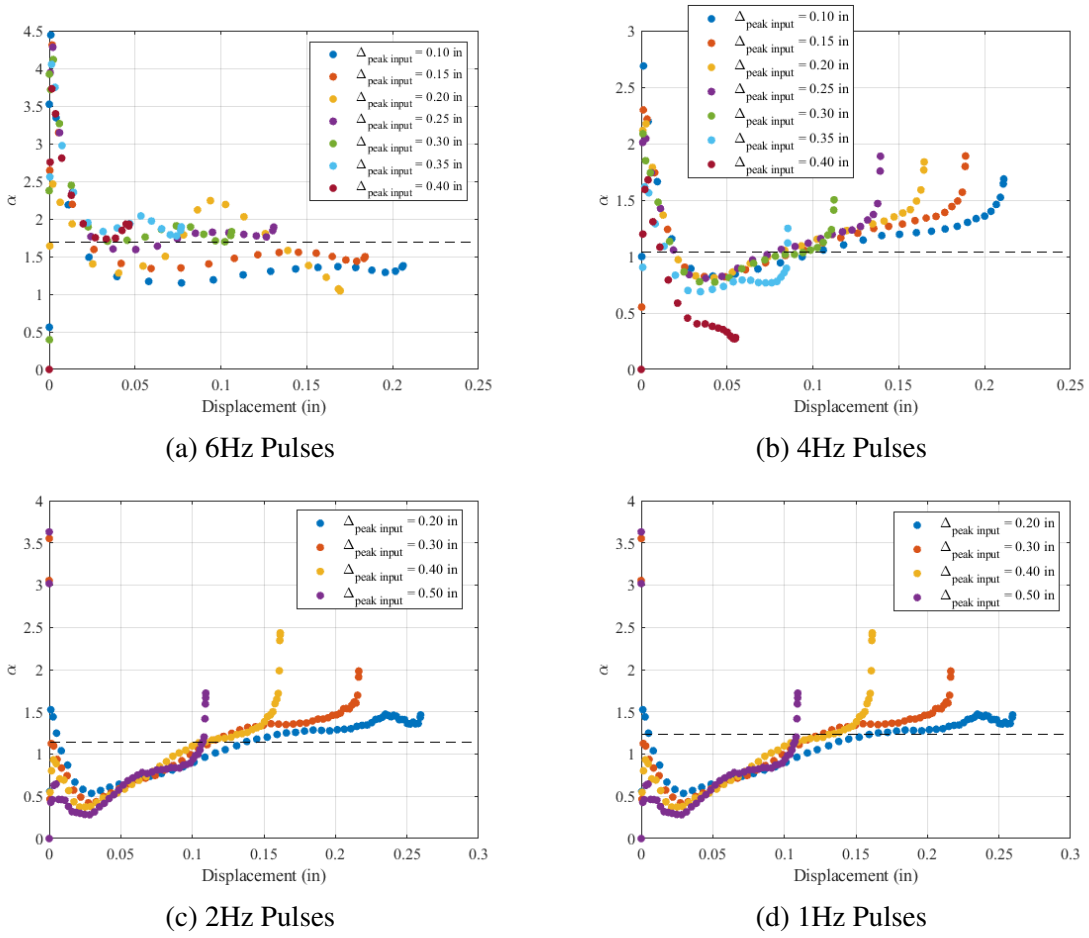

(a) 6Hz Pulses

(b) 4Hz Pulses

(c) 2Hz Pulses

(d) 1Hz Pulses

Figure 5.43: Calculated rate dependent damping constant, α, obtained using the SLT data in parallel with the RLT measurements

Similar to Balderas-Meca (2004), the damping constant determined for each pulse is compared to the maximum displacement and velocity of each respective pulse shown in Figure 5.44 and 5.45, respectively. This was calculated using the computed damping constants from Figure 5.43 and the measured peak displacement and velocity of each individual pulse. From this comparison of all applied loads, the damping constant α converges on the value of 1.34.

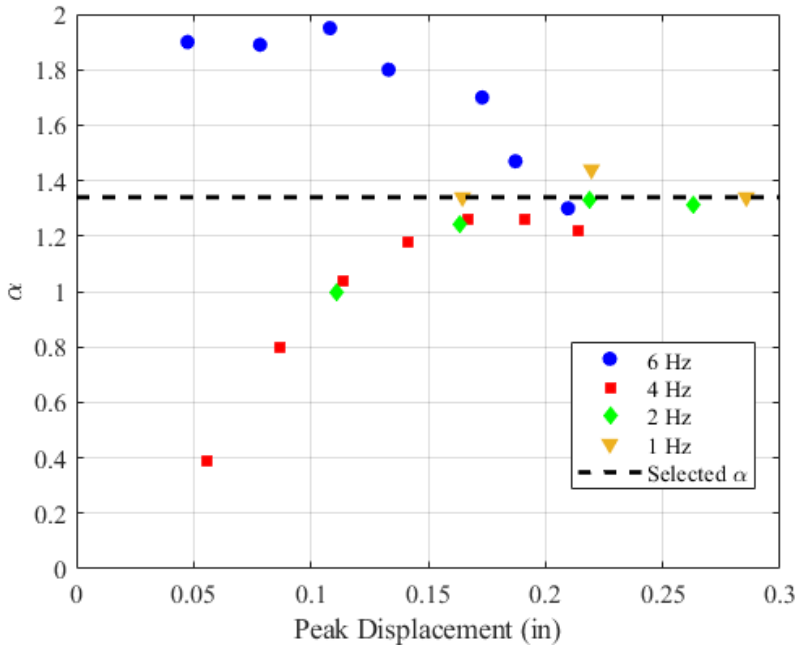

Figure 5.44: Estimated rate dependent damping constant, α, as a function of peak measured displacement for the RLT pulses

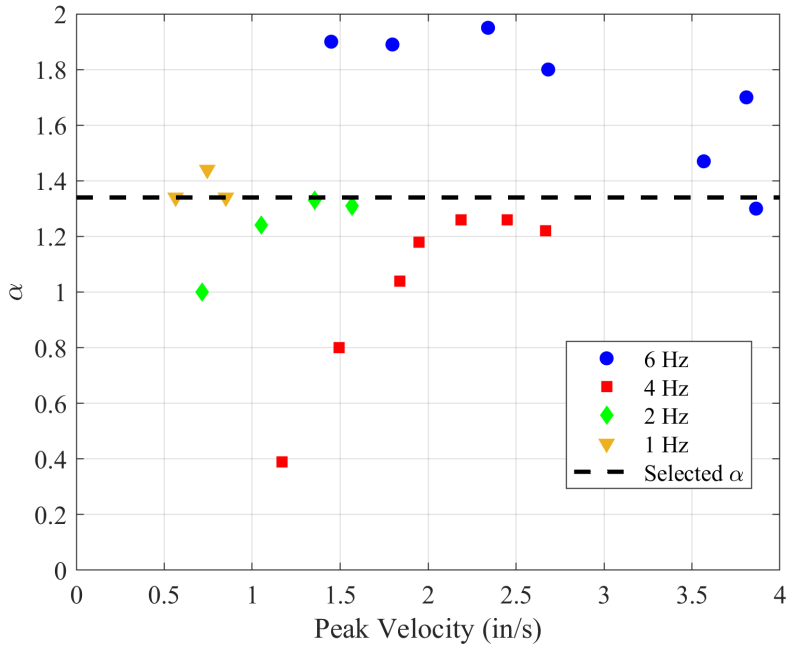

Figure 5.45: Estimated rate dependent damping constant, α, as a function of peak measured velocity for the RLT pulses

It was also observed that the damping constant parameter, α, values were initially higher with the 6Hz pulses when compared to other pulses with different specified duration (Figure 5.44). One explanation of this observation could be that the 6Hz pulses were the first set of loads applied to the pile system after inundating the soil around the sheet piles. Thus, there is a possibility of initial changes in the soil damping due to effects of the change in the water content, the permeability of the soil, or settlement of the soil after the first set of applied loads. Additionally, as previously noted in Chapter 4, there was pause in testing between the 6Hz pulses and the remaining pulses (Figure 4.14). Despite the difference in trend at measured low peak displacements, the damping constants estimated for the 6Hz pulse tests still converge to the same value as the other load duration tests at the largest peak displacements. Comparing Figure 5.45 to Figure 5.44 suggest that the rate parameter, α, is most likely a function of peak displacement rather than peak velocity.

While using Equation 2.27 with the damping constant parameters, α and β, established as 1.34 and 0.2, respectively, the static load versus displacement was estimated for each pulse. The estimated static response obtained using these rate dependent damping constants for the largest displacement pulse of the 6Hz, 4Hz, 2Hz and 1Hz duration tests are presented in Figures 5.46, 5.47, 5.48, 5.49, respectively. The estimated static load versus displacement response from this work compares more favorably with the static load versus displacement response obtained from SLT than the estimates obtained with the empirical damping constants. However, it must be stated that this conclusion was expected since the damping constant was obtained using the SLT data. The rate dependent damping constant of $\alpha = 1.34$ is only moderately higher than empirical values and within the range of plausible values based on the set sourced from the literature (Table 2.1).

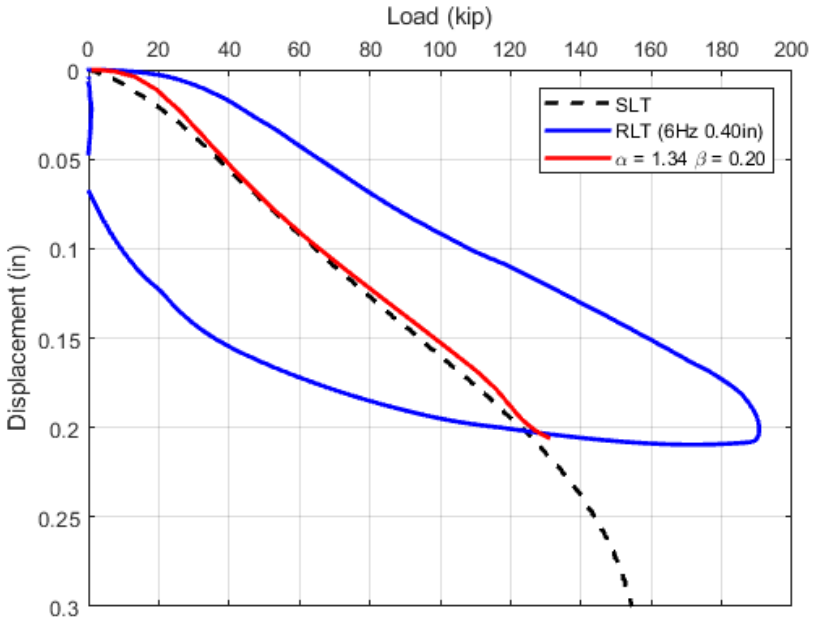

Figure 5.46: Estimated static load versus displacement response for the 6Hz 0.40in pulse using damping constants computed using the SLT

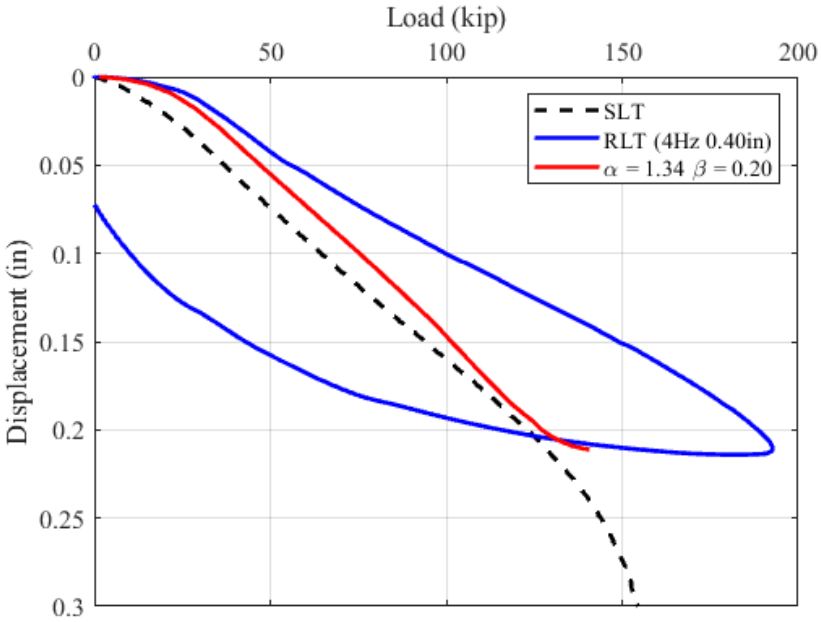

Figure 5.47: Estimated static load versus displacement response for the 4Hz 0.40in pulse using damping constants computed using the SLT

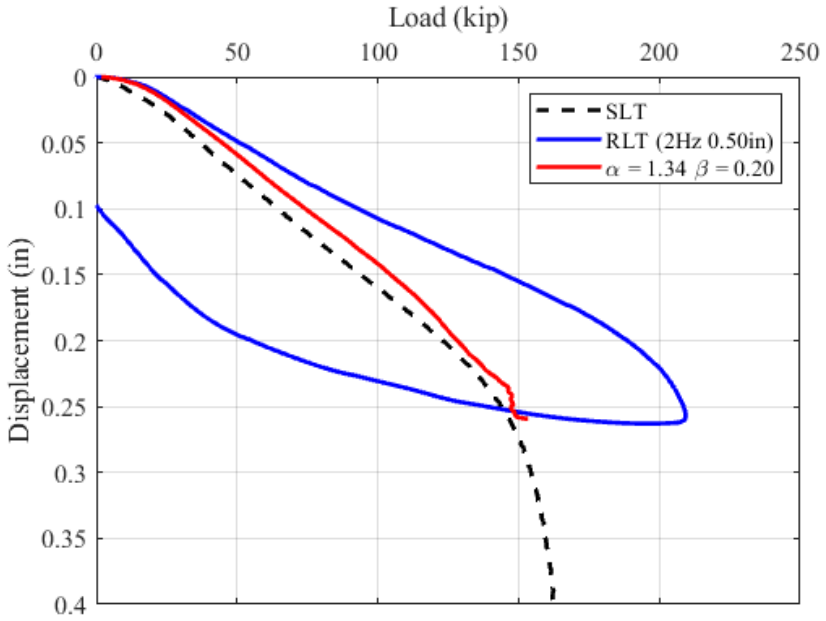

Figure 5.48: Estimated static load versus displacement response for the 2Hz 0.50in pulse using damping constants computed using the SLT

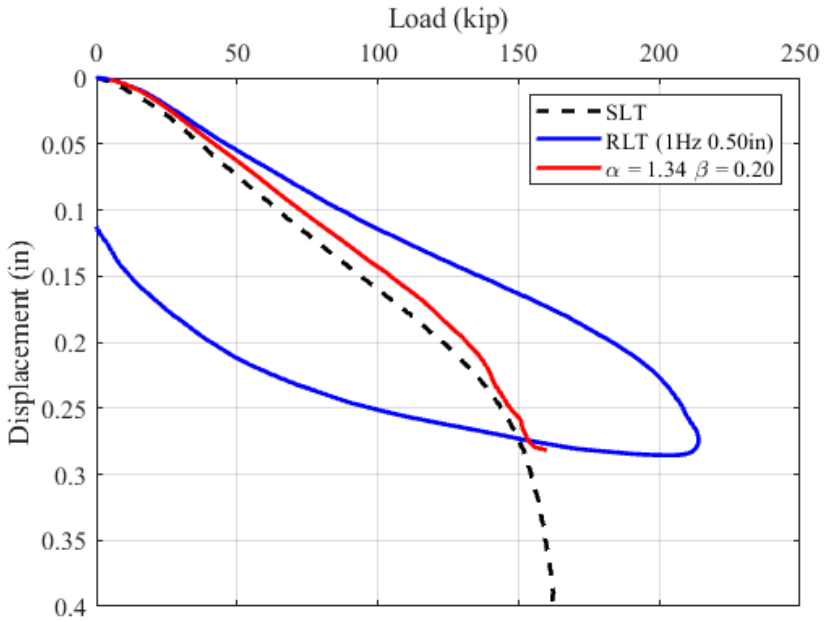

Figure 5.49: Estimated static load versus displacement response for the 1Hz 0.50in pulse using damping constants computed using the SLT

CHAPTER 6: ANALYSIS AND RESULTS OF DYNAMIC TESTS

The experimental program for the dynamic load test procedure concluded with nine blows for the restrike test of the sheet pile and four blows for the restrike test of the H-pile, as described in Chapter 4.2. In this chapter, an analysis of total axial capacity developed during each blow on the sheet pile and H-pile is first performed using the relatively simple Case method. Using the capacity estimate from the static load test, appropriate Case damping constants are determined for each blow and the variation in these damping constants with successive blows is investigated. An analytical model is then developed for each pile using the method of characteristics, which is then subsequently used in a signal matching routine to identify 14 unknown soil parameters that consist of soil quake, ultimate resistance, unloading stiffnesses and resistances, damping constants, and toe soil gap. Two match quality functions for quantifying the model correlation in the signal matching process are investigated and the performance of each is evaluated through comparison to capacity and load transfer measurements acquired during the static load test. Lastly, variation in the identified parameters is analyzed to explore the uncertainty in the parameter estimates and possible trends that might develop during the application of successive blows to each pile.

6.1 Case Method

The theory on the Case method presented in Chapter 3.4 was used to estimate the total static capacity for the piles in the field site. Total dynamic resistance at the instance of maximum internal force measurement (typically denoted in pile driving analysis software as IFMX) is plotted for each of the blows applied to the sheet pile and the H-pile in Figure 6.1. While there is significant variation in the total dynamic resistance, it is important to note that the hammer energy also varied significantly across the blows. With the static axial capacity estimates obtained from the respective SLTs, the Case damping coefficient that would be needed to adjust the total dynamic resistance for each blow to the measured static axial capacity was calculated. Figure 6.2 presents these back-calculated Case damping coefficients associated with Case method capacity estimation at the instance of maximum internal force measurement. The results indicate that both the sheet pile and H-pile exhibit similar magnitudes for Case damping coefficients that trend toward a reduction in damping as the number of blows increases.

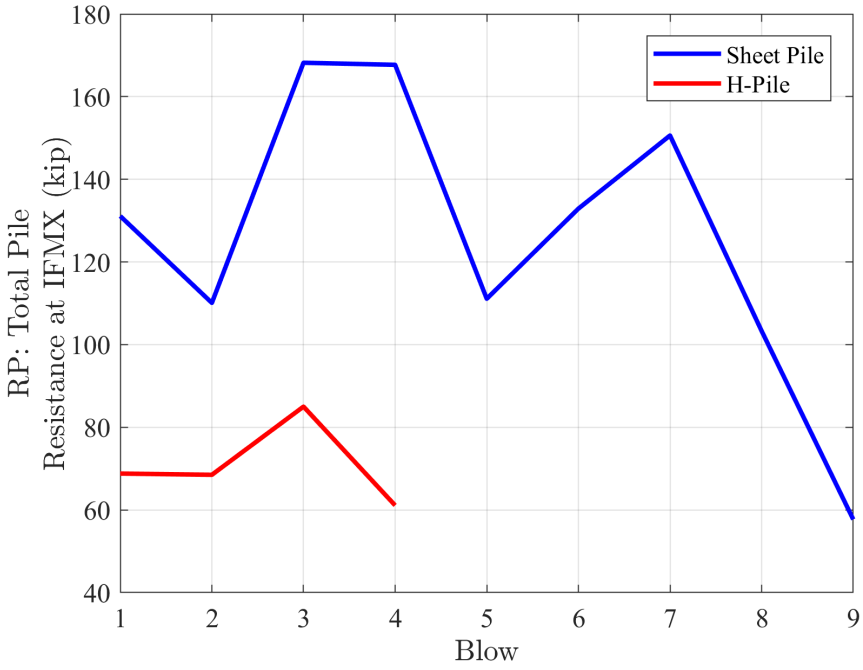

Figure 6.1: Case method total dynamic resistance at the instance of maximum internal force for sheet pile and H-pile

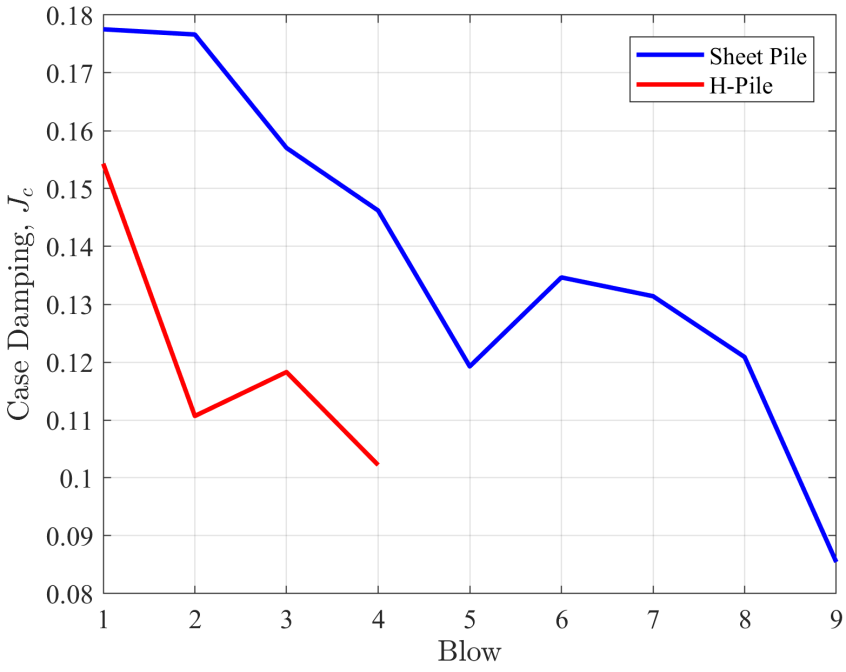

Figure 6.2: Case damping coefficient back calculated at the instance of maximum internal force for sheet pile and H-pile

As an alternative to computing the static resistance at the instance of maximum internal force measurement, the Case method can be applied at the instance in time where the static resistance, associated with a particular Case damping coefficient, is found to be maximum. The RX7 static capacity estimate, which is associated with a Case damping coefficient of 0.7 is typically used if no site-specific damping coefficient has been developed. Figure 6.3 presents the RX7 static capacity estimates obtained from applying the Case method and finding the instance in time where the static resistance is maximized. The results indicate that the RX7 static capacity estimate varies significantly across the blows and is a poor estimator of the actual capacity for the sheet pile. For the H-pile, the RX7 estimates were all zero, which suggests that a Case damping coefficient of 0.7 is too high of a value to use with the H-pile. An iterative optimization was performed to try to identify optimal Case damping coefficients to use while computing the static resistance with the time-shift approach that attempts to locate the instance in time where the static resistance is maximized, rather than the instance of maximum internal force measurement. The results are shown in Table 6.1. In several cases, no damping coefficient could be determined that would result in a calculation leading to the static axial capacity measured in the static load test. In these cases, the Case damping coefficient is denoted with a N/A. For the cases where a damping coefficient was successfully identified, the values vary significantly across the sheet pile blows, while they are more consistent for the H-pile.

Table 6.1: Identified optimal Case damping coefficients for the Case method at the instance of maximum static resistance

Blow ID	Optimal Case Damping, J_c
Sheet pile Blow #1	0.391
Sheet pile Blow #2	0.507
Sheet pile Blow #3	N/A
Sheet pile Blow #4	1.852
Sheet pile Blow #5	N/A
Sheet pile Blow #6	0.991
Sheet pile Blow #7	N/A
Sheet pile Blow #8	0.378
Sheet pile Blow #9	0.815
H-pile Blow #1	0.154
H-pile Blow #2	0.215
H-pile Blow #3	N/A
H-pile Blow #4	0.147

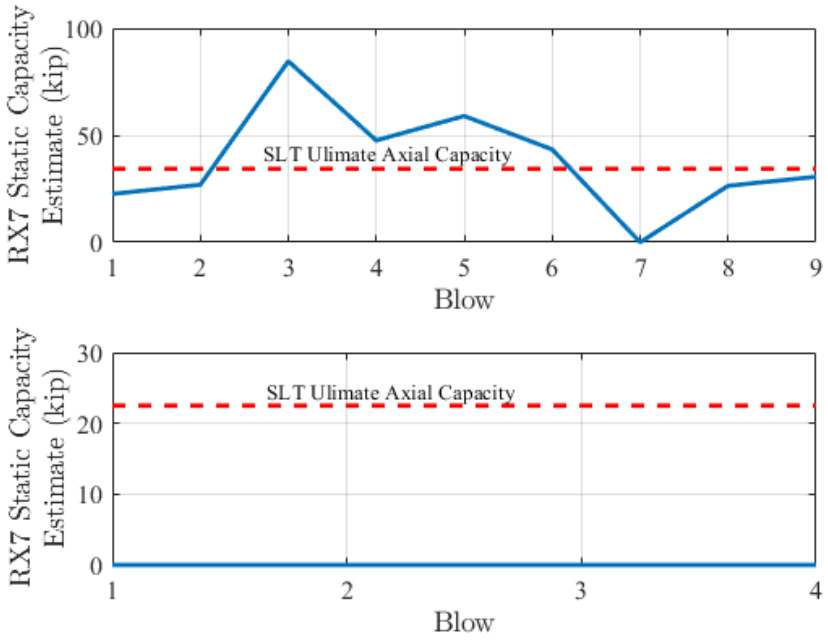

Figure 6.3: Case method analysis results for sheet pile

Ultimately, the Case method was found to be an unreliable estimator for the static capacity if the estimate was developed using the time-shifting technique. However, the Case

method did produce plausible results when the resistance calculations were performed at the instance when the internal force measurement was maximum. For such applications, the Case damping coefficients were approximately 0.18 for the sheet pile and 0.15 for the H-pile and decreased at a rate of approximately 0.01 per blow as the number of blows increased.

6.2 Pile Dynamic Analysis Signal Matching

6.2.1 Soil-Structure Interaction Model

As described in Chapter 4, both the sheet pile and H-pile were 20ft long and initially driven to 16ft below grade and, through the restrike test, driven an additional foot to a final embedment of 17ft below grade. The strain gage and accelerometer instrumentation was installed 18in below the head of the pile, shown in Figure 6.4a, which corresponds to 18.5ft above the toe of the pile. A numerical model was developed for the sheet pile and H-pile using the method of characteristics. The length of the pile included in each model was the 18.5ft below the instrumentation at the head of the pile. The remaining portion of the pile above the instrumentation at the head of the pile does not need to be included in the analysis model because the force of the downward traveling wave, obtained from the instrumentation, is used as an input to the model and this inherently includes all wave reflections and pile dynamics that occur above the instrumentation. The pile model was discretized into five equal length segments, each 44.4 inches long, and the respective cross sectional area for sheet pile and H-pile including the cover plate, found in Table 4.4, were used to establish the axial rigidity of each pile to convert measured strains to internal force measurements. The incremental time step is found using the calculated wave speed, c_L, for

each respective blow using Eq. 3.10. For all analyses, the longitudinal wave speed was set as 201,692.9in/s, following the guidance in the ASTM D4945 standard for dynamic testing of steel piles.

The soil-structure interaction for the pile is modeled as a series of nonlinear, inelastic springs defined by the parameters described in Section 3.2.2 and shown in Fig. 3.7. At each elevation, nonlinear dampers are placed in parallel with the nonlinear springs and the damping resistance is defined by Eq. 3.42 or 3.43, in which the side damping is defined by J_s and the toe damping is defined by J_t. The method of characteristics model, along with each respective parameter associated with each spring and dashpot, is shown in Figure 6.4b. It should be noted that side frictional resistance was not modeled in the last segment of the pile model because it was expected that uniqueness issues would arise in the determination of the nonlinear spring stiffness parameters if this segment included both side frictional resistance and toe bearing resistance that would simultaneously influence the same traveling wave forces.

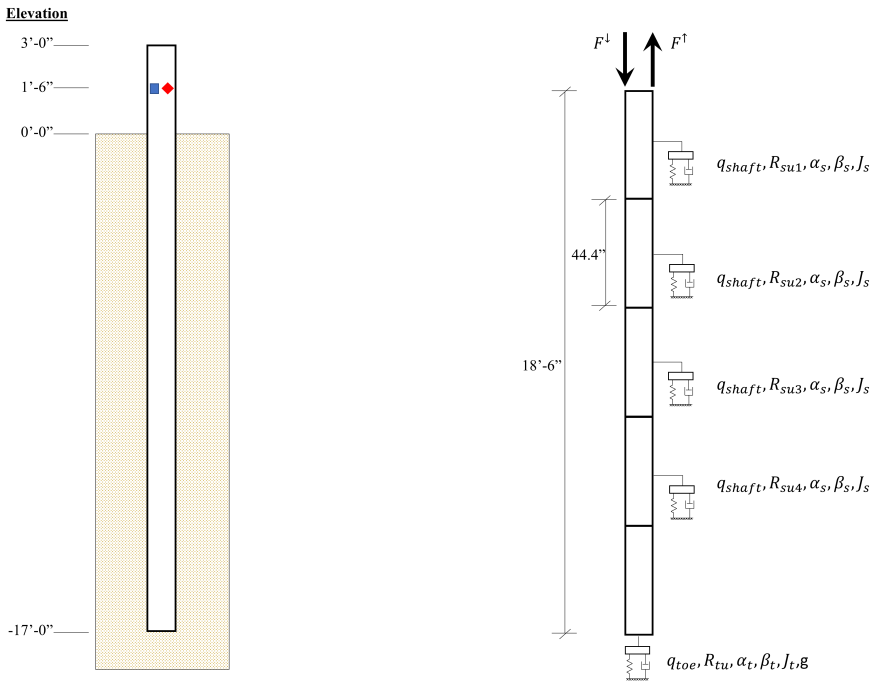

(a) Field condition schematic (b) Method of characteristic model

Figure 6.4: Representation of pile elevation and corresponding analytical model

6.2.2 Proposed Parameter Identification Routine

As stated in the literature (GRL Engineers Inc and Pile Dynamics Inc (2008, 2013)), the identification of uncertain parameters in the soil-structure interaction models is a challenging inverse problem due to the large number of unknowns and effects of measurement noise on the signal match, both of which contribute to a difficulty in determining the global minimum of the match quality function and ensuring uniqueness of the result. CAPWAP analysis requires the experience of an engineer to select and iterate on appropriate input parameters to determine the best match quality between measured and predicted signals. This can lead to incorrect or arbitrary parameter selections, especially if the engineer does not understand the relationships between each parameter. iCAP attempts to resolve this issue, but the literature suggests that some input is still required to arrive at suitable estimates for

the parameters in the soil-structure interaction models.

The development of an automatic signal matching technique allows for immediate results to be obtained during the pile testing or shortly thereafter (Likins et al. (2012)). The method of characteristics and standard soil-structure interaction models were adopted within the iCAP automatic signal matching procedure. This procedure takes the measured force and velocity data from the PDA and generates a pile-soil model with 6.56ft (2m) segments. The program assigns initial soil variables and begins searching for an appropriate shaft resistance distribution by comparing the computed capacity to the assumed capacity from the Case Method with a damping factor of 0.7 (RX7). Afterwards, the best toe resistance parameters are determined through similar processes. Finally, the ratio between shaft resistance and toe resistance is searched for and a determination is made on whether the ratio is acceptable. During this process, it is still implied that an outside source (i.e. an engineer) determines the acceptability of the results by limiting the capacity prior to the search. Many case studies were selected to compare the results of iCAP to that of standard CAPWAP results and it was determined that reasonable agreement occurs in more than 80% of the cases (Likins et al. (2012)). The iCAP procedure was designed for driven piles with uniform cross section, except for timber piles, and a corresponding traditional CAPWAP analysis was still recommended to support the plausibility of the iCAP result in practice.

To remove subjectivity while determining acceptable parameters for a given blow, the method presented in this dissertation attempts to remove the need for manual tuning or oversight beyond the selection of an initial plausible range for each parameter. This is facilitated by using a global optimization routine to automatically identify the set of parameter assignments within the bounded range that leads to the best model correlation with the

measured data. Specifically, a genetic algorithm is proposed for performing the minimization of match quality objective functions. First, a genetic algorithm generates a population of different parameter sets within the given upper and lower bounds and the signal match is evaluated to evaluate and rank the match quality for all of the individuals in the population. The genetic algorithm then retains a fixed portion of the best matches from this population, referred to as the elites, and generates a new population through processes of cross-over and mutation. Cross-over generates new possible solutions by randomly mixing features of the parameter sets from the prior population with the features of elites. This encourages a searching process that tends toward convergence on a minimum. The mutation process introduces new possible solutions by random changes in the parameter sets. This ensures that the optimization continues to look across the potentially large search space for better parameter sets before converging too soon on a local minimum rather than the global minimum (Konak et al. (2006)). After running this process repeatedly over generations of populations, the algorithm will converge on a set of assignments for the uncertain parameters in the model that it has determined will minimize the objective function. If a genetic algorithm is run long enough, then it will find the globally optimal solution, however there is no way of determining whether the algorithm has been run sufficiently long and, consequently, the parameter set identified by a genetic algorithm is associated with a global minimum or a local minima. Since the inverse problem of identifying the parameters in the soil-structure interaction models for a pile driving analysis is challenging and possibly non-unique, the approach taken in this dissertation was to run several instances of the genetic algorithm on the same data sets in order to study whether consistent estimates for individual parameter assignments were developed.

6.2.3 Verification of Method of Characteristics Routine

To facilitate the signal matching processes used in this dissertation, a routine was written in the Matlab computational environment to implement the method of characteristics for pile driving analysis. In order to verify correct implementation of the methodology, comparisons for predicted downward and upward traveling wave forces and particle velocities were made against results obtained from a simple 1-D finite element model developed in the commercial SAP2000 software package. The FEA model used for verification was built to simulate, but not exactly replicate, the pile used in the field testing program, thus the pile model was established as 20ft long and comprised of 21 equally spaced nodes and 20 beam elements with a cross sectional area of 27.57in^2, an elastic modulus, E, of 29000ksi and a material density of 490pcf. The corresponding model in the developed software routine for implementing the method of characteristics was assigned the same geometry and properties as FEA model. No system damping was introduced in either model. Three cases were used to validate the responses predicted by the developed method of characteristics software routine. In the first case, Case #1 (Figure 6.5a), the pile was modeled as friction-free with no toe resistance, which serves to verify the correctness of wave propagation through the pile itself. In the second case, Case #2 (Figure 6.5b), the pile was modeled as friction-free with a fixed restraint at the toe, which serves to verify the correctness of the wave propagation when the stress wave is affected by bearing resistance at the toe of the pile. In the final case, Case #3 (Figure 6.5c), the fixed restraint at the toe was retained and an elastic spring with a stiffness of 2000k/in was applied to the node 9ft below the head of the pile, which serves to verify the correctness of the wave propagation when the stress wave is affected by

side frictional resistance. It is noted that this spring was assigned a linear elastic stiffness to keep the verification process simplified in order to eliminate any numerical inaccuracies in the FEA analysis due to using a non-linear spring. For all cases, the load applied at the head of the pile was modeled as a half-sinusoidal pulse of 1.25ms duration and a 100kip amplitude (Figure 6.6).

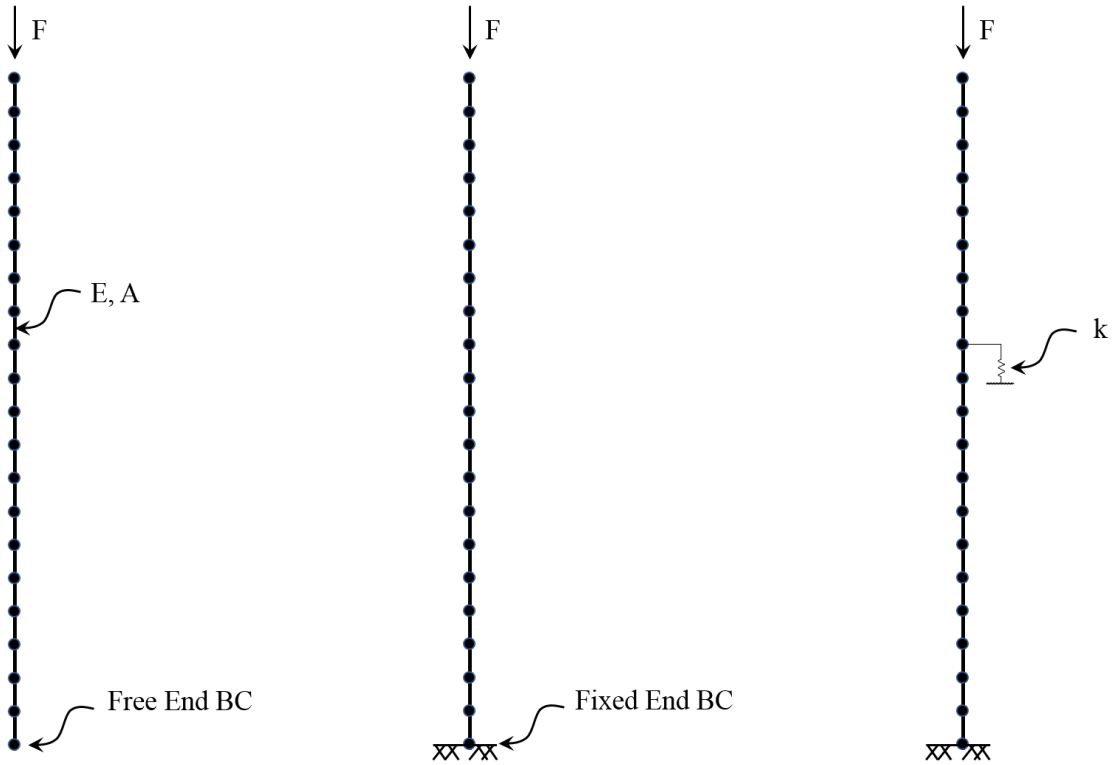

(a) Case #1 (b) Case #2 (c) Case #3

Figure 6.5: Schematic of FEA models used to verify the developed method of characteristics software routine

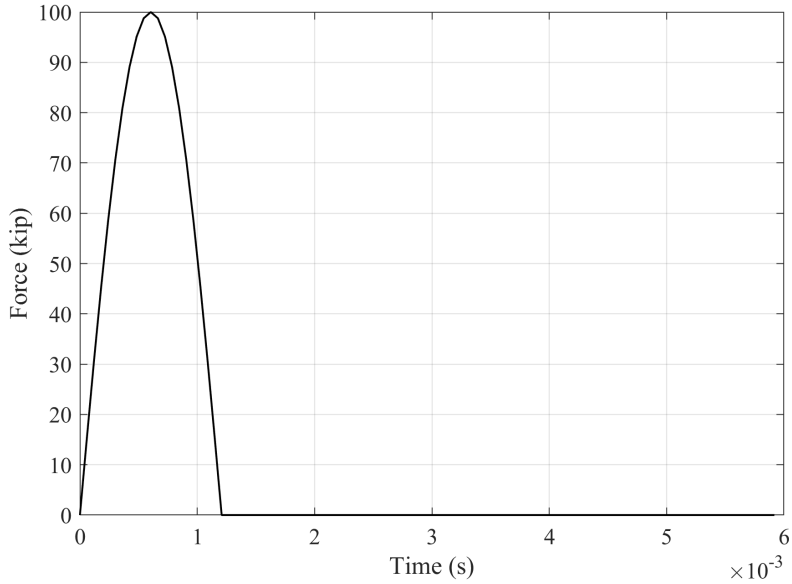

Figure 6.6: Load applied to the head of the pile in the models used for verification of the developed software routine

The forces in the downward and upward traveling waves, as predicted by the developed method of characteristics software routine and the commercial FEA software, for Case #1, Case #2, and Case #3 are shown in Figures 6.7, 6.8, and 6.9, respectively. The method of characteristics estimates for Case #1 and Case #2 were essentially exact matches to the solution from the commercial software and correspond exactly to the expectations from the wave propagation theory presented in Chapter 3. It is also important to note that the FEA model does show the start of instabilities that quickly dissipate at the end of each observed reflected wave, although these numerical instabilities are low enough in amplitude that they are not readily apparent in the provided figures. When adding the side frictional spring to the model in Case #3, it was observed that while the signals do generally agree and respond as the theory suggest, a degree of discrepancy between the FEA and method of characteristics solutions exists. This discrepancy continues to grow as the wave continues

to experience multiple reflections at the pile ends. For this case, the difference is attributed to differences in how the side friction is modeled in the method of characteristics model relative to the FEA. In the method of characteristics, the side friction occurs over the length of the segment, while in the FEA the side frictional resistance is represented by a spring that is positioned at a node, which corresponds to the end of an element.

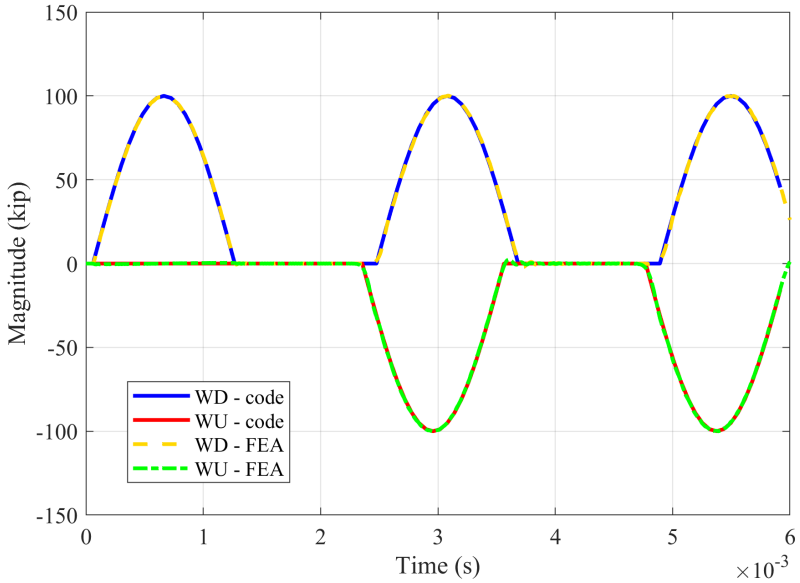

Figure 6.7: Forces in downward and upward traveling waves for Case #1 verification

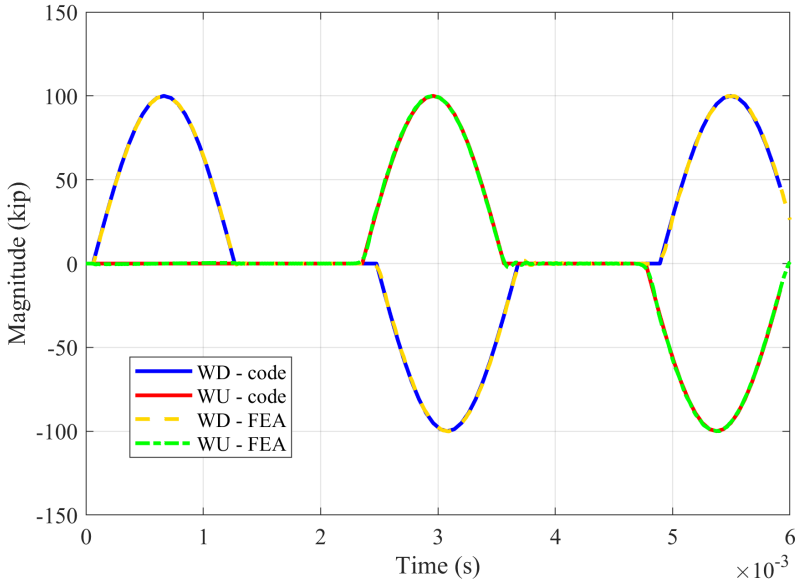

Figure 6.8: Forces in downward and upward traveling waves for Case #2 verification

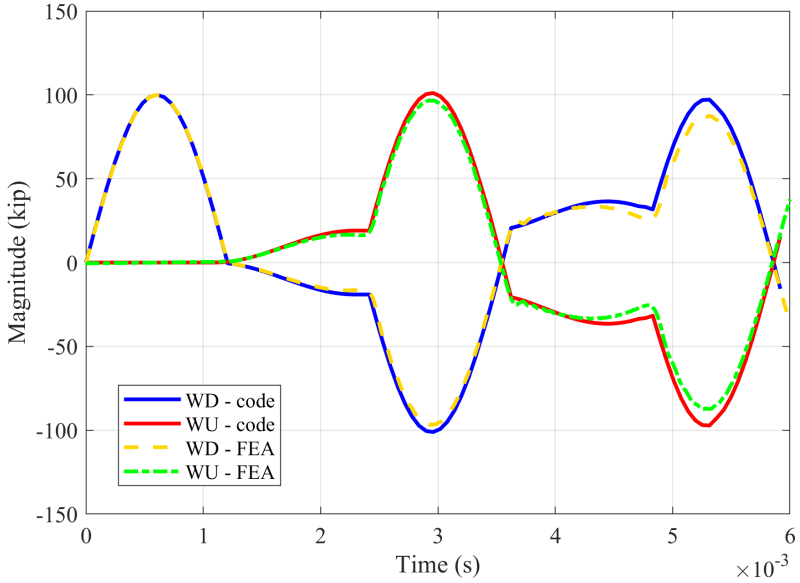

Figure 6.9: Forces in downward and upward traveling waves for Case #3 verification

6.3 Application to Field Measurements

6.3.1 Definition of Match Quality

The traditional definition of match quality, shown in Equation 6.1, was empirically developed as a tool to assist with manual signal matching by studying the the effects of parameters in soil-structure interaction models on the stress wave phenomena, as described in Chapter 3. The current definition of the zones, presented earlier in Figure 3.12, in which the quality of the signal match is determined, are based on the assumption that the pile stops, or slows down significantly after about 20-30 ms, or 4-8 L/c_L.

$$MQ_{trad} = \sum_{j=1}^{4zones} \sum_{i=1}^{\#points} \frac{|F^{\uparrow}_{j,i,measured} - F^{\uparrow}_{j,i,predicted}|}{max(F^{\uparrow}_{measured})} \tag{6.1}$$

When reviewing the dynamic measurements obtained from the field tests presented in this dissertation, the duration of loading was determined to be close to the threshold between rapid and dynamic response. The loading duration was short enough that stress wave phenomena are clearly apparent in the measurement, but the pile response was long enough in duration that the standard definition of zones used in the traditional MQ did not capture the peak displacement or unloading response of the piles. As a result, signal matching applied with a match quality definition developed with the conventionally used zones would not provide a plausible means of identifying the parameters in the soil-structure interaction models associated with unloading. To account for this, the boundaries of the zones used in the traditional MQ were redefined using the duration required to reached the peak displacement. The zones used in this dissertation are shown in Figures 6.10 and 6.11 for the force response and displacement response, respectively. In the redefinition of the zones,

the Zone 1 start time and duration are unchanged from the traditional definition, while the durations of the remaining zones are established based on the time from the end of Zone 1 to the instance at which the maximum displacement at the head of the pile is achieved, t_{umax}. Zone 3 is defined to start from the end of Zone 1 and have a duration equal to 90% of t_{umax}. Zone 2 is also defined to start from the end of Zone 1, but has a duration of 60% of the duration assigned to Zone 3. This ratio of the Zone 2 to Zone 3 durations was established to maintain consistency with the relative durations for Zone 2 and Zone 3 in the traditional definition of zones. Lastly, Zone 4 was redefined to start at the end of Zone 1 and extend for a fixed 50ms duration. For the piles tested in this dissertation, this duration is long enough to capture the peak displacement and an additional 10-15ms.

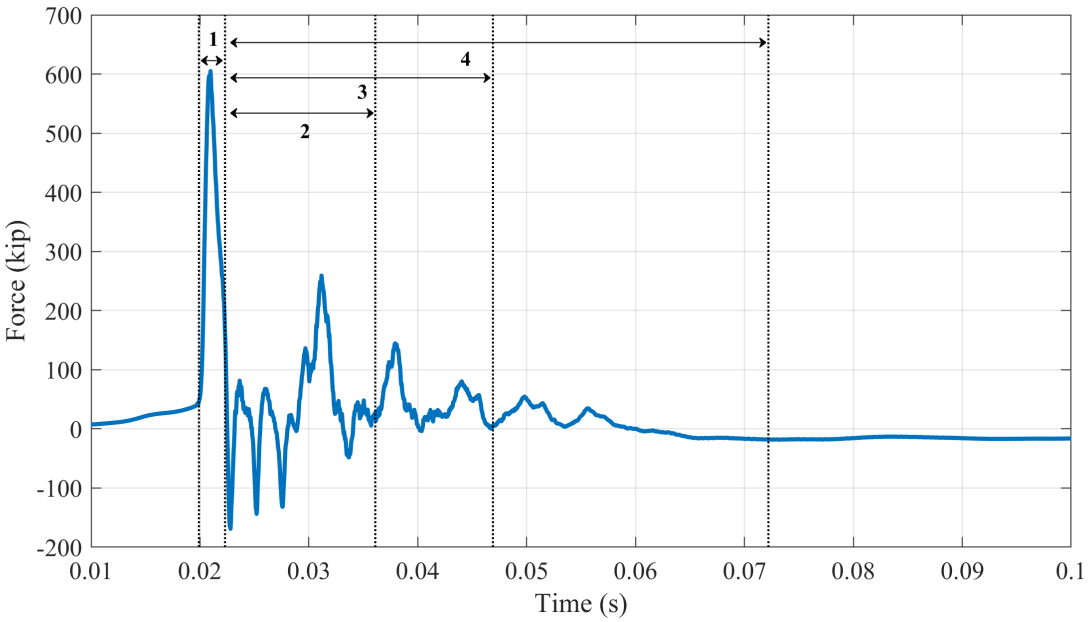

Figure 6.10: Modified definitions of match quality zones superimposed on typical force measurement signal

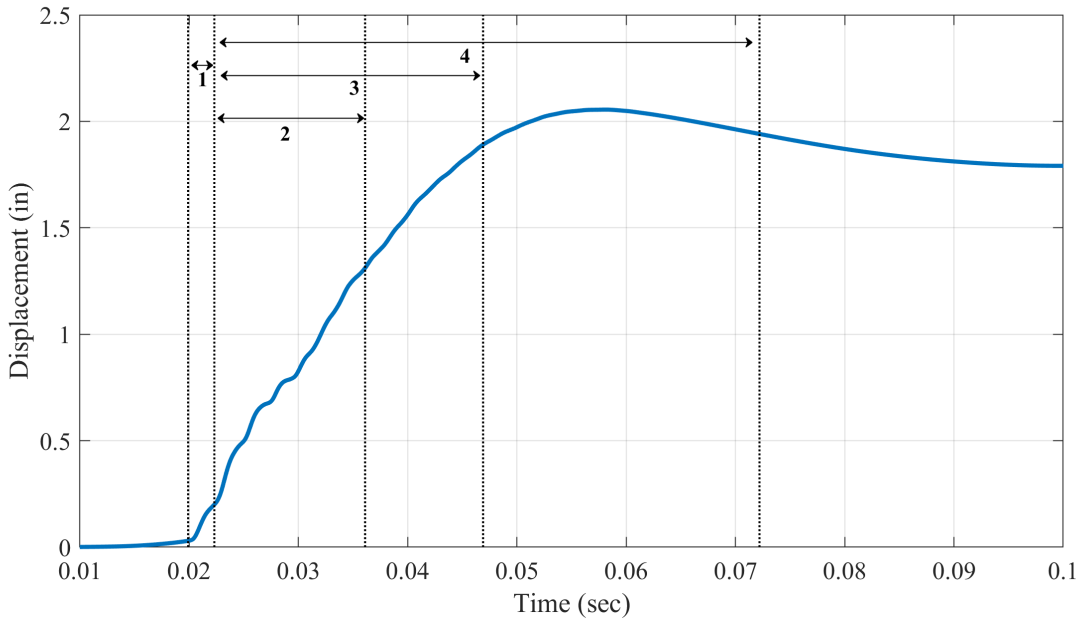

Figure 6.11: Modified definitions of match quality zones superimposed on typical pile head displacement

While the traditional match quality objective function is in widespread use for signal matching in pile driving analysis, it is clear that the definitions of the zones is subjective and the standard definition may not be suitable for all cases. The zones were originally developed to assist with manual calibration of parameters in the soil-structure interaction models, although no evidence was found in the literature to support extending these zones to a match quality for automated signal matching based on global optimization. The zone definitions can significantly affect the identified parameters because regions where zones overlap introduce weighting of the relative importance of the measurement data. For example, in the region immediately after Zone 1 where Zones 2, 3, and 4 overlap, the correlation between the predicted and measured upward traveling wave force is weighted as three times more important than any instance in time within Zone 1.

In this dissertation, a second match quality function was defined based on a simple resid-

ual sum of squares (RSS) between the measured force in the upward traveling wave and the force for the upward traveling wave predicted by the method of characteristics analysis, shown in Equation 6.2.

$$MQ_{RSS} = \sum_{i=1}^{\#points} \left(F^{\uparrow}_{j,i,measured} - F^{\uparrow}_{j,i,predicted} \right)^2 \tag{6.2}$$

Residual sum of squares objective functions are commonly used for parameter identification in inverse problems and the simple RSS match quality function investigated does not involve the use of any zones for additional weighting of the importance of select measurement data. Consequently, this second match quality function is less subjective than the traditional match quality function and could be applied to any pile without re-examining the suitability of the zone.

6.3.2 Application of Automated Signal Matching to Field Measurements

Parameter identification using the traditional MQ and RSS definitions was performed on each blow recorded during the restrike testing of the sheet pile and the H-pile. For each test, the force for the downward traveling wave, obtained from the measured force and velocity at the pile head, was used as an input to the previously described method of characteristics model and the solution for the force in the upward traveling wave was computed to facilitate calculation of the match qualities. The longitudinal wave speed, c_L, was set to 201,692.9in/s, per the ASTM D4945 standard for steel piles. Prior to the dynamic analysis, the data was resampled from 250,000Sps to 4,626.8Sps in order to establish a time increment for the data that would correspond to the exact time required for the downward and upward traveling wave to traverse the discretized length of each segment of the pile.

For the traditional MQ function, the modified zone definitions described in the previous subsection were used for both the sheet pile and the H-pile. A blow count penalty was not included in this traditional MQ function because double integration of the acceleration time histories exhibited low frequency drift and the string potentiometer measurement was deemed not sufficiently accurate for the purposes of signal matching since the potentiometer was oriented at an angle to the longitudinal axis of the pile (as shown in Figure 4.26). For the second match quality function developed using the RSS, a total of 91 data points, or 19.5ms of data, following the initial rise was used to establish the duration over which the match quality function was computed for of the sheet pile response, and 161 data points, or 34.8ms of data, was used used to establish the duration over which the match quality function was computed for the H-pile response. A longer duration was used for the H-pile response because the magnitude of the force of the downward traveling wave was significant for a longer period of time.

The signal matching process was performed using a genetic algorithm to optimize the unknown parameters in the soil-structure interaction model. This genetic algorithm used a population size of 10,000 individuals with an elite count of 500 individuals, a cross-over rate of 80%, and a mutation rate of 15%. The upper and lower bounds established for all unknown parameters are summarized in Table 6.2. The genetic algorithm ran over a fixed number of 50 generation, which corresponds to over a half a million simulations, to converge on an optimal set of assigned values for the unknown parameters. For each blow, this same genetic algorithm was performed five times to examine if a unique solution could be determined for this challenging global optimization problem involving an extensive number of unknown parameters. If a unique solution was not found, the goal was to examine

Table 6.2: Parameter bounds used in the signal matching routine for analysis of the field tests

Parameter	Symbol	Unit	Lower Bound	Upper Bound
Shaft Quake	q_{shaft}	in	0.02	0.30
Toe Quake	q_{shaft}	in	0.02	0.30
Ultimate Resistance, Shaft Spring 1	$R_{u,1}$	kip	0.1	50
Ultimate Resistance, Shaft Spring 2	$R_{u,2}$	kip	0.1	50
Ultimate Resistance, Shaft Spring 3	$R_{u,3}$	kip	0.1	50
Ultimate Resistance, Shaft Spring 4	$R_{u,4}$	kip	0.1	50
Ultimate Resistance, Toe Spring	$R_{u,toe}$	kip	0.3	20
Shaft Unloading Stiffness	$\alpha_s = \frac{E_{un,i}}{E_{u,i}}$	–	0.3	3.3
Toe Unloading Stiffness	$\alpha_t = \frac{E_{un,toe}}{E_{u,toe}}$	–	0.3	3.3
Shaft Unloading Resistance	$\beta_s = -\frac{R_{un,i}}{R_{u,i}}$	–	0.0	1.0
Toe Unloading Resistance	$\beta_t = -\frac{R_{un,toe}}{R_{u,toe}}$	–	0.0	1.0
Shaft Damping	J_{shaft}	$\frac{s}{in}$	0.001	0.036
Toe Damping	J_{toe}	$\frac{s}{in}$	0.001	0.036
Toe Gap	g_{toe}	in	0.0	0.03

the variability of the parameters in the different solutions that were generated.

To assess the performance of the two match quality definitions, the set of identified parameters across five signal matching analyses over all blows were averaged for the sheet pile and the H-pile. The assumption used was that, if either match quality function performed suitably, then average parameter estimates obtained across this relatively large number of analyses would produce estimates for static capacity and load transfer that would correlate well with that measured directly in the static load test.

After performing the automatic signal matching analysis five times on the dynamic measurements for each blow on the sheet pile and H-pile, the identified parameters for all blows and optimization runs were averaged. These averages for the identified parameters are presented in Table 6.3. The results indicate that, on average, the automated signal matching generated consistent estimates for certain parameters in the soil-structure interaction mod-

els, while significant differences were generated for other identified parameters when the match quality function was changed. For example, the traditional MQ and RSS functions developed different estimates for the distribution of shaft resistance, with the RSS function suggesting that the majority of the side frictional resistance was mobilized in the first layer for both the sheet pile and the H-pile. However, despite these differences in the estimated distribution of side frictional resistance, the traditional MQ and RSS functions produce similar estimates for the total shaft resistance, toe resistance, and total resistance mobilized for sheet pile as well as the H-pile, with the RSS function producing only slightly higher capacity estimates for both piles. Likewise, while the traditional MQ and RSS definitions typically produced different parameter estimates for the quakes, toe gap, and unloading parameters, the estimates for the damping constant for the shaft and toe were generally consistent across both pile types for both match quality functions.

A representative signal match obtained for the upward traveling wave in the sheet pile using the average parameter sets obtained using the traditional and RSS match quality definitions for the sheet pile and H-pile is provided in Figure 6.12. While both signal matches generally fit the measured upward traveling wave force, the match developed with the RSS match quality definition estimates the initial response better than the traditional MQ definition for both the sheet pile and H-pile. This initial region of the upward traveling wave response is considered important for the identification of key parameters in the soil-structure interaction models, including the ultimate resistance of the shaft and toe springs. After this initial region, other parameters, such as shaft and toe damping constants and unloading parameters become important to the quality of the signal match.

Table 6.3: Average of identified soil-structure interaction parameters across all blows (note: values in italics are summations and not independent parameter estimates)

Parameter	Sheet Pile Trad. MQ	Sheet Pile RSS	H-Pile Trad. MQ	H-Pile RSS
R_{u_1}	2.50	12.55	0.13	7.10
$R_{u,2}$	7.70	7.38	0.21	0.34
$R_{u,3}$	6.82	0.51	4.28	0.69
$R_{u,4}$	3.96	2.76	4.76	4.42
$R_{u,shaft}$	*20.98*	*23.19*	*9.38*	*12.55*
$R_{u,toe}$	9.71	10.41	4.60	3.26
$R_{u,total}$	*28.89*	*33.60*	*13.98*	*15.81*
q_{shaft}	0.037	0.032	0.063	0.044
q_{toe}	0.070	0.026	0.055	0.031
$\alpha_s = \frac{E_{un}}{E_u}$	1.38	1.94	0.86	2.01
$\alpha_t = \frac{E_{un}}{E_u}$	2.31	2.40	0.72	2.11
$\beta_s = -\frac{R_{un}}{R_u}$	0.12	0.47	0.60	0.49
$\beta_t = -\frac{R_{un}}{R_u}$	0.49	0.56	0.52	0.57
J_{shaft}	0.018	0.009	0.016	0.019
J_{toe}	0.027	0.026	0.023	0.027
g_{toe}	0.051	0.015	0.016	0.019

6.3.3 Comparison of Capacity and Load Transfer Estimates to Static Load Test

As previously detailed in Chapter 4, static load tests revealed the total static capacity of the sheet pile and the H-pile, by Davisson's criteria, to be 34.3kip and 22.5kip, respectively. The average total static capacity estimates obtained across all blows and optimization runs using the traditional MQ function were 28.9kip and 14.0kip, respectively. These estimates under-predict the measured static capacity by 15.7% and 37.8%, respectively. Likewise, the average total static capacity estimates obtained across all blows and optimization runs using the RSS function were 33.6kip and 15.8kip, respectively. These estimates under-predict the measured static capacity by 2.0% and 29.8%, respectively. The reason for the greater under-prediction of capacity for the H-pile is not apparent. However, as will be shown in a future subsection, the identified resistance parameters were found to exhibit a

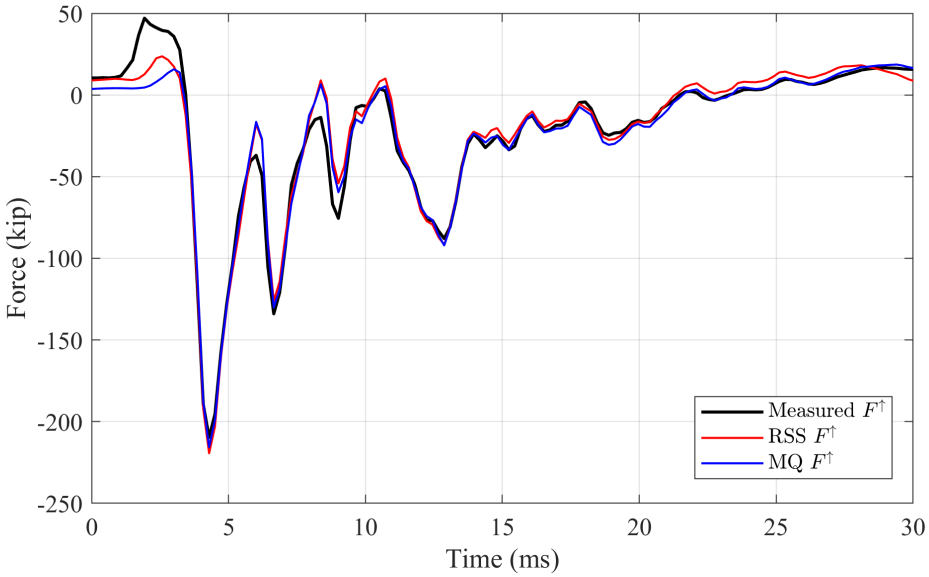

(a) Sheet Pile

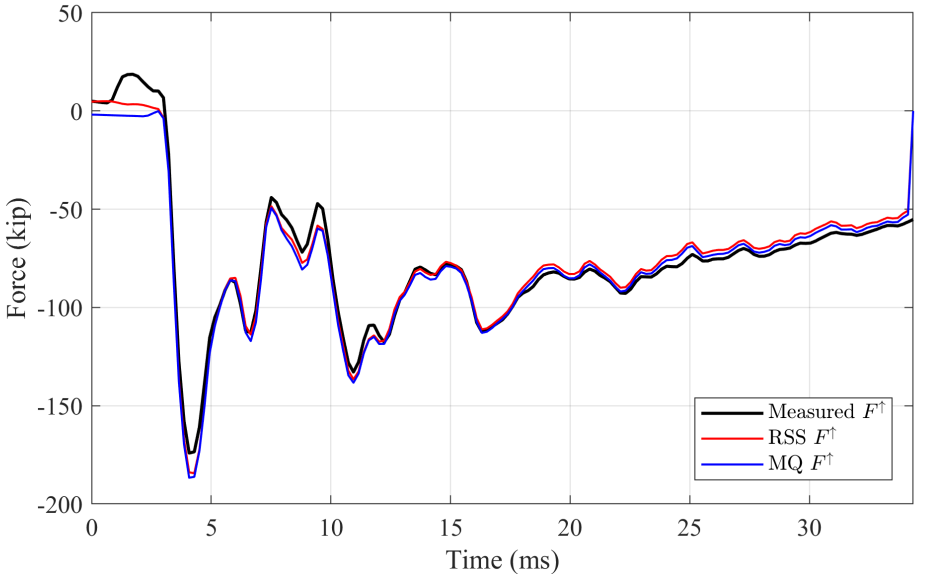

(b) H-pile

Figure 6.12: Representative signal match for the upward traveling wave from one blow

trend toward lower capacity as successive blows were applied to the piles, so the average capacity estimate across all blows during the restrike testing may not serve as the best estimate for the static capacity of each pile.

In order to assess the plausibility of the identified soil resistance along the length of the

pile for each match quality definition, the force distribution using the identified resistance parameters of the traditional and RSS match quality definitions for sheet pile and H-pile are compared to the measured force distribution during the SLT of the sheet pile. The load transfer estimates obtained from the traditional match quality definition are shown in Figure 6.13a while the load transfer estimates for the RSS match quality definition are shown in Figure 6.13b. The load transfer from the SLT is plotted to the depth of the strain gage closest to the toe of the pile, while the load transfer estimates from the signal matches are plotted to the bottom of the fourth pile segment, which is the last segment featuring a nonlinear side frictional resistance model. While the profile of the load transfer for the sheet pile developed from the identified parameters obtained using the traditional match quality definition generally aligns better with the load transfer curves from the SLT the total capacity estimate is under-estimated and the significant resistance in the upper layers of the gravel and medium stiff clay are not reflected in the load transfer obtained from the signal matching with the traditional MQ function.The profile of the load transfer for the sheet pile developed from the identified parameters obtained using the RSS match quality definition appears to better reflect the total capacity and resistance in the upper soil layers, although the overall shape of the load transfer does appear to match the load transfer obtained from the SLT as well. Although load transfer measurements from the SLT are not available for the H-pile due to damage to strain gage wiring during the pile installation, it should be expected that the load transfer for the H-pile would be similar to that of the sheet pile since the two piles were driven in nearly identical site conditions. For both the traditional MQ and RSS functions, the average load transfer obtained for the H-pile is very similar in profile to the average load transfer obtained for the sheet pile. This consistency in the

load transfer estimates between the two pile types further supports the plausibility of the identified resistance parameters obtained from the signal matching.

Using the identified shaft quake and resistance parameters, side friction resistance responses, presented as t-z curves for each segment of the analytical model were developed and are compared to those calculated from the SLT. First, the average side friction response identified through the traditional MQ and RSS definitions for the sheet piles are shown in Figures 6.14 and 6.15, respectively. Since the layers developed by the instrumentation for

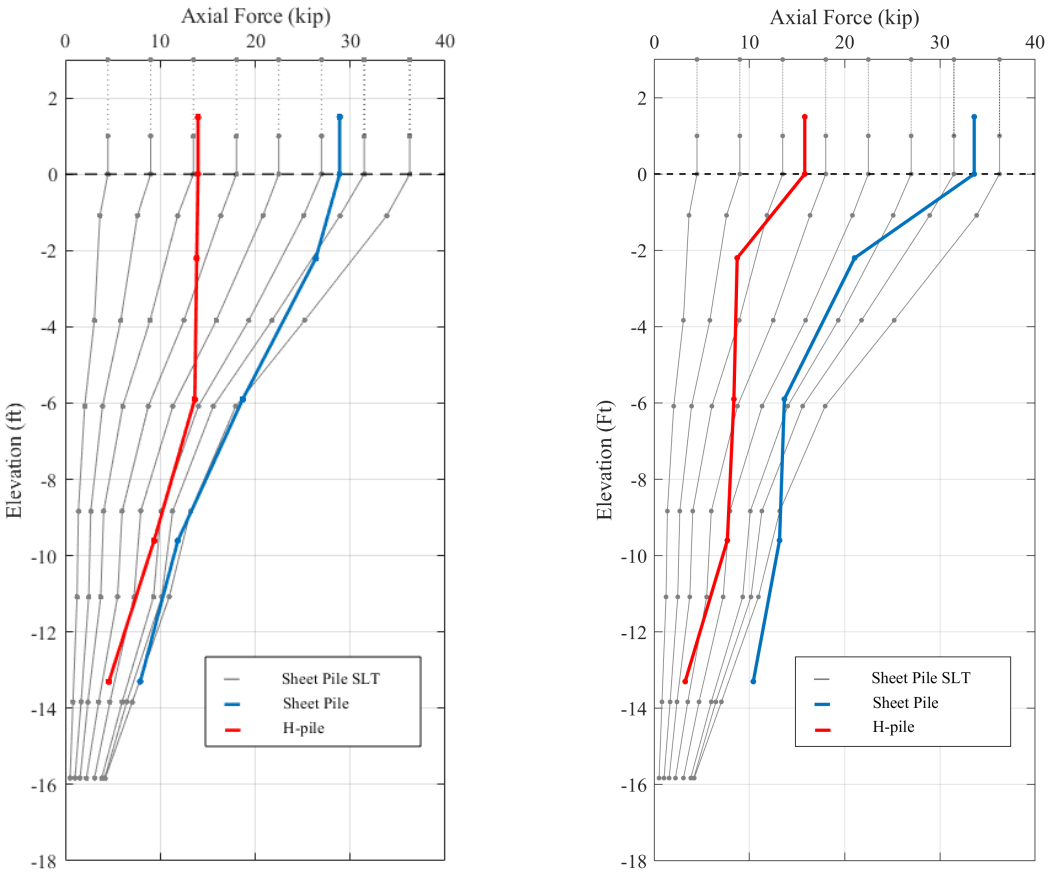

(a) Traditional match quality definition

(b) RSS match quality definition

Figure 6.13: Predicted load transfer in the sheet pile and H-pile from the average parameter estimates obtained from signal matching

the SLT do not correspond with the segment lengths of the method of characteristics model, direct comparisons between individual t-z curves obtained from the static load tests and t-z curves developed from the signal matching is not possible. However, it can be concluded that both the traditional MQ and RSS functions developed t-z curves that have plausible magnitudes since the ultimate resistances are in a similar range to those obtained from the SLT. While the magnitudes of the average t-z curves produced with the traditional MQ function are more similar in magnitude with those obtained from the SLT, the signal matching with the traditional MQ function does under-predict the significant resistance mobilized in the shallowest layer of soil. Conversely, while the signal matching with the RSS function more closely predicts the side frictional resistance mobilized in the shallowest layer of soil, the side frictional resistance in the deeper layers are under-predicted. For both the traditional MQ and RSS functions, the average t-z curves produced by the signal matching appear to represent the initial stiffness of the t-z curves well through the identified shaft quakes. The developed side friction response from the H-pile, for the traditional MQ and RSS functions, are shown in Figure 6.16 and Figure 6.17, respectively. It was concluded that both the traditional MQ and RSS functions developed t-z curves for the H-pile have plausible magnitudes since the ultimate resistances are in a similar range to those obtained from the sheet pile test.

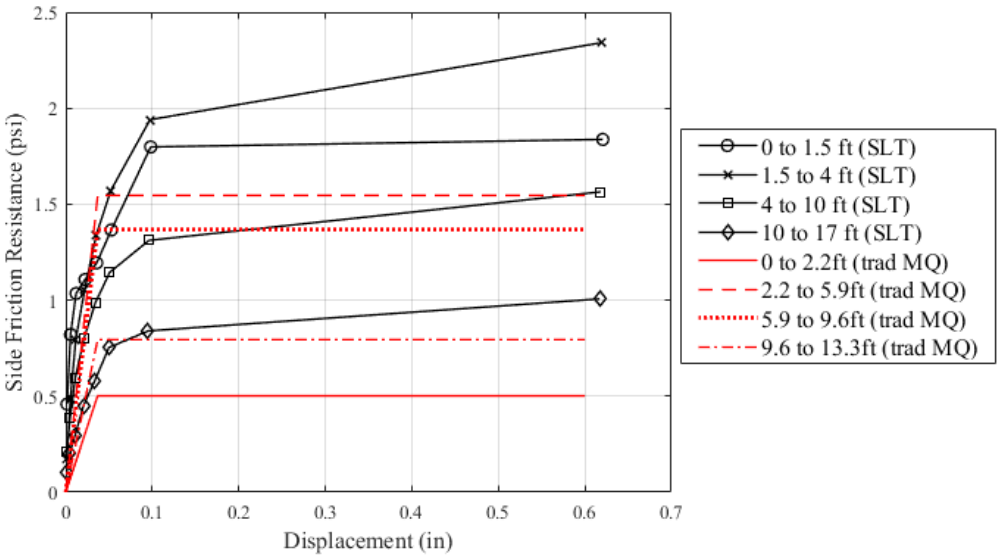

Figure 6.14: Side friction resistance shown as t-z curves from parameters identified through the traditional MQ definition signal match of the sheet pile

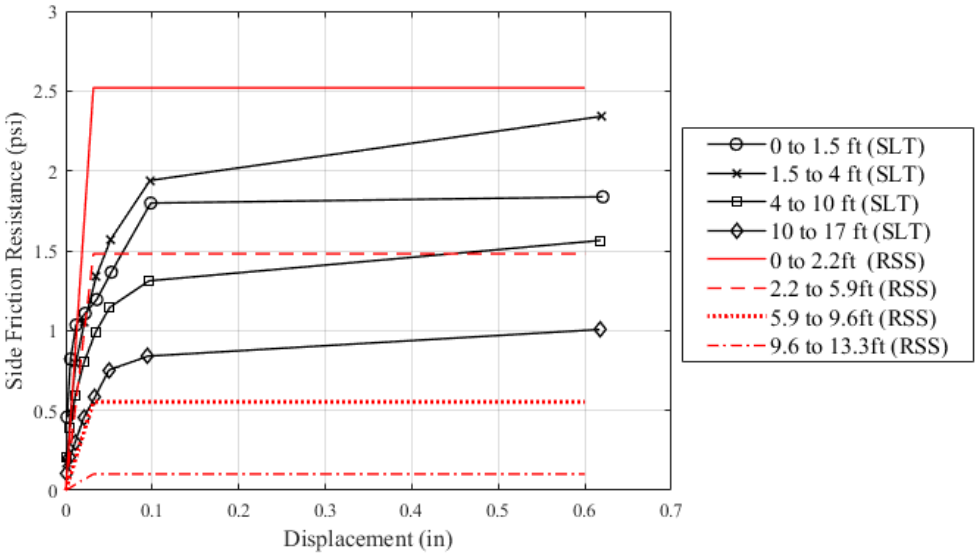

Figure 6.15: Side friction resistance shown as t-z curves from parameters identified through the RSS definition signal match of the sheet pile

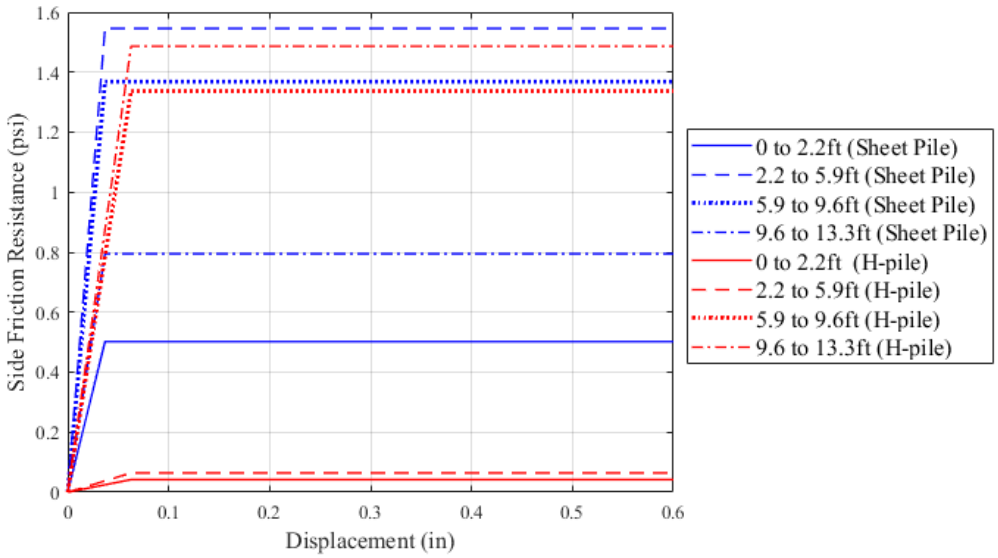

Figure 6.16: Side friction resistance shown as t-z curves from parameters identified through the traditional MQ definition signal match of the H-pile

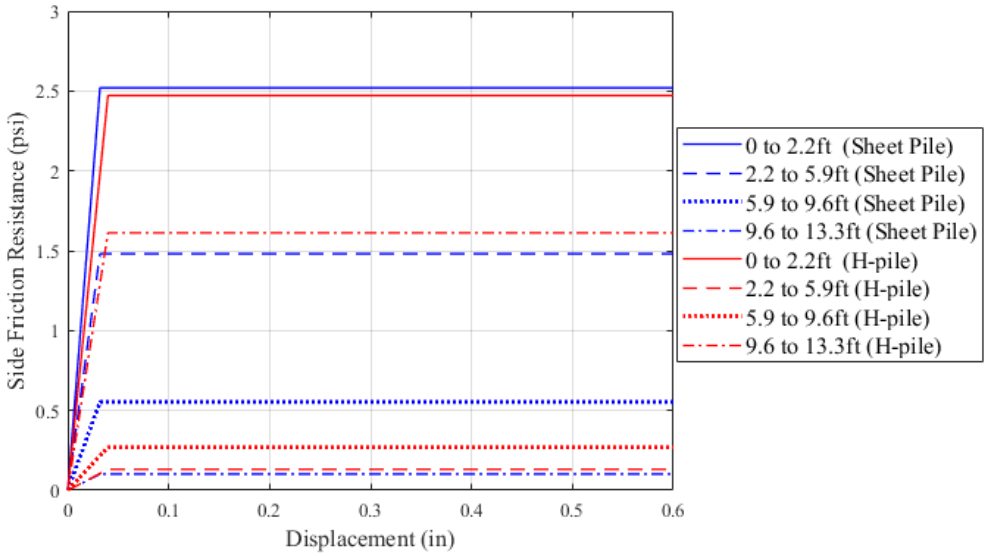

Figure 6.17: Side friction resistance shown as t-z curves from parameters identified through the RSS definition signal match of the H-pile

Using the average identified parameters for the toe quake, toe gap, and toe ultimate resistance obtained from the signal matching using the traditional MQ and RSS functions in the signal match, the predicted toe bearing resistance response of the sheet pile and H-

pile is compared to the toe bearing resistance measured from the sheet pile during the SLT, shown as q-z curves in Figure 6.18 and Figure 6.19, respectively. Since the last segment of the analytical model used for the signal matching did not include side frictional resistance, the toe resistance for the signal match includes all soil resistance in the final 3.7ft of the pile. Consequently, instead of comparing the toe q-z curves developed from the signal matching to the q-z curve extrapolated to the toe of the pile in the SLT, as previously presented in Chapter 4, the strain measurements at 3.2ft from the bottom of the pile were used to estimate a consistent toe resistance model for the SLT for comparison to the signal matching results. The predicted toe bearing resistance compares well to the measured toe bearing resistance from the SLT when using the traditional MQ definition. Larger discrepancies exist between predicted toe bearing resistance predicted from the RSS definition when compared to the measured toe bearing resistance from the SLT. It is noted that no toe gap was measured during the SLT. However, the toe gap did not have a significant influence on the signal match. If the toe gap is neglected in the soil-structure interaction models, then the initial slope of the q-z curves from derived from the signal matching exhibit strong agreement with the q-z curve developed from the static load test data.

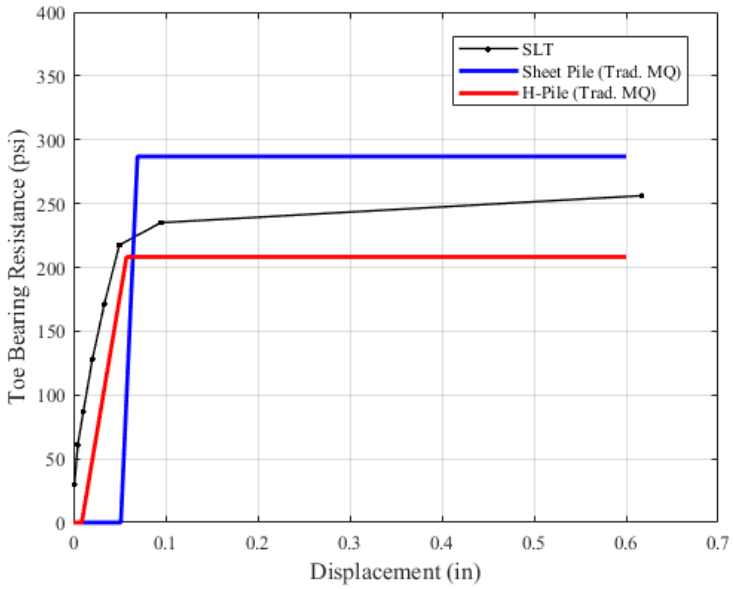

Figure 6.18: Toe bearing resistance shown as q-z curve from parameters identified through the traditional MQ definition signal match of the sheet pile

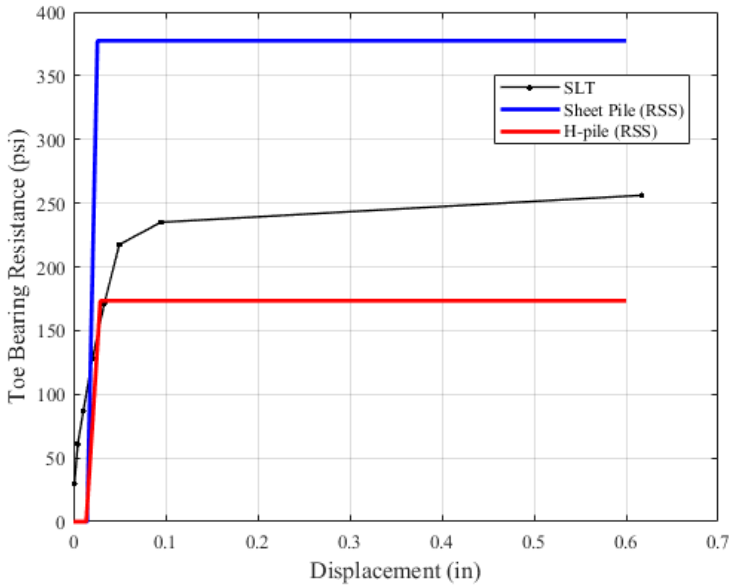

Figure 6.19: Toe bearing resistance shown as Q-z curve from parameters identified through the RSS definition signal match of the sheet pile

6.4 Variation in Parameter Estimates Across Blows and Optimization Runs

The load transfer estimates developed from the average of the soil-structure interaction parameters identified from all of the signal matches performed across all blows and optimization runs was shown in the prior subsection to compare well to measurements from the static load test. However, significant variation in the identified parameters across individual optimization runs and blows was present. These variations are further analyzed to examine potential issues related to uncertainty in the parameter estimates as well as to identify potential trends in the soil-structure interaction response as successive blows are applied to each pile.

Appendix C provides a series of tables that document the identified parameters for each individual application of the genetic algorithm for automated signal matching. The variation of side friction, toe bearing, and total resistance in the signal matches obtained using the traditional MQ definition is presented in Figure 6.22 for the sheet pile and Figure 6.23 for the H-pile. The variation of side friction, toe bearing, and total resistance in the signal matches obtained using the RSS definition is presented in Figure 6.20 for the sheet pile and Figure 6.21 for the H-pile. It is important to note, in all cases, that the range of the total static capacity estimate is less than the sum of the ranges for the shaft resistance and toe resistance. This is significant because, in the cases where the signal match incorrectly under predicts a shaft resistance, the predicted toe resistance is predicted on the higher end of the range and, ultimately, the error in the total static resistance estimate is not as significant as if the signal match had simultaneously identified both low shaft and toe resistance. For both the traditional MQ and RSS functions, there is significant variation in the predicted

shaft resistance and toe resistance across all of the analyses for the sheet pile. However, the distributions for these resistances appear to be close to normal distributions, with fairly high numbers of models predicting shaft resistance and toe resistance similar to the mean and similar to the estimates from the SLT. The total static capacity estimates for the sheet pile also exhibit significant variation for both match quality functions, which suggests that averaging a large number of signal matches is necessary to arrive at a reliable estimate of the axial capacity. For the H-pile, the distributions for the estimated parameters do not appear to be normally distributed. This difference may be a consequence of the relatively few number of blows, and as a result, less optimization runs, that were performed on H-pile measurements.

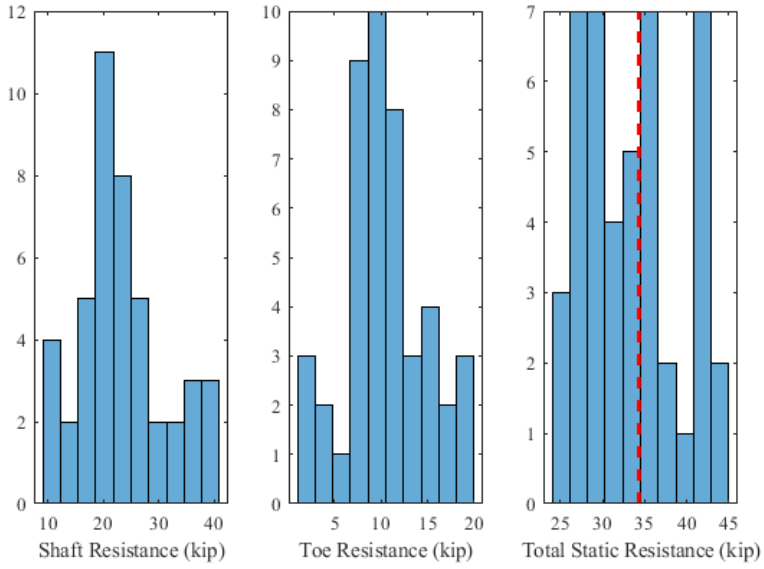

Figure 6.20: Distributions of shaft, toe, and total resistance obtained when applying the RSS match quality definition for signal matching of the sheet pile blows (red line equates to total static capacity from corresponding SLT)

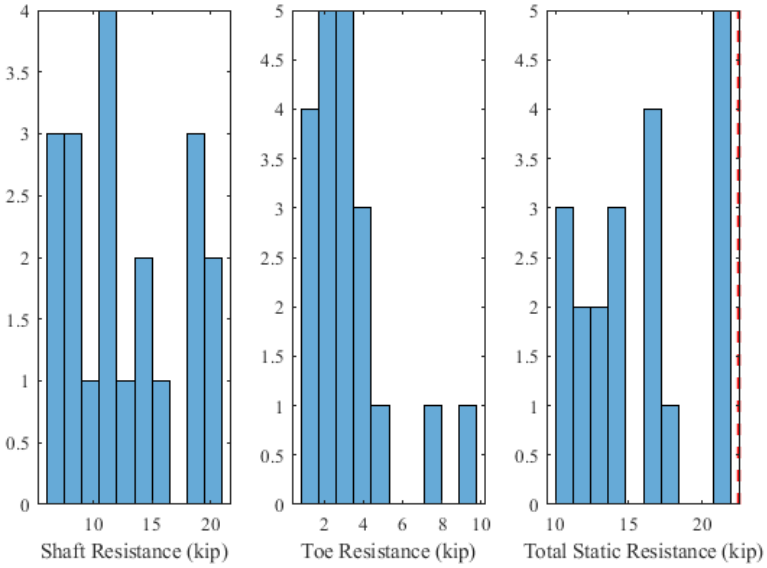

Figure 6.21: Distributions of shaft, toe, and total resistance found through the RSS definition signal match of the H-pile (red line equates to total static capacity from corresponding SLT)

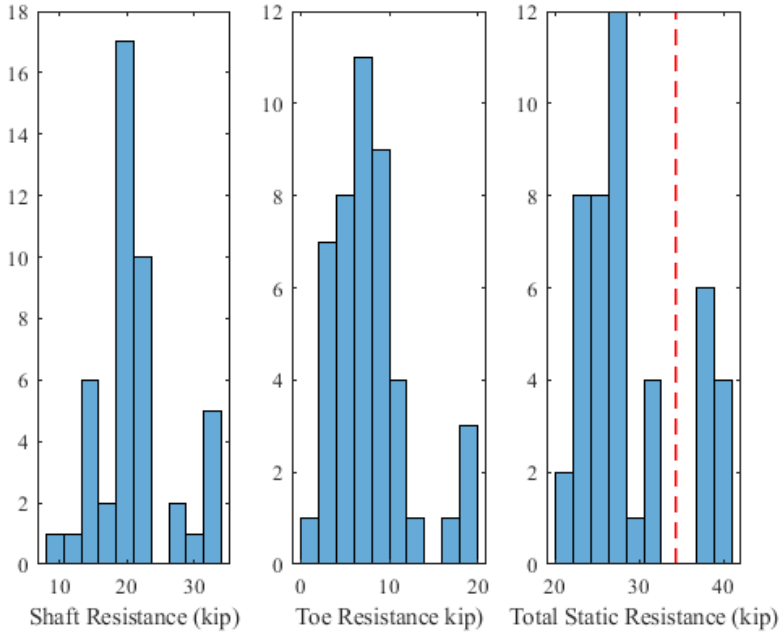

Figure 6.22: Distributions of shaft, toe, and total resistance found through the traditional MQ definition signal match of the sheet pile (red line equates to total static capacity from corresponding SLT)

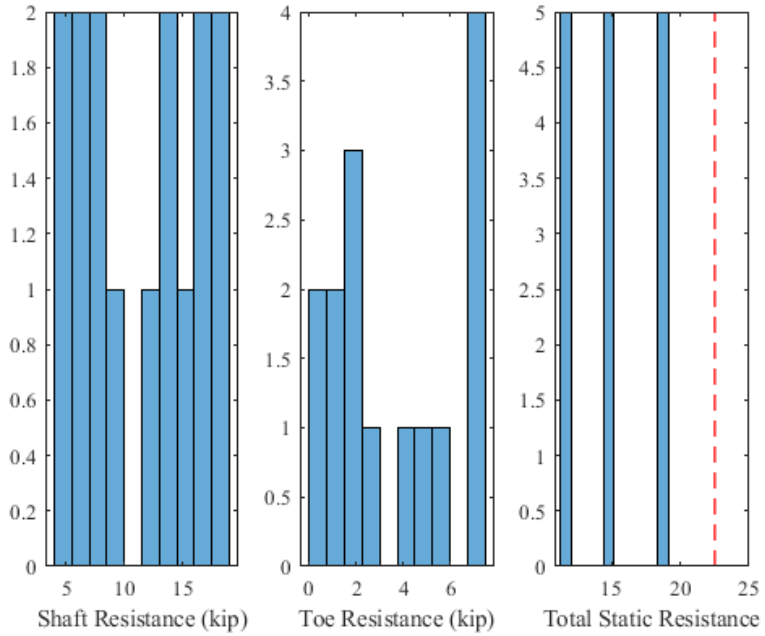

Figure 6.23: Distributions of shaft, toe, and total resistance found through the traditional MQ definition signal match of the H-pile (red line equates to total static capacity from corresponding SLT)

Some of the observed variation in the shaft, toe, and total static resistances predicted by the automated signal matching may likely be a result of physical changes in these values that occur during successive blows to the pile. Changes in pore water pressures, residual stresses, and other phenomena will lead to differences in the static resistance of the soil for each individual blow. To investigate possible evidence of changes in the shaft, toe, and total static resistance with blow count, only the five optimization runs performed on each individual blow were averaged to produce estimates for these resistances over successive blows. Figure 6.26 and present the average shaft, toe, and total static resistance estimates obtained for the individual blows on the sheet pile and the H-pile, respectively, using the traditional MQ function for the signal matching. Figure 6.26 and Figure 6.27 present the average shaft, toe, and total static resistance estimates obtained for the individual blows on

the sheet pile and the H-pile, respectively, using the RSS function for the signal matching.

For both the traditional MQ and RSS functions, the estimated total shaft resistance for the sheet pile initially increases significantly after the first blow, but then exhibits a general trend of a significant decrease in resistance with additional blows, while the estimate toe resistance remains fairly constant. Since the total shaft resistance contributes more significantly to the total static resistance than the toe bearing resistance for this pile, the total static resistance exhibits the same trends as the shaft resistance. The estimated total shaft resistance for the H-pile exhibits a similar trend with an initial increase in resistance after the first blow, followed by a decreases with successive blows, while the estimate toe resistance remains fairly constant. The consistency of this trend occurring for both pile types and for both match quality functions supports the plausibility of these variations in resistance being the result of physical phenomena, rather than a result of uncertainties in the identified soil-structure interaction parameters.

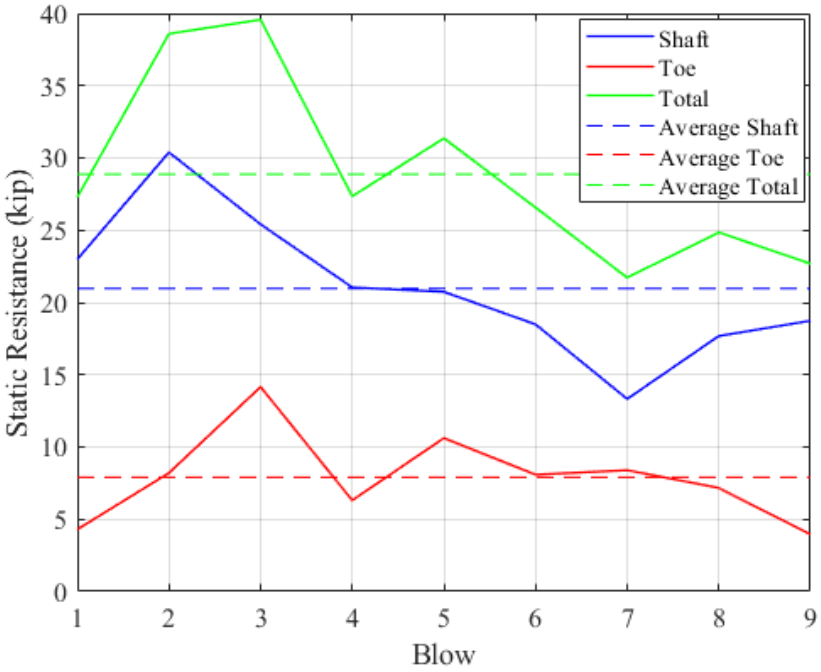

Figure 6.24: Change of shaft, toe, and total resistance estimated through the traditional MQ definition signal matching routine of sheet pile

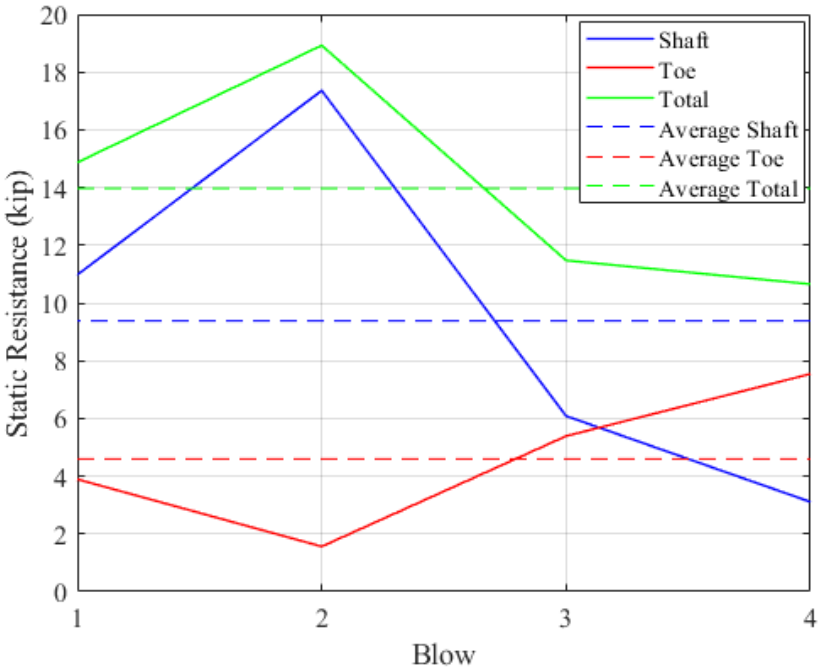

Figure 6.25: Change of shaft, toe, and total resistance estimated through the traditional MQ definition signal matching routine of H-pile

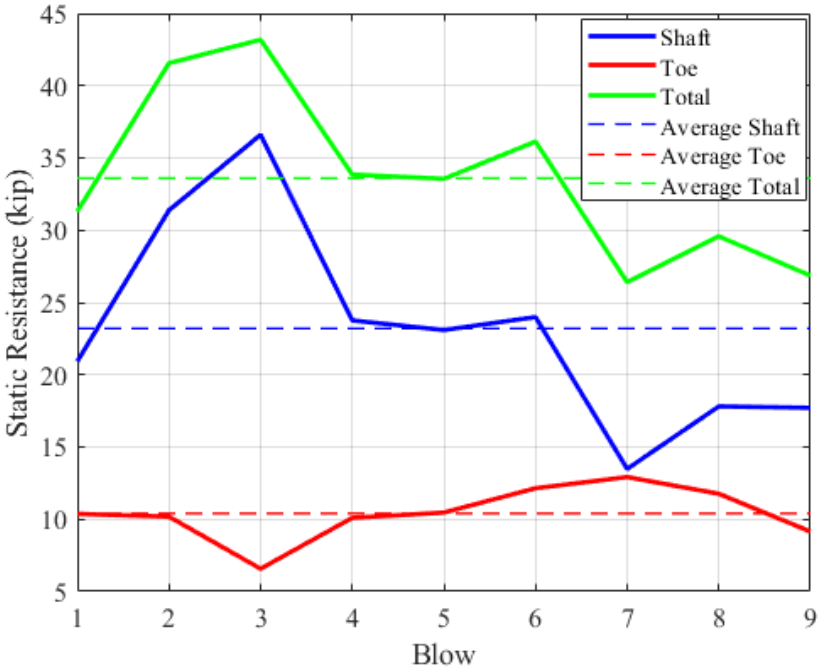

Figure 6.26: Variation of shaft, toe, and total resistance estimated from signal matching routine using the RSS match quality definition of the sheet pile

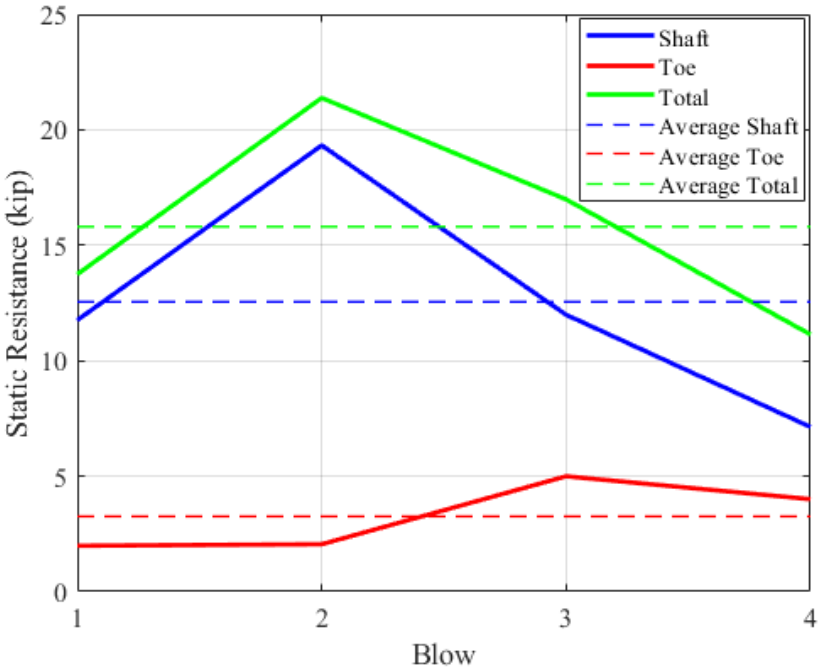

Figure 6.27: Variation of shaft, toe, and total resistance estimated from signal matching routine using the RSS match quality definition of H-pile

As stated previously in the literature, the uniqueness of soil-structure interaction parameters identified by signal matching programs, such as CAPWAP, has been questioned. To further investigate the variation in soil-structure interaction parameters identified by the automated signal matching, histograms were developed for the identified parameters across all signal matches performed for each pile using each match quality function. These histograms for the traditional MQ function are presented in Figure 6.28 for the sheet pile and Figure 6.29 for the H-pile, while similar histograms for the RSS function are provided in Appendix C. Each distribution is bounded by the input parameter bounds presented in Table 6.2 in order to convey the certainty associated with the identified parameter relative to the plausible bounds. In general, while there is spread in the estimates for the quakes and ultimate resistance parameters, the distributions generally suggest consistent estimates, especially considering the previously disclosed variation in resistance with successive blows. The distributions of the identified parameters for the shaft and toe unloading stiffnesses, shaft and toe unloading resistances, and shaft and toe damping constants generally exhibit spread across the entire range, thus suggesting that the signal matching algorithm has difficulty identifying a unique value for these parameters. While these parameters may exhibit variation due to physical changes resulting from successive blows, it is concluded that the variation in the unloading response and damping parameters was significantly large that they could not be uniquely identified for either the sheet pile or H-pile in this study. Fortunately, these parameters do not affect the estimate for the static capacity of the pile foundation, which is the typically the primary objective of dynamic testing. In general, it is also concluded that signal matching using a simple and less subjective RSS match quality function produces equally plausible identification of soil-structure interaction parameters

as the traditional match quality definition, which involves the use of weighted zones.

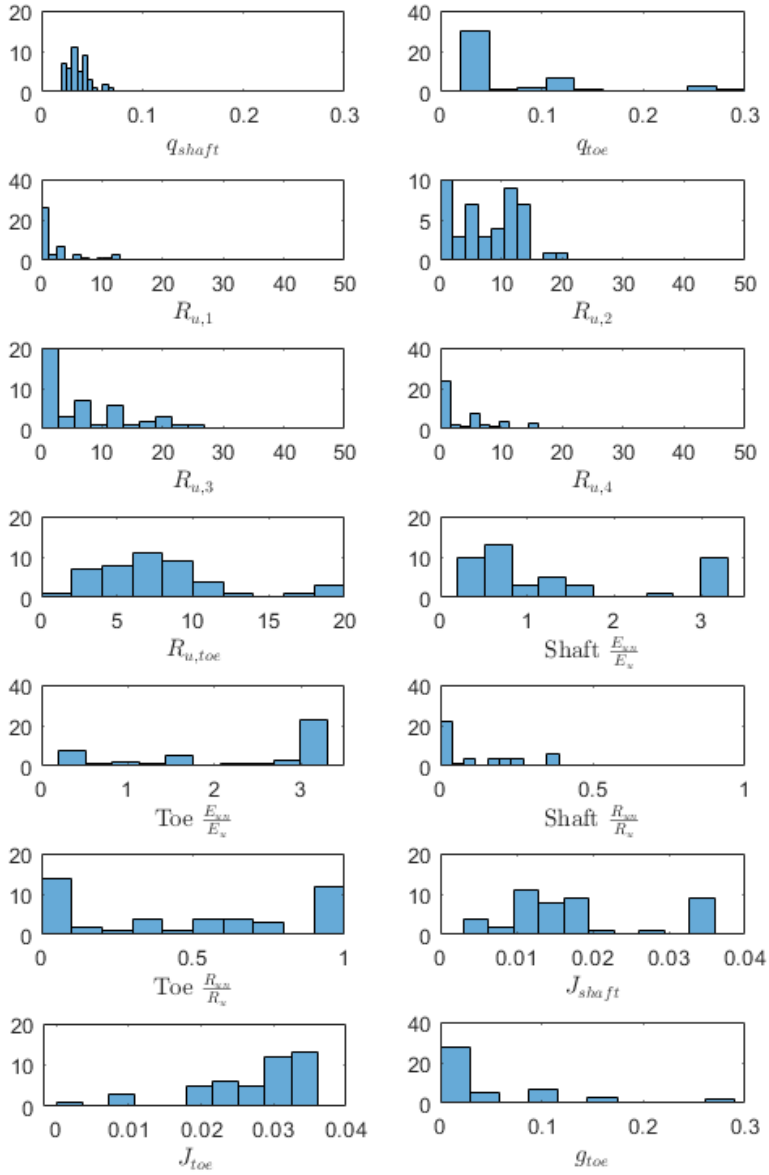

Figure 6.28: Distributions of parameters found through the traditional match quality definition signal match of the sheet pile

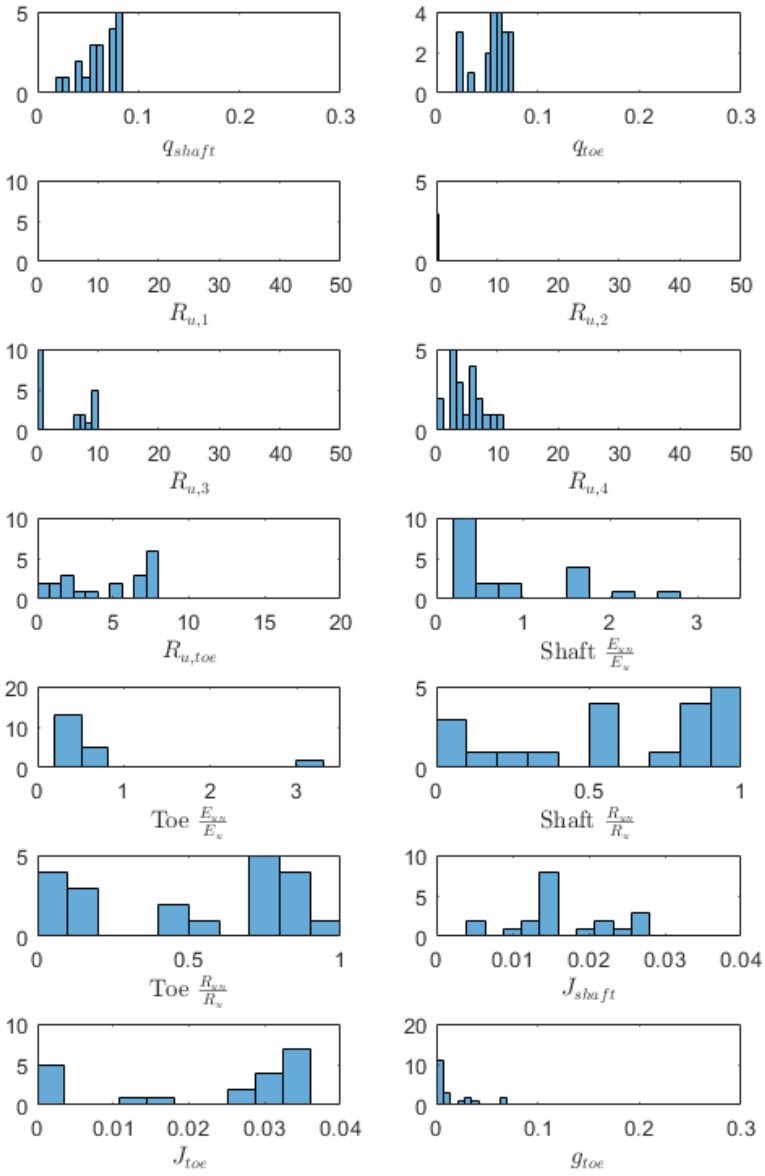

Figure 6.29: Distributions of parameters found through the traditional match quality definition signal match of the H-pile

CHAPTER 7: CONCLUSION

7.1 Summary

This study examines two commonly used field testing approaches, rapid and dynamic load testing, to determine the static axial load capacity and load transfer in driven sheet piles. Two testing programs were conducted at full-scale to evaluate the performance of methodologies conventionally used to evaluate rapid and dynamic load test data to investigate whether the application of these methods to sheet piles requires the introduction of special empirical correction factors or modified soil-structure interaction models. The laboratory test program involved a series of rapid load tests performed on a short section of sheet pile wall followed by a static load test to provide a direct means of assessing the accuracy of the static axial load capacity and load transfer estimates obtained from the rapid load test analyses. The field test program involved acquisition of dynamic measurements during restrike impact driving of a pair of sheet piles and an H-pile followed by static load testing of both piles to provide a similar direct measure of the static axial load capacity and load transfer for comparison with the estimates obtained using the Case method and signal matching. The testing and analysis of each type of loading is different and is described in detail.

The rapid load tests were performed in a 12ft x 12ft wide by 10ft deep geotechnical pit in the Structural Highbay Laboratory of the Energy Production and Infrastructure Center at

UNC Charlotte. The soil was selected by the North Carolina Department of Transportation and consist of clayey sand to silty, clayey sand. Four PZ27 sheet piles, two of which were highly instrumented, were installed as a wall in the geotechnical pit and a dynamic hydraulic actuator was used to apply rapid axial loads with a half-sine waveform to the wall. The duration and amplitude of the load pulses were varied across 24 total rapid tests conducted on the sheet pile wall to provide data for assessing the variation in rate effects and damping with load duration and amplitude. Conventional methodologies for interpreting rapid load testing measurements were applied to the data obtained from the rapid load testing, including the Unloading Point method, Modified Unloading Point method, Segmental Unloading Point method, and Embedded Data Collector method. From each method, static axial capacity estimates were determined and, following the application of empirical corrections for rate effects, the results compared well with those obtained from the static load testing program. Time invariant and time variant damping constants were also derived for each rapid load test to investigate the variation in soil damping with load duration and amplitude. Several empirical approaches used to compensate for dynamic soil resistance due to damping and rate effects were also evaluated.

The dynamic load tests were performed in a field setting in Matthews, North Carolina that included layered soils, which were well characterized using in-situ and laboratory geotechnical testing techniques. A pair of highly instrumented PZ27 sheet piles and a HP12x53 were driven to 17ft below grade using vibratory hammer installation followed by impact hammer installation. The dynamic load tests were performed during restrike testing of the piles approximately one week after the initial driving. Using the data collected, the Case method was used to calculate static axial capacity estimates at the instance of max-

imum force measurement and using a time-shifting technique to identify the instance of maximum static resistance. The measured static capacity obtained from static load tests were used to identify appropriate Case damping constants for each blow. In addition to this, an automatic signal matching program was developed and used to analyze all nine restrike testing blows on the sheet pile and all four restrike testing blows on the H-pile. Two match quality definitions, one based on the traditional match quality (MQ) function and one developed with a simple residual sum of squares (RSS), were investigated for the signal matching of 14 unknown parameters in the soil-structure interaction models. Five signal matching analyses were performed for each blow in order to examine the variations in the identified parameters. The total static resistance, shaft resistance, and toe resistance estimates obtained by averaging all signal matching results for the sheet pile compared well to corresponding SLT resistances for both the traditional MQ and RSS definitions. The distribution of identified soil-structure interaction parameters was investigated to determine the uniqueness of the solutions and it was found that the quake and ultimate resistance parameters were consistently identified while the signal matching algorithm had difficulty identifying unloading stiffnesses, unloading resistances, and damping constants.

7.2 Conclusions

Based on the research presented in this dissertation, the following conclusions have been developed:

Rapid Load Testing

- Conventional methods for the analysis of rapid load test measurements can be successfully applied to sheet pile foundations to determine their axial static load capac-

ity and load transfer. The Unloading Point Method and Segmental Unloading Point Method produced reasonable estimates for the static capacity and load transfer, respectively, when empirical rate effect correction parameters were used. However, the empirical rate correction factors in the available literature have a wide range of uncertainty and future research is needed to improve the ability to predict site-specific rate effect correction factors. In this study, a rate correction factor of 0.8, which is the average of the empirical values recommended in the the literature for clay and sand, was found to best predict the ultimate static capacity of the pile group, as measured by the static load test. However, this dissertation research also demonstrated that the rate effect correction parameter is dependent not only on soil type, but also on load duration and amplitude. Also, while the Segmental Unloading Point Method successfully predicted the initial stiffness, general profiles, and ultimate resistances of the t-z curves developed by the static load test when a empirical rate correction factor of 0.8 was used, the Q-z curve was more accurately predicted without a rate effect correction factor. This suggests that different rate effect correction factors may be needed for the side friction and toe bearing contributions.

- For this study, the Modified Unloading Point method did not offer significant changes to inertia effects on the system and would not significantly change the estimated total static axial capacity, due to the small differences in head and toe acceleration measurements and small system mass. Additionally, the Embedded Data Collector method, a new technique for interpretation of rapid load test data, was applied to the measurements and found to over predicted the static toe resistance of the static

load test by a factor of 2. It was not possible to conclude that the poor correlation between the toe model obtained from the Embedded Data Collector method was a result of shortcomings in the method, such as not accounting for rate effects or its use of a time invariant damping constant, or due to the signal-to-noise ratio limitations resulting from the instrumentation used.

- Rate dependent damping constants, α and β, were estimated using three approaches that included using empirical data sourced by the literature, estimating by using the plasticity index of the soil, and directly calculating the damping constants by using the data from the existing static load test. The use of the damping constants found in the literature over predicts the static force displacement response by only approximately 10-15% when compared to the static load test. Similarly, the damping constants estimated through using the plasticity index of the soil also moderately over predicted the static force displacement response. The discrepancy between the estimated static response and the measured load-displacement response from the SLT is likely explained by the effects of pore water pressures that were not accounted for using the methods described. It was also demonstrated that the predicted static response was only moderately over estimated and produced more accurate estimates of static capacity when using rate effect correction factors sourced by the literature. By using the static load test measurements, the rate dependent damping constant, α, was calculated to be 1.34 when β is set to a fixed value of 0.2.

- A time invariant damping constant that is used in the equation of motion for the pile was also estimated using the theory supplied by the literature. The calculated static

force displacement response showed an unfavorable result as it produced negative static forces at the beginning of the response, which suggest that the time invariant damping constant may not accurately predict the overall static force response of the pile. However, time invariant damping constants that were computed using a back calculation method applied to the rapid load test data using the static load test measurements to define the static soil resistance. The time invariant damping constant was found to vary as a function of the displacement at the head of the pile and was characterized by an increase in the damping constant as displacement increased. The time invariant damping constant was found to vary with the duration of the loading. However, the amplitude of the loading did not significantly affect the relationship between the time invariant damping constant and head displacement.

- While the original theory presented in the literature did not account for pore water pressure effects, the rate effect correction factor was used as a constant to estimate the pore water pressure effects and estimates of time variant damping constants were made. The back calculated time variant damping constants were found to be consistent with displacement for each test conducted with the same load duration. There were instances of zero, or slightly negative, damping constants for 1Hz and 2Hz pulses. It was concluded that inertia effects from including additional soil mass due to a soil plug did not explain the zero, or slightly negative damping constants. However, it was concluded that the likely source of the unexpected damping constants was the assumption adopted when accounting for pore water pressure effects using the rate effect correction parameter.

Dynamic Load Testing

- Overall, the dissertation results suggest that conventional methods for the analysis of dynamic, or pile driving, measurements to obtain static axial capacity and load transfer estimates can be successfully applied to sheet piles without introducing any special corrections or soil-structure interaction models.

- The Case method was used to estimate the total static capacity for the sheet pile and H-pile at the field site. The Case method was found to be an unreliable way to estimate the static axial capacity developed using the time-shifting technique. It was also concluded that the commonly assumed Case damping coefficient of 0.7 did not lead to reasonable estimates of the actual static axial capacity. However, the Case method did produce reasonable estimates of static axial capacity when using the maximum internal force measurement technique. The Case damping constant for use with this technique was found to be around 0.15-0.18 for both the sheet pile and H-pile and was observed to decrease as successive blows were applied to each pile.

- An automatic signal matching routine using a genetic algorithm was developed in this dissertation and applied for identification of soil-structure interaction parameters in analytical models of a sheet pile and an H-pile solved using the method of characteristics. Both the traditional match quality and residual sum of square definitions generally predicted the total static axial capacity and load transfer for the sheet piles and H-pile. The estimated side friction resistance response compared reasonably well with the side friction resistance responses measured from the static load test. Additionally, the estimated toe bearing resistance compares well to the toe

bearing resistance measured from the static load test. The soil-structure interaction parameters associated with soil quakes, shaft resistance, toe resistance, and toe gap were found to be reasonably well identified while the signal matching algorithm had difficulty identifying unique unloading parameters and damping constants. This conclusion may be a result of the difficulty of identifying the multitude of parameters using a single objective function. Finally, the RSS definition proved to be useful in estimating side friction resistance, toe bearing resistance, and total static axial capacity, while eliminating any subjective definitions of zones that were used in the traditional match quality definition.

7.3 Future Work

From the study of the literature review and results of this study, the following recommendations for future work are as follows:

- It was shown that the lack of rapid and dynamic test data of sheet piles in the literature does not adequately support the development of specific design recommendations for the estimation and field determination of the axial load capacity of sheet piles in bridge foundations. Even though this dissertation produces an extensive analysis of rapid and dynamic load testing of sheet piles, it is highly recommended that further rapid and dynamic testing of sheet piles should be performed in order to increase confidence in, and develop recommendations for, the evaluation of the axial load capacity of sheet pile foundations.

- Further research is required to study pore water pressure effects and plugging effects of sheet piles during rapid load testing. Comparing data from dry soil conditions to

wet soil conditions could aid in the development of a methodology to account for pore water pressure effects on the axial capacity predictions. The use of a high speed pore water pressure instrumentation around the sheet pile could supply valuable data that can relate increased pore water pressures directly to dynamic forces that must be removed from the response of a rapid load test to accurately predict the static axial capacity. Recommendations should be developed to supply engineers with a methodology on how to accurately predict pore water pressure effects on sheet piles during rapid load testing. Additionally, further research is recommended to develop methodology to predict the development and extent of plugging in sheet piles, as well as the effect of plugging on the load capacity under rapid and static loading. A means of accurately determining the additional mass contribution in the analysis of forces during a rapid load test would be a valuable contribution to the current state of knowledge.

- Additionally, further research is needed with the analysis of dynamic load testing. The automatic signal matching routine developed in this dissertation is a reasonable approach that could be used in analyzing additional dynamic load testing of sheet piles provided that a sufficient number of optimizations are performed to facilitate a statistical analysis of the identified parameters. This would validate and further increase the confidence of the automatic signal matching routine on piles. More advanced soil models, such as the inclusion of radiation damping, could be investigated as part of the existing signal matching routine in order to increase accuracy. However, it is predicted that the computational time would further increase with the addition of

more advanced soil models. Further development of a quicker analysis program, that maintains accuracy of predicting static axial capacity along with developing accurate soil models, would also benefit the current state of knowledge.

REFERENCES

AASHTO (2016). *LRFD Bridge Design Specifications: Design and Construction of Drive Pile Foundations. FHWA-NHI-16-009.* 7th edition.

ASTM International (2010). D7383 - 10 standard test methods for axial compressive force pulse (rapid) testing of deep foundations.

ASTM International (2017). D4945-17 standard test method for high-strain dynamic testing of deep foundations.

Balderas-Meca, J. (2004). *Rate Effects of Rapid Loading in Clay Soils*. Thesis.

Brown, D. (1994). Evaluation of static capacity of deep foundations from statnamic testing. *Geotechnical Testing Journal*, 17(4):403–414.

Brown, M. (2004). *The rapid load testing of piles in fine grained soils*. Phd dissertation.

Brown, M., Wood, T., and Suckling, T. (2006). Statnamic pile testing case studies. volume 31, pages 627–634, Amsterdam, Holland. The 10th International Conference on Piling and Deep Foundations.

Coyle, H. and Gibson, G. (1970). Empirical damping constants for sands and clays. *Journal of Soil Mechanics and Foundations Division*, 96(3):949–965.

Deckner, F., Viking, K., and Hintze, S. (2015). Vibration transfer during sheet pile driving – a full-scale field test. Christchurch, New Zealand. The 6th International Conference on Earthquake Geotechnical Engineering.

Eiber, R. (1958). *A Preliminary Laboratory Investigation of the Prediction of Static Pile Resistances in Sand*. PhD thesis, Master's Thesis, Dept. of Civil Engineering, Case Institute of Technology.

Eiksund, G. and Nordal, S. (1996). Dynamic model pile testing with pore pressure measurements. In *The 5th International Conference on Application of Stress-Wave Theory to Piles*, pages 581–588.

European Committee for Standardization (2007). *Eurocode 3: Design of Steel Structures Part 5: Piling. EN 1993-5.*

Fischer, H. (1960). On longitudinal impact iv: New graphodynamical pulse method of computing pile-driving processes. *Applied Scientific Research*, 9(1).

Goble, G. G., Likins Jr, G., and Rausche, F. (1975). Bearing capacity of piles from dynamic measurements. Technical report.

Gonin, H. (1984). Theory and performance of a new dynamic method of pile testing. Stockholm. The 2nd International Conference of Application of Stress-Wave Theory of Piles.

GRL Engineers Inc and Pile Dynamics Inc (2008). Capwap: Models, procedures, parameters.

GRL Engineers Inc and Pile Dynamics Inc (2013). Capwap: Models, procedures, parameters, performance.

Hannigan, P. J., Rausche, F., Likins, G. E., Robinson, B. R., and Becker, M. L. (2016). Design and construction of driven pile foundations: Volume 1. Report FHWA-NHI-16-009, Federal Highway Administration.

Holeyman, A. (1992). Keynote lecture: Technology of pile dynamic testing. In *Proceedings of the 4th International Conference on the Application of Stress Waves Theory to Piles*, pages 195–215.

Holeyman, A. (1993). Hipervib 1: An analytical model-based computer program to evaluate the penetration speed of vibratory driven sheet piles. *Report for Belgian Building Research Institute (BBRI)*.

Holeyman, A. and Whenham, V. (2017). Critical review of the hypervib1 model to assess pile vibro-drivability. *Geotechnical and Geological Engineering*, 35:1933–1951.

Holscher, P., Brassinga, H., Brown, M., Middendorp, P., Profittlich, M., and van Tol, F. (2012). CRC Press.

Holscher, P., van Tol, A., and Middendorp, P. (2008). European standard and guideline for rapid load test in santos, j.a. In *The 8th International Conference on the Application of Stress-Wave Theory to Piles*.

Hyde, A., Robinson, S., and Anderson, W. (2000). Rate effects in clay soils and their relevance to statnamic testing. pages 303–309, Tokyo Japan. The 2nd International Statnamic Seminar.

Iversen, K., Augustesen, A., and Nielsen, B. (2010). Vertical equilibrium of sheet pile walls with emphasis on toe capcity and plugging. Report, Aalborg University.

Janes, M. and Bermingham (1986). An innovative approach to load testing of high capacity piles. London. The International Conference on Piling and Deep Foundations.

Justason, M. (1997). Report of load testing at the taipei municipal incinerator expansion project. *Taipie City, Taiwan*.

Konak, A., Coit, D. W., and Smith, A. E. (2006). Multi-objective optimization using genetic algorithms: A tutorial. *Reliability Engineering & System Safety*, 91(9):992–1007.

Likins, G., Liang, L., and Hyatt, T. (2012). Development of automatic signal matching procedure-icap. *Proceedings from Testing and Design Methods for Deep Foundations*, pages 97–104.

Litkouhi, S. and Poskitt, T. (1980). Damping constants for pile driveability claculations. *Geotechnique*, 30(1):77–86.

Matsuzawa, K., Nakashima, Y., and Matsumoto, T. (2008). Spring hammer rapid load test method and its validation. In *International Conference on Foundations*, pages 223–234, Scotland.

McVay, M., Kuo, C., and Guisinger, A. (2003). Calibrating resistance factor in load and resistance factor design of statnamic load testing. Report 4910-4504-823-12, Flordia Department of Transportation.

Middendorp, P. (1995). Statnamic load testing and the influence of stress wave phenomena. In *Proc. of 1st Statnamic Seminar*, pages 35–44.

Middendorp, P., Berminghamd, P., and Kuiper, B. (1992). Statnamic load testing of foundation piles. In *Proceedings of the 4th International Conference on the Application of Stress-Wave Theory to Piles*. A.A. Balkema Publishers.

Mullins, G., Lewis, C. L., and Justason, M. D. (2002). *Advancements in Statnamic data regression techniques*, pages 915–930.

Ochiai, H., Kusakabe, O., Sumi, K., and Matsumnoto, T. (1997). Dynamic and statnamic load tests on offshore steel pipe piles with regard to failure mechanisms of pile-soil interfaces at external and internal shafts. In *International Conference on Foundation Failures*, pages 327–338.

Paikowsky, S. (2006). Innovative load testing systems. Report, Transportation Research Board.

Pile Dynamics, Inc. (2015). Pile driving analyzer manual; model 8g.

Poskitt, T. and Leonard, C. (1982). Effect of velocity on penetrometer resistance. In *Proceedings of the European Symposium on Penetration Testing*, pages 331–336. ESOPT-2.

Poulos, H. (1998). Pile testing-from the designer's viewpoint. In *The 2nd International Statnamic Seminar*.

Powell, J. and Brown, M. (2006). Statnamic pile testing for foundation re-use. pages 223–236, Watford, UK. The International Conference on the re-use of foundations for urban sites.

Randolph, M. and Deeks, A. (1992). Dynamic and static soil models for axial pile response. In *The 4th International Conference of on the Application of Stress Wave Theory to Piles*, pages 3–14, The Hague, The Netherlands.

Rausche, F. (1970). Soil response from dynamic analysis and measurements on piles.

Rausche, F., Goble, G. G., and Likins Jr, G. E. (1985). Dynamic determination of pile capacity. *Journal of Geotechnical Engineering*, 111(3):367–383.

Rausche, F., Likins, G., Liang, L., and Hussein, M. (2010). *Static and dynamic models for CAPWAP signal matching*, pages 534–553.

Rausche, F., Moses, F., and Goble, G. G. (1972). Soil resistance predictions from pile dynamics. *Journal of the Soil Mechanics and Foundations Division*, 98(9):917–937.

Schellingerhout, A. and Revoort, E. (1996). Pseudo static pile load tester. The 5th International Conference on the Application of Stress Wave Theory to Piles.

Smith, E. (1960). Pile driving analysis by the wave equation. *Journal of Soil Mechanics and Foundations Division*, 86(4):35–61.

Stokes, M., Mullins, G., Ealy, C., and D., W. (2008). Statnamic damping coefficient: Numerical modeling approach. *Journal of Geotechnical and Geoenvironmental Engineering*, 134(9):1290–1298.

Sylvain, M. (2019). *A Study on Soil-Structure Interaction of Axially Loaded Sheet Piles*. Thesis.

Tran, K., McVay, M., Herrera, R., and Lai, P. (2012a). Estimating static tip resistance of driven piles with bottom pile instrumentation. *Canadian Geotechnical Journal*, 49(4):381–393.

Tran, K., McVay, M., Herrera, R., and Lai, P. (2012b). Estimation of nonlinear static skin friction on multiple pile segments using teh measured hammer impact response at the top and bottom of the pile. *Computers and Geotechnics*, 41:79–89.

Tran, K., Wasman, S., McVay, M., and Herrera, R. (2017). Capacity evaluation of voided driven piles with embedded data collector. *Canadian Geotechnical Journal*.

Tran, K. T., McVay, M., Nguyen, T. D., and Wasman, S. J. (2016). Evaluation of drilled shaft capacity using embedded sensors and statnamic testing. *Journal of Bridge Engineering*, 21(11).

Underwood, C. A., GE, D., et al. (2019). The use of steel sheet pile as permanent building foundation walls: Lessons learned over 15 years of design in minneapolis, minnesota, usa. *Journal of Geotechnical and Geoenvironmental Engineering*.

Underwood, C. A. and Greenlee, R. M. (2010). Steel sheet pile used as permanent foundation and retention systems-design and construction. In *Earth Retention Conference 3*, pages 129–136.

Van Koten, H., Middendorp, P., and Van Brederode, P. (1980). An analysis of dissipative wave propagation in a pile. In *Proc. of Int. Seminar on the Application of Stress-Wave Theory on Piles*, pages 23–40.

Van Weele, A. and Kay, S. (1984). Analytical results with numerical programs. In *Proceedings of the Second International Conference on the Application of Stress-Wave Theory On Piles*.

Viking, K. (2002). *Vibro-Driveability: A Field Study of Vibratory Driven Sheet Piles in Non-Choesive Soils*. Thesis.

Voitus van Hamme, G., Jansz, J., Bomer, H., and Arentsen, D. (1974). Hydroblok and improved pile driving analysis. *De Ingenieur*, 86(8):344–352.

Whenham, V., Areias, L., Rocher-Lacoste, F., Vie, D., Bourdouxhe, M., and Holeyman, A. (2009). Full scale sheet pile vibro-driving tests. Alexandria, Egypt. The 17th International Conference on Soil Mechanics and Geotechnical Engineering.

APPENDIX A: ADDITIONAL TEST INFORMATION

Table A.1: Instrumentation information for rapid load tests

Channel	Attribute	Model No.	Sensor No.	Sensitivity
1	Accelerometer #1	353 B31	94031	4.969 $mV/m/s^2$
2	Accelerometer #2	353 B31	95014	4.980 $mV/m/s^2$
3	Accelerometer #3	353 B31	95022	5.300 $mV/m/s^2$
4	Accelerometer #4	353 B31	95020	4.960 $mV/m/s^2$
5	Accelerometer #5	353 B31	94032	5.060 $mV/m/s^2$
6	Accelerometer #6	353 B31	95021	5.350 $mV/m/s^2$
7	Accelerometer #7	353 B03	109074	1.020 $mV/m/s^2$
8	Accelerometer #8	353 B03	109338	1.020 $mV/m/s^2$
9	Accelerometer #9	350 B04	N/A	1.020 $mV/m/s^2$
10	Accelerometer #10	350 B04	N/A	1.020 $mV/m/s^2$
11	LVDT #1	N/A	N/A	0.16022 V/in
12	LVDT #2	N/A	N/A	0.16435 V/in
13	LVDT #3	N/A	N/A	0.16392 V/in
14	LVDT #4	N/A	N/A	0.161323 V/in
15	BDI Strain Transducer #1	ST350	5855	331.6
16	BDI Strain Transducer #2	ST350	5686	336.9
17	BDI Strain Transducer #1	ST350	5688	334.4
18	BDI Strain Transducer #2	ST350	6841	338.0
19	BDI Strain Transducer #1	ST350	5689	339.0
20	BDI Strain Transducer #2	ST350	6842	331.2
21	BDI Strain Transducer #1	ST350	6843	336.1
22	BDI Strain Transducer #2	ST350	5684	328.6
23	BDI Strain Transducer #1	ST350	5883	339.8
24	BDI Strain Transducer #2	ST350	5682	339.3
25	RSG #1	CEA-06-250UN-350		
26	RSG #2	CEA-06-250UN-350		
27	RSG #3	CEA-06-250UN-350		
28	RSG #4	CEA-06-250UN-350		
29	RSG #5	CEA-06-250UN-350		
30	RSG #6	CEA-06-250UN-350		
31	RSG #7	CEA-06-250UN-350		
32	RSG #8	CEA-06-250UN-350		
33	RSG #9	CEA-06-250UN-350		
34	RSG #10	CEA-06-250UN-350		
35	RSG #11	CEA-06-250UN-350		
36	RSG #12	CEA-06-250UN-350		
37	RSG #13	CEA-06-250UN-350		
38	RSG #14	CEA-06-250UN-350		
39	RSG #15	CEA-06-250UN-350		
40	RSG #16	CEA-06-250UN-350		
41	RSG #17	CEA-06-250UN-350		
42	RSG #18	CEA-06-250UN-350		
43	RSG #19	CEA-06-250UN-350		
44	RSG #20	CEA-06-250UN-350		
45	RSG #21	CEA-06-250UN-350		
46	RSG #22	CEA-06-250UN-350		
47	RSG #23	CEA-06-250UN-350		
48	RSG #24	CEA-06-250UN-350		
49	MTS Data #1			
50	MTS Data #2			

Table A.2: Instrumentation information for dynamic load tests

Channel	Attribute	Model No.	Sensor No.	Sensitivity
1	Accelerometer #1	350B04	48658	0.086 $mV/m/s^2$
2	Accelerometer #2	350B04	48663	0.0882 $mV/m/s^2$
3	Accelerometer #3	350B04	48664	0.087 $mV/m/s^2$
4	Accelerometer #4	350B04	34423	0.092 $mV/m/s^2$
5	Stringpot Displacement	SP2-25	N/A	2 V/in
6	RSG #1	LWK-06-W250B-350		
7	RSG #2	LWK-06-W250B-350		
8	RSG #4	LWK-06-W250B-350		
9	RSG #5	LWK-06-W250B-350		
10	RSG #6	LWK-06-W250B-350		
11	RSG #7	LWK-06-W250B-350		
12	RSG #8	LWK-06-W250B-350		
13	RSG #9	LWK-06-W250B-350		
14	RSG #11	LWK-06-W250B-350		
15	RSG #12	LWK-06-W250B-350		
16	RSG #13	LWK-06-W250B-350		
17	RSG #14	LWK-06-W250B-350		
18	RSG #15	LWK-06-W250B-350		
19	RSG #16	LWK-06-W250B-350		
20	RSG #17	LWK-06-W250B-350		
21	RSG #18	LWK-06-W250B-350		
22	RSG #19	LWK-06-W250B-350		
23	RSG #21	LWK-06-W250B-350		
24	RSG #22	LWK-06-W250B-350		
25	RSG #23	LWK-06-W250B-350		
26	RSG #24	LWK-06-W250B-350		
27	RSG #25	LWK-06-W250B-350		
28	RSG #27	LWK-06-W250B-350		
29	RSG #28	LWK-06-W250B-350		
30	RSG #29	LWK-06-W250B-350		
31	RSG #30	LWK-06-W250B-350		
32	RSG #31	LWK-06-W250B-350		
33	RSG #32	LWK-06-W250B-350		
34	BDI Strain Transducer #1	ST350	6842	331.2
35	BDI Strain Transducer #2	ST350	5689	339.0
36	BDI Strain Transducer #3	ST350	6843	336.1
37	BDI Strain Transducer #4	ST350	5686	336.9

APPENDIX B: ADDITIONAL INFORMATION FOR RAPID LOAD TEST

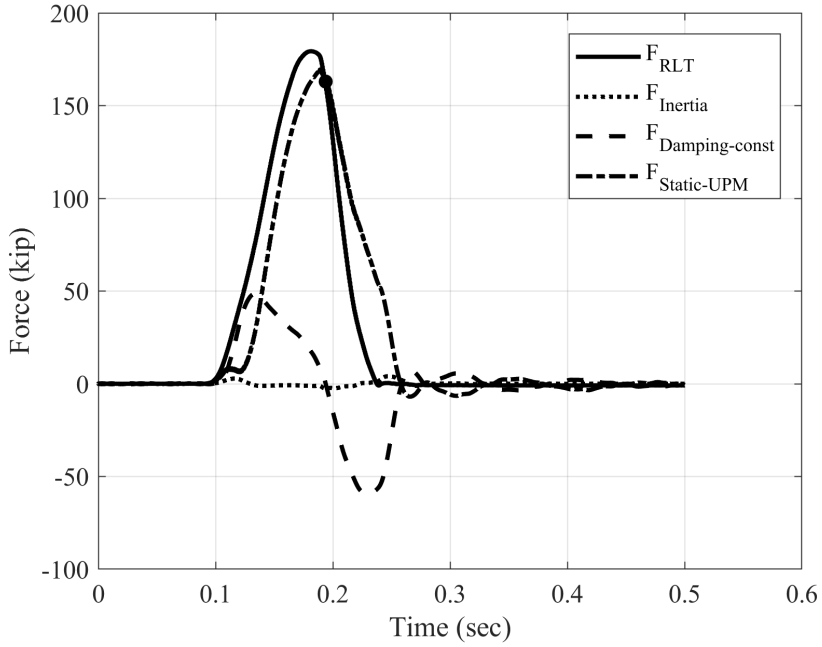

Figure B.1: Separation of forces for the pulse corresponding to 6Hz and 0.35in peak input displacement

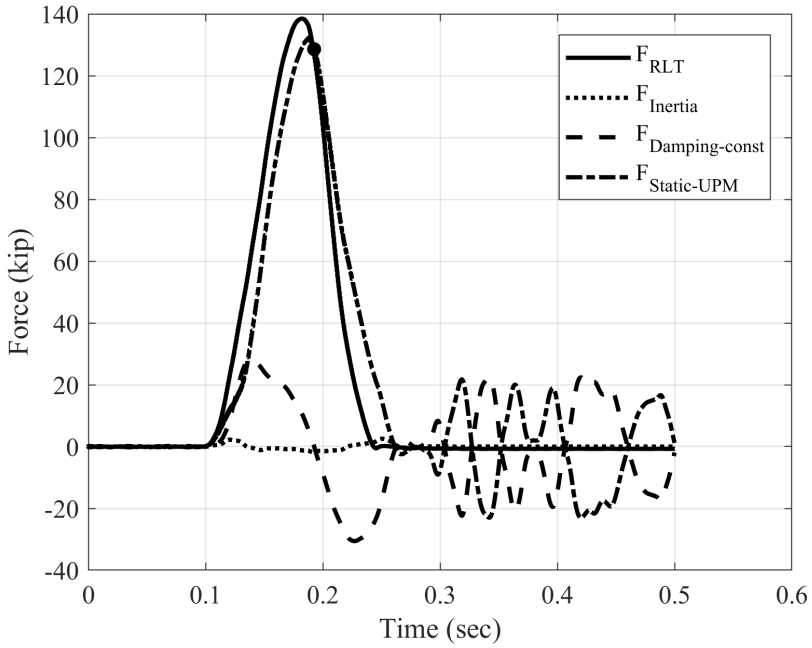

Figure B.2: Separation of forces for the pulse corresponding to 6Hz and 0.25in peak input displacement

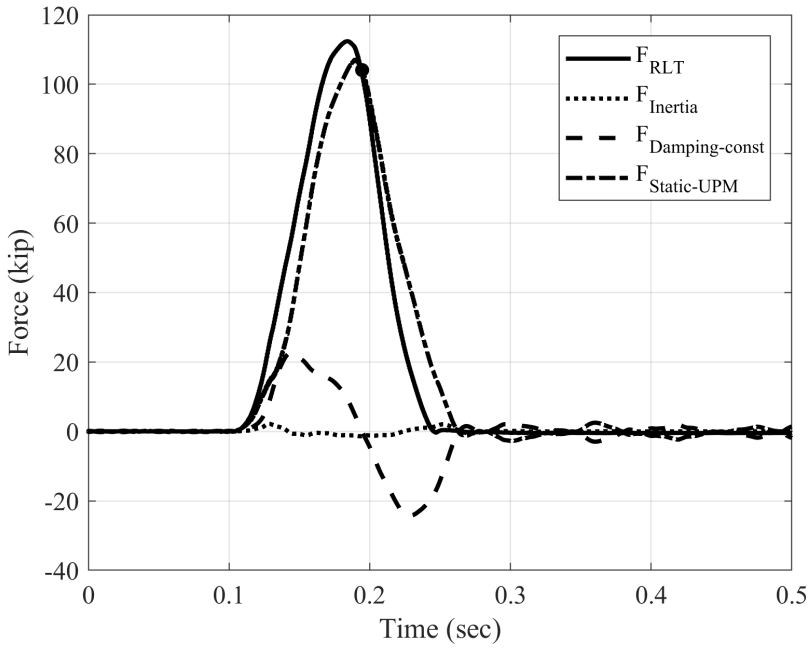

Figure B.3: Separation of forces for the pulse corresponding to 6Hz and 0.20in peak input displacement

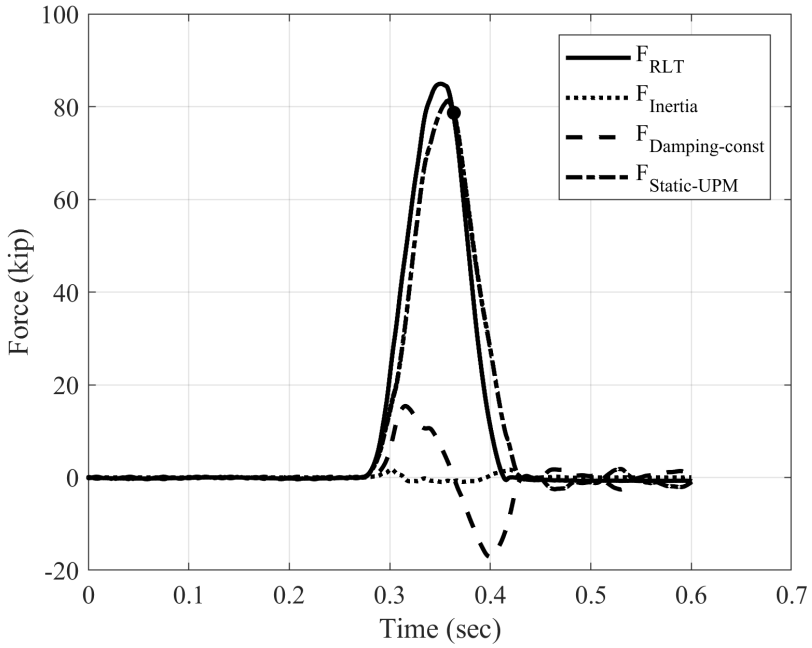

Figure B.4: Separation of forces for the pulse corresponding to 6Hz and 0.15in peak input displacement

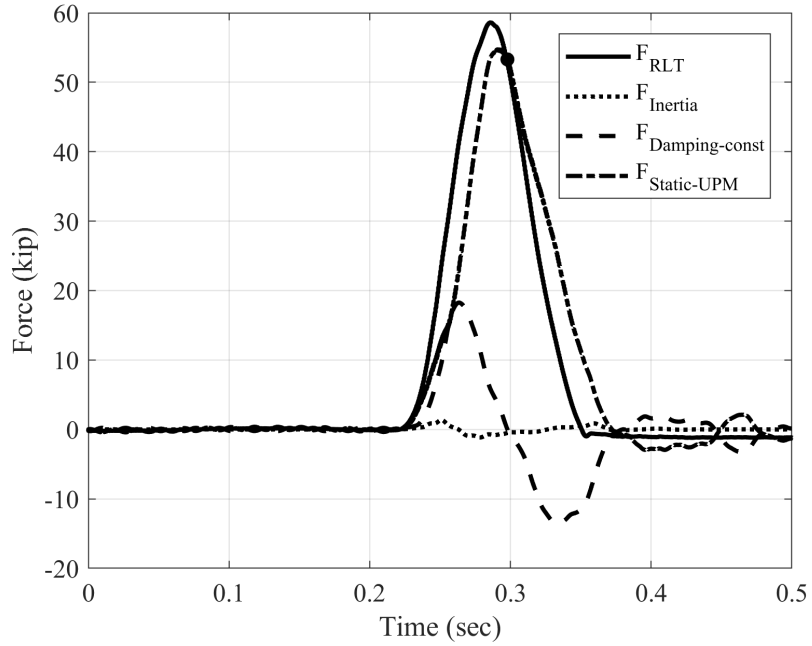

Figure B.5: Separation of forces for the pulse corresponding to 6Hz and 0.10in peak input displacement

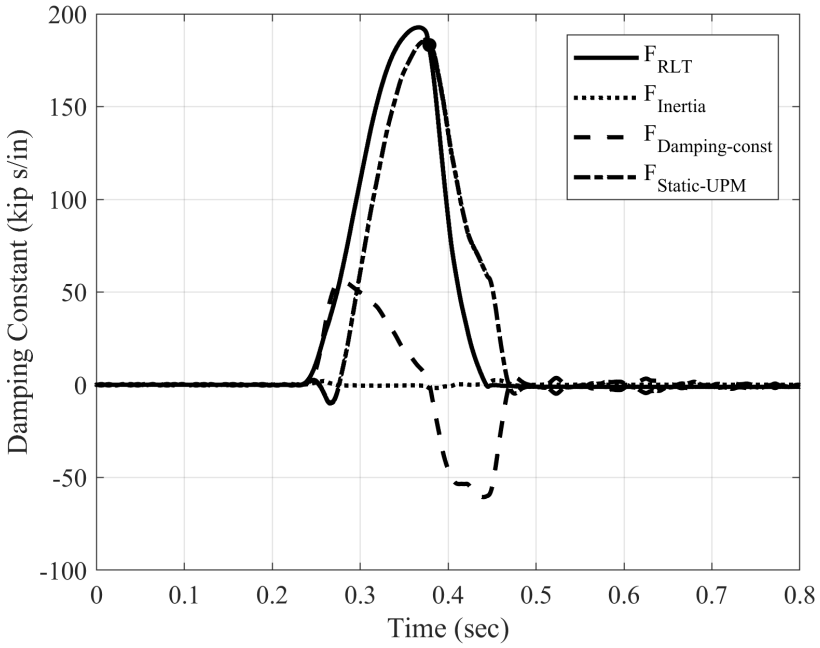

Figure B.6: Separation of forces for the pulse corresponding to 4Hz and 0.40in peak input displacement

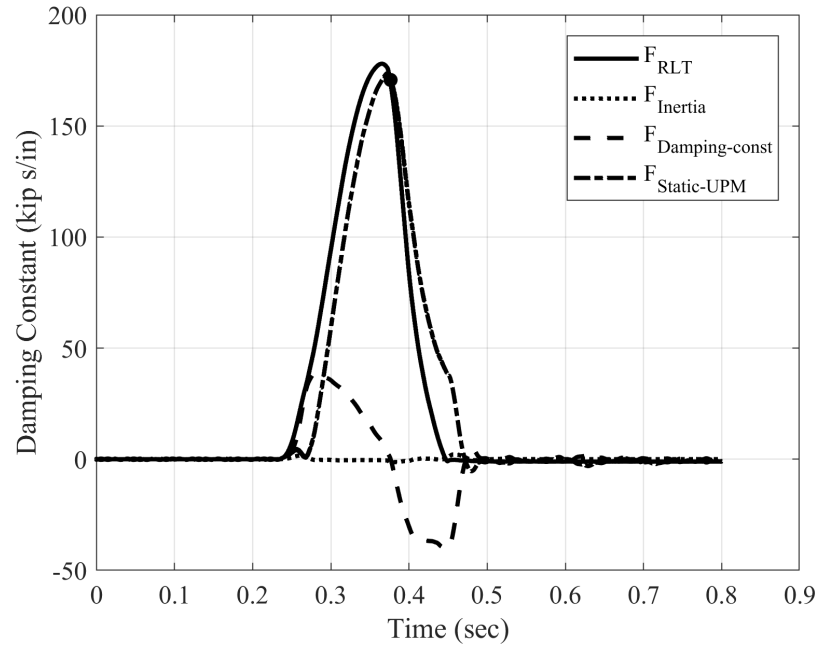

Figure B.7: Separation of forces for the pulse corresponding to 4Hz and 0.35in peak input displacement

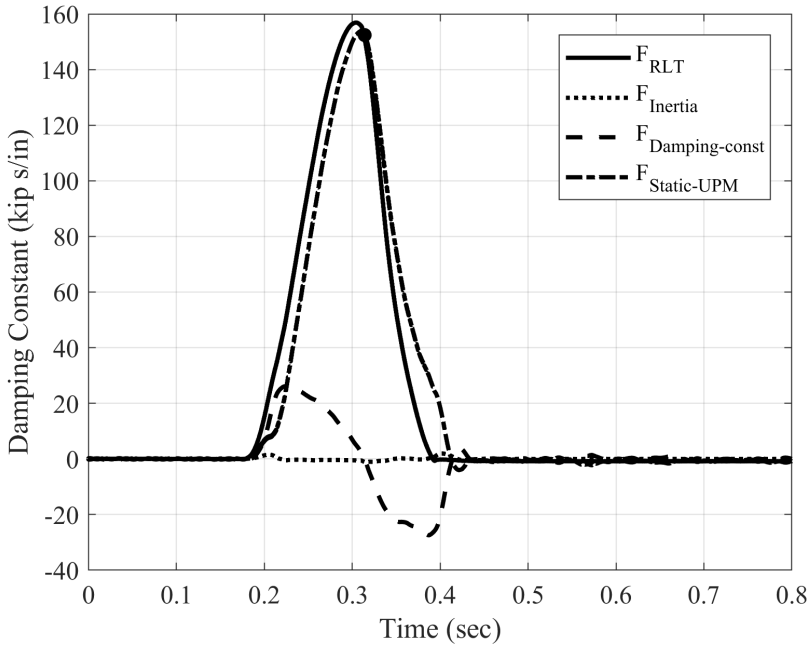

Figure B.8: Separation of forces for the pulse corresponding to 4Hz and 0.30in peak input displacement

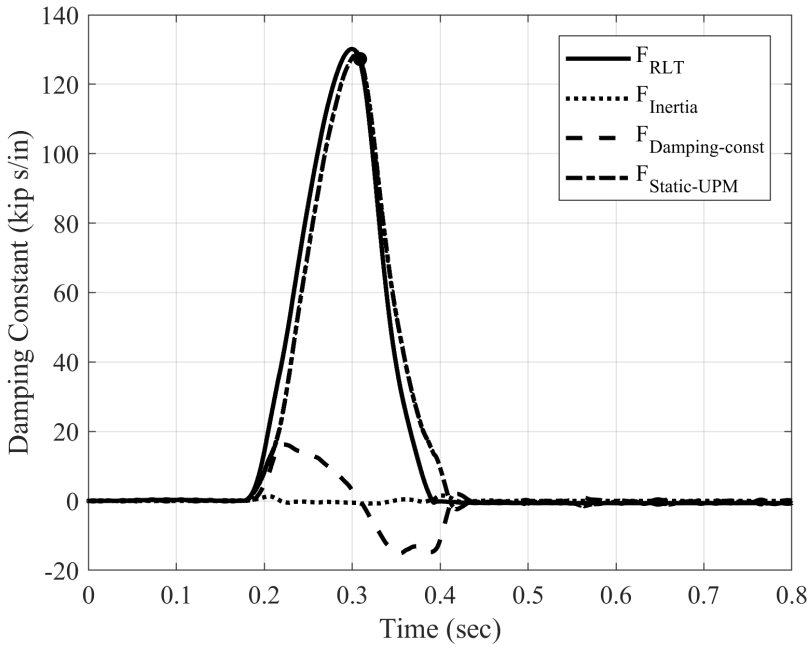

Figure B.9: Separation of forces for the pulse corresponding to 4Hz and 0.25in peak input displacement

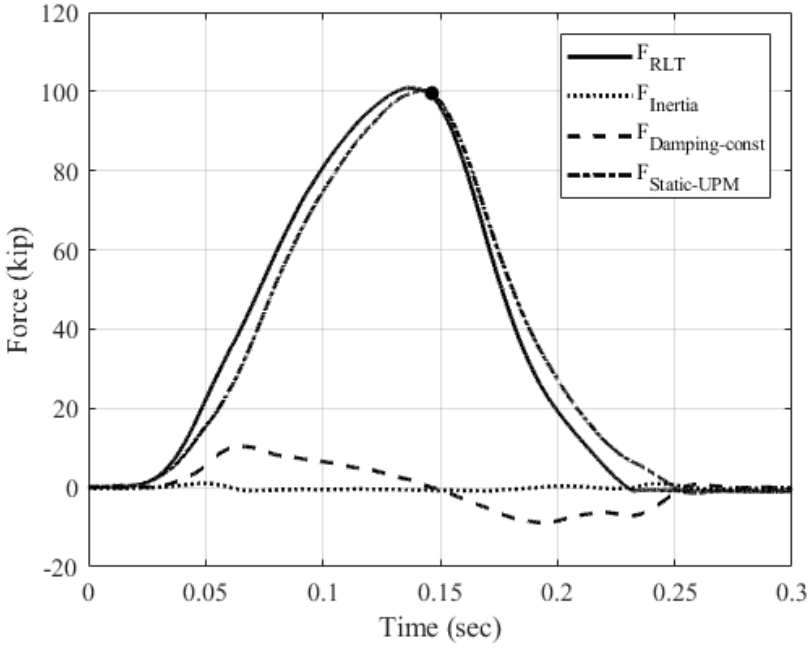

Figure B.10: Separation of forces for the pulse corresponding to 4Hz and 0.20in peak input displacement

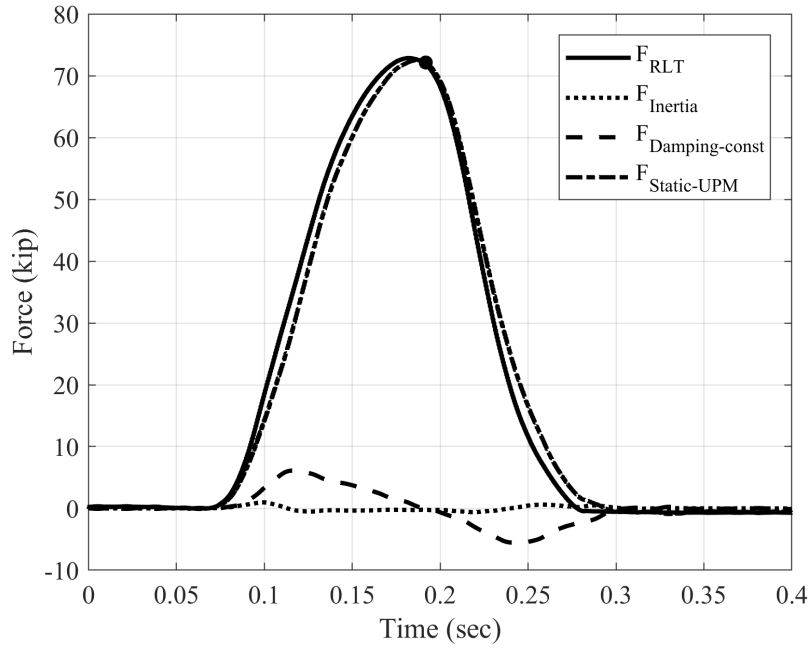

Figure B.11: Separation of forces for the pulse corresponding to 4Hz and 0.15in peak input displacement

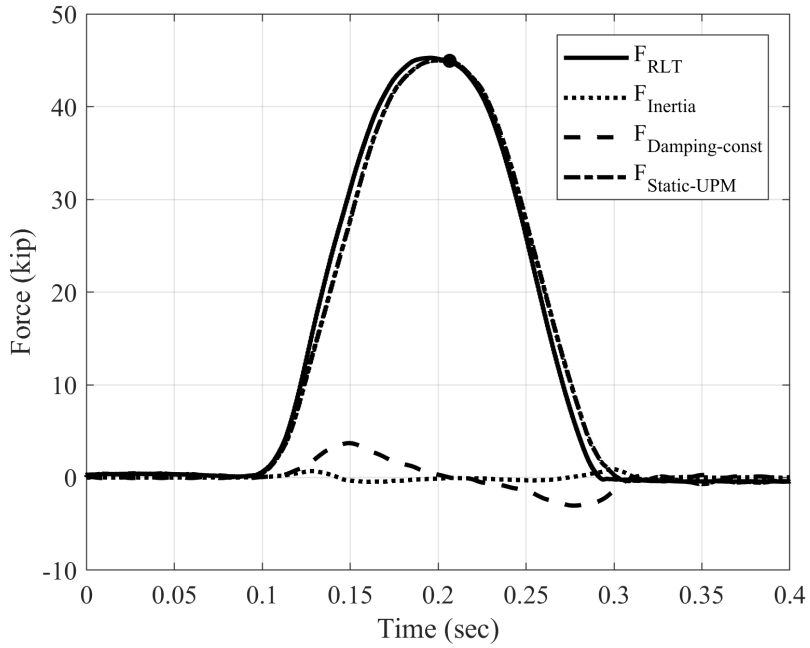

Figure B.12: Separation of forces for the pulse corresponding to 4Hz and 0.10in peak input displacement

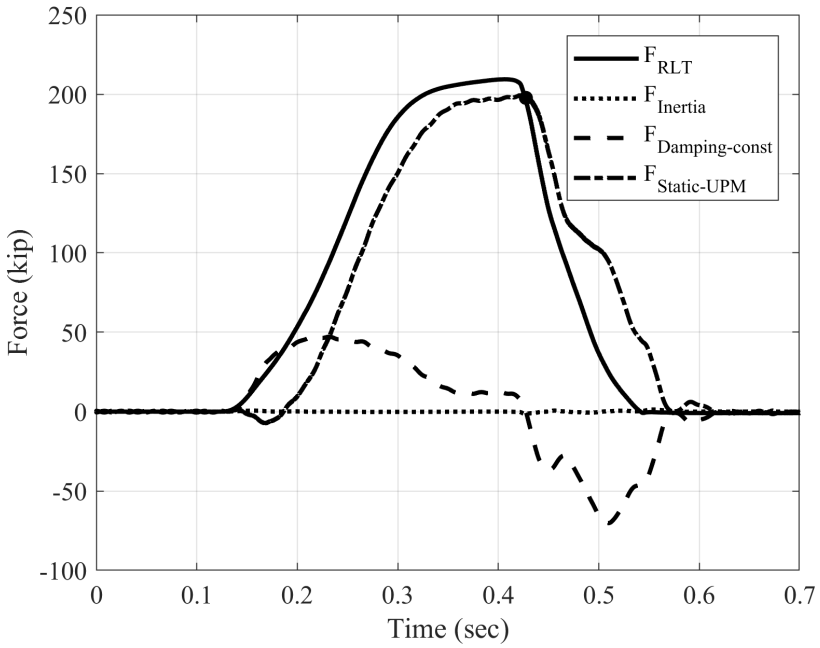

Figure B.13: Separation of forces for the pulse corresponding to 2Hz and 0.50in peak input displacement

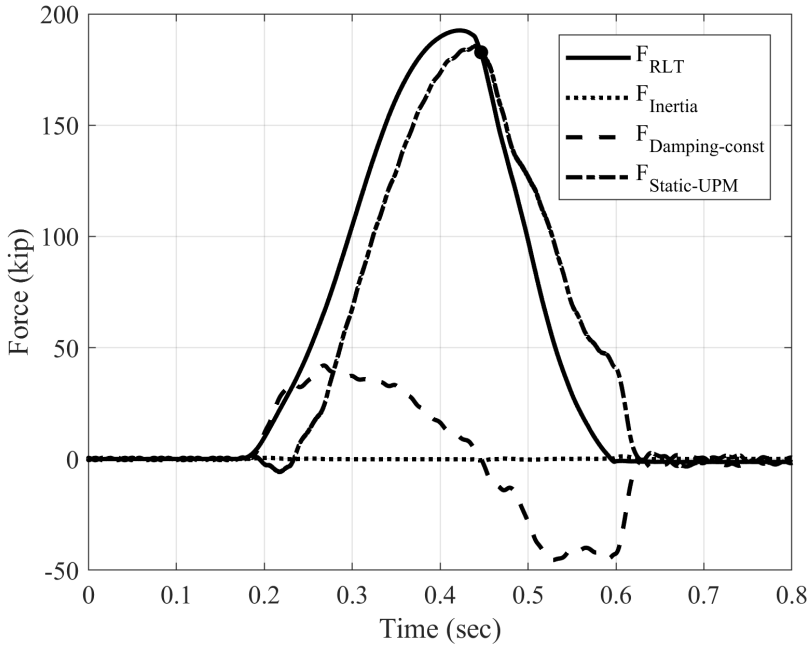

Figure B.14: Separation of forces for the pulse corresponding to 2Hz and 0.40in peak input displacement

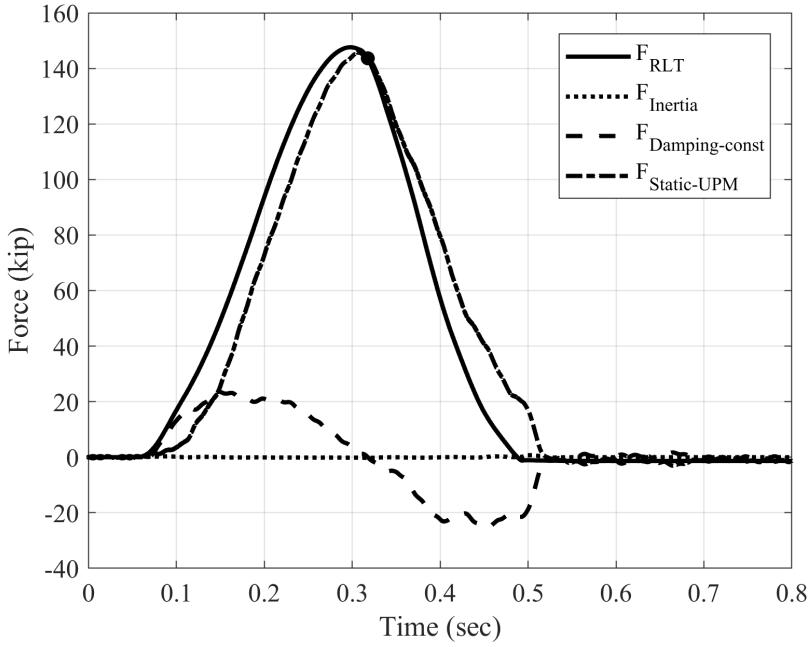

Figure B.15: Separation of forces for the pulse corresponding to 2Hz and 0.30in peak input displacement

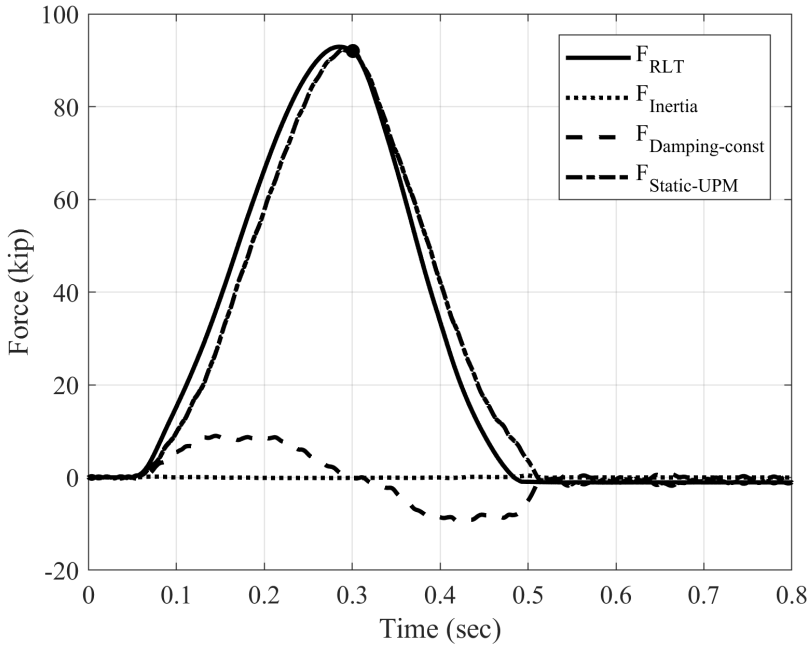

Figure B.16: Separation of forces for the pulse corresponding to 2Hz and 0.20in peak input displacement

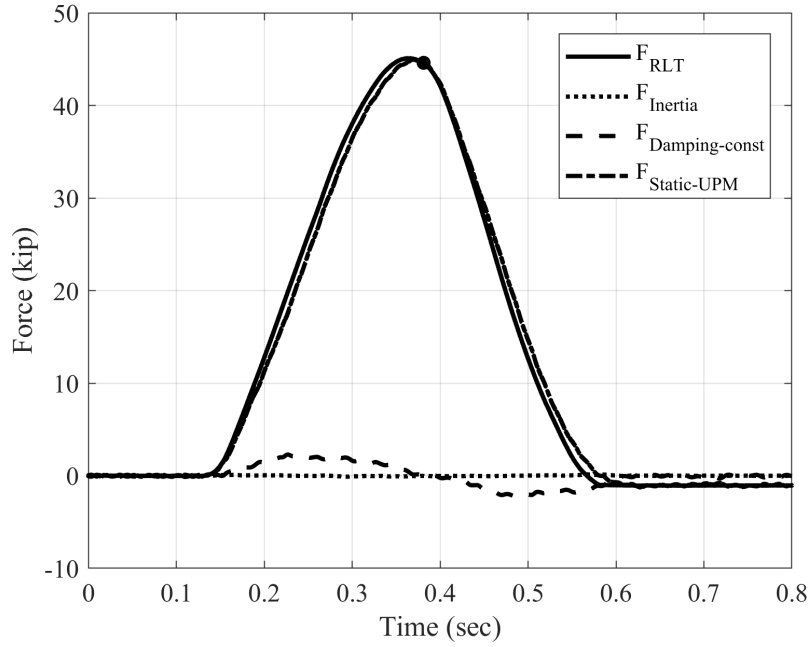

Figure B.17: Separation of forces for the pulse corresponding to 2Hz and 0.10in peak input displacement

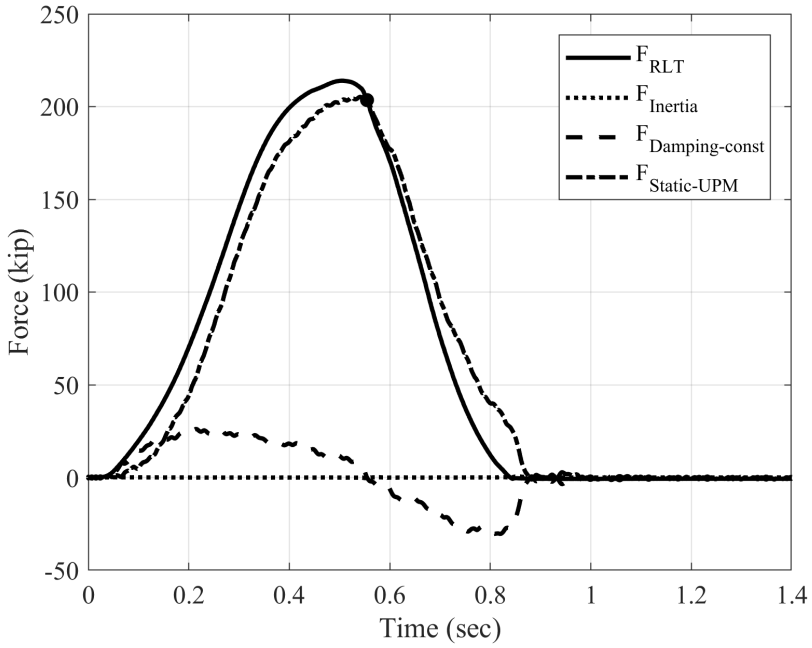

Figure B.18: Separation of forces for the pulse corresponding to 1Hz and 0.50in peak input displacement

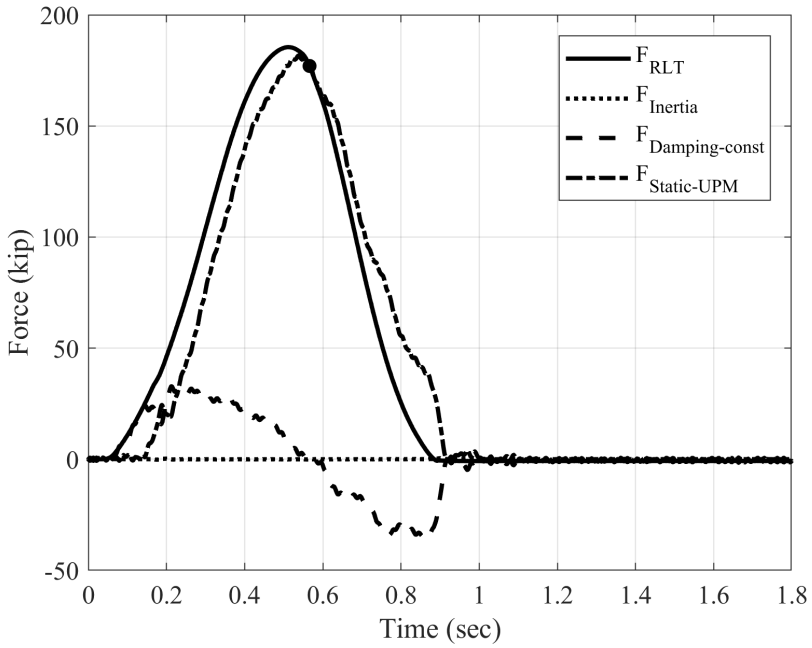

Figure B.19: Separation of forces for the pulse corresponding to 1Hz and 0.40in peak input displacement

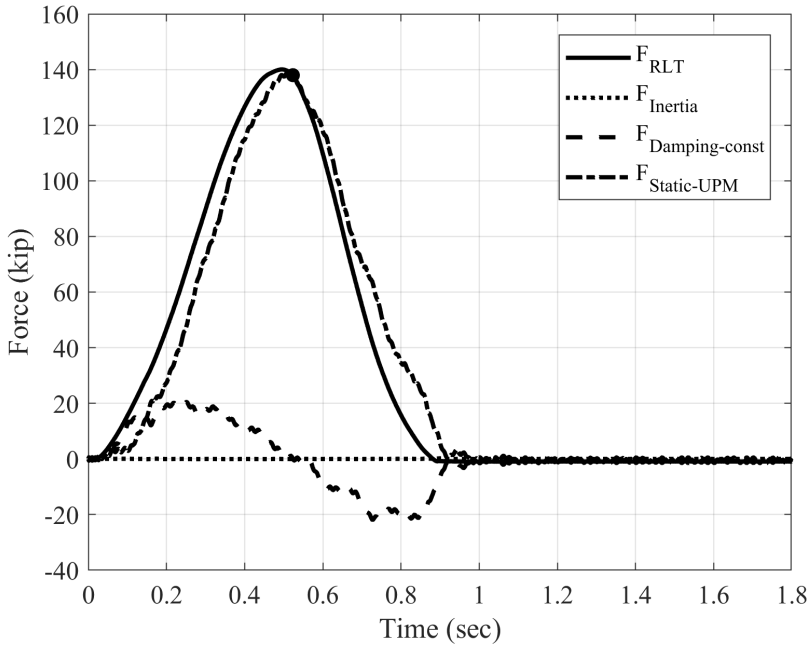

Figure B.20: Separation of forces for the pulse corresponding to 1Hz and 0.30in peak input displacement

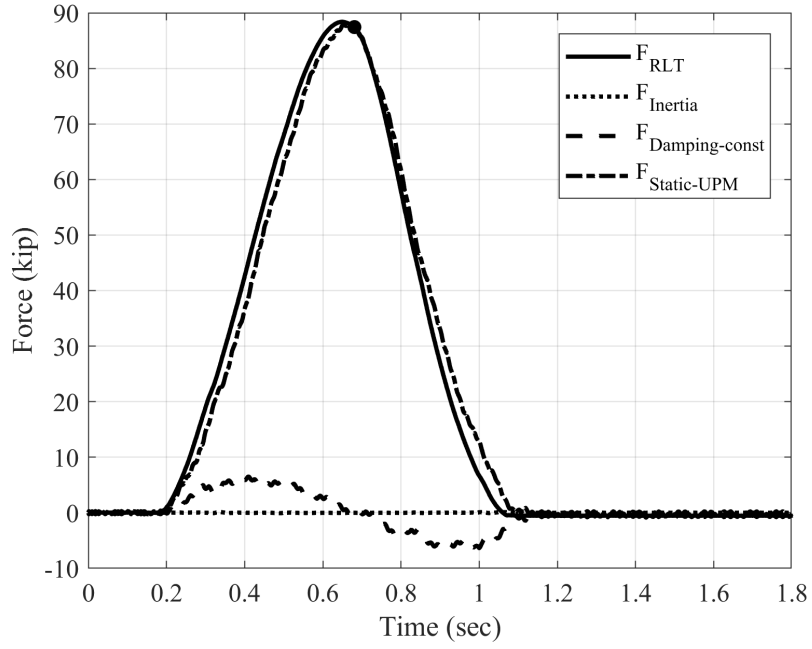

Figure B.21: Separation of forces for the pulse corresponding to 1Hz and 0.20in peak input displacement

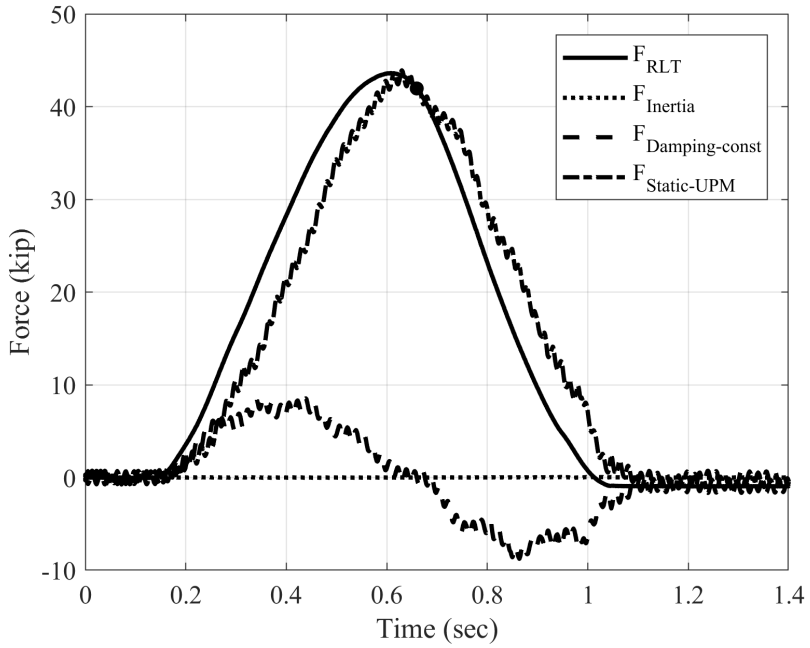

Figure B.22: Separation of forces for the pulse corresponding to 1Hz and 0.10in peak input displacement

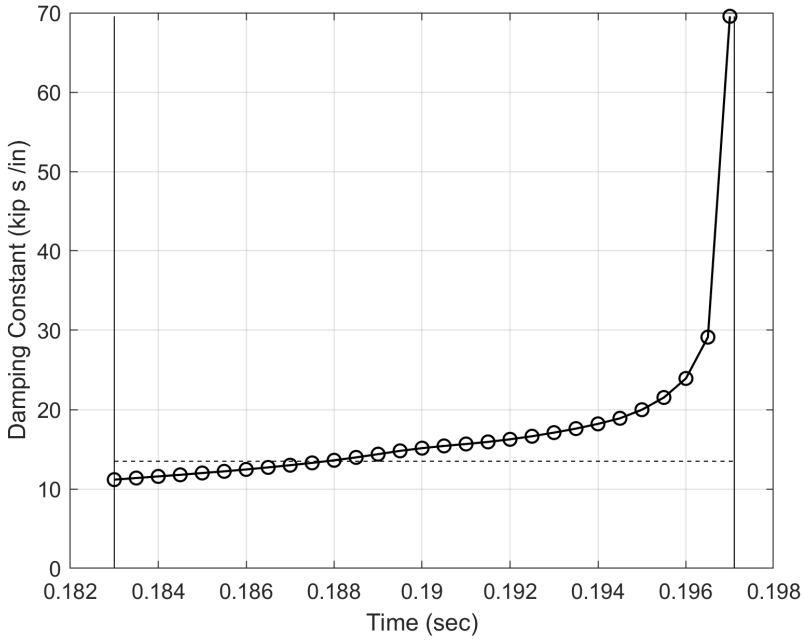

Figure B.23: Estimating the damping constant for 6Hz and 0.30in pulse using the UP method

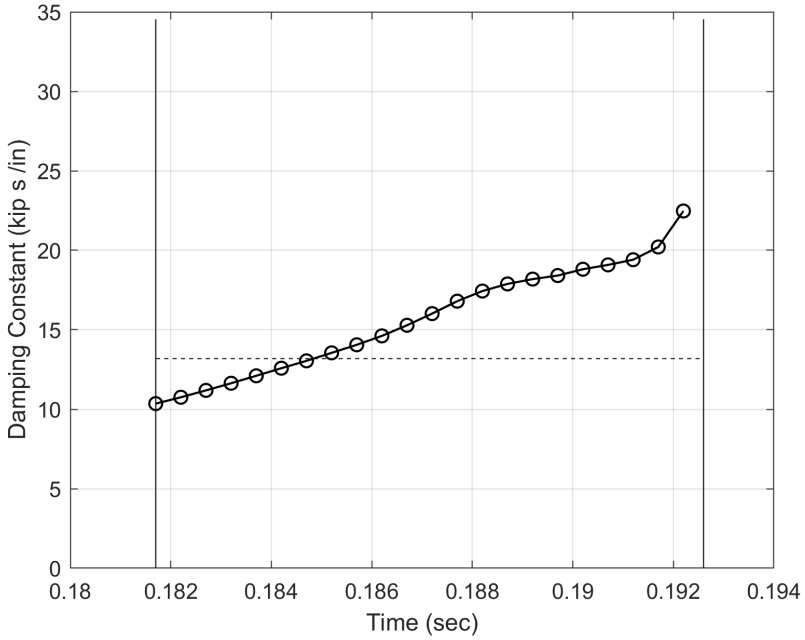

Figure B.24: Estimating the damping constant for 6Hz and 0.25in pulse using the UP method

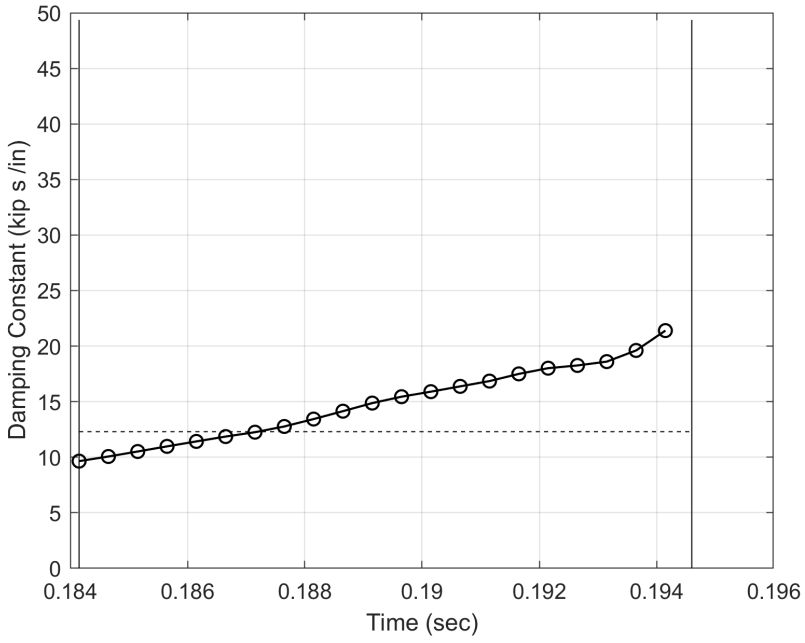

Figure B.25: Estimating the damping constant for 6Hz and 0.20in pulse using the UP method

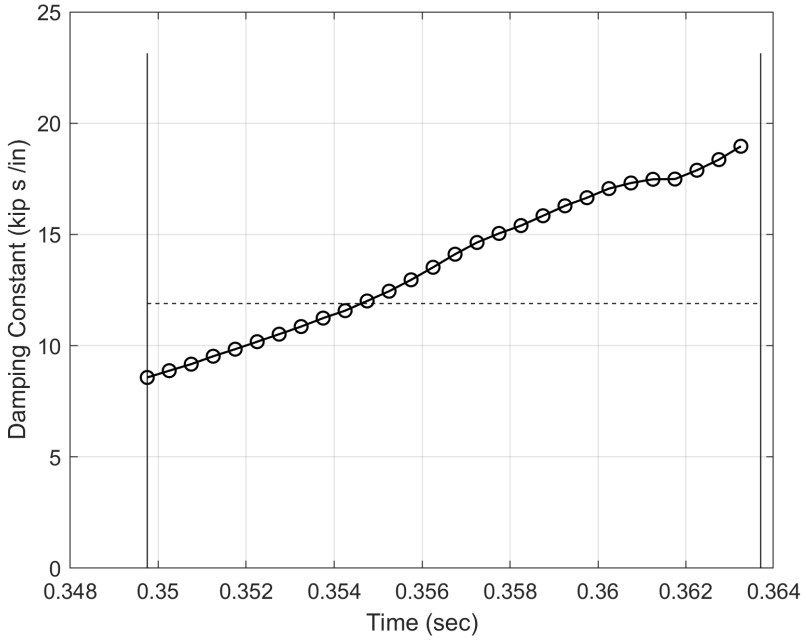

Figure B.26: Estimating the damping constant for 6Hz and 0.15in pulse using the UP method

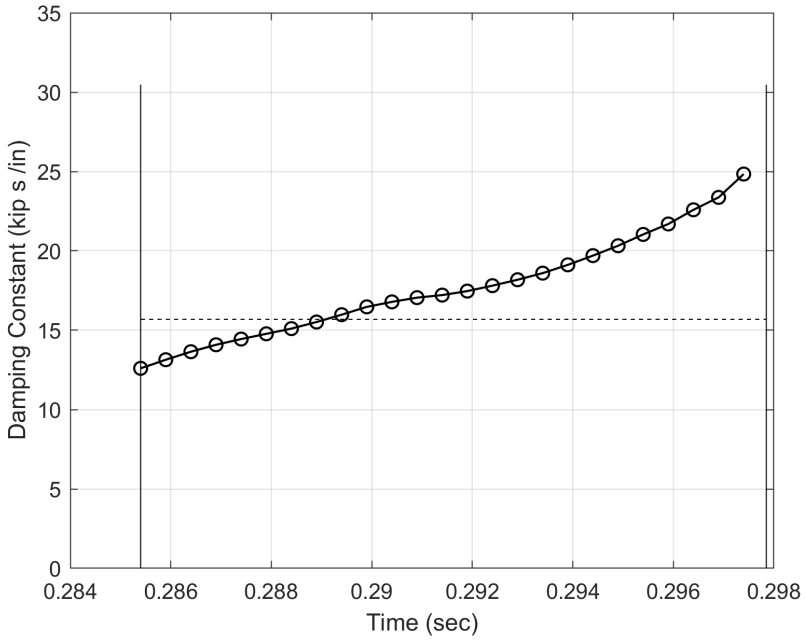

Figure B.27: Estimating the damping constant for 6Hz and 0.10in pulse using the UP method

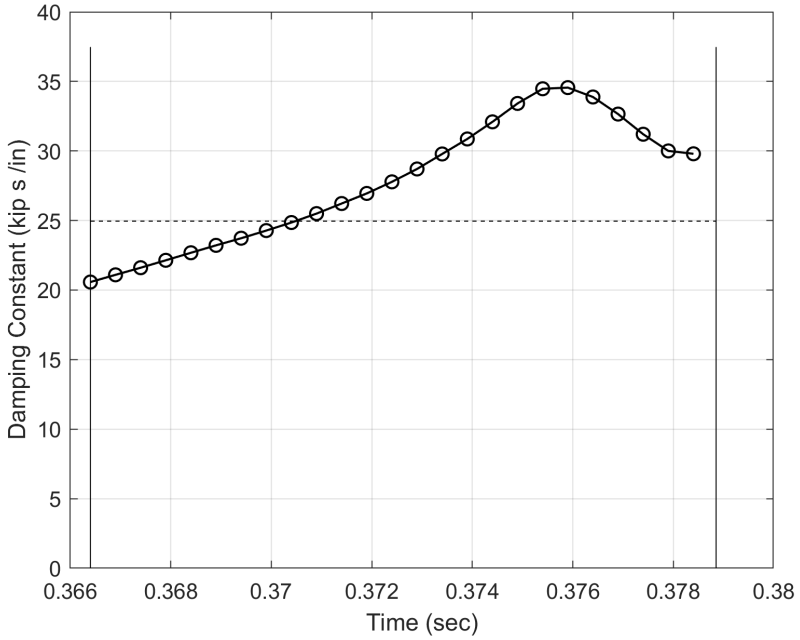

Figure B.28: Estimating the damping constant for 4Hz and 0.40in pulse using the UP method

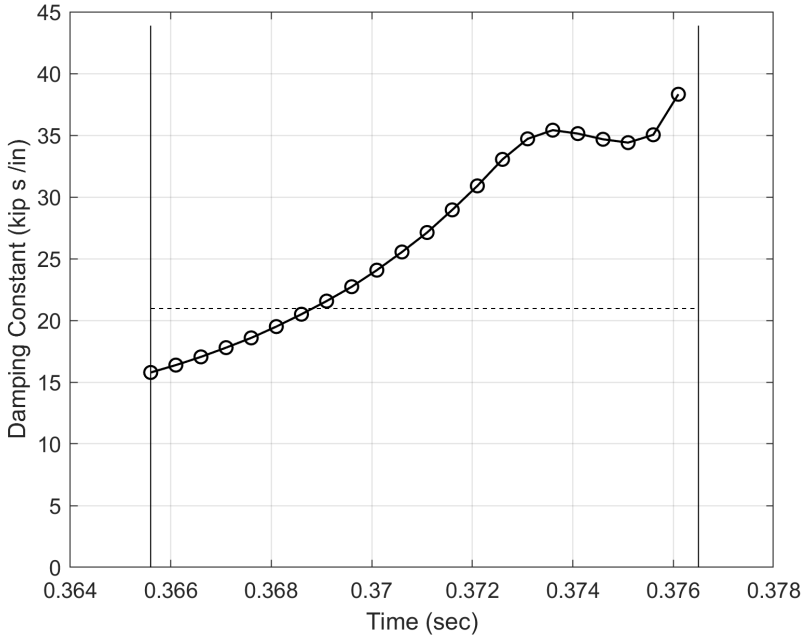

Figure B.29: Estimating the damping constant for 4Hz and 0.35in pulse using the UP method

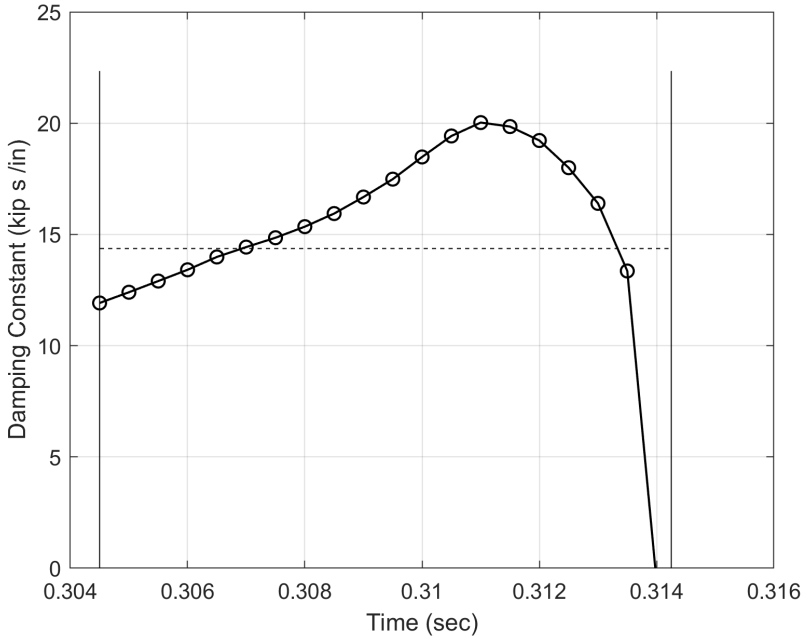

Figure B.30: Estimating the damping constant for 4Hz and 0.30in pulse using the UP method

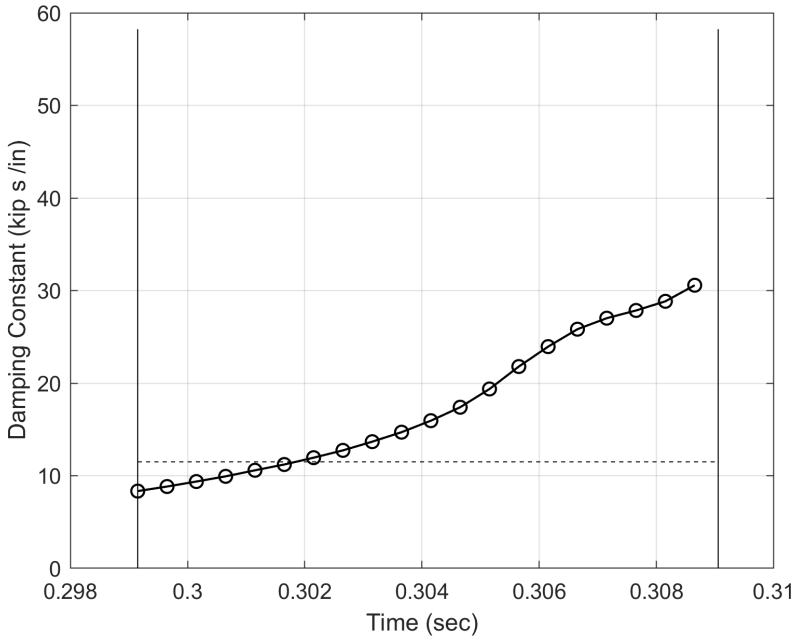

Figure B.31: Estimating the damping constant for 4Hz and 0.25in pulse using the UP method

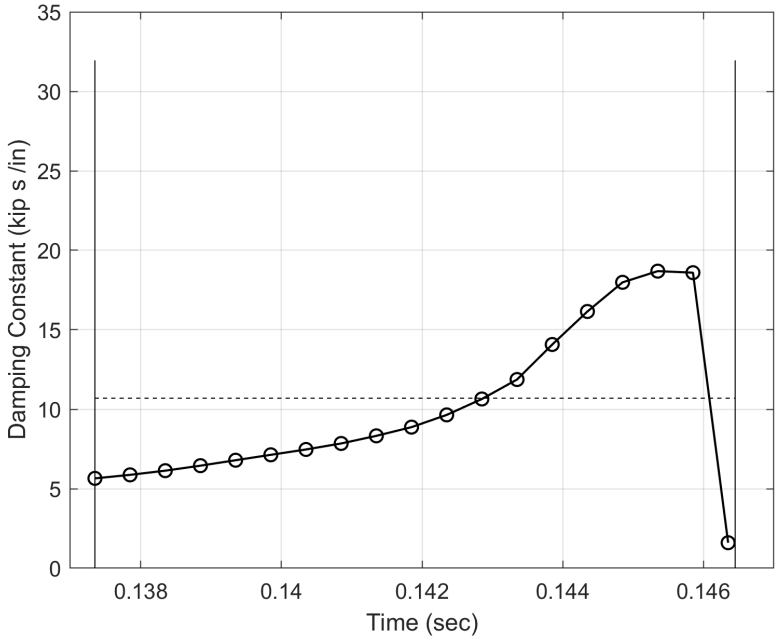

Figure B.32: Estimating the damping constant for 4Hz and 0.20in pulse using the UP method

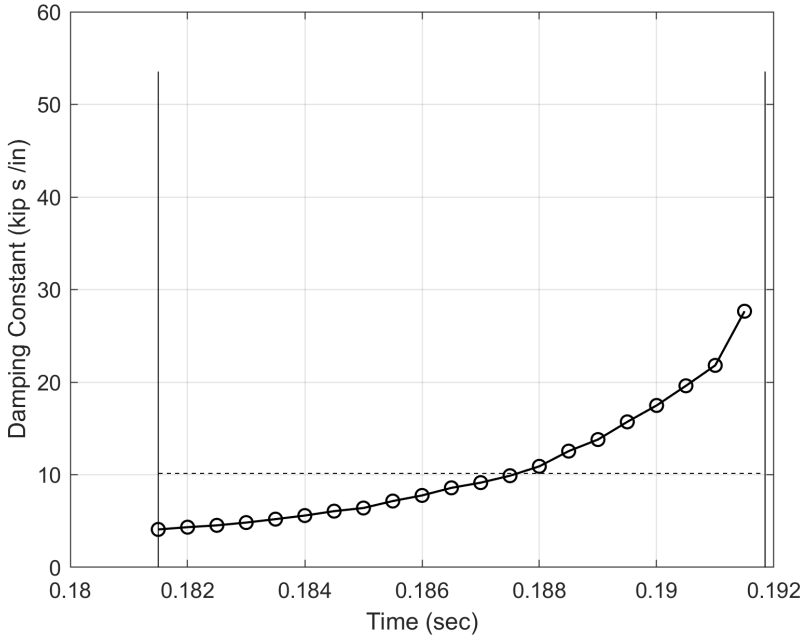

Figure B.33: Estimating the damping constant for 4Hz and 0.15in pulse using the UP method

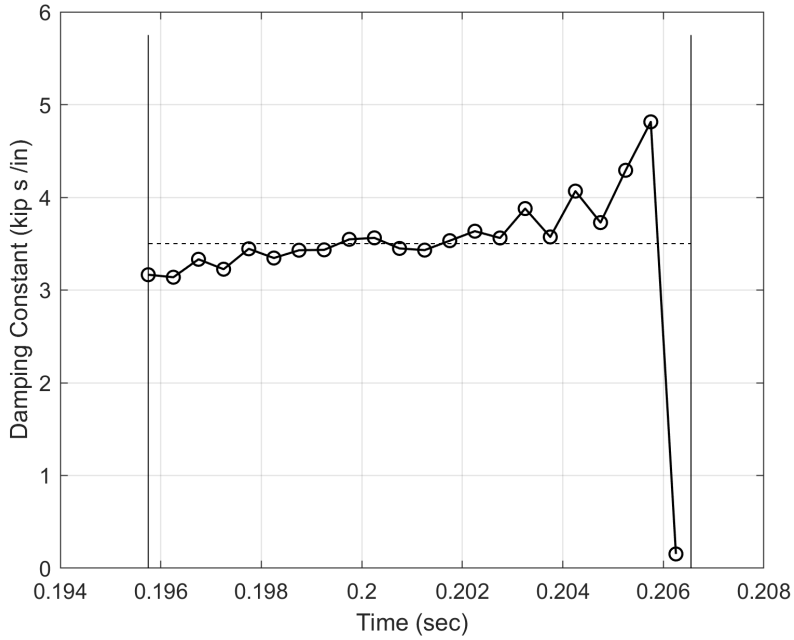

Figure B.34: Estimating the damping constant for 4Hz and 0.10in pulse using the UP method

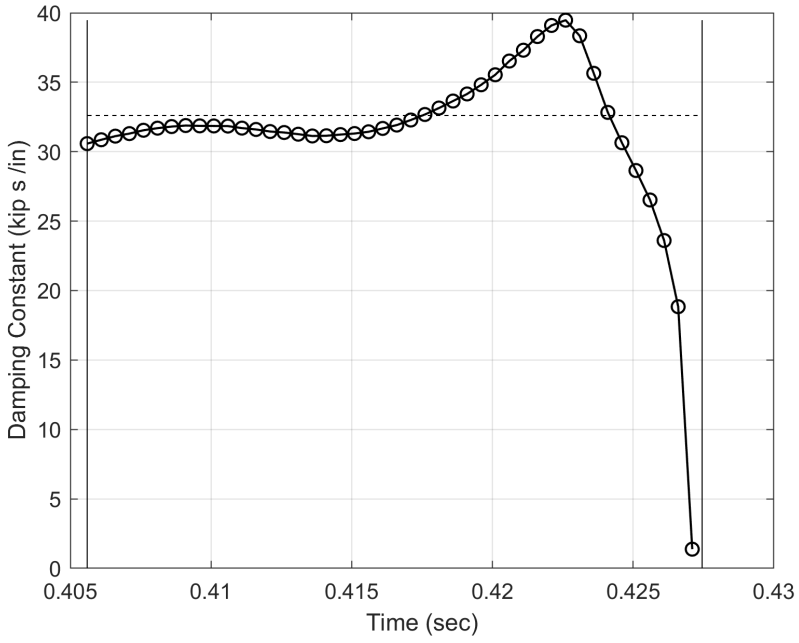

Figure B.35: Estimating the damping constant for 2Hz and 0.50in pulse using the UP method

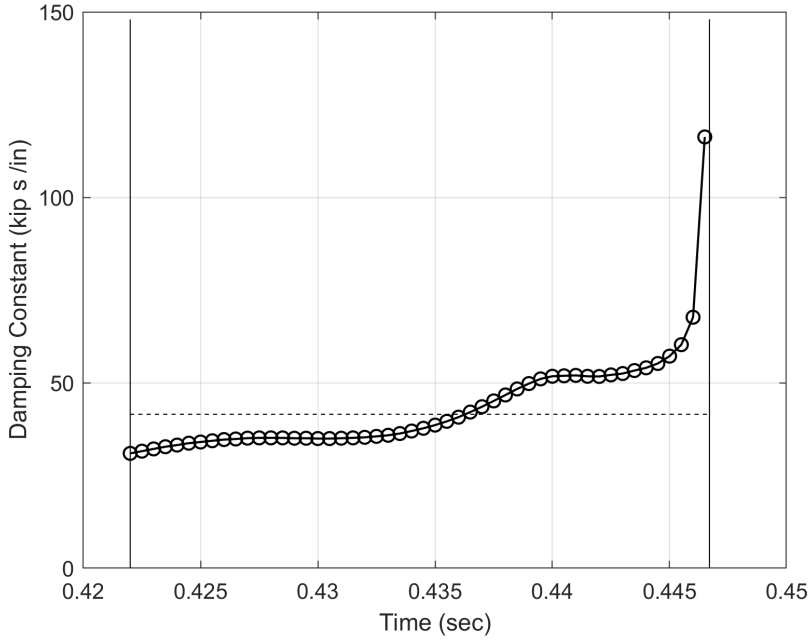

Figure B.36: Estimating the damping constant for 2Hz and 0.40in pulse using the UP method

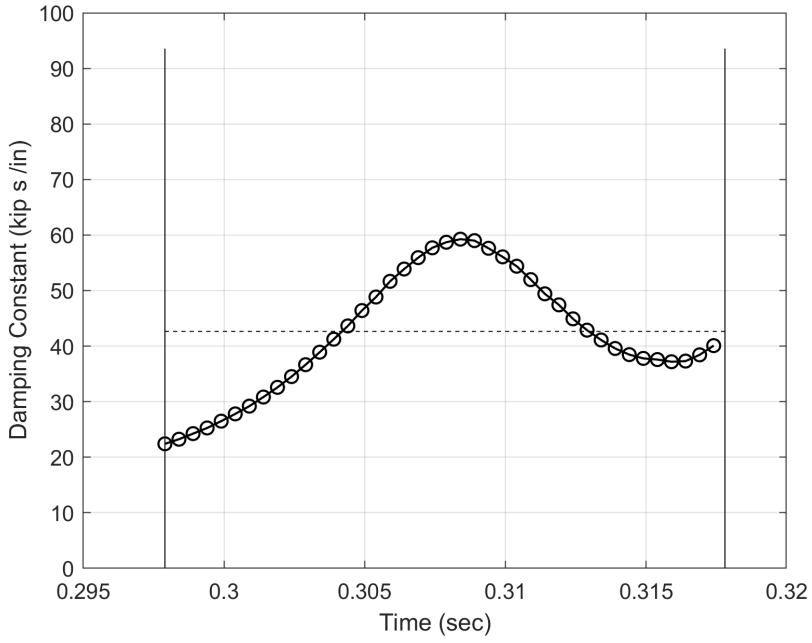

Figure B.37: Estimating the damping constant for 2Hz and 0.30in pulse using the UP method

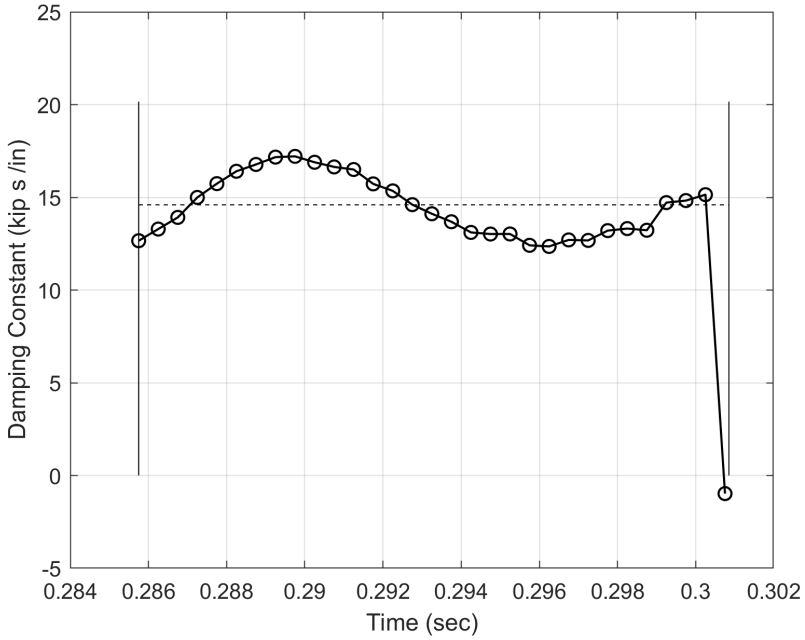

Figure B.38: Estimating the damping constant for 2Hz and 0.20in pulse using the UP method

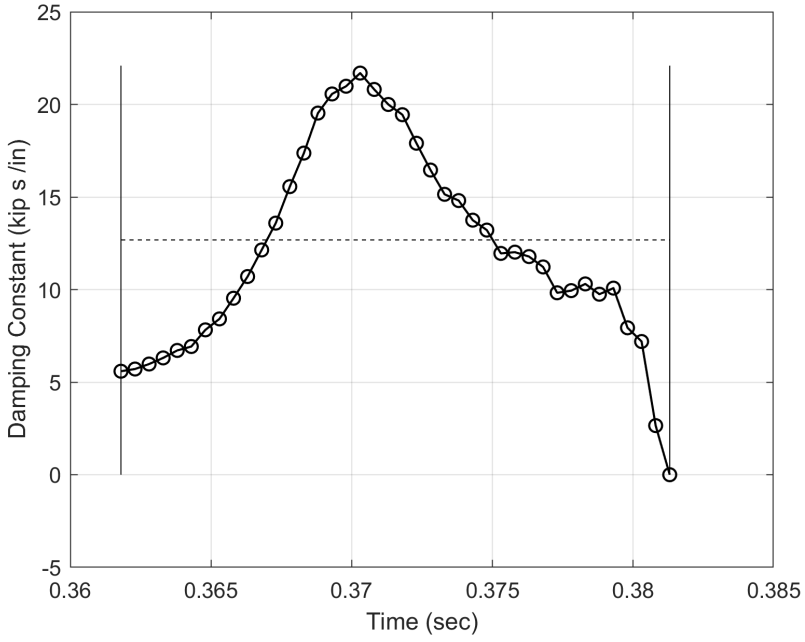

Figure B.39: Estimating the damping constant for 2Hz and 0.10in pulse using the UP method

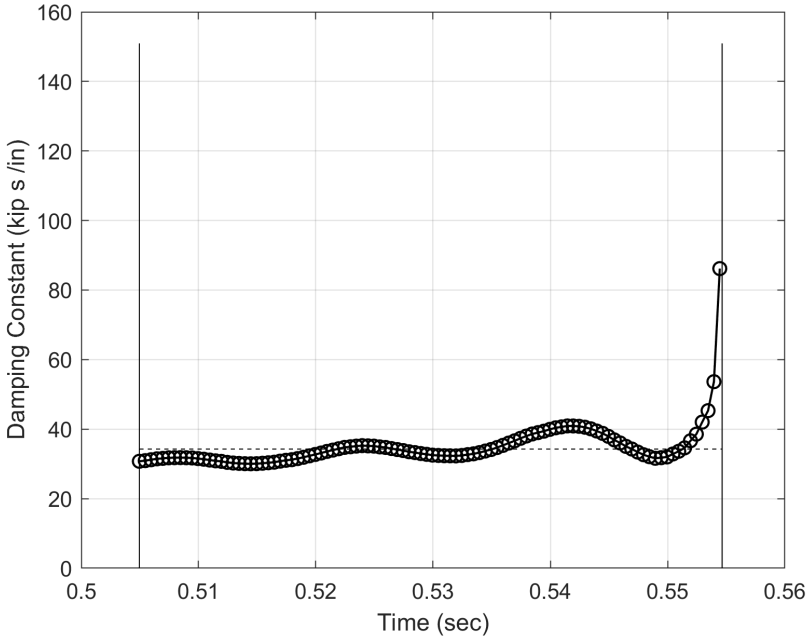

Figure B.40: Estimating the damping constant for 1Hz and 0.50in pulse using the UP method

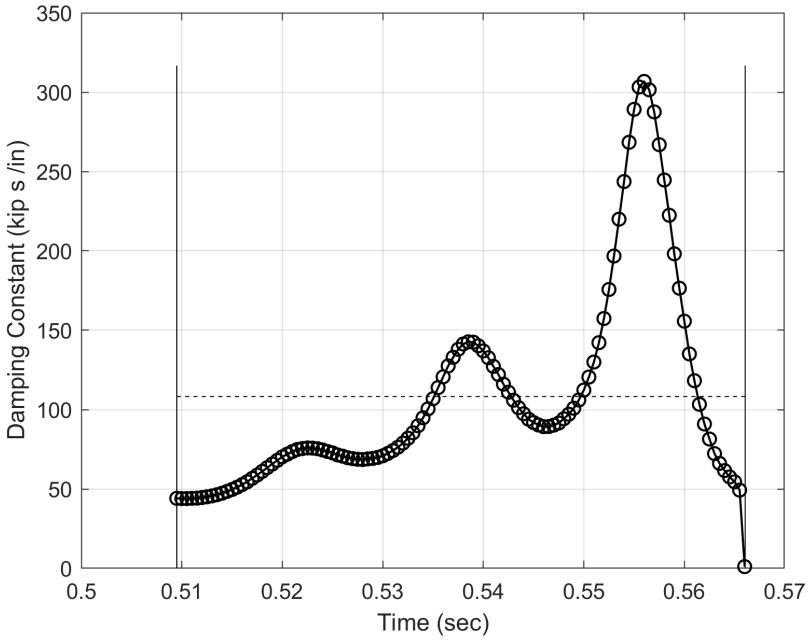

Figure B.41: Estimating the damping constant for 1Hz and 0.40in pulse using the UP method

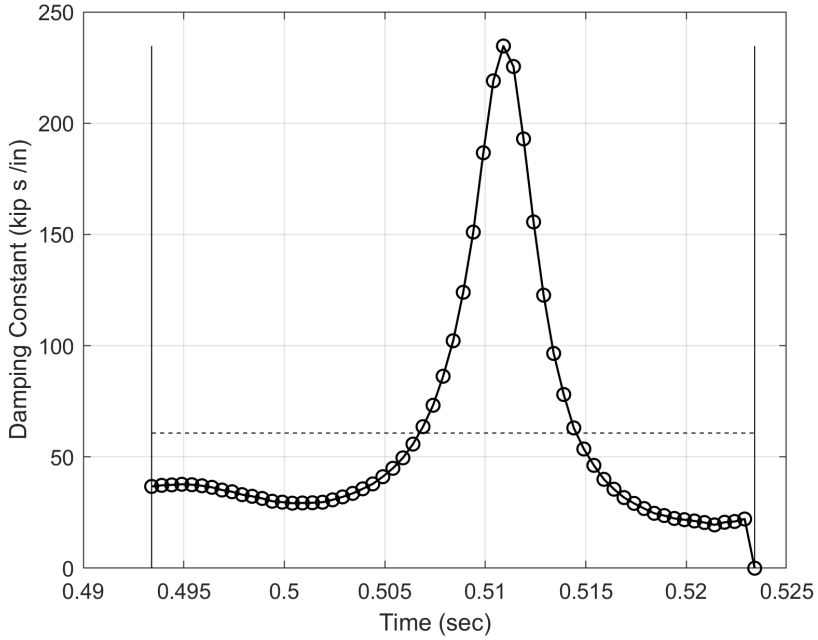

Figure B.42: Estimating the damping constant for 1Hz and 0.30in pulse using the UP method

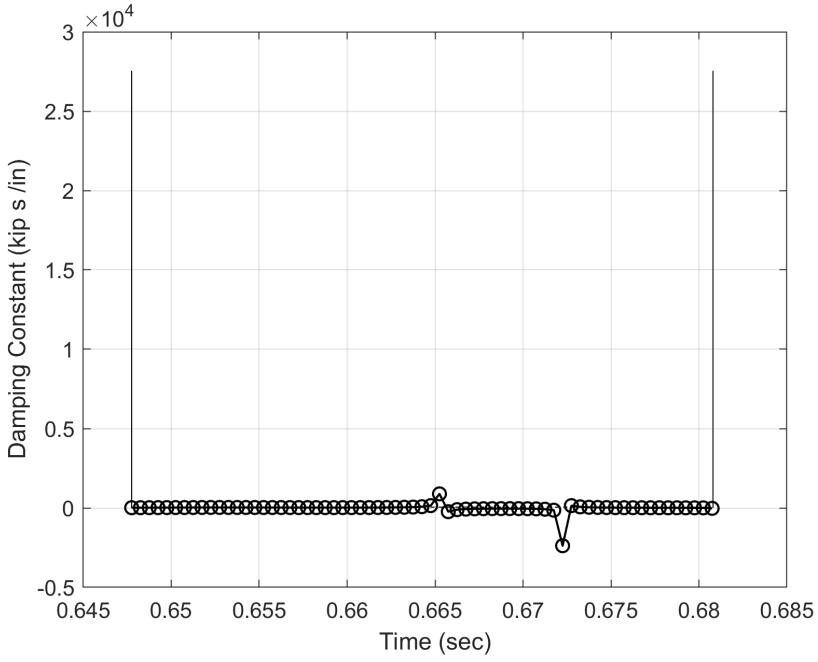

Figure B.43: Estimating the damping constant for 1Hz and 0.20in pulse using the UP method

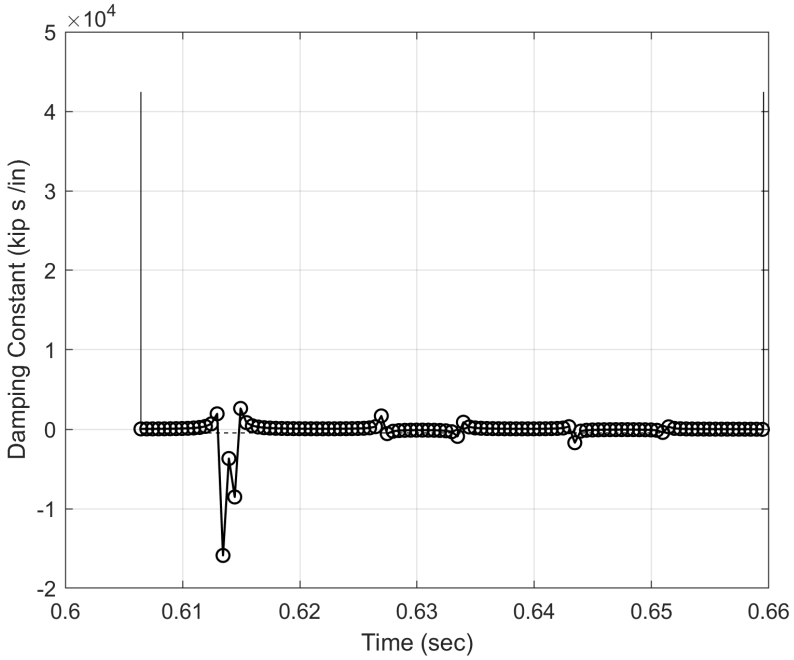

Figure B.44: Estimating the damping constant for 1Hz and 0.10in pulse using the UP method

APPENDIX C: ADDITIONAL INFORMATION FOR DYNAMIC LOAD TEST

Table C.1: Identified resistance parameters for sheet pile Using the RSS definition

Case	MQ	$R_{u,1}$	$R_{u,2}$	$R_{u,3}$	$R_{u,4}$	R_{shaft}	$R_{u,toe}$	$R_{u,total}$
Blow 1 Run 1	10421.581	17.03	0.26	0.12	0.10	**17.52**	**15.06**	**32.58**
Blow 1 Run 2	10487.949	20.56	0.27	0.25	0.23	**21.31**	**8.42**	**29.73**
Blow 1 Run 3	10446.368	19.01	1.60	0.22	0.14	**20.98**	**10.88**	**31.86**
Blow 1 Run 4	10432.466	20.56	1.57	0.14	0.22	**22.50**	**9.12**	**31.62**
Blow 1 Run 5	10451.749	21.65	0.28	0.21	0.20	**22.33**	**8.39**	**30.73**
Blow 2 Run 1	4956.080	16.98	4.68	0.27	12.11	**34.05**	**8.33**	**42.38**
Blow 2 Run 2	4946.225	23.84	3.94	3.58	0.15	**31.51**	**9.96**	**41.48**
Blow 2 Run 3	4963.311	19.39	2.24	0.55	7.50	**29.68**	**10.56**	**40.24**
Blow 2 Run 4	5013.149	15.09	5.76	0.11	19.75	**40.71**	**2.11**	**42.82**
Blow 2 Run 5	4961.582	17.09	3.55	0.17	0.13	**20.94**	**19.94**	**40.88**
Blow 3 Run 1	50954.348	8.99	25.25	2.16	1.81	**38.21**	**3.89**	**42.10**
Blow 3 Run 2	50991.577	8.70	25.13	0.48	1.42	**35.73**	**7.00**	**42.73**
Blow 3 Run 3	50730.532	7.72	24.04	2.94	0.21	**34.90**	**9.35**	**44.25**
Blow 3 Run 4	50881.044	8.36	25.87	1.03	0.28	**35.54**	**8.41**	**43.95**
Blow 3 Run 5	51340.833	8.61	26.28	0.24	3.50	**38.64**	**4.23**	**42.87**
Blow 4 Run 1	41845.379	14.08	10.88	0.14	0.13	**25.23**	**8.12**	**33.34**
Blow 4 Run 2	41756.691	8.28	7.64	0.15	0.12	**16.18**	**18.88**	**35.07**
Blow 4 Run 3	42613.079	13.51	5.89	0.32	4.54	**24.26**	**4.89**	**29.15**
Blow 4 Run 4	41818.654	12.22	14.68	0.10	0.16	**27.16**	**9.29**	**36.45**
Blow 4 Run 5	41780.182	14.11	11.47	0.25	0.12	**25.96**	**9.30**	**35.25**
Blow 5 Run 1	22333.076	14.17	11.60	1.08	0.31	**27.16**	**8.78**	**35.94**
Blow 5 Run 2	22427.084	8.98	9.96	0.25	0.44	**19.63**	**13.42**	**33.05**
Blow 5 Run 3	22516.943	11.97	10.21	0.20	0.32	**22.70**	**8.49**	**31.19**
Blow 5 Run 4	22395.430	8.13	12.96	0.13	0.33	**21.55**	**12.23**	**33.78**
Blow 5 Run 5	22372.943	9.33	14.84	0.15	0.11	**24.43**	**9.40**	**33.83**
Blow 6 Run 1	38678.209	0.12	17.63	0.16	5.68	**23.59**	**12.33**	**35.92**
Blow 6 Run 2	38649.713	0.35	13.07	1.39	10.61	**25.42**	**11.20**	**36.62**
Blow 6 Run 3	38616.579	1.21	8.38	0.85	10.08	**20.51**	**16.26**	**36.77**
Blow 6 Run 4	38735.321	1.27	14.45	0.62	12.59	**28.93**	**7.02**	**35.95**
Blow 6 Run 5	38714.662	1.87	14.51	2.11	3.00	**21.49**	**13.93**	**35.42**
Blow 7 Run 1	44044.305	17.72	0.11	0.10	0.12	**18.05**	**7.01**	**25.06**
Blow 7 Run 2	44037.274	12.51	0.13	0.13	0.10	**12.88**	**13.37**	**26.25**
Blow 7 Run 3	44043.316	11.23	0.12	0.14	0.12	**11.61**	**15.11**	**26.72**
Blow 7 Run 4	44057.223	15.27	0.12	0.13	0.10	**15.63**	**11.92**	**27.55**
Blow 7 Run 5	44045.908	8.85	0.15	0.10	0.14	**9.24**	**17.18**	**26.43**
Blow 8 Run 1	14864.233	10.05	0.27	0.11	0.11	**10.53**	**19.42**	**29.95**
Blow 8 Run 2	14904.539	13.79	0.77	0.44	5.08	**20.08**	**9.32**	**29.40**
Blow 8 Run 3	14868.534	19.00	0.13	0.25	0.18	**19.56**	**10.17**	**29.72**
Blow 8 Run 4	14869.321	18.18	0.31	0.20	0.19	**18.87**	**10.70**	**29.57**
Blow 8 Run 5	14874.718	19.30	0.31	0.30	0.10	**20.01**	**9.22**	**29.24**
Blow 9 Run 1	2840.391	11.23	0.10	0.13	0.12	**11.58**	**16.00**	**27.58**
Blow 9 Run 2	2847.732	16.17	0.16	0.11	0.18	**16.62**	**11.52**	**28.14**
Blow 9 Run 3	2841.855	11.98	0.14	0.18	0.11	**12.40**	**15.32**	**27.72**
Blow 9 Run 4	3014.833	13.75	0.10	0.10	9.39	**23.34**	**1.52**	**24.87**
Blow 9 Run 5	2986.977	12.72	0.11	0.10	11.68	**24.61**	**1.37**	**25.98**
Average	25697.198	**12.55**	**7.38**	**0.51**	**2.76**	**23.194**	**10.41**	**33.602**
Std. Dev.	-	**5.87**	**8.41**	**0.77**	**4.66**	**7.804**	**4.46**	**5.782**

Table C.2: Identified resistance parameters for H-Pile using the RSS definition

Case	MQ	$R_{u,1}$	$R_{u,2}$	$R_{u,3}$	$R_{u,4}$	R_{shaft}	$R_{u,toe}$	$R_{u,total}$
Blow 1 Run 1	5902.531	8.57	1.01	2.25	0.11	**11.95**	**1.76**	**13.70**
Blow 1 Run 2	5904.041	8.41	1.29	1.84	0.14	**11.68**	**2.32**	**14.00**
Blow 1 Run 3	5902.863	8.32	0.85	2.41	0.17	**11.75**	**1.77**	**13.51**
Blow 1 Run 4	5902.451	8.33	0.93	2.06	0.10	**11.41**	**2.50**	**13.92**
Blow 1 Run 5	5902.526	8.34	0.85	2.24	0.58	**12.00**	**1.59**	**13.59**
Blow 2 Run 1	7855.447	6.18	0.12	0.17	11.86	**18.34**	**2.96**	**21.30**
Blow 2 Run 2	7856.134	7.07	0.11	0.12	11.03	**18.33**	**3.49**	**21.82**
Blow 2 Run 3	7858.446	6.95	0.21	0.81	10.89	**18.85**	**2.05**	**20.91**
Blow 2 Run 4	7854.824	6.74	0.16	0.35	13.26	**20.52**	**0.89**	**21.41**
Blow 2 Run 5	7853.908	7.11	0.12	0.11	13.26	**20.60**	**0.87**	**21.46**
Blow 3 Run 1	13153.949	7.26	0.10	0.11	8.04	**15.51**	**1.58**	**17.09**
Blow 3 Run 2	13133.273	10.56	0.11	0.14	3.03	**13.84**	**2.76**	**16.60**
Blow 3 Run 3	13127.502	8.06	0.16	0.12	0.73	**9.06**	**7.84**	**16.90**
Blow 3 Run 4	13127.981	11.75	0.11	0.11	1.91	**13.88**	**3.05**	**16.94**
Blow 3 Run 5	13137.956	5.06	0.16	0.14	2.30	**7.65**	**9.75**	**17.40**
Blow 4 Run 1	4866.311	5.05	0.10	0.10	2.29	**7.54**	**3.62**	**11.16**
Blow 4 Run 2	4864.697	4.45	0.10	0.10	2.47	**7.13**	**3.96**	**11.09**
Blow 4 Run 3	4866.046	4.64	0.12	0.13	1.82	**6.72**	**4.16**	**10.88**
Blow 4 Run 4	4867.984	4.74	0.15	0.27	3.00	**8.15**	**3.16**	**11.31**
Blow 4 Run 5	4862.850	4.34	0.10	0.20	1.49	**6.13**	**5.11**	**11.23**
Average	7940.086	**7.10**	**0.34**	**0.69**	**4.42**	**12.551**	**3.26**	**15.811**
Std. Dev.	-	**2.03**	**0.39**	**0.89**	**4.87**	**4.789**	**2.21**	**3.931**

Table C.3: Identified other parameters for sheet piles using RSS match quality definition

Case	q_{shaft}	q_{toe}	Shaft $\frac{E_{un}}{E_u}$	Toe $\frac{E_{un}}{E_u}$	Shaft -$\frac{R_{un}}{R_u}$	Toe -$\frac{R_{un}}{R_u}$	J_{shaft}	J_{toe}	g_{toe}
Blow 1 Run 1	0.044	0.024	0.833	2.738	0.071	0.086	0.027	0.018	0.018
Blow 1 Run 2	0.029	0.022	3.032	2.590	0.222	0.910	0.030	0.034	0.005
Blow 1 Run 3	0.030	0.021	2.397	2.179	0.260	0.674	0.027	0.027	0.010
Blow 1 Run 4	0.028	0.029	2.136	2.629	0.286	0.901	0.026	0.032	0.001
Blow 1 Run 5	0.032	0.033	3.101	0.999	0.176	0.861	0.027	0.035	0.001
Blow 2 Run 1	0.025	0.023	1.014	2.207	0.817	0.584	0.011	0.015	0.001
Blow 2 Run 2	0.028	0.025	2.773	1.756	0.473	0.359	0.011	0.026	0.001
Blow 2 Run 3	0.024	0.021	2.573	1.888	0.310	0.735	0.017	0.015	0.004
Blow 2 Run 4	0.022	0.020	3.116	2.020	0.083	0.986	0.013	0.034	0.001
Blow 2 Run 5	0.034	0.021	0.439	2.527	0.423	0.378	0.017	0.014	0.007
Blow 3 Run 1	0.022	0.023	2.555	3.199	0.584	0.561	0.007	0.035	0.001
Blow 3 Run 2	0.021	0.022	1.797	3.266	0.776	0.862	0.008	0.026	0.001
Blow 3 Run 3	0.020	0.020	2.745	3.227	0.293	0.850	0.007	0.021	0.001
Blow 3 Run 4	0.022	0.020	1.689	3.201	0.952	0.408	0.007	0.023	0.003
Blow 3 Run 5	0.022	0.028	0.665	3.261	0.926	0.656	0.008	0.036	0.000
Blow 4 Run 1	0.031	0.024	0.839	2.673	0.201	0.690	0.006	0.027	0.009
Blow 4 Run 2	0.031	0.021	1.053	0.360	0.264	0.959	0.009	0.015	0.010
Blow 4 Run 3	0.025	0.028	1.888	1.851	0.745	0.366	0.013	0.036	0.002
Blow 4 Run 4	0.026	0.024	2.105	1.792	0.383	0.254	0.004	0.031	0.001
Blow 4 Run 5	0.024	0.023	1.595	3.108	0.433	0.110	0.006	0.030	0.002
Blow 5 Run 1	0.048	0.021	1.678	3.021	0.708	0.628	0.001	0.031	0.027
Blow 5 Run 2	0.035	0.034	0.568	3.157	0.572	0.201	0.007	0.020	0.001
Blow 5 Run 3	0.037	0.030	1.731	3.293	0.007	0.595	0.008	0.031	0.009
Blow 5 Run 4	0.036	0.029	2.829	3.266	0.759	0.491	0.005	0.023	0.007
Blow 5 Run 5	0.042	0.023	2.927	3.173	0.427	0.368	0.004	0.031	0.019
Blow 6 Run 1	0.036	0.031	0.533	2.341	0.722	0.626	0.001	0.019	0.004
Blow 6 Run 2	0.029	0.021	2.100	3.097	0.155	0.531	0.001	0.023	0.007
Blow 6 Run 3	0.027	0.023	2.695	1.810	0.394	0.313	0.001	0.016	0.003
Blow 6 Run 4	0.029	0.021	2.635	1.318	0.785	0.471	0.002	0.036	0.008
Blow 6 Run 5	0.031	0.024	2.989	2.506	0.862	0.430	0.002	0.019	0.008
Blow 7 Run 1	0.035	0.031	2.357	2.450	0.196	0.982	0.005	0.035	0.006
Blow 7 Run 2	0.033	0.023	3.052	2.997	0.759	0.934	0.006	0.022	0.016
Blow 7 Run 3	0.033	0.024	0.802	1.671	0.053	0.419	0.006	0.020	0.015
Blow 7 Run 4	0.029	0.030	2.695	1.415	0.026	0.387	0.003	0.026	0.000
Blow 7 Run 5	0.044	0.021	2.547	2.261	0.425	0.123	0.009	0.017	0.023
Blow 8 Run 1	0.050	0.032	1.919	0.903	0.155	0.347	0.001	0.014	0.022
Blow 8 Run 2	0.039	0.038	0.889	2.729	0.513	0.972	0.002	0.033	0.001
Blow 8 Run 3	0.022	0.027	2.834	2.633	0.800	0.133	0.001	0.031	0.008
Blow 8 Run 4	0.023	0.026	1.671	2.335	0.023	0.905	0.001	0.030	0.010
Blow 8 Run 5	0.039	0.037	0.369	3.011	0.653	0.844	0.002	0.033	0.003
Blow 9 Run 1	0.055	0.040	2.214	3.286	0.915	0.968	0.008	0.016	0.016
Blow 9 Run 2	0.027	0.034	1.334	2.335	0.997	0.508	0.003	0.028	0.005
Blow 9 Run 3	0.048	0.032	2.006	2.816	0.440	0.601	0.007	0.020	0.018
Blow 9 Run 4	0.035	0.026	1.152	2.105	0.631	0.114	0.022	0.035	0.177
Blow 9 Run 5	0.037	0.024	2.442	0.574	0.555	0.277	0.019	0.035	0.179
Average	**0.032**	**0.026**	**1.940**	**2.399**	**0.471**	**0.564**	**0.009**	**0.026**	**0.015**
Std. Dev.	**0.009**	**0.005**	**0.850**	**0.771**	**0.291**	**0.280**	**0.008**	**0.007**	**0.036**

Table C.4: Identified other parameters for H-pile using RSS match quality definition

Case	q_{shaft}	q_{toe}	Shaft $\frac{E_{un}}{E_u}$	Toe $\frac{E_{un}}{E_u}$	Shaft -$\frac{R_{un}}{R_u}$	Toe -$\frac{R_{un}}{R_u}$	J_{shaft}	J_{toe}	g_{toe}
Blow 1 Run 1	0.062	0.042	1.451	2.001	0.367	0.615	0.024	0.033	0.027
Blow 1 Run 2	0.052	0.040	2.855	2.977	0.018	0.428	0.026	0.032	0.019
Blow 1 Run 3	0.053	0.043	0.848	1.618	0.234	0.559	0.027	0.035	0.018
Blow 1 Run 4	0.056	0.033	1.175	1.449	0.416	0.786	0.027	0.029	0.027
Blow 1 Run 5	0.054	0.030	2.138	0.670	0.505	0.717	0.028	0.032	0.029
Blow 2 Run 1	0.030	0.020	2.204	3.028	0.465	0.804	0.011	0.007	0.010
Blow 2 Run 2	0.030	0.021	0.442	3.161	0.869	0.083	0.010	0.015	0.010
Blow 2 Run 3	0.026	0.023	1.934	1.609	0.653	0.455	0.011	0.017	0.003
Blow 2 Run 4	0.026	0.022	1.775	2.182	0.732	0.412	0.010	0.027	0.000
Blow 2 Run 5	0.027	0.022	1.868	0.635	0.959	0.880	0.010	0.032	0.007
Blow 3 Run 1	0.041	0.024	1.242	2.457	0.442	0.108	0.010	0.032	0.014
Blow 3 Run 2	0.038	0.032	3.079	2.812	0.375	0.887	0.010	0.035	0.007
Blow 3 Run 3	0.045	0.024	2.203	2.413	0.108	0.922	0.012	0.015	0.022
Blow 3 Run 4	0.036	0.037	2.505	2.898	0.063	0.921	0.008	0.036	0.002
Blow 3 Run 5	0.021	0.025	2.899	1.883	0.993	0.247	0.017	0.009	0.013
Blow 4 Run 1	0.070	0.069	1.833	3.224	0.542	0.980	0.025	0.031	0.005
Blow 4 Run 2	0.020	0.029	2.574	0.847	0.935	0.062	0.032	0.028	0.031
Blow 4 Run 3	0.064	0.038	2.165	1.240	0.775	0.834	0.032	0.030	0.032
Blow 4 Run 4	0.060	0.021	2.280	2.542	0.016	0.182	0.028	0.034	0.043
Blow 4 Run 5	0.069	0.020	2.632	2.472	0.357	0.578	0.033	0.026	0.054
Average	**0.044**	**0.031**	**2.005**	**2.106**	**0.491**	**0.573**	**0.019**	**0.027**	**0.019**
Std. Dev.	**0.016**	**0.012**	**0.700**	**0.833**	**0.315**	**0.310**	**0.009**	**0.009**	**0.014**

Table C.5: Identified resistance parameters for sheet pile Using the traditional MQ definition

Case	MQ	$R_{u,1}$	$R_{u,2}$	$R_{u,3}$	$R_{u,4}$	R_{shaft}	$R_{u,toe}$	$R_{u,total}$
Blow 1 Run 1	7.862	3.24	6.28	7.87	6.19	**23.59**	**3.76**	**27.35**
Blow 1 Run 2	7.862	3.24	6.28	7.87	6.19	**23.59**	**3.76**	**27.35**
Blow 1 Run 3	7.862	3.24	6.28	7.87	6.19	**23.59**	**3.76**	**27.35**
Blow 1 Run 4	7.963	1.77	9.00	4.37	11.13	**26.26**	**0.63**	**26.90**
Blow 1 Run 5	7.624	1.49	10.20	3.46	2.75	**17.91**	**9.58**	**27.49**
Blow 2 Run 1	8.553	0.32	10.68	11.12	10.03	**32.15**	**6.70**	**38.85**
Blow 2 Run 2	8.553	0.32	10.68	11.12	10.03	**32.15**	**6.70**	**38.85**
Blow 2 Run 3	8.553	0.32	10.68	11.12	10.03	**32.15**	**6.70**	**38.85**
Blow 2 Run 4	8.133	0.15	20.20	5.87	0.32	**26.54**	**11.90**	**38.45**
Blow 2 Run 5	8.799	0.31	4.78	16.86	6.99	**28.94**	**9.02**	**37.96**
Blow 3 Run 1	10.379	0.17	7.65	12.53	0.13	**20.49**	**19.68**	**40.17**
Blow 3 Run 2	10.379	0.17	7.65	12.53	0.13	**20.49**	**19.68**	**40.17**
Blow 3 Run 3	10.379	0.17	7.65	12.53	0.13	**20.49**	**19.68**	**40.17**
Blow 3 Run 4	10.272	0.10	5.57	26.54	0.28	**32.49**	**5.66**	**38.14**
Blow 3 Run 5	10.225	0.14	10.76	22.10	0.10	**33.10**	**6.07**	**39.17**
Blow 4 Run 1	8.952	0.16	0.31	19.44	0.51	**20.42**	**7.15**	**27.57**
Blow 4 Run 2	8.952	0.16	0.31	19.44	0.51	**20.42**	**7.15**	**27.57**
Blow 4 Run 3	8.952	0.16	0.31	19.44	0.51	**20.42**	**7.15**	**27.57**
Blow 4 Run 4	8.906	0.19	0.46	14.44	6.39	**21.49**	**5.45**	**26.93**
Blow 4 Run 5	8.982	0.47	0.39	17.76	3.85	**22.46**	**4.64**	**27.10**
Blow 5 Run 1	9.172	5.35	13.73	1.09	0.24	**20.41**	**11.75**	**32.16**
Blow 5 Run 2	9.172	5.35	13.73	1.09	0.24	**20.41**	**11.75**	**32.16**
Blow 5 Run 3	9.172	5.35	13.73	1.09	0.24	**20.41**	**11.75**	**32.16**
Blow 5 Run 4	9.286	2.32	18.56	0.80	0.31	**21.99**	**8.86**	**30.85**
Blow 5 Run 5	9.349	0.28	14.05	0.49	5.64	**20.47**	**9.00**	**29.47**
Blow 6 Run 1	11.354	0.13	11.87	6.19	0.43	**18.63**	**7.47**	**26.09**
Blow 6 Run 2	11.354	0.13	11.87	6.19	0.43	**18.63**	**7.47**	**26.09**
Blow 6 Run 3	11.354	0.13	11.87	6.19	0.43	**18.63**	**7.47**	**26.09**
Blow 6 Run 4	11.326	0.13	9.77	3.84	0.20	**13.94**	**12.87**	**26.81**
Blow 6 Run 5	11.455	0.16	11.36	9.68	1.42	**22.62**	**5.16**	**27.77**
Blow 7 Run 1	9.433	0.17	12.99	0.22	0.34	**13.72**	**8.65**	**22.37**
Blow 7 Run 2	9.433	0.17	12.99	0.22	0.34	**13.72**	**8.65**	**22.37**
Blow 7 Run 3	9.433	0.17	12.99	0.22	0.34	**13.72**	**8.65**	**22.37**
Blow 7 Run 4	9.401	0.16	11.64	0.44	2.16	**14.39**	**7.07**	**21.46**
Blow 7 Run 5	9.367	0.10	9.19	0.60	1.16	**11.05**	**8.95**	**20.00**
Blow 8 Run 1	8.512	2.60	2.83	0.30	15.74	**21.47**	**3.25**	**24.72**
Blow 8 Run 2	8.512	2.60	2.83	0.30	15.74	**21.47**	**3.25**	**24.72**
Blow 8 Run 3	8.512	2.60	2.83	0.30	15.74	**21.47**	**3.25**	**24.72**
Blow 8 Run 4	8.472	3.12	4.85	0.41	0.24	**8.62**	**16.77**	**25.39**
Blow 8 Run 5	8.520	7.31	5.92	1.94	0.20	**15.38**	**9.33**	**24.70**
Blow 9 Run 1	15.749	12.43	0.10	0.16	6.00	**18.69**	**4.01**	**22.70**
Blow 9 Run 2	15.749	12.43	0.10	0.16	6.00	**18.69**	**4.01**	**22.70**
Blow 9 Run 3	15.749	12.43	0.10	0.16	6.00	**18.69**	**4.01**	**22.70**
Blow 9 Run 4	15.650	11.26	0.32	0.14	7.72	**19.44**	**3.32**	**22.76**
Blow 9 Run 5	15.324	9.29	0.20	0.21	8.45	**18.15**	**4.39**	**22.54**
Average	9.977	**2.50**	**7.70**	**6.82**	**3.96**	**20.976**	**7.91**	**28.885**
Std. Dev.	-	**3.72**	**5.42**	**7.34**	**4.70**	**5.624**	**4.47**	**6.163**

Table C.6: Identified resistance parameters for H-Pile using the traditional MQ definition

Case	MQ	$R_{u,1}$	$R_{u,2}$	$R_{u,3}$	$R_{u,4}$	R_{shaft}	$R_{u,toe}$	$R_{u,total}$
Blow 1 Run 1	12.818	0.19	0.35	6.66	0.15	**7.35**	**7.42**	**14.77**
Blow 1 Run 2	12.818	0.19	0.35	6.66	0.15	**7.35**	**7.42**	**14.77**
Blow 1 Run 3	12.827	0.10	0.14	9.14	2.77	**12.15**	**2.54**	**14.69**
Blow 1 Run 4	12.792	0.13	0.18	8.38	5.38	**14.08**	**0.93**	**15.01**
Blow 1 Run 5	12.791	0.14	0.17	7.77	5.87	**13.95**	**1.17**	**15.12**
Blow 2 Run 1	11.090	0.16	0.30	9.73	6.96	**17.15**	**1.63**	**18.78**
Blow 2 Run 2	11.090	0.16	0.30	9.73	6.96	**17.15**	**1.63**	**18.78**
Blow 2 Run 3	11.106	0.16	0.18	9.11	5.73	**15.18**	**3.80**	**18.98**
Blow 2 Run 4	11.086	0.13	0.35	7.43	10.81	**18.71**	**0.37**	**19.09**
Blow 2 Run 5	11.078	0.22	0.38	9.43	8.58	**18.60**	**0.39**	**19.00**
Blow 3 Run 1	9.164	0.11	0.12	0.26	3.94	**4.42**	**7.12**	**11.55**
Blow 3 Run 2	9.164	0.11	0.12	0.26	3.94	**4.42**	**7.12**	**11.55**
Blow 3 Run 3	9.266	0.12	0.13	0.15	9.04	**9.44**	**2.01**	**11.45**
Blow 3 Run 4	9.198	0.14	0.21	0.16	5.68	**6.19**	**5.10**	**11.29**
Blow 3 Run 5	9.159	0.10	0.16	0.16	5.52	**5.94**	**5.59**	**11.54**
Blow 4 Run 1	8.885	0.10	0.14	0.10	2.56	**2.90**	**7.73**	**10.63**
Blow 4 Run 2	8.885	0.10	0.14	0.10	2.56	**2.90**	**7.73**	**10.63**
Blow 4 Run 3	8.840	0.10	0.12	0.10	2.55	**2.87**	**7.92**	**10.78**
Blow 4 Run 4	8.896	0.10	0.11	0.20	3.51	**3.92**	**6.43**	**10.34**
Blow 4 Run 5	8.837	0.12	0.19	0.10	2.55	**2.96**	**7.92**	**10.88**
Average	10.490	**0.13**	**0.21**	**4.28**	**4.76**	**9.382**	**4.60**	**13.979**
Std. Dev.	-	**0.04**	**0.09**	**4.31**	**2.83**	**5.867**	**2.95**	**3.350**

Table C.7: Identified resistance parameters for H-pile using traditional MQ definition

Case	$R_{u,1}$	$R_{u,2}$	$R_{u,3}$	$R_{u,4}$	R_{shaft}	R_{toe}	$R_{u,total}$
Blow 1 Run 1	0.19	0.35	6.66	0.15	**7.35**	**7.42**	**14.77**
Blow 1 Run 2	0.19	0.35	6.66	0.15	**7.35**	**7.42**	**14.77**
Blow 1 Run 3	0.10	0.14	9.14	2.77	**12.15**	**2.54**	**14.69**
Blow 1 Run 4	0.13	0.18	8.38	5.38	**14.08**	**0.93**	**15.01**
Blow 1 Run 5	0.14	0.17	7.77	5.87	**13.95**	**1.17**	**15.12**
Blow 2 Run 1	0.16	0.30	9.73	6.96	**17.15**	**1.63**	**18.78**
Blow 2 Run 2	0.16	0.30	9.73	6.96	**17.15**	**1.63**	**18.78**
Blow 2 Run 3	0.16	0.18	9.11	5.73	**15.18**	**3.80**	**18.98**
Blow 2 Run 4	0.13	0.35	7.43	10.81	**18.71**	**0.37**	**19.09**
Blow 2 Run 5	0.22	0.38	9.43	8.58	**18.60**	**0.39**	**19.00**
Blow 3 Run 1	0.11	0.12	0.26	3.94	**4.42**	**7.12**	**11.55**
Blow 3 Run 2	0.11	0.12	0.26	3.94	**4.42**	**7.12**	**11.55**
Blow 3 Run 3	0.12	0.13	0.15	9.04	**9.44**	**2.01**	**11.45**
Blow 3 Run 4	0.14	0.21	0.16	5.68	**6.19**	**5.10**	**11.29**
Blow 3 Run 5	0.10	0.16	0.16	5.52	**5.94**	**5.59**	**11.54**
Blow 4 Run 1	0.10	0.14	0.10	2.56	**2.90**	**7.73**	**10.63**
Blow 4 Run 2	0.10	0.14	0.10	2.56	**2.90**	**7.73**	**10.63**
Blow 4 Run 3	0.10	0.12	0.10	2.55	**2.87**	**7.92**	**10.78**
Blow 4 Run 4	0.10	0.11	0.20	3.51	**3.92**	**6.43**	**10.34**
Blow 4 Run 5	0.12	0.19	0.10	2.55	**2.96**	**7.92**	**10.88**
Average	**0.13**	**0.21**	**4.28**	**4.76**	**9.382**	**4.60**	**13.979**
Std. Dev.	**0.04**	**0.09**	**4.31**	**2.83**	**5.867**	**2.95**	**3.350**

Table C.8: Identified other parameters for H-pile using traditional MQ definition

Case	q_{shaft}	q_{toe}	Shaft $\frac{E_{un}}{E_u}$	Toe $\frac{E_{un}}{E_u}$	Shaft -$\frac{R_{un}}{R_u}$	Toe -$\frac{R_{un}}{R_u}$	J_{shaft}	J_{toe}	g_{toe}
Blow 1 Run 1	0.076	0.050	1.558	0.681	0.007	0.123	0.015	0.030	0.030
Blow 1 Run 2	0.076	0.050	1.558	0.681	0.007	0.123	0.015	0.030	0.030
Blow 1 Run 3	0.081	0.061	1.545	0.423	0.012	0.763	0.020	0.035	0.009
Blow 1 Run 4	0.058	0.032	0.923	3.291	0.986	0.010	0.022	0.028	0.009
Blow 1 Run 5	0.050	0.021	0.800	3.298	0.871	0.022	0.024	0.001	0.037
Blow 2 Run 1	0.057	0.057	0.300	0.362	0.869	0.715	0.014	0.002	0.001
Blow 2 Run 2	0.057	0.057	0.300	0.362	0.869	0.715	0.014	0.002	0.001
Blow 2 Run 3	0.060	0.063	0.316	0.307	0.920	0.763	0.016	0.001	0.003
Blow 2 Run 4	0.063	0.064	0.300	0.413	0.779	0.473	0.012	0.016	0.001
Blow 2 Run 5	0.061	0.057	0.300	0.311	0.872	0.780	0.013	0.011	0.000
Blow 3 Run 1	0.079	0.065	0.303	0.307	0.903	0.888	0.004	0.033	0.005
Blow 3 Run 2	0.079	0.065	0.303	0.307	0.903	0.888	0.004	0.033	0.005
Blow 3 Run 3	0.077	0.075	0.300	0.360	0.980	0.571	0.027	0.002	0.000
Blow 3 Run 4	0.084	0.075	0.300	0.337	0.211	1.000	0.021	0.026	0.000
Blow 3 Run 5	0.085	0.073	0.301	0.315	0.502	0.850	0.015	0.030	0.004
Blow 4 Run 1	0.043	0.020	0.550	0.342	0.597	0.098	0.014	0.036	0.070
Blow 4 Run 2	0.043	0.020	0.550	0.342	0.597	0.098	0.014	0.036	0.070
Blow 4 Run 3	0.020	0.069	2.254	0.617	0.367	0.824	0.026	0.030	0.005
Blow 4 Run 4	0.077	0.056	1.632	0.673	0.552	0.192	0.027	0.034	0.026
Blow 4 Run 5	0.029	0.061	2.770	0.690	0.177	0.476	0.009	0.036	0.012
Average	**0.063**	**0.055**	**0.858**	**0.721**	**0.599**	**0.519**	**0.016**	**0.023**	**0.016**
Std. Dev.	**0.019**	**0.018**	**0.759**	**0.892**	**0.352**	**0.345**	**0.007**	**0.014**	**0.022**

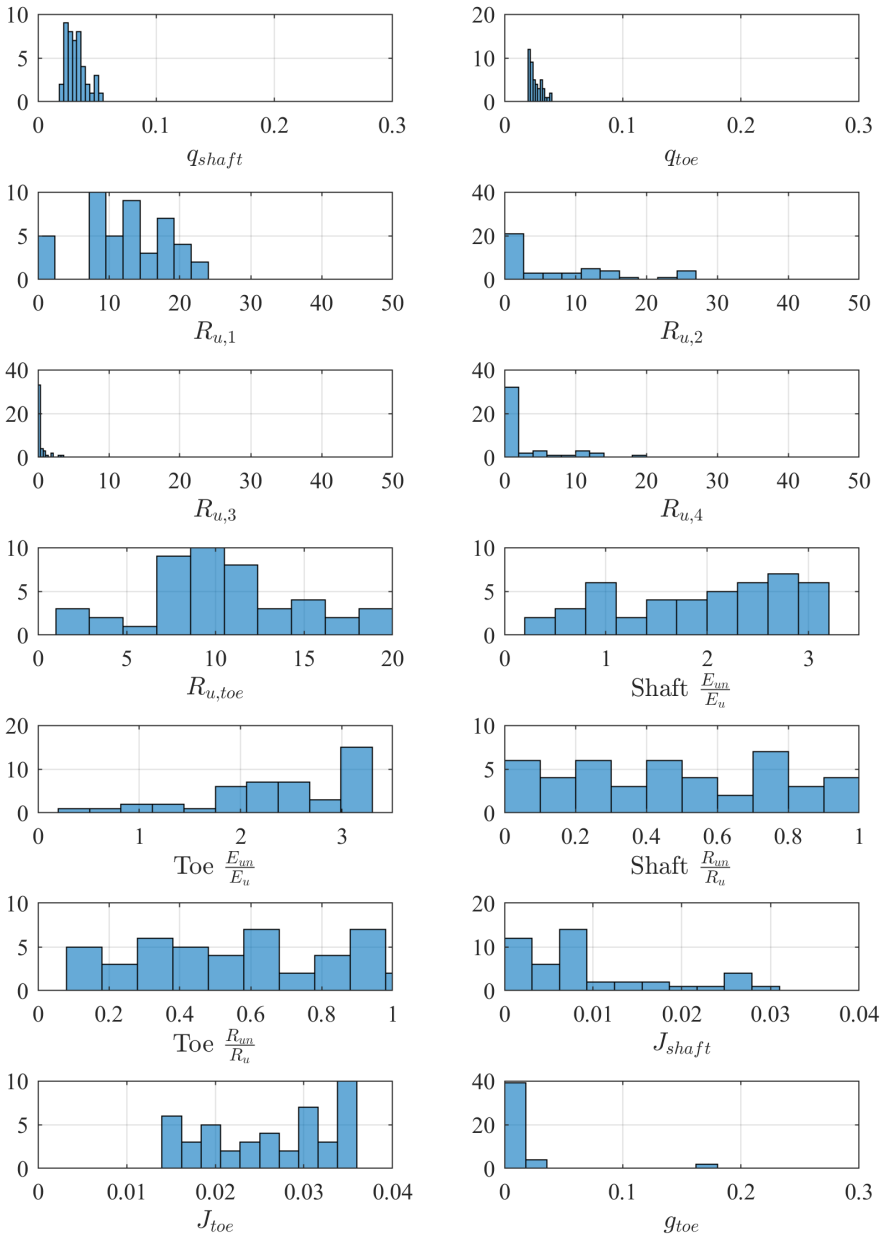

Figure C.1: Distributions of parameters found through the RSS definition signal match of the sheet pile

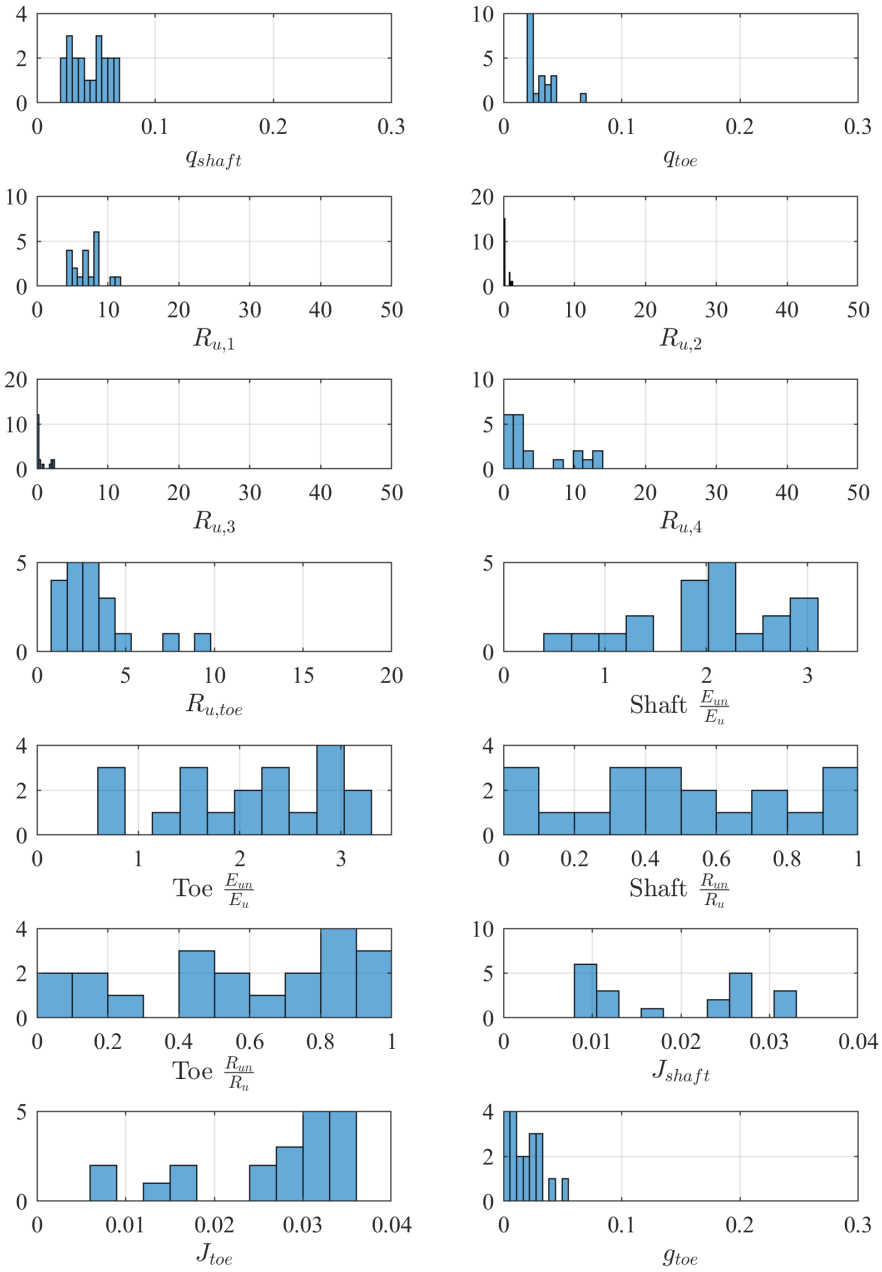

Figure C.2: Distributions of parameters found through the RSS definition signal match of the H-pile